Experimental and Theoretical Studies of Hexagonal Boron Nitride Single Crystal Growth

by

Song Liu

B.S., Beijing University of Chemical Technology, 2013

AN ABSTRACT OF A DISSERTATION

submitted in partial fulfillment of the requirements for the degree

DOCTOR OF PHILOSOPHY

Department of Chemical Engineering
College of Engineering

KANSAS STATE UNIVERSITY
Manhattan, Kansas

2018

Abstract

Hexagonal boron nitride (hBN) has recently been envisioned for electronic, optoelectronic, and nanophotonic applications due to its strong anisotropy and unique properties. To realize these applications, the ability to synthesize single crystals with large size and low defect density is required. Furthermore, a detailed mechanistic understanding of hBN growth process is helpful for understanding and optimizing the synthesis technique for high quality crystals.

In this dissertation, the production of large-scale, high-quality hBN single crystals via precipitation from metal solvents, including Ni-Cr and Fe-Cr, was demonstrated. The use of Fe-Cr mixture provides a lower cost alternative to the more common Ni-Cr solvent for growing comparable crystals. The clear and colorless crystals have a maximum domain size of around 2 mm and a thickness of around 200 μm. Detailed characterizations demonstrated that the crystals produced are pure hBN phase, with low defect and residual impurity concentrations. The temperature-dependent optical response of excitons showed that the exciton-phonon interaction in bulk hBN is in the strong-coupling regime.

A new growth method for monoisotopic hBN single crystals, i.e. $h^{10}BN$ and $h^{11}BN$, was developed, by which hBN single crystals were grown using a Ni-Cr solvent and pure boron and nitrogen sources at atmospheric pressure. The chemical bonding analysis revealed that the B-N bond in $h^{11}BN$ is slightly stronger than that in $h^{10}BN$. The polariton lifetime in our monoisotopic hBN samples increases threefold over the naturally abundant hBN, and the isotopic substitution changes the electron density distribution and the energy bandgap of hBN. The ability to produce crystals in this manner opens the door to isotopically engineering the properties and performance of hBN devices.

Atomistic-scale insights into the growth of hBN were obtained from multiscale modeling combining density functional theory (DFT) and reactive molecular dynamics (rMD). The energetics and kinetics of BN species on Ni(111) and Ni(211) surfaces were calculated by DFT. These DFT calculations data were subsequently used to generate a classical description of the Ni-B and Ni-N pair interactions within the formulation of the reactive force field, i.e., ReaxFF. MD simulations under the newly developed potential helped reveal the elementary nucleation and growth process of an hBN monolayer - nucleation initiates from the growth of linear BN chains, which further evolve into branched and then hexagonal lattices.

In the end, molecular dynamics simulations demonstrated that the thermodynamic preference of hBN geometries varying from triangle to hexagonal can be tuned by B to N molar ratios, and gas phase N_2 partial pressure, which is also supported by quantum mechanics calculations. The modeling confirms that the nitrogen species indeed plays an important role in dictating sizes and edge terminations of hBN sheets.

Experimental and Theoretical Studies of Hexagonal Boron Nitride Single Crystal Growth

by

Song Liu

B.S., Beijing University of Chemical Technology, 2013

A DISSERTATION

submitted in partial fulfillment of the requirements for the degree

DOCTOR OF PHILOSOPHY

Department of Chemical Engineering
College of Engineering

KANSAS STATE UNIVERSITY
Manhattan, Kansas

2018

Approved by:

Major Professor
James H. Edgar

Copyright

Abstract

Hexagonal boron nitride (hBN) has recently been envisioned for electronic, optoelectronic, and nanophotonic applications due to its strong anisotropy and unique properties. To realize these applications, the ability to synthesize single crystals with large size and low defect density is required. Furthermore, a detailed mechanistic understanding of hBN growth process is helpful for understanding and optimizing the synthesis technique for high quality crystals.

In this dissertation, the production of large-scale, high-quality hBN single crystals via precipitation from metal solvents, including Ni-Cr and Fe-Cr, was demonstrated. The use of Fe-Cr mixture provides a lower cost alternative to the more common Ni-Cr solvent for growing comparable crystals. The clear and colorless crystals have a maximum domain size of around 2 mm and a thickness of around 200 μm. Detailed characterizations demonstrated that the crystals produced are pure hBN phase with low defect and residual impurity concentrations. The temperature-dependent optical response of excitons showed that the exciton-phonon interaction in bulk hBN is in the strong-coupling regime.

A new growth method for monoisotopic hBN single crystals, i.e. $h^{10}BN$ and $h^{11}BN$, was developed, by which hBN single crystals were grown using a Ni-Cr solvent and pure boron and nitrogen sources at atmospheric pressure. The chemical bonding analysis revealed that the B-N bond in $h^{11}BN$ is slightly stronger than that in $h^{10}BN$. The polariton lifetime in our monoisotopic hBN samples increases threefold over the naturally abundant hBN, and the isotopic substitution changes the electron density distribution and the energy bandgap of hBN. The ability to produce crystals in this manner opens the door to isotopically engineering the properties and performance of hBN devices.

Atomistic-scale insights into the growth of hBN were obtained from multiscale modeling combining density functional theory (DFT) and reactive molecular dynamics (rMD). The energetics and kinetics of BN species on Ni(111) and Ni(211) surfaces were calculated by DFT. These DFT calculations data were subsequently used to generate a classical description of the Ni-B and Ni-N pair interactions within the formulation of the reactive force field, i.e., ReaxFF. MD simulations under the newly developed potential helped reveal the elementary nucleation and growth process of an hBN monolayer - nucleation initiates from the growth of linear BN chains, which further evolve into branched and then hexagonal lattices.

In the end, molecular dynamics simulations demonstrated that the thermodynamic preference of hBN geometries varying from triangle to hexagonal can be tuned by B to N molar ratios and gas phase N_2 partial pressure, which is also supported by quantum mechanics calculations. The modeling confirms that the nitrogen species indeed plays an important role in dictating sizes and edge terminations of hBN sheets.

Table of Contents

List of Figures

List of Tables

Acknowledgements

I would like to express my deepest gratitude to my two advisors, Dr. James H. Edgar and Dr. Bin Liu, for mentoring and inspiring me during the last five years. I have been very fortunate to be co-advised by them who have strong expertise, critical thinking, and broad vision. They have been supportive not only my research but also my routine life throughout the whole Ph.D. period. I also feel grateful to Dr. Christine Aikens for her professional guidance on my simulation studies. I would also like to thank my committee members, Dr. John Schlup, Dr. Paul Smith, and Dr. Glenn Horton-Smith, for their valuable time and suggestions on my research.

I'm very grateful to all of my research collaborators, including Dr. Joshua Caldwell and Dr. Tom Folland at Vanderbilt University, who collaborated with us on the nanophotonics investigation. Dr. Guillaume Cassabois and Dr. Bernard Gil at University Montpellier, who explored several new physical properties in our hBN crystal. Dr. Peining Li and Dr. Rainer Hillenbrand at CIC nanoGune, who fabricated infrared hyperbolic metasurfaces from our hBN crystals. Dr. Neelam Khan at Georgia Gwinnett College, who performed AFM analysis. Dr. Rui He and Dr. Hongxing Jiang at Texas Tech University, who did Raman and Photoluminescence measurements for our samples.

I would like to thank all the department staff in Chemical Engineering, especially David Threewit, Debra Wahl, Karen Strathman, and Danita Deters, for their tremendous support. I also want to acknowledge all Beocat staff members, including Adam Tygart, David Turner, and Kyle Hutson, for their technical support on my simulation research.

Last but not least, I am forever grateful to my beloved parents who have been supporting me unconditionally no matter what. Without their dedications and sacrifices, none of this would have been possible. I will never forget that!

Dedication

To my family and my dream!

Chapter 1 - Introduction

This chapter will first introduce the basics of hexagonal boron nitride (hBN) and its physical and chemical properties. Then, the traditional and new applications of hBN will be described. After that, a literature review of hBN synthesis methods will be introduced. In the end, theoretical methods that are used to investigate hBN growth mechanism will be discussed.

1.1 Hexagonal Boron Nitride

Hexagonal boron nitride (hBN), which has a similar structure with graphite, is a wide band gap (~ 5.97 eV) III-V semiconductor with distinguished physical properties and remarkable chemical and thermal stabilities.[1] It consists of stacked layers with sp^2 hybridized boron and nitrogen in a two-dimensional (2D) honeycomb plane, as shown in Figure 1.1. The in-plane boron and nitrogen atoms are bound together with strong covalent bonds, while the layers interact with each other via weak van der Waals force.

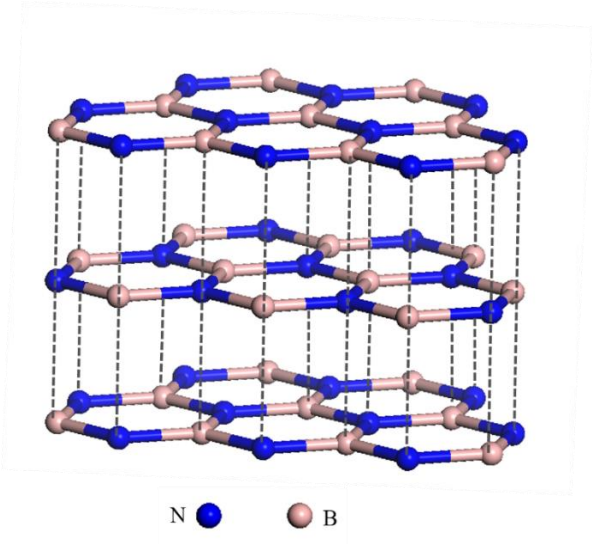

Figure 1.1. Crystal structures of hexagonal boron nitride

hBN is electrically insulating with an ultra-smooth surface, which makes it a promising dielectric substrate to tune the carrier mobility of other 2D materials, such as graphene and BP, by reducing scattering.[2,3] The strong covalent sp^2 bonds in hBN make it have high temperature stability (the melting point is around 2600 ℃), chemical inertness (corrosion resistance against acids), and chemical stability (stable in air up to 1000 °C).[4] In contrast to its electrical insulation, hBN has a high thermal conductivity, which is comparable to that of stainless steel.[5] The other properties include high elastic modulus, low friction coefficient, and strong cathodoluminescence (CL) emission in the deep ultraviolet range.[6,7] Recently, hBN was demonstrated to be a natural hyperbolic metamaterial,[8] which has several unique nanophotonic properties including strong optical confinement and low-loss of phonon-polariton.

The most common hBN has the natural distribution of boron isotopes, which is 19.9% ^{10}B and 80.1% ^{11}B. However, the hBN properties can be impacted by the boron isotopes concentrations in the crystal. Since ^{10}B has a capture cross-section of 3840 b for thermal neutrons (with 0.025 eV energy), hBN with pure ^{10}B enrichment ($h^{10}BN$) is very efficient as a neutron detector[9,10]. Both experimental and theoretical studies[11-13] have shown that the thermal conductivity of hBN can be significantly enhanced in isotopically pure materials, as the phonon-isotope scattering in the crystal is much weaker than that in naturally abundant hBN. Most recently, Giles *et al.*[14] demonstrated that the polariton lifetime in isotopically enriched hBN has a threefold improvement over the naturally abundant hBN, and Vuong *et al.*[15] found that the boron isotope concentration slightly changes the energy bandgap in hBN.

1.2 Hexagonal Boron Nitride Applications

For more than fifty years, hexagonal boron nitride (hBN) has been employed in

applications exploiting its high thermal conductivity,[16,17] chemical stability,[18,19] refractory nature,[20,21] high electrical resistivity,[22,23] and lubricity[24,25]. For these applications, powders, polycrystalline ceramics, and pyrolytic forms are sufficient. Grain, domain, and particle sizes can be small, and no control of the hBN's crystallographic orientation is required.

Over the past ten years, new applications have been envisioned, which utilize the optical hyperbolicity,[26] nuclear, atomically flat surfaces,[27] flexoelectricity,[28] and electronic properties of hBN, in a wide variety of forms: bulk crystals, atomically thin layers (nanosheets), and nanotubes. Examples include hBN deep ultraviolet light emitters (i.e., light emitting diodes and laser diodes),[29,30] neutron detectors,[31,32] nanophotonics,[8,33] and single photon emitters,[34] as will be listed below.

1.2.1 Deep Ultraviolet (DUV) Light Emitter

Deep ultraviolet (DUV) light emitters have been widely applied in areas of water sterilization,[35] medical equipment,[36] fluorescence probe in protein and photocatalysis.[37] However, conventional DUV systems suffer from high cost, large size and weight, and low efficiency. These drawbacks motivate the rapid development of high-efficiency DUV light emitters with longer operating lives, such as III-nitride semiconductors. For example, DUV LEDs fabricated by AlGaN material demonstrate stable light emission at 278 nm with a high efficiency.[38] hBN is another promising material that has attracted much interest for DUV emitter fabrication due to its wide bandgap (~5.97 eV) as well as the ultraviolet luminescence property. High-purity hBN shows intense excitonic luminescence bands from 215 to 227 nm,[39,40] which are sufficient to cause strong UV emission. For example, Watanabe *et al.*[41] designed a DUV emitter based on hBN, which

demonstrated stable operation with an output power of 0.2 mW at 225 nm. This device can even be driven by dry batteries.

1.2.2 Neutron Detector

Neutron detectors with high detection efficiency are needed in a wide range of applications, such as nuclear materials sensing,[42] neutron therapy,[43] oil exploration,[44] and medical imaging.[45] Currently, neutron detectors are mainly fabricated using ^{3}He gas.[46] However, due to the global shortage of ^{3}He and transportation difficulty, a replacement technology for neutron detection is highly desired. ^{10}B has a capture cross-section of about 3840 b for thermal neutrons,[47] which enables conversions of thermal neutrons that undergo two different decay channels as described below[48]:

I. $^{10}_{5}\mathrm{B} + \mathrm{n} \rightarrow {}^{7}_{3}\mathrm{Li} + \alpha \rightarrow {}^{7}_{3}\mathrm{Li} + \alpha + \gamma(0.48\ \mathrm{MeV}) + 2.31\ \mathrm{MeV}$ (94%)

II. $^{10}_{5}\mathrm{B} + \mathrm{n} \rightarrow {}^{7}_{3}\mathrm{Li} + \alpha + 2.79\ \mathrm{MeV}$ (6%)

where the first one is the most common pathway with an occurring chance of 94%. However, an ^{10}B layer coated device shows a very low detection efficiency (< 5%) for thermal neutrons due to the conflict of the layer thickness and the escape rate of products (α and Li). The advantages of h^{10}BN (isotopic enriched with ^{10}B) as a solid-state neutron detector have recently been demonstrated; such devices can have an extremely high detection efficiency (~88.6%) of thermal neutron.[49] The single crystalline structure of hBN contains very few charge traps and allows the rapid escape of electrons produced by the reaction, which leads to a high charge collection efficiency.

1.2.3 Substrate for 2D Materials

Since the first exfoliation of graphene by Novoselov *et al* in 2004,[50] research on two-dimensional (2D) materials has exploded due to their unique properties and low dimensional structures distinct from their bulk forms. 2D materials have been widely applied in novel electronic and optical devices, in which the substrates play an important role in devices performance. Traditional substrates, including SiO_2, SiC, and Al_2O_3, limit the device function due to their charged surface states, surface roughness, and impurities.[51-55] For example, graphene devices on SiO_2 exhibited properties that are far inferior to the theoretical prediction.[56-58] In contrast, hBN is a superior substrate for 2D materials due to its smooth surfaces, large bandgap, high electric insulation, high thermal conductivity, and surface optical modes.[59,60] The lattice constant mismatch between hBN and graphene is only 1.8%, which makes hBN a suitable candidate as a graphene substrate. Dean *et al*[61] demonstrated high mobility in graphene devices on hBN, which are almost an order of magnitude better than the devices on SiO_2. These devices also demonstrate reduced disorder and chemical reactivity. In addition, Lee *et al.* have fabricated flexible and transparent MoS_2 field-effect transistors (FETs) on a hBN substrate, with a field-effect mobility of up to 45 cm^2/Vs and operating gate voltage below 10V.[62]

1.2.4 2D Heterostructures

Interest in hBN-based heterostructures has exploded due to the remarkable properties of its devices. For example, Woessner *et al.*[63] have demonstrated that encapsulation of graphene between two hBN films allows one to reduce the plasmon scattering from impurities and defects, which increases their inverse damping ratio by a factor of 4 and possesses ultralow-loss of plasmons compared with bare graphene. Moreover, such heterostructures are possible to have a regime

where the plasmon polaritons in graphene and the phonon polaritons in hBN can strongly couple and form plasmon-phonon polaritons.[64,65] Successful synthesis of those heterostructures is crucial for devices performance. Among the most explored methods for hBN heterostructure growth, chemical vapor deposition (CVD) was mostly commonly used, as it can directly grow vertically stacked and in-plane heterostructures with controlled domain sizes.

1.2.5 Nanophotonic Devices

Electric dipoles, such as excitons, phonons, and plasmons, can be excited in many materials when illuminated,[66-68] and strongly couple with photons to form hybrid quasiparticles called polaritons. Polaritons, which can be sustained as electromagnetic modes with frequency ranges from hundreds of gigahertz to several terahertz, play an important role in high-resolution imaging and infrared sensing applications. However, in reality, the propagation of polaritons in many materials decays quickly, which limits the devices performance. hBN has been reported as a natural hyperbolic metamaterial[8], which possesses low-loss and strong confinement of phonon-polariton. Dai *et al.*[69] have investigated phonon-polariton (PhP) at hBN surface by using a scanning near-field optical microscopy (SNOM). This study demonstrated that the phonon-polariton resonance can be tuned by the number of hBN layers. In addition, Li *et al.*[70] have fabricated infrared hyperbolic metasurfaces from monoisotopic hBN, which allows for new flatland infrared and optoelectronic applications, such as infrared chemical sensing and flatland hyperlensing and exotic optical coupling.

1.3 Hexagonal Boron Nitride Synthesis

The earliest preparation of hexagonal boron nitride by Balmain can be traced back to the mid-19th century.[5] Since then, a variety of methods have been developed to synthesize hBN powders, bulk crystals, nanosheets, and nanotubes for different applications. Among them, chemical vapor deposition for nanosheets synthesis and metal flux method for bulk crystal preparation are mostly utilized. Here, both methods will be reviewed in detail.

1.3.1 Chemical Vapor Deposition

Chemical vapor deposition (CVD) of hBN on transition metal substrates, such as Ni,[71-76] Cu,[4,77-79] Pd,[80,81] and Pt,[82-84] has been employed to synthesize nanosheets with monolayers or multilayers. hBN nanosheet growth on Rh(111)[85], Ru(111)[86], and Ir(111)[87] has been observed by a real-time microscopy. The formation process is proposed as follows: the precursors introduced into the system first adsorb onto the substrate surface and then decompose to form mobile species. The diffusion and coalescence of those species lead to the formation of small hBN islands which serve as the nuclei for larger domain development and eventually combine together to form large-scale and compact hBN nanosheets.

The experimental conditions, such as precursor stoichiometry, substrate roughness, and reaction temperature, can significantly affect the synthesized hBN quality, size and thickness. Stehle *et al.*[88] demonstrated that hBN crystal shapes formed on Cu substrates change from triangular to truncated triangular and further to hexagonal by decreasing the nitrogen to boron (N: B) ratio. They also suggested that the highest temperatures are most suitable for high quality hBN growth, as the activation energy for both nucleation (~ 5 eV) and growth (~ 3.5 eV) on copper

substrate is very large. The substrates are usually pretreated at high temperature to recrystallize the metal to produce larger grain sizes, which in turn helps to make the hBN have a larger size too.

Other than the common substrates with single metals, alloy substrates were also explored. For example, Stehle *et al.*[89] have successfully synthesized single crystal hBN with sizes up to 7500 μm^2 on rational designed Cu-Ni alloy foils, which is about two orders of magnitude larger than those formed on single Cu or Ni substrates. Cabeva *et al.*[90] have demonstrated that the nucleation densities for monolayer hBN formation can be controlled to a very low range by tuning Si concentration in Fe substrate.

Although the CVD method is a promising technique to prepare atomically thin hBN nanomeshes, the presence of high-density grain boundaries and other defects degrades the properties of hBN obtained from CVD.[71,76,91] Alternatively, the best quality hBN single crystals can be precipitated from molten metal solutions.

1.3.2 Metal Flux Method

The metal flux method has been widely used for hBN bulk crystal synthesis, in which hBN powder is the commonly used source material which is dissolved into a liquid metal, followed by the precipitation of single crystals on the metal surface by slow cooling. A suitable metal solution must have a sufficient solubility for boron and nitrogen. Also, it should be thermodynamically stable at the reaction temperature.

Taniguchi[92] and Zhigadlo[93] have produced hBN crystals from metal solutions under high pressures (>30 kbar). However, crystals of similar quality can also be produced at atmospheric pressure. For example, Kubota *et al.*[39] first demonstrated atmospheric hBN crystal growth from a Ni-Mo solvent. They reported a Raman peak width of 9.0 cm^{-1} at 1367 cm^{-1}, which is much

narrower than what is typically reported for hBN produced by chemical vapor deposition, i.e., > 15 cm^{-1}.[94,95] The maximum cathodoluminescence energy of these materials was 5.76 eV, indicating a high crystal quality.

Near atmospheric growth is advantageous, since the crystal growth apparatus is simpler and thus easier to implement a lower cost. A later study by Kubota *et al*.[96] demonstrated that a 50 wt% mixture of Ni and Cr is an even better solvent for the atmospheric pressure solution growth of hBN single crystals. This alloy succeeds because Ni is a good solvent for boron with a maximum solubility of 18.5 at%,[97] and Cr can dissolve more nitrogen when compared to molybdenum.[98] Edgar's group has employed a Ni-Cr flux to produce hBN crystals that were (0001) orientated, a couple of millimeters across and up to 200 microns thick.[99,100] These crystals had excellent high energy deep ultraviolet photoluminescence spectra with an S-series excitonic emission at ~5.8 eV at room temperature.[101] They were also sufficiently thick (200 microns) to demonstrate interference-less absorption at infrared frequencies.[102] Liu *et al.*[103] have demonstrated that hBN Fe-Cr flux can provide a lower cost alternative to the Ni-Cr solvent for growing large-scale hBN of comparable quality.

1.4 Defects in Hexagonal Boron Nitride

Various defects, such as vacancies, edges, and grain boundaries, have been observed in the basal planes of hBN crystals. Those imperfections are mainly introduced during the synthesis process or by environmental contaminations. Gibb *et al.*[104] observed grain boundaries (GBs) in hBN sheets via ultra-high-resolution transmission electron microscopy at elevated temperature, where 5|7 defects are located along the grain boundary. Those 5|7 defects can migrate one unit cell in 4s, which was caused by the defect-defect repulsion with different orientations. Gibb *et al.*

performed systematic scanning tunneling microscopy/spectroscopy (STM/STS) studies on the grain boundaries composed of 5|7 and 4|8 pairs in hBN grown on Cu(111) surface. They found that the two types of GBs exhibit significantly different electronic properties, where the bandgap of 5|7 GBs is much lower than that of 4|8 GBs. This result has been verified by theoretical calculations.

In addition to the defects in the basal planes, the defects along the c-axis in hBN, such as dislocations, were also explored by using transmission electron microscopy (TEM) and x-ray diffraction studies to identify defects.[10,11] Stacking disorder, the imperfect alignment of basal planes, is common, and a consequence of the weak van der Waals bonding between layers. Delamination voids and misaligned stacked planes (causing rhombohedral stacking disorder) can form in hBN as it is cooled during the growth process due to external strain from the differences in thermal expansion at an hBN-metal interface. Twinning also occurs, as hBN has a limited number of slip systems. Many of the defects in hBN are similar to those common in graphite, since the structures of both are comparable, formed by a hexagonal lattice of atoms strongly bonded together in sp^2 configuration, with weak interlayer van der Waals bonds.[12]

1.5 Theoretical Studies on Hexagonal Boron Nitride

Current hBN crystals growth techniques are still imperfect, the small sizes and high-density defects limit the applications of these materials.[71,76,91] For this reason, a detailed mechanistic understanding of hBN growth process is desirable to improve the synthesis technique for high quality crystals. There are number of outstanding issues unresolved regarding hBN single crystal growth: how the termination and shape of hBN islands are governed by the chemical environment; how the defect structures are induced during growth; and how the hBN nucleation and growth are

influenced by the crystal facets and the electronic character of the metal catalyst.

1.5.1 Density Functional Theory

Density functional theory (DFT) calculations have matured into a powerful tool to accurately describe the physical and chemical properties relevant to various aspects associated with hBN characterization and synthesis. For instance, Grad *et al.*[105] and Díaz *et al.*[106] have determined and discussed the periodic hBN monolayer adsorption on transition metal substrates. For instance, on Ni(111), N prefers top sites, while B prefers either fcc or hcp sites. DFT calculations were employed to identify the favorable edge termination and the shape of hBN islands.[107] Furthermore, the decomposition chemistry of hBN precursors (e.g., BH_2NH_2) and the relationship with the compositions of substrates (e.g., Ni, Ni-Cu alloy) were modeled.[71] Most recently, using first-principles-based analysis, Zhang *et al.*[108] explored the shapes of hBN islands at varying boron chemical potentials on Cu(111) and Ni(111) with detailed growth kinetics of hBN edge structures.

1.5.2 Reactive Molecular Dynamic Simulation

Modeling of materials synthesis, including hBN, via the quantum mechanical approach rapidly becomes complex, thus rendering explicit DFT calculations inefficient or even impossible for thorough understanding of the structure evolution leading to the hBN lattice formation. As such, it is highly desirable to develop the capability by extending the modeling power of quantum mechanics to address the above critical questions regarding hBN growth. Molecular dynamics (MD) simulations, applying classical force field, can be utilized to handle large scale system and adding temperature effect.[109,110] However, most classical force fields, like MM3[111], Dreiding[112],

Amber[113], are incapable of simulating chemical reactions. For this reason, reactive molecular dynamics (rMD) simulation is an attractive alternative since it can provide a dynamic perspective of the crystal growth, especially for larger molecular systems with more than hundreds or thousands of atoms. In particular, it can model bond formation and breaking under a ReaxFF[114] reactive force field, which can be developed from quantum mechanical method.

1.6 Thesis Overview

The content in this chapter serves as background information of the thesis. The work mainly focused on synthesis and characterization of hBN single crystals by using both experimental and simulation methods. Chapter 2 introduces the experimental and theoretical methods utilized in this thesis. Chapter 3 and Chapter 4 describe hBN single crystal growth from Ni-Cr and Fe-Cr. In Chapter 5, monoisotopic hBN growth along with its unique properties and applications is discussed. Chapter 6 focuses on the synthesis of graphite single crystals from a Fe-Cr flux. Chapter 7 investigates the growth mechanism of monolayer hBN from first-principles-based rMD simulations. Chapter 8 presents the atomistic insights of hBN morphologies from rMD simulations.

References

1. Watanabe, K.; Taniguchi, T.; Kanda, H. Direct-bandgap properties and evidence for ultraviolet lasing of hexagonal boron nitride single crystal. *Nature Materials* **2004**, *3*, 404.
2. Cai, Y.; Zhang, G.; Zhang, Y. Electronic properties of phosphorene/graphene and phosphorene/hexagonal boron nitride heterostructures. *The Journal of Physical Chemistry C* **2015**, *119*, 13929-13936.

3. Doganov, R. A.; Koenig, S. P.; Yeo, Y.; Watanabe, K.; Taniguchi, T.; Özyilmaz, B. Transport properties of ultrathin black phosphorus on hexagonal boron nitride. *Appl. Phys. Lett.* **2015**, *106*, 083505.

4. Kim, K. K.; Hsu, A.; Jia, X.; Kim, S. M.; Shi, Y.; Hofmann, M.; Nezich, D.; Rodriguez-Nieva, J. F.; Dresselhaus, M.; Palacios, T. Synthesis of monolayer hexagonal boron nitride on Cu foil using chemical vapor deposition. *Nano Letters* **2011**, *12*, 161-166.

5. Lipp, A.; Schwetz, K. A.; Hunold, K. Hexagonal boron nitride: fabrication, properties and applications. *Journal of the European Ceramic Society* **1989**, *5*, 3-9.

6. Gao, R.; Yin, L.; Wang, C.; Qi, Y.; Lun, N.; Zhang, L.; Liu, Y.; Kang, L.; Wang, X. High-yield synthesis of boron nitride nanosheets with strong ultraviolet cathodoluminescence emission. *The Journal of Physical Chemistry C* **2009**, *113*, 15160-15165.

7. Yu, J.; Qin, L.; Hao, Y.; Kuang, S.; Bai, X.; Chong, Y.; Zhang, W.; Wang, E. Vertically aligned boron nitride nanosheets: chemical vapor synthesis, ultraviolet light emission, and superhydrophobicity. *ACS Nano* **2010**, *4*, 414-422.

8. Caldwell, J. D.; Kretinin, A. V.; Chen, Y.; Giannini, V.; Fogler, M. M.; Francescato, Y.; Ellis, C. T.; Tischler, J. G.; Woods, C. R.; Giles, A. J. Sub-diffractional volume-confined polaritons in the natural hyperbolic material hexagonal boron nitride. *Nature Communications* **2014**, *5*, 5221.

9. Li, J.; Dahal, R.; Majety, S.; Lin, J.; Jiang, H. Hexagonal boron nitride epitaxial layers as neutron detector materials. *Nuclear Instruments and Methods in Physics Research Section A: Accelerators, Spectrometers, Detectors and Associated Equipment* **2011**, *654*, 417-420.

10. Doan, T.; Majety, S.; Grenadier, S.; Li, J.; Lin, J.; Jiang, H. Fabrication and characterization of solid-state thermal neutron detectors based on hexagonal boron nitride epilayers. *Nuclear*

Instruments and Methods in Physics Research Section A: Accelerators, Spectrometers, Detectors and Associated Equipment **2014**, *748*, 84-90.

11. Chang, C.; Fennimore, A.; Afanasiev, A.; Okawa, D.; Ikuno, T.; Garcia, H.; Li, D.; Majumdar, A.; Zettl, A. Isotope effect on the thermal conductivity of boron nitride nanotubes. *Phys. Rev. Lett.* **2006**, *97*, 085901.
12. Lindsay, L.; Broido, D.; Reinecke, T. Phonon-isotope scattering and thermal conductivity in materials with a large isotope effect: A first-principles study. *Physical Review B* **2013**, *88*, 144306.
13. Cuscó, R.; Artús, L.; Edgar, J. H.; Liu, S.; Cassabois, G.; Gil, B. Isotopic effects on phonon anharmonicity in layered van der Waals crystals: Isotopically pure hexagonal boron nitride. *Physical Review B* **2018**, *97*, 155435.
14. Giles, A. J.; Dai, S.; Vurgaftman, I.; Hoffman, T.; Liu, S.; Lindsay, L.; Ellis, C. T.; Assefa, N.; Chatzakis, I.; Reinecke, T. L. Ultralow-loss polaritons in isotopically pure boron nitride. *Nature Materials* **2018**, *17*, 134.
15. Vuong, T.; Liu, S.; Van der Lee, A.; Cuscó, R.; Artús, L.; Michel, T.; Valvin, P.; Edgar, J.; Cassabois, G.; Gil, B. Isotope engineering of van der Waals interactions in hexagonal boron nitride. *Nature Materials* **2018**, *17*, 152.
16. Sichel, E.; Miller, R.; Abrahams, M.; Buiocchi, C. Heat capacity and thermal conductivity of hexagonal pyrolytic boron nitride. *Physical Review B* **1976**, *13*, 4607.
17. Ishida, H.; Rimdusit, S. Very high thermal conductivity obtained by boron nitride-filled polybenzoxazine. *Thermochimica Acta* **1998**, *320*, 177-186.
18. Blase, X.; Rubio, A.; Louie, S.; Cohen, M. Stability and band gap constancy of boron nitride nanotubes. *EPL (Europhysics Letters)* **1994**, *28*, 335.

19. Solozhenko, V.; Lazarenko, A.; Petitet, J.; Kanaev, A. Bandgap energy of graphite-like hexagonal boron nitride. *Journal of Physics and Chemistry of Solids* **2001**, *62*, 1331-1334.

20. Pierson, H. O. In *Handbook of refractory carbides and nitrides: properties, characteristics, processing and applications;* William Andrew: Burlington, 1996.

21. Eichler, J.; Lesniak, C. Boron nitride (BN) and BN composites for high-temperature applications. *Journal of the European Ceramic Society* **2008**, *28*, 1105-1109.

22. Zhi, C.; Bando, Y.; Terao, T.; Tang, C.; Kuwahara, H.; Golberg, D. Towards thermoconductive, electrically insulating polymeric composites with boron nitride nanotubes as fillers. *Advanced Functional Materials* **2009**, *19*, 1857-1862.

23. Oshima, C.; Nagashima, A. Ultra-thin epitaxial films of graphite and hexagonal boron nitride on solid surfaces. *Journal of Physics: Condensed Matter* **1997**, *9*, 1.

24. Yi, G.; Yan, F. Effect of hexagonal boron nitride and calcined petroleum coke on friction and wear behavior of phenolic resin-based friction composites. *Materials Science and Engineering: A* **2006**, *425*, 330-338.

25. Martin, J.; Le Mogne, T.; Chassagnette, C.; Gardos, M. N. Friction of hexagonal boron nitride in various environments. *Tribol. Trans.* **1992**, *35*, 462-472.

26. Dai, S.; Ma, Q.; Andersen, T.; Mcleod, A.; Fei, Z.; Liu, M.; Wagner, M.; Watanabe, K.; Taniguchi, T.; Thiemens, M. Subdiffractional focusing and guiding of polaritonic rays in a natural hyperbolic material. *Nature Communications* **2015**, *6*.

27. Dean, C. R.; Young, A. F.; Meric, I.; Lee, C.; Wang, L.; Sorgenfrei, S.; Watanabe, K.; Taniguchi, T.; Kim, P.; Shepard, K. Boron nitride substrates for high-quality graphene electronics. *Nature Nanotechnology* **2010**, *5*, 722-726.

28. Naumov, I.; Bratkovsky, A. M.; Ranjan, V. Unusual Flexoelectric Effect in Two-Dimensional Noncentrosymmetric sp^2-Bonded Crystals. *Phys. Rev. Lett.* **2009**, *102*, 217601.

29. Watanabe, K.; Taniguchi, T.; Niiyama, T.; Miya, K.; Taniguchi, M. Far-ultraviolet plane-emission handheld device based on hexagonal boron nitride. *Nature Photonics* **2009**, *3*, 591-594.

30. Jiang, H.; Lin, J. Hexagonal boron nitride for deep ultraviolet photonic devices. *Semiconductor Science and Technology* **2014**, *29*, 084003.

31. Ahmed, K.; Dahal, R.; Weltz, A.; Lu, J.; Danon, Y.; Bhat, I. Growth of hexagonal boron nitride on (111) Si for deep UV photonics and thermal neutron detection. *Appl. Phys. Lett.* **2016**, *109*, 113501.

32. Maity, A.; Doan, T.; Li, J.; Lin, J.; Jiang, H. Realization of highly efficient hexagonal boron nitride neutron detectors. *Appl. Phys. Lett.* **2016**, *109*, 072101.

33. Taylor, K. Hot pressed boron nitride. *Industrial & Engineering Chemistry* **1955**, *47*, 2506-2509.

34. Tran, T. T.; Zachreson, C.; Berhane, A. M.; Bray, K.; Sandstrom, R. G.; Li, L. H.; Taniguchi, T.; Watanabe, K.; Aharonovich, I.; Toth, M. Quantum Emission from Defects in Single-Crystalline Hexagonal Boron Nitride. *Physical Review Applied* **2016**, *5*, 034005.

35. Shur, M. S.; Gaska, R. Deep-ultraviolet light-emitting diodes. *IEEE Trans. Electron Devices* **2010**, *57*, 12-25.

36. Tang, L.; Ji, R.; Li, X.; Bai, G.; Liu, C. P.; Hao, J.; Lin, J.; Jiang, H.; Teng, K. S.; Yang, Z. Deep ultraviolet to near-infrared emission and photoresponse in layered N-doped graphene quantum dots. *ACS Nano* **2014**, *8*, 6312-6320.

37. Tang, L.; Ji, R.; Cao, X.; Lin, J.; Jiang, H.; Li, X.; Teng, K. S.; Luk, C. M.; Zeng, S.; Hao, J. Deep ultraviolet photoluminescence of water-soluble self-passivated graphene quantum dots. *ACS Nano* **2012**, *6*, 5102-5110.

38. Shatalov, M.; Sun, W.; Lunev, A.; Hu, X.; Dobrinsky, A.; Bilenko, Y.; Yang, J.; Shur, M.; Gaska, R.; Moe, C. AlGaN deep-ultraviolet light-emitting diodes with external quantum efficiency above 10%. *Applied Physics Express* **2012**, *5*, 082101.

39. Kubota, Y.; Watanabe, K.; Tsuda, O.; Taniguchi, T. Deep ultraviolet light-emitting hexagonal boron nitride synthesized at atmospheric pressure. *Science* **2007**, *317*, 932-934.

40. Tsuda, O.; Watanabe, K.; Taniguchi, T. Crystallization of hexagonal boron nitride exhibiting excitonic luminescence in the deep ultraviolet region at room temperature via thermal chemical vapor phase deposition. *Diamond and Related Materials* **2010**, *19*, 83-90.

41. Watanabe, K.; Taniguchi, T.; Niiyama, T.; Miya, K.; Taniguchi, M. Far-ultraviolet plane-emission handheld device based on hexagonal boron nitride. *Nature Photonics* **2009**, *3*, 591.

42. Knoll, G. F. *Radiation Detection and Measurement*, 4th ed.; John Wiley & Sons: Hoboken, 2010.

43. Yan, X.; Titt, U.; Koehler, A.; Newhauser, W. Measurement of neutron dose equivalent to proton therapy patients outside of the proton radiation field. *Nuclear Instruments and Methods in Physics Research Section A: Accelerators, Spectrometers, Detectors and Associated Equipment* **2002**, *476*, 429-434.

44. Li, J.; Dahal, R.; Majety, S.; Lin, J.; Jiang, H. Hexagonal boron nitride epitaxial layers as neutron detector materials. *Nuclear Instruments and Methods in Physics Research Section A: Accelerators, Spectrometers, Detectors and Associated Equipment* **2011**, *654*, 417-420.

45. Anderson, I. S.; McGreevy, R. L.; Bilheux, H. Z. Neutron imaging and applications. *Springer Science Business Media* **2009**, *200*, 987-980.

46. Kouzes, R. T.; Ely, J. H.; Erikson, L. E.; Kernan, W. J.; Lintereur, A. T.; Siciliano, E. R.; Stephens, D. L.; Stromswold, D. C.; Van Ginhoven, R. M.; Woodring, M. L. Neutron detection alternatives to ^{3}He for national security applications. *Nuclear Instruments and Methods in Physics Research Section A: Accelerators, Spectrometers, Detectors and Associated Equipment* **2010**, *623*, 1035-1045.

47. McGregor, D.; Unruh, T.; McNeil, W. Thermal neutron detection with pyrolytic boron nitride. *Nuclear Instruments and Methods in Physics Research Section A: Accelerators, Spectrometers, Detectors and Associated Equipment* **2008**, *591*, 530-533.

48. Henske, M.; Klein, M.; Köhli, M.; Lennert, P.; Modzel, G.; Schmidt, C.; Schmidt, U. The ^{10}B based Jalousie neutron detector–An alternative for ^{3}He filled position sensitive counter tubes. *Nuclear Instruments and Methods in Physics Research Section A: Accelerators, Spectrometers, Detectors and Associated Equipment* **2012**, *686*, 151-155.

49. Uher, J.; Pospisil, S.; Linhart, V.; Schieber, M. Efficiency of composite boron nitride neutron detectors in comparison with helium-3 detectors. *Appl. Phys. Lett.* **2007**, *90*, 124101.

50. Novoselov, K. S.; Geim, A. K.; Morozov, S. V.; Jiang, D.; Zhang, Y.; Dubonos, S. V.; Grigorieva, I. V.; Firsov, A. A. Electric field effect in atomically thin carbon films. *Science* **2004**, *306*, 666-669.

51. Ando, T. Screening effect and impurity scattering in monolayer graphene. *Journal of the Physical Society of Japan* **2006**, *75*, 074716.

52. Nomura, K.; MacDonald, A. Quantum transport of massless Dirac fermions. *Phys. Rev. Lett.* **2007**, *98*, 076602.

53. Hwang, E.; Adam, S.; Sarma, S. D. Carrier transport in two-dimensional graphene layers. *Phys. Rev. Lett.* **2007**, *98*, 186806.

54. Ishigami, M.; Chen, J.; Cullen, W.; Fuhrer, M.; Williams, E. Atomic structure of graphene on SiO_2. *Nano Letters* **2007**, *7*, 1643-1648.

55. Katsnelson, M. I.; Geim, A. K. Electron scattering on microscopic corrugations in graphene. *Philos. Trans. A. Math. Phys. Eng. Sci.* **2008**, *366*, 195-204.

56. Geim, A. K.; Novoselov, K. S. The rise of graphene. *Nature Materials* **2007**, *6*, 183.

57. Neto, A. C.; Guinea, F.; Peres, N. M.; Novoselov, K. S.; Geim, A. K. The electronic properties of graphene. *Reviews of Modern Physics* **2009**, *81*, 109.

58. Fratini, S.; Guinea, F. Substrate-limited electron dynamics in graphene. *Physical Review B* **2008**, *77*, 195415.

59. Giovannetti, G.; Khomyakov, P. A.; Brocks, G.; Kelly, P. J.; Van Den Brink, J. Substrate-induced band gap in graphene on hexagonal boron nitride: Ab initio density functional calculations. *Physical Review B* **2007**, *76*, 073103.

60. Zhang, K.; Feng, Y.; Wang, F.; Yang, Z.; Wang, J. Two dimensional hexagonal boron nitride (2D-hBN): synthesis, properties and applications. *Journal of Materials Chemistry C* **2017**, *5*, 11992-12022.

61. Dean, C. R.; Young, A. F.; Meric, I.; Lee, C.; Wang, L.; Sorgenfrei, S.; Watanabe, K.; Taniguchi, T.; Kim, P.; Shepard, K. L. Boron nitride substrates for high-quality graphene electronics. *Nature Nanotechnology* **2010**, *5*, 722.

62. Lee, G.; Yu, Y.; Cui, X.; Petrone, N.; Lee, C.; Choi, M. S.; Lee, D.; Lee, C.; Yoo, W. J.; Watanabe, K. Flexible and transparent MoS_2 field-effect transistors on hexagonal boron nitride-graphene heterostructures. *ACS Nano* **2013**, *7*, 7931-7936.

63. Woessner, A.; Lundeberg, M. B.; Gao, Y.; Principi, A.; Alonso-González, P.; Carrega, M.; Watanabe, K.; Taniguchi, T.; Vignale, G.; Polini, M. Highly confined low-loss plasmons in graphene–boron nitride heterostructures. *Nature Materials* **2015**, *14*, 421.

64. Dai, S.; Ma, Q.; Liu, M.; Andersen, T.; Fei, Z.; Goldflam, M.; Wagner, M.; Watanabe, K.; Taniguchi, T.; Thiemens, M. Graphene on hexagonal boron nitride as a tunable hyperbolic metamaterial. *Nature Nanotechnology* **2015**, *10*, 682-686.

65. Brar, V. W.; Jang, M. S.; Sherrott, M.; Kim, S.; Lopez, J. J.; Kim, L. B.; Choi, M.; Atwater, H. Hybrid surface-phonon-plasmon polariton modes in graphene/monolayer h-BN heterostructures. *Nano Letters* **2014**, *14*, 3876-3880.

66. Ritchie, R. Plasma losses by fast electrons in thin films. *Physical Review* **1957**, *106*, 874.

67. Pekar, S. The theory of electromagnetic waves in a crystal in which excitons are produced. *Sov. Phys. JETP* **1958**, *6*, 785.

68. Low, T.; Chaves, A.; Caldwell, J. D.; Kumar, A.; Fang, N. X.; Avouris, P.; Heinz, T. F.; Guinea, F.; Martin-Moreno, L.; Koppens, F. Polaritons in layered two-dimensional materials. *Nature Materials* **2017**, *16*, 182.

69. Dai, S.; Fei, Z.; Ma, Q.; Rodin, A. S.; Wagner, M.; McLeod, A. S.; Liu, M. K.; Gannett, W.; Regan, W.; Watanabe, K.; Taniguchi, T.; Thiemens, M.; Dominguez, G.; Castro Neto, A. H.; Zettl, A.; Keilmann, F.; Jarillo-Herrero, P.; Fogler, M. M.; Basov, D. N. Tunable phonon polaritons in atomically thin van der Waals crystals of boron nitride. *Science* **2014**, *343*, 1125-1129.

70. Li, P.; Dolado, I.; Alfaro-Mozaz, F. J.; Casanova, F.; Hueso, L. E.; Liu, S.; Edgar, J. H.; Nikitin, A. Y.; Vélez, S.; Hillenbrand, R. Infrared hyperbolic metasurface based on nanostructured van der Waals materials. *Science* **2018**, *359*, 892-896.

71. Lu, G.; Wu, T.; Yuan, Q.; Wang, H.; Wang, H.; Ding, F.; Xie, X.; Jiang, M. Synthesis of large single-crystal hexagonal boron nitride grains on Cu–Ni alloy. *Nature Communications* **2015**, *6*.

72. Kobayashi, Y.; Nakamura, T.; Akasaka, T.; Makimoto, T.; Matsumoto, N. Hexagonal boron nitride on Ni (111) substrate grown by flow-rate modulation epitaxy. *J. Cryst. Growth* **2007**, *298*, 325-327.

73. Chatterjee, S.; Luo, Z.; Acerce, M.; Yates, D. M.; Johnson, A. C.; Sneddon, L. G. Chemical vapor deposition of boron nitride nanosheets on metallic substrates via decaborane/ammonia reactions. *Chemistry of Materials* **2011**, *23*, 4414-4416.

74. Auwärter, W.; Suter, H. U.; Sachdev, H.; Greber, T. Synthesis of one monolayer of hexagonal boron nitride on Ni (111) from B-Trichloroborazine $(ClBNH)_3$. *Chemistry of Materials* **2004**, *16*, 343-345.

75. Ismach, A.; Chou, H.; Ferrer, D. A.; Wu, Y.; McDonnell, S.; Floresca, H. C.; Covacevich, A.; Pope, C.; Piner, R.; Kim, M. J. Toward the controlled synthesis of hexagonal boron nitride films. *ACS Nano* **2012**, *6*, 6378-6385.

76. Lee, Y.; Liu, K.; Lu, A.; Wu, C.; Lin, C.; Zhang, W.; Su, C.; Hsu, C.; Lin, T.; Wei, K. Growth selectivity of hexagonal-boron nitride layers on Ni with various crystal orientations. *RSC Advances* **2011**, *2*, 111-115.

77. Song, L.; Ci, L.; Lu, H.; Sorokin, P. B.; Jin, C.; Ni, J.; Kvashnin, A. G.; Kvashnin, D. G.; Lou, J.; Yakobson, B. I. Large scale growth and characterization of atomic hexagonal boron nitride layers. *Nano Letters* **2010**, *10*, 3209-3215.

78. Gibb, A.; Alem, N.; Zettl, A. Low pressure chemical vapor deposition synthesis of hexagonal boron nitride on polycrystalline metal foils. *Phys. Status Solidi B* **2013**, *250*, 2727-2731.

79. Guo, N.; Wei, J.; Fan, L.; Jia, Y.; Liang, D.; Zhu, H.; Wang, K.; Wu, D. Controllable growth of triangular hexagonal boron nitride domains on copper foils by an improved low-pressure chemical vapor deposition method. *Nanotechnology* **2012**, *23*, 415605.

80. Nagashima, A.; Tejima, N.; Gamou, Y.; Kawai, T.; Oshima, C. Electronic structure of monolayer hexagonal boron nitride physisorbed on metal surfaces. *Phys. Rev. Lett.* **1995**, *75*, 3918.

81. Morscher, M.; Corso, M.; Greber, T.; Osterwalder, J. Formation of single layer h-BN on Pd (111). *Surf. Sci.* **2006**, *600*, 3280-3284.

82. Kim, G.; Jang, A.; Jeong, H. Y.; Lee, Z.; Kang, D. J.; Shin, H. S. Growth of high-crystalline, single-layer hexagonal boron nitride on recyclable platinum foil. *Nano Letters* **2013**, *13*, 1834-1839.

83. Gao, Y.; Ren, W.; Ma, T.; Liu, Z.; Zhang, Y.; Liu, W.; Ma, L.; Ma, X.; Cheng, H. Repeated and controlled growth of monolayer, bilayer and few-layer hexagonal boron nitride on Pt foils. *ACS Nano* **2013**, *7*, 5199-5206.

84. Park, J.; Park, J. C.; Yun, S. J.; Kim, H.; Luong, D. H.; Kim, S. M.; Choi, S. H.; Yang, W.; Kong, J.; Kim, K. K. Large-area monolayer hexagonal boron nitride on Pt foil. *ACS Nano* **2014**, *8*, 8520-8528.

85. Dong, G.; Fourré, E. B.; Tabak, F. C.; Frenken, J. W. How boron nitride forms a regular nanomesh on Rh (111). *Phys. Rev. Lett.* **2010**, *104*, 096102.

86. Sutter, P.; Lahiri, J.; Albrecht, P.; Sutter, E. Chemical vapor deposition and etching of high-quality monolayer hexagonal boron nitride films. *ACS Nano* **2011**, *5*, 7303-7309.

87. Orlando, F.; Larciprete, R.; Lacovig, P.; Boscarato, I.; Baraldi, A.; Lizzit, S. Epitaxial growth of hexagonal boron nitride on Ir (111). *The Journal of Physical Chemistry C* **2011**, *116*, 157-164.

88. Stehle, Y.; Meyer III, H. M.; Unocic, R. R.; Kidder, M.; Polizos, G.; Datskos, P. G.; Jackson, R.; Smirnov, S. N.; Vlassiouk, I. V. Synthesis of hexagonal boron nitride monolayer: control of nucleation and crystal morphology. *Chemistry of Materials* **2015**, *27*, 8041-8047.

89. Lu, G.; Wu, T.; Yuan, Q.; Wang, H.; Wang, H.; Ding, F.; Xie, X.; Jiang, M. Synthesis of large single-crystal hexagonal boron nitride grains on Cu–Ni alloy. *Nature Communications* **2015**, *6*, 6160.

90. Caneva, S.; Weatherup, R. S.; Bayer, B. C.; Brennan, B.; Spencer, S. J.; Mingard, K.; Cabrero-Vilatela, A.; Baehtz, C.; Pollard, A. J.; Hofmann, S. Nucleation control for large, single crystalline domains of monolayer hexagonal boron nitride via Si-doped Fe catalysts. *Nano Letters* **2015**, *15*, 1867-1875.

91. Gibb, A. L.; Alem, N.; Chen, J.; Erickson, K. J.; Ciston, J.; Gautam, A.; Linck, M.; Zettl, A. Atomic resolution imaging of grain boundary defects in monolayer chemical vapor deposition-grown hexagonal boron nitride. *J. Am. Chem. Soc.* **2013**, *135*, 6758-6761.

92. Taniguchi, T.; Watanabe, K. Synthesis of high-purity boron nitride single crystals under high pressure by using Ba–BN solvent. *J. Cryst. Growth* **2007**, *303*, 525-529.

93. Zhigadlo, N. Crystal growth of hexagonal boron nitride (hBN) from Mg–B–N solvent system under high pressure. *J. Cryst. Growth* **2014**, *402*, 308-311.

94. Ahmed, K.; Dahal, R.; Weltz, A.; Lu, J.; Danon, Y.; Bhat, I. Growth of hexagonal boron nitride on (111) Si for deep UV photonics and thermal neutron detection. *Appl. Phys. Lett.* **2016**, *109*, 113501.

95. Li, X.; Jordan, M. B.; Ayari, T.; Sundaram, S.; El Gmili, Y.; Alam, S.; Alam, M.; Patriarche, G.; Voss, P. L.; Salvestrini, J. P. Flexible metal-semiconductor-metal device prototype on wafer-scale thick boron nitride layers grown by MOVPE. *Scientific Reports* **2017**, *7*, 786.

96. Kubota, Y.; Watanabe, K.; Tsuda, O.; Taniguchi, T. Hexagonal Boron Nitride Single Crystal Growth at Atmospheric Pressure Using Ni− Cr Solvent. *Chemistry of Materials* **2008**, *20*, 1661-1663.

97. Portnoi, K.; Romashov, V.; Chubarov, V.; Levinskaya, M. K.; Salibekov, S. Phase diagram of the system nickel-boron. *Powder Metallurgy and Metal Ceramics* **1967**, *6*, 99-103.

98. Kowanda, C.; Speidel, M. Solubility of nitrogen in liquid nickel and binary Ni–Xi alloys (Xi= Cr, Mo, W, Mn, Fe, Co) under elevated pressure. *Scr. Mater.* **2003**, *48*, 1073-1078.

99. Edgar, J. H.; Hoffman, T. B.; Clubine, B.; Currie, M.; Du, X.; Lin, J.; Jiang, H. Characterization of bulk hexagonal boron nitride single crystals grown by the metal flux technique. *J. Cryst. Growth* **2014**, *403*, 110-113.

100. Hoffman, T. B.; Clubine, B.; Zhang, Y.; Snow, K.; Edgar, J. H. Optimization of Ni–Cr flux growth for hexagonal boron nitride single crystals. *J. Cryst. Growth* **2014**, *393*, 114-118.

101. Cao, X.; Clubine, B.; Edgar, J.; Lin, J.; Jiang, H. Two-dimensional excitons in three-dimensional hexagonal boron nitride. *Appl. Phys. Lett.* **2013**, *103*, 191106.

102. Baranov, D.; Edgar, J. H.; Hoffman, T.; Bassim, N.; Caldwell, J. D. Perfect interferenceless absorption at infrared frequencies by a van der Waals crystal. *Physical Review B* **2015**, *92*, 201405.

103. Liu, S.; He, R.; Ye, Z.; Du, X.; Lin, J.; Jiang, H.; Liu, B.; Edgar, J. H. Large-Scale Growth of High-Quality Hexagonal Boron Nitride Crystals at Atmospheric Pressure from an Fe–Cr Flux. *Crystal Growth & Design* **2017**, *17*, 4932-4935.

104. Gibb, A. L.; Alem, N.; Chen, J.; Erickson, K. J.; Ciston, J.; Gautam, A.; Linck, M.; Zettl, A. Atomic resolution imaging of grain boundary defects in monolayer chemical vapor deposition-grown hexagonal boron nitride. *J. Am. Chem. Soc.* **2013**, *135*, 6758-6761.

105. Grad, G.; Blaha, P.; Schwarz, K.; Auwärter, W.; Greber, T. Density functional theory investigation of the geometric and spintronic structure of h-BN/Ni (111) in view of photoemission and STM experiments. *Physical Review B* **2003**, *68*, 085404.

106. Díaz, J. G.; Ding, Y.; Koitz, R.; Seitsonen, A. P.; Iannuzzi, M.; Hutter, J. Hexagonal boron nitride on transition metal surfaces. *Theoretical Chemistry Accounts* **2013**, *132*, 1-17.

107. Liu, Y.; Bhowmick, S.; Yakobson, B. I. BN white graphene with "colorful" edges: The energies and morphology. *Nano Letters* **2011**, *11*, 3113-3116.

108. Zhang, Z.; Liu, Y.; Yang, Y.; Yakobson, B. I. Growth mechanism and morphology of hexagonal boron nitride. *Nano Letters* **2016**, *16*, 1398-1403.

109. Mann, D. J.; Halls, M. D.; Hase, W. L. Direct dynamics studies of CO-assisted carbon nanotube growth. *The Journal of Physical Chemistry B* **2002**, *106*, 12418-12425.

110. Elert, M.; Zybin, S.; White, C. Molecular dynamics study of shock-induced chemistry in small condensed-phase hydrocarbons. *J. Chem. Phys.* **2003**, *118*, 9795-9801.

111. Allinger, N. L.; Yan, L. Molecular mechanics (MM3). Calculations of furan, vinyl ethers, and related compounds. *J. Am. Chem. Soc.* **1993**, *115*, 11918-11925.

112. Mayo, S. L.; Olafson, B. D.; Goddard, W. A. DREIDING: a generic force field for molecular simulations. *J. Phys. Chem.* **1990**, *94*, 8897-8909.

113. Cornell, W. D.; Cieplak, P.; Bayly, C. I.; Gould, I. R.; Merz, K. M.; Ferguson, D. M.; Spellmeyer, D. C.; Fox, T.; Caldwell, J. W.; Kollman, P. A. A second generation force field

for the simulation of proteins, nucleic acids, and organic molecules. *J. Am. Chem. Soc.* **1995**, *117*, 5179-5197.

114. Van Duin, A. C.; Dasgupta, S.; Lorant, F.; Goddard, W. A. ReaxFF: a reactive force field for hydrocarbons. *The Journal of Physical Chemistry A* **2001**, *105*, 9396-9409.

Chapter 2 - Methodology

This chapter presents the experimental setup for hBN crystal growth, which is followed by a detailed description of the crystal growth procedure. The crystal transfer technique from metal surface to substrate is discussed. Then, the characterization techniques that are used to analyze crystal quality and properties are introduced. At the end, relevant molecular modeling methods for hBN growth mechanism studies are described.

2.1 Experimental Setup

As a part of the project, I have designed and built a furnace system for hBN single crystal growth, as shown in Figure 2.1. It consists of three main parts: CM furnace, gas supply, and pressure control systems.

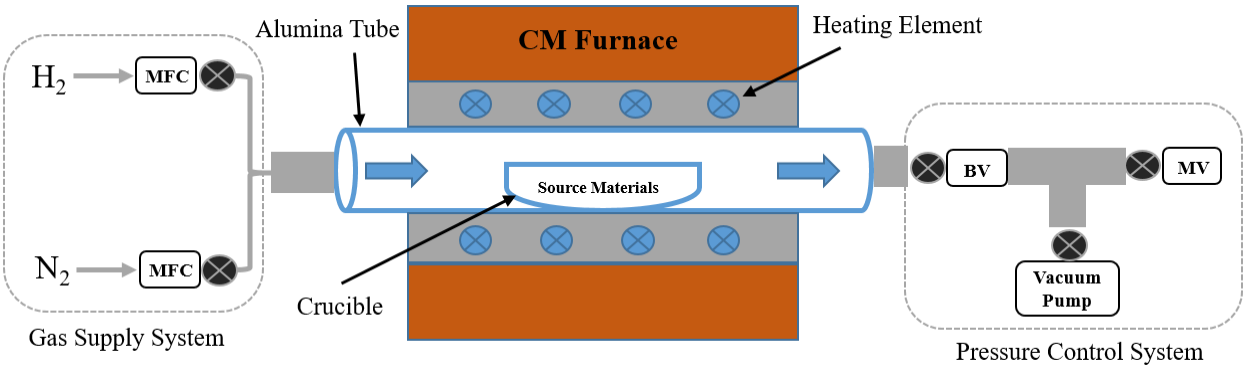

Figure 2.1. Schematic experimental setup for hBN crystal growth from metal flux method.

The CM furnace, as shown in Figure 2.2a, is a single-zone horizontal tube furnace, which can reach a maximum temperature of 1600 °C. Type B thermocouples, which are made of platinum-30% rhodium and platinum-6% rhodium, are used in the furnace to measure the temperature. A power controller, consisting of a multiple segment programmable microprocessor

and a step-down transformer, controls the furnace temperature. The microprocessor receives the signal from thermocouples and then regulates the current to the transformer, thereby controlling the power to heat the furnace. Kanthal Super 1700 molydisilicide heating elements are installed in the furnace chamber, offering fast heat up and slow cooling rates. The furnace is equipped with a 1.5" OD alumina tube with a length of 36". As can be seen from Figure 2.2b, a second CM furnace was put on a tiltable table, which is capable of performing a tilting experiment to separate hBN crystals from metal flux at high temperature. The table can be tilted at up to 30° in either direction.

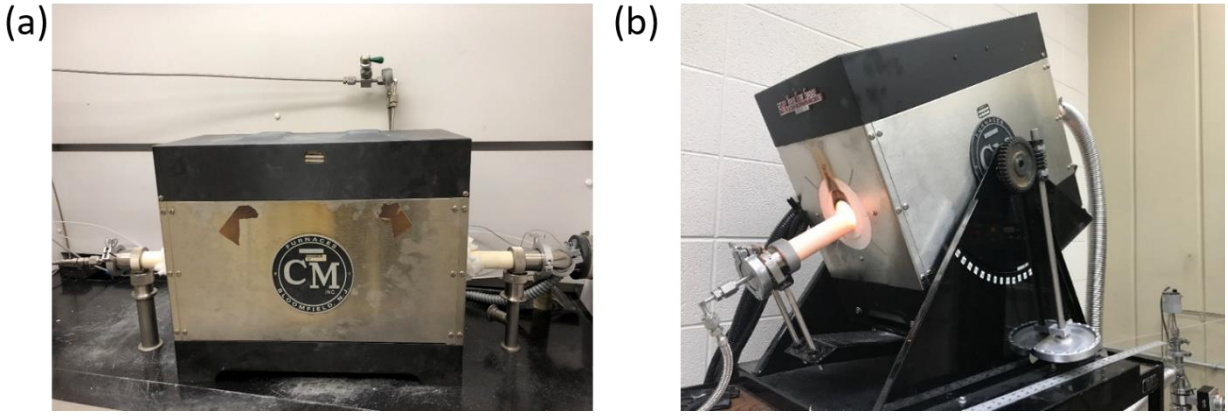

Figure 2.2. Photographs of (a) CM furnace in a horizontal fume hood, (b) CM furnace on a tiltable table.

The gas supply system in Figure 2.1 is comprised of gas cylinders, i.e. H_2 and N_2, and mass flow controllers (MFC). The gas cylinders with ultra-purity grade were supplied by Matheson Tri-gas Inc. N_2 gas not only stabilizes the reaction pressure but also provides the N source for hBN crystal growth. H_2 gas was used to eliminate oxygen and carbon impurities in the source materials. The mass flow controllers regulate the amount of gas streams supplied to the tube during the experiment.

The pressure control system consists of a vacuum pump, a butterfly valve (BV), and a manual valve (MV). After loading the sample into the tube, the inside air was exhausted by the vacuum pump before the H_2 and N_2 gases were fed in. During the experiment, the butterfly controller was used to stabilize the reaction pressure. The manual valve was kept open during the experiment to release the exhaust from the tube.

2.2 Crystal Growth Method

Although chemical vapor deposition offers a promising method to produce large-scale hBN films, the crystal perfection and crystallographic orientation of currently CVD-grown hBN have remained problematic[1-3]. Alternatively, hBN crystals grown by the metal flux method exhibit a narrower Raman peak width[4,5] and higher cathodoluminescence energy.[6,7] Hence, we used the metal flux method for high-quality hBN crystal growth in this work. A mixture of nickel and chromium (Ni-Cr) or iron and chromium (Fe-Cr) was used as the solvent because of their high solubility for boron and nitrogen, respectively. In pure hot nitrogen, chromium reacts to form Cr_2N while nickel and iron remain unreacted.

2.2.1 Naturally Abundant hBN Crystal Growth

In this work, hBN crystals with the natural distribution of isotopes (19.9 at% ^{10}B and 80.1 at% ^{11}B) were produced using a hot-pressed boron nitride ceramic boat, which served as both the container for the metal flux and as the B and N sources. Again, the schematic of the experimental set-up for the crystal growth is illustrate in Figure 2.3a. The flux was a mixture of 50 wt% Ni and 50 wt% Cr powders. After loading the crucible, the furnace was evacuated, then filled with N_2 gas and forming gas (5% hydrogen in balance argon) to around 850 Torr. The N_2 and forming gases

continuously flowed through the system during crystal growth process with flow rates of 125 sccm and 25 sccm, respectively. The furnace was rapidly heated up to a dwell temperature of 1550 °C at a rate of 200 °C /h. After a dwell time of 24 hours at that temperature, the hBN crystals were precipitated on the metal surface by cooling at a rate of 0.5 °C /h to 1525 °C, and then the system was quickly quenched to room temperature. A scheme for the crystal growth process is illustrated in Figure 2.3b. In our experiments, forming gas helps to minimize oxygen and carbon impurities, which were considered as the main contaminants in hBN crystals.[8,9]

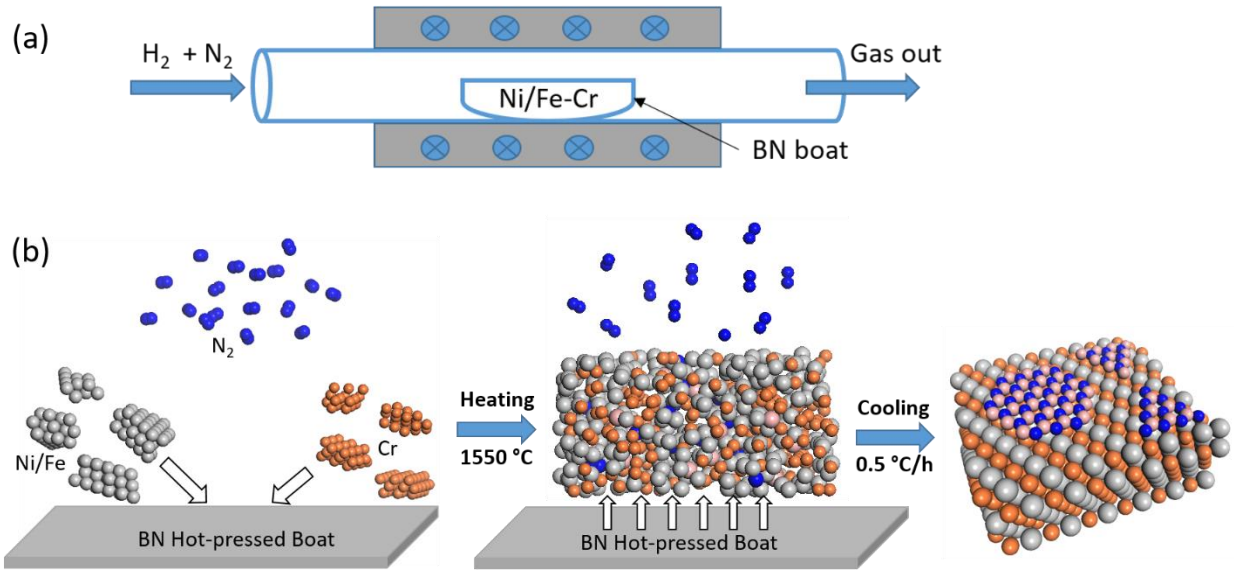

Figure 2.3. Schematic illustration showing (a) the experimental set-up for naturally abundant hBN growth, (b) the procedure of hBN growth.

2.2.2 Monoisotopic hBN Crystal Growth

Since hot-pressed boron nitride ceramics are only available with the natural distribution of boron isotopes, the procedure for growing isotopically pure hBN crystals was different: elemental boron was the source material. Therefore, the boron nitride boat was replaced with an alumina crucible. The experimental set-up is shown in Figure 2.4a. High purity B-10 (99.22 at%) or B-11 (99.41 at%) powders were mixed with Ni and Cr powders to give overall concentrations of 4 wt% B, 48 wt% Ni and 48 wt% Cr. In this case, all nitrogen in the hBN originated from the flowing N_2 gas. Other than these changes, the procedure was the same as previously described. The scheme for monoisotopic hBN crystal growth is illustrated in Figure 2.4b.

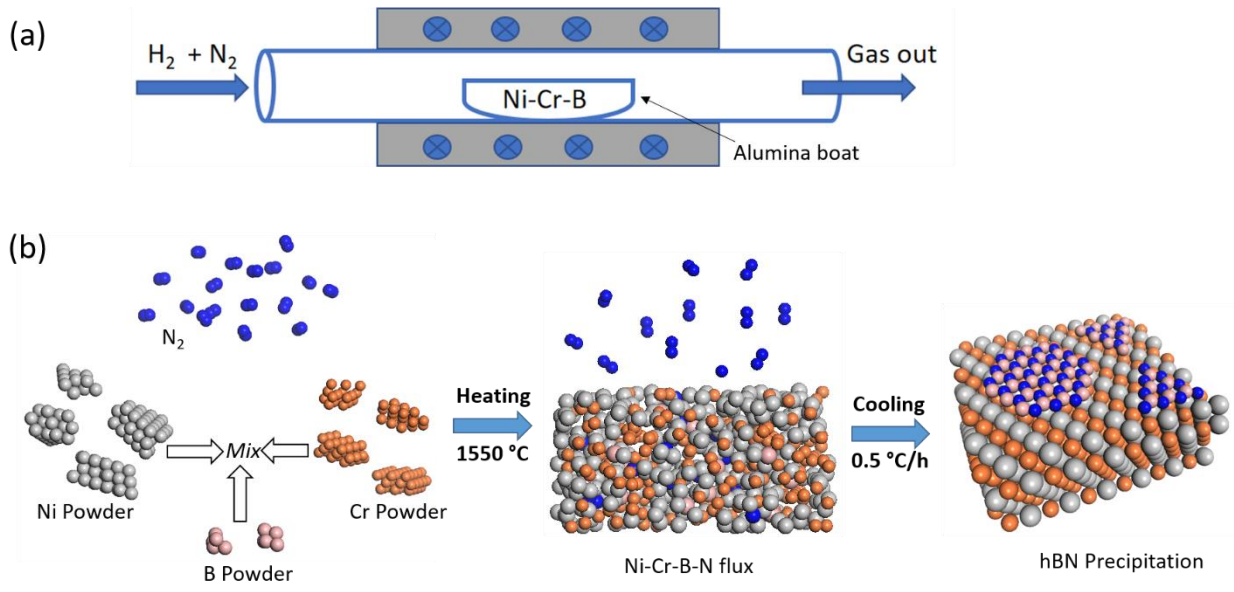

Figure 2.4. Schematic illustration showing (a) the experimental set-up for monoisotopic hBN growth, (b) the procedure of hBN growth.

2.2.3 Tilting Experiment

For practical applications, hBN crystals need to be separated from the solidified metal ingot. However, the current crystal transfer technique that mechanically removes hBN crystals from the metal surface could lead to cracking. To better separate the crystals from the metal flux and obtain larger free-standing crystals, tilting experiments were performed. Initially, the furnace was tilted 20° to one side after loading the source material described in Section 1.2.1. After a dwell time of 24 hours at 1550 °C, the furnace was cooled down to a tilting temperature (1525 °C) at a rate of 0.5 °C/h, and then quickly tilted to another direction with a 30° incline. It was then held at the tilting temperature for 5 hours before the quenching. The initial and final states of the tilting experiments set-up are illustrated by Figure 2.5.

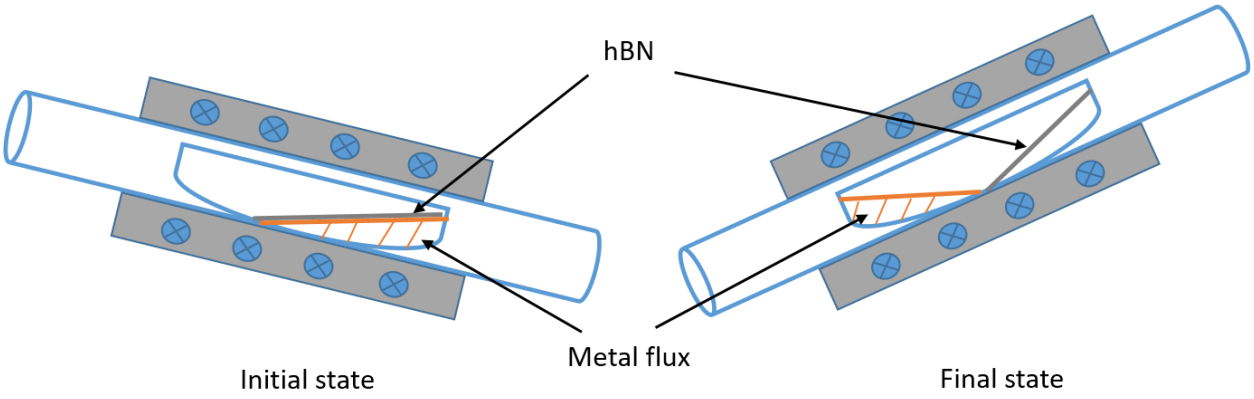

Figure 2.5. Schematic illustration of the initial and final states of the tilting experiments for hBN crystal separation from the metal flux.

2.3 Crystal Exfoliation Technique

The hBN crystals grown in the horizontal CM furnace exist over the solidified metal surface. For characterization and application purposes, we need to obtain free-standing hBN

crystals by exfoliating them from the metal surface. Mechanical exfoliation method is feasible due to the layered structure of hBN and the weak van der Waals bond between the layers. This method has been widely used to cleave and deposit layers of graphite/graphene onto a substrate.[10,11]

Here we used single-slide thermal release tapes to adhere and peel the crystals from the metal surface, as shown in Figure 2.6a, and then heated the tape at 150 °C for 10 seconds to release the adhesive and transfer the crystals onto a substrate. Figure 2.6b shows the free-standing hBN flakes exfoliated from the solidified metal surface.

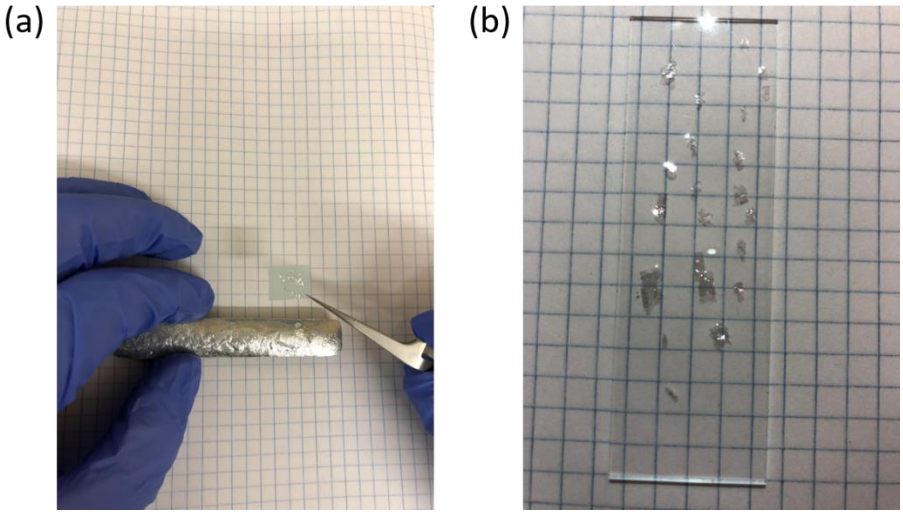

Figure 2.6. Optical photographs of (a) mechanical exfoliation of hBN crystals from the metal surface by using a thermal release tape, (b) free-standing hBN flakes on a glass substrate.

2.4 Characterization Techniques

Several characterization techniques were performed to analyze the crystal qualities and properties, including optical microscopy, electron microscopy, Raman spectroscopy, x-ray diffraction, atomic force microscopy, photoluminescence spectroscopy, and x-ray photoelectron spectroscopy.

Optical Microscopy. The size, thickness and morphology of the crystals grown in this project was evaluated by this technique. Optical micrographs were taken with a Nikon Eclipse LV100 scope with magnification range from 50x to 1000x. This system is equipped with a high intensity 50W halogen light source incorporating a fly-eye lens design. The focus stroke is 30 mm, facilitating observation of tall samples. An image capture system, enabled the production and analysis of optical micrographs. A DS-Fi3 microscope camera along with a 5.9-megapixel CMOS sensor is equipped to enable fast 15 fps acquisition of high definition images of up to 2280 x 2048 pixels.

Scanning Electron Microscopy. The microstructure features of the crystal surface were analyzed by high-resolution electron microscopy. The scanning electron microscopy (SEM) images were taken by a FEI Versa3D Dual Beam SEM system. This system can be operated from 1-30 kV (1 nm resolution at 30 kV) at different vacuum modes, including high vacuum (HiVac), low vacuum (LoVac)， and environmental (ESEM). Each mode corresponds different detectors. An energy dispersive x-ray spectroscopy (EDS) detector is also equipped in the system, allowing for the elemental analysis and chemical characterization of the sample.

Focused Ion Beam. An FEI Nova 600 dual-beam focused ion beam (FIB) microscope was used to prepare the cross-sections in the [0001] direction (perpendicular to the basal plane) for TEM imaging. A high-resolution ion (5 nm) column is equipped, which allows Ga milling at 5-30 kV. The beam spot size is range from 7 to 15 nm. This system is also equipped with a OmniProbe^{TM} 200 in-situ sample lift-out system, allowing the preparation of TEM samples without support films.

Transmission electron microscopy. The crystal cross-sections prepared by FIB was investigated by a Hitachi UHV-H9000 high-resolution electron microscope. This instrument can

be operated from 100-300 kV at mid-10^{-11} torr and resolve at about 0.18 nm for bulk spacings and 0.25 nm for atomic structure of surfaces. This system was also equipped with a Gatan Parallel EELS and CCD Camera, both interfaced to computers.

Raman Spectroscopy. Raman spectroscopy was used to investigate the phonon energies and the presence of structural defects in the crystal lattice. Raman spectra were taken at room temperature using a Horiba Labram HR Raman microscope system. This spectrometer is equipped with an ultralow frequency filter that allows access to the ultralow frequency down to ~5 cm^{-1}. A linearly polarized 532 nm laser source was used, which could be focused to a spot diameter of ~2 μm by a 50× long-working-distance objective lens. Laser power was kept below 0.8 mW to avoid heating the samples. Instrument resolution was ~0.5 cm^{-1} by using an 1800 groove/mm grating.

X-ray Diffraction. X-ray powder diffraction (XRD) is a technique to characterize the 3D ordering and presence of stacking faults, plane sipping and polycrystallinity within samples. XRD was carried out using a Rigaku Miniflex II desktop X-ray diffractometer with monochromatic Cu Kα radiation ($\lambda = 0.154$ nm). This system is equipped with an automated 6 position sample changer with sample spinning capability. The scanning range of 2θ for this system is from 5 to 150° with a scanning rate from 0.01°/min to 100°/min. Phases were identified by comparing obtained patterns with a JCPDS database.

Atomic Force Microscopy. The surface topography of the samples was investigated by a Bruker Innova atomic force microscopy (AFM) system. This instrument includes stacked piezo XY and Z scanners with resolution as high as < 0.02 and < 0.01 nm, respectively. The 3 primary AFM modes are included in this system, i.e., Contact Mode, Tapping Mode and Non-Contact Mode. A sample size up to 45 mm*45 mm*18 mm can be measurement by this instrument.

Photoluminescence Spectroscopy. Photoluminescence (PL) spectroscopy was performed to probe the electronic structure and photoexcitation processes in hBN. The room temperature PL measurement system includes a frequency-quadruped Ti-sapphire laser with wavelength of 195 nm, 76 MHz repetition rate, 100 fs pulse width, and average optical power of ~ 1 mW. The emitted light was collected with a 1.3-meter long monochromator onto a microchannel plate photomultiplier tube.

X-ray Photoelectron Spectroscopy. X-ray photoelectron spectroscopy (XPS) is a technique that measures the elemental composition, chemical state and electronic state of the elements in a material. XPS spectra were measured on Kratos Axis Ultra^{DLD} system at a base pressure of 10^{-9} Torr using monochromatic Al Kα line. Survey XPS scans were run at 160 eV pass energy and high-resolution scans at 20 eV pass energy. XPS spectra was calibrated with the C 1s peak from the sample and set to BE = 284.6 eV. All samples were in electronic equilibrium with the spectrometer via a metallic clip on the sample, and characterized at normal take-off angle. XPS peak fits were done with CasaXPS Software 2.2.8 using mixed Gaussian/Lorentzian distributions to minimize *chi* squared value.

2.5 Density Functional Theory (DFT)

Over the last decades, DFT has become a very powerful method for studying many-body systems due to its high accuracy at an efficient computational cost. DFT is capable of producing electronic structures of atoms, molecules, surfaces, and crystals. Therefore, it is a suitable method to characterize molecular structures and chemical bonding in relation to hBN growth. In this section, the DFT method based on Kohn-Sham formalism, utilized in this work, will be discussed in detail.

2.5.1 The Kohn-Sham Theory

The properties of a many body system can be obtained by solving the Schrödinger equation (Equation. (1)):

$$H\Psi(r_1, r_2 \ldots . R_1, R_2 \ldots .) = E\Psi(r_1, r_2 \ldots . R_1, R_2 \ldots .) \quad (1)$$

where H is the Hamiltonian, E is the total energy of the system, and $\Psi(r_1, r_2 \ldots . R_1, R_2 \ldots .)$ is the many-body wavefunction, depending on the electron position r_n, and the nuclei R_n. However, the analytical solution is only available for a handful of simple systems (e.g., H atoms, He^+).

In 1965, Kohn and Sham[12] used a fictitious non-interacting system that generates the same density to treat the real N-particle interacting system. The formulation for these non-interacting particles within the Kohn-Sham framework can be expressed by Equation (2), where the effective potential $v_{eff}(\boldsymbol{r})$ is a function of electron density $n(\boldsymbol{r})$. The kinetic energy of a single particle is represented by the Laplacian ($-\frac{\hbar^2}{2m}{\nabla_i}^2$):

$$\left[-\frac{\hbar^2}{2m}{\nabla_i}^2 + v_{eff}(\boldsymbol{r})\right]\Psi_i(\boldsymbol{r}) = \varepsilon_i\Psi_i(\boldsymbol{r}) \quad (2)$$

The electron density, $n(\boldsymbol{r})$,can be written as,

$$n(\boldsymbol{r}) = \sum_i^N |\varphi_i(\boldsymbol{r})|^2 \quad (3)$$

$$v_{eff}(\boldsymbol{r}) = v_{ext}(\boldsymbol{r}) + \int \frac{n(\boldsymbol{r}')}{|\boldsymbol{r} - \boldsymbol{r}'|} d\boldsymbol{r}' + V_{xc}(\boldsymbol{r}) \quad (4)$$

The exchange-correlation potential, $V_{xc}(\boldsymbol{r})$, to account for electron correlation and exchange effects of interacting N-electron systems, is given by Equation (5). Details about the functionals are the function derivative discussed in the next section.

$$V_{xc}(\boldsymbol{r}) = \frac{\delta E_{xc}[n(\boldsymbol{r})]}{\delta n(\boldsymbol{r})} \quad (5)$$

2.5.2 Exchange-Correlation Functionals

The total energy expression in Equation (2) can be obtained only when the exact form of the exchange-correlation potential, $V_{xc}(\boldsymbol{r})$, in Equation (5) is known. However, the exact expression for this functional is unknown. Therefore, approximations for this term need to be implemented with respect to the energy of exact ground state.

The Local Density Approximation (LDA)[12] was first proposed, by which the electron density is treated locally as a uniform electron gas. However, for some systems, where the electron density varies quickly, the LDA becomes insufficient. For example, the transition oxides can be predicted to show either semiconductors or metals characters according to LDA, while in fact they are mostly insulators. To overcome these limitations, generalized gradient approximation (GGA) functionals[13,14] were developed, which considers both the local density and gradient of the electron density. The exchange-correlation functional can be then written as:

$$E_{xc}[n(\boldsymbol{r})] = \int f(n(\boldsymbol{r}), |\nabla n(\boldsymbol{r})|) d\boldsymbol{r} \quad (6)$$

in which $f(n(\boldsymbol{r}), |\nabla n(\boldsymbol{r})|)$ is a suitably chosen function of its two variables.[15] Perdew-Wang (PW91)[16], Perdew-Burke-Ernzerhof (PBE)[17,18], revised PBE (RPBE)[18], re-parameterized PBE functional for solids and surfaces (PBEsol)[19] and Becke-Lee-Yang-Parr (BLYP)[20] functionals are commonly used in standard DFT calculations.

2.5.3 Pseudopotential

Due to the screening of the nucleus charge from the core electrons, the valance electrons are much weakly bound than the core electrons. Since atomic properties are mainly determined by valence electrons, they are directly responsible for the physicochemical properties of materials. Pseudopotentials, which vary smoothly in the core region, provides a way to replace the strong Coulomb potential in the core region with a weaker potential, as shown in Figure 2.7[21]. The valence electrons under the pseudopotential approximation experience the same potential outside the core region as in the all-electron treatment.

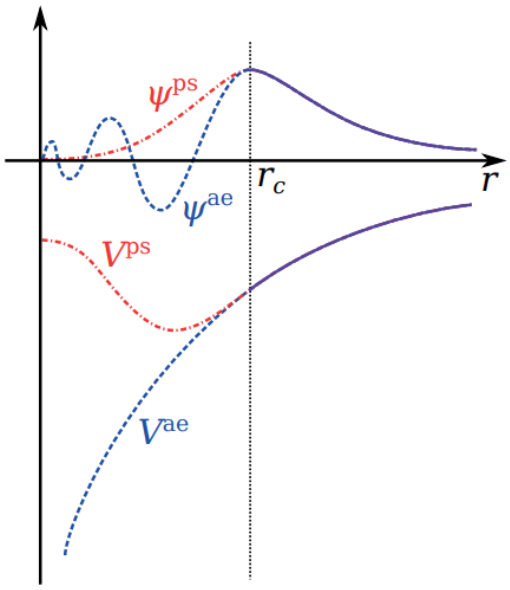

Figure 2.7. Schematic representation of the pseudopotential concept. The pseudopotential $\boldsymbol{V^{PS}}$ and pseudo-wavefunction $\boldsymbol{\psi^{PS}}$ (red line) match the all electron potential $\boldsymbol{V^{ae}}$ and wavefunction $\boldsymbol{\psi^{ae}}$ (blue line) beyond the cutoff radius, $\boldsymbol{r_c}$.

2.5.4 Transition State Searches in DFT

Identifying the minimum energy path (MEP) for a rearrangement of a group of atoms from one stable configuration to another is very important in condensed mater physics and theoretical chemistry. The potential energy maximum along the MEP is the transition state (saddle point) which gives the reaction energy barrier, a quantity for estimating the reaction kinetics. Many different methods[22] have been proposed to find MEP and saddle point, such as the nudged elastic band (NEB)[23] and dimer[24] methods we used in this project.

2.5.4.1 Nudged Elastic Band Method

Nudged elastic band (NEB) method is an algorithm to determine the MEP from an initial state to a final state. The intermediate images can be constructed by making a linear interpolation

from the initial to the final state. The MEP is then found by connecting those images by springs and then relaxing to find the minimum energy. The path of springs acts like an elastic band, in which the images feel the forces from both the spring and potential so that each image tries to minimize its potential energy. However, when the energy barrier is narrow compared with the MEP length, few images land is the neighborhood of the saddle point and the energy barrier can be inaccurate.

The addition of the Climbing Image (CI) to the NEB method allows for locating the saddle point more accurately. In the CI-NEB[25] method, the highest energy image is forced to the saddle point by replacing the spring forces with an inverted force that acts tangent to the path of the point. By this way, the image is forced towards the maximum point along the MEP, while still minimizing its potential energy.

2.5.4.2 Dimer Method

When the final state of a transition is unknown, the search for the saddle point in the MEP is challenging by using NEB method. The dimer method is developed to find saddle points only requiring first derivatives of the energy and no diagonalization.[24] The force acting on the center of a dimer (two replicas of the system) is modified by inverting the direction component of the dimer. This effective force will take the dimer to a saddle point after an optimization scheme is applied, such as conjugate gradients.

2.6 Reactive Molecular Dynamics (rMD) Simulations

Due to the high computational cost, DFT systems are usually limited to hundreds of atoms. For this reason, molecular dynamics (MD) simulations, which are capable of simulating large-

scale systems (thousands of atoms), such as protein folding[26,27], nanomaterials formation[28,29], and catalysts[30,31] are more frequently used. In this work, reactive MD simulations, while are able to describe chemical bond breaking and formation, will be used to simulate large-scale hBN growth process.

2.6.1 Molecular Dynamics Mechanics

Molecular dynamics is a numerical method that is developed to describe atomic or molecular motion in a N-particle system, by integrating Newton's equation of motion, as shown in Equation (7).

$$\boldsymbol{F}_i(t) = m_i \frac{d^2\boldsymbol{r}_i(t)}{dt^2}, \;\; i = 1,2, \ldots . N \tag{7}$$

where m_i is the particle mass, $\boldsymbol{F}_i(t)$ and $\boldsymbol{r}_i(t)$ are the force and position vectors of particle i at time step t. By using the velocity-Verlet algorithm[32], Equation (7) can be numerically integrated to obtain the particle position and velocity at the next time step $t + \Delta t$, as expressed in Equations (8) and (9).

$$\boldsymbol{r}_i(t + \Delta t) = \boldsymbol{r}_i(t) + \boldsymbol{v_i}(t)\Delta t + \frac{\boldsymbol{F}_i(t)}{2m_i}\Delta t^2 \tag{8}$$

$$\boldsymbol{v}_i(t + \Delta t) = \boldsymbol{v}_i(t) + \frac{\boldsymbol{F}_i(t + \Delta t) + \boldsymbol{F}_i(t)}{2m_i}\Delta t \tag{9}$$

The force vector $\boldsymbol{F}_i(t)$ can be obtained from the potential energy force field. Therefore, accurate predication of particle movement strongly depends on the accuracy of force field used.

A number of empirical force fields have been developed to describe different systems, including AMBER (assisted model building and energy refinement)[33], GROMOS (Groningen molecular simulation system)[34], UFF(Universal force field)[35], and Tipos[36].

2.6.2 ReaxFF Force Field and Development

The conventional force fields mentioned above may provide accurate predictions for biological molecules, hydrocarbons, and charges. However, they fail to describe chemical reactivities, i.e., bond breaking and formation. ReaxFF reactive force field[37] is a general bond-order-based potential that can smoothly describe the changes of bond connectivity during chemical reactions. The total system energy in the ReaxFF can be described by Equation (10):

$$E_{system} = E_{bond} + E_{lp} + E_{over} + E_{under} + E_{val} + E_{pen} + E_{coa} + E_{tors} + E_{conj} + E_{H-bond} + E_{vdWaals} + E_{Coulomb} \quad (10)$$

a detailed description of each term in Equation (10) can be found elsewhere.[37]

In order to obtain an appropriate ReaxFF force field to describe a certain system, its parameters need to be optimized against a mainly quantum mechanics (QM) derived database, called a training set, which includes atomic charges, bond dissociation energies, angle strain, heats of formation, vibrational frequencies, and transition-state energies. The parameters in the ReaxFF potential are optimized through a single-parameter search procedure[38] performed by minimizing the total error:

$$Error = \sum_{i=1}^{n} \left[\frac{X_{i,QM} - X_{i,ReaxFF}}{\sigma_i} \right]^2 \quad (11)$$

where n is the number of data points in the training set, σ_i is the weight assigned to each data, $X_{i,QM}$ and $X_{i,ReaxFF}$ are the QM and ReaxFF calculated values, respectively. In the optimization process, ReaxFF parameters are tuned in a way that decreases the total error.

ReaxFF is an empirical pair-wise potential, in which the energy contributions from chemical bonding, valence angle, and torsion angles are formulated as functionals of the bond order, which is expressed as a function of atomic-pair distance. Thus, the total system energy in ReaxFF, as shown in Equation (10), can be partitioned into the expression below:

$$E_{system} = E_{valence} + E_{Coulomb} + E_{vdWaals} \quad (12)$$

where $E_{valence}$, $E_{Coulomb}$ and $E_{vdWaals}$ represent the valence, Coulombic, and van der Waals contributions to the system energy, respectively. $E_{valence}$ itself is the sum of all the bond order dependent term in the ReaxFF formulation. This term will disappear as the corresponding chemical bond is broken (*i.e.*, bond order approaches zero).

In order to elucidate the mechanism of hBN growth on Ni, we have developed a ReaxFF force field based on a quantum mechanical training set for Ni-B and Ni-N pair potentials. The parameters in ReaxFF are optimized through Equation (11). The bond, angle, and torsion parameters for B-B, N-N, B-N pairs and bulk Ni systems were adopted from previous work[39]. The complete set of ReaxFF force field is included in Appendix A.

2.7 Computational Methods

In our project, all periodic DFT calculations were performed with spin polarization using Vienna *Ab initio* Simulation Package (VASP)[40]. The generalized gradient approximation (GGA) Perdew−Burke−Ernzerhof (PBE)[17] functional was employed to account for the electron exchange−correlation potential. The electron-ion interaction was described using the projector-augmented wave (PAW) method[41]. All the rMD simulations were performed by LAMMPS.[42]

2.7.1 Simulation Models Generation in DFT

The simulation models used in our DFT calculations are either bulk or surface crystals. The bulk models were directly obtained from the database in Materials Studio, a software for materials design. Both body-centered cubic (BCC) and face-centered cubic (FCC) crystals were used. The surface models were generated through the cleavage of an optimized bulk crystal, in which a thick vacuum space was implemented to avoid interference between periodic images along the perpendicular direction. In our DFT calculations, single-crystal (100) and (111) facets were modeled to represent terrace surfaces, while the (211) facet was used to mimic a stepped surface. In addition to the surface adsorption sites, including top, bridge, fcc, bcc and 4-fold sites, we also considered the sublayer adsorption sites, i.e., octahedral and tetrahedral sites.

2.7.2 Simulation Models Generation in rMD

A rectangular shaped nickel slab with the close-packed (111) facet was used to represent the Ni substrate, where elemental B and N were deposited initially for hBN nucleation and growth. The Ni slab consists of 5 atomic layers, with lateral dimensions of 12 × 12 Ni atoms, for a total of 720 Ni atoms. Periodic boundary conditions were imposed on all dimensions. The bottom (5th) layer was fixed so that the Ni atoms remained in their bulk lattice structures during the simulation

to represent the interior bulk region, while the top 4 layers were relaxed along the vertical direction to represent the surface and sublayer regions. A 90 Å vacuum space was implemented to avoid interference between periodic images along the perpendicular direction.

References

1. Lu, G.; Wu, T.; Yuan, Q.; Wang, H.; Wang, H.; Ding, F.; Xie, X.; Jiang, M. Synthesis of large single-crystal hexagonal boron nitride grains on Cu–Ni alloy. *Nature Communications* **2015**, *6*.
2. Gibb, A. L.; Alem, N.; Chen, J.; Erickson, K. J.; Ciston, J.; Gautam, A.; Linck, M.; Zettl, A. Atomic resolution imaging of grain boundary defects in monolayer chemical vapor deposition-grown hexagonal boron nitride. *J. Am. Chem. Soc.* **2013**, *135*, 6758-6761.
3. Lee, Y.; Liu, K.; Lu, A.; Wu, C.; Lin, C.; Zhang, W.; Su, C.; Hsu, C.; Lin, T.; Wei, K. Growth selectivity of hexagonal-boron nitride layers on Ni with various crystal orientations. *RSC Advances* **2011**, *2*, 111-115.
4. Ahmed, K.; Dahal, R.; Weltz, A.; Lu, J.; Danon, Y.; Bhat, I. Growth of hexagonal boron nitride on (111) Si for deep UV photonics and thermal neutron detection. *Appl. Phys. Lett.* **2016**, *109*, 113501.
5. Li, X.; Jordan, M. B.; Ayari, T.; Sundaram, S.; El Gmili, Y.; Alam, S.; Alam, M.; Patriarche, G.; Voss, P. L.; Salvestrini, J. P. Flexible metal-semiconductor-metal device prototype on wafer-scale thick boron nitride layers grown by MOVPE. *Scientific Reports* **2017**, *7*, 786.
6. Kubota, Y.; Watanabe, K.; Tsuda, O.; Taniguchi, T. Deep ultraviolet light-emitting hexagonal boron nitride synthesized at atmospheric pressure. *Science* **2007**, *317*, 932-934.

7. Gao, R.; Yin, L.; Wang, C.; Qi, Y.; Lun, N.; Zhang, L.; Liu, Y.; Kang, L.; Wang, X. High-yield synthesis of boron nitride nanosheets with strong ultraviolet cathodoluminescence emission. *The Journal of Physical Chemistry C* **2009**, *113*, 15160-15165.

8. Taniguchi, T.; Watanabe, K. Synthesis of high-purity boron nitride single crystals under high pressure by using Ba–BN solvent. *J. Cryst. Growth* **2007**, *303*, 525-529.

9. Silly, M.; Jaffrennou, P.; Barjon, J.; Lauret, J.; Ducastelle, F.; Loiseau, A.; Obraztsova, E.; Attal-Tretout, B.; Rosencher, E. Luminescence properties of hexagonal boron nitride: Cathodoluminescence and photoluminescence spectroscopy measurements. *Physical Review B* **2007**, *75*, 085205.

10. Lin, T.; Tang, Y.; Wang, Y.; Bi, H.; Liu, Z.; Huang, F.; Xie, X.; Jiang, M. Scotch-tape-like exfoliation of graphite assisted with elemental sulfur and graphene–sulfur composites for high-performance lithium-sulfur batteries. *Energy & Environmental Science* **2013**, *6*, 1283-1290.

11. Caldwell, J. D.; Anderson, T. J.; Culbertson, J. C.; Jernigan, G. G.; Hobart, K. D.; Kub, F. J.; Tadjer, M. J.; Tedesco, J. L.; Hite, J. K.; Mastro, M. A. Technique for the dry transfer of epitaxial graphene onto arbitrary substrates. *ACS Nano* **2010**, *4*, 1108-1114.

12. Kohn, W.; Sham, L. J. Self-consistent equations including exchange and correlation effects. *Physical Review* **1965**, *140*, A1133.

13. Perdew, J. P. Density-functional approximation for the correlation energy of the inhomogeneous electron gas. *Physical Review B* **1986**, *33*, 8822.

14. Perdew, J. P.; Chevary, J. A.; Vosko, S. H.; Jackson, K. A.; Pederson, M. R.; Singh, D. J.; Fiolhais, C. Atoms, molecules, solids, and surfaces: Applications of the generalized gradient approximation for exchange and correlation. *Physical Review B* **1992**, *46*, 6671.

15. Kohn, W.; Becke, A. D.; Parr, R. G. Density functional theory of electronic structure. *J. Phys. Chem.* **1996**, *100*, 12974-12980.

16. Perdew, J. P.; Wang, Y. Accurate and simple analytic representation of the electron-gas correlation energy. *Physical Review B* **1992**, *45*, 13244.

17. Ernzerhof, M.; Scuseria, G. E. Assessment of the Perdew–Burke–Ernzerhof exchange-correlation functional. *J. Chem. Phys.* **1999**, *110*, 5029-5036.

18. Hammer, B.; Hansen, L. B.; Nørskov, J. K. Improved adsorption energetics within density-functional theory using revised Perdew-Burke-Ernzerhof functionals. *Physical Review B* **1999**, *59*, 7413.

19. Perdew, J. P.; Ruzsinszky, A.; Csonka, G. I.; Vydrov, O. A.; Scuseria, G. E.; Constantin, L. A.; Zhou, X.; Burke, K. Restoring the density-gradient expansion for exchange in solids and surfaces. *Phys. Rev. Lett.* **2008**, *100*, 136406.

20. Lee, C.; Yang, W.; Parr, R. G. Development of the Colle-Salvetti correlation-energy formula into a functional of the electron density. *Physical Review B* **1988**, *37*, 785.

21. Kocevski, V. *Theory and Modelling of Functional Materials* **2015**.

22. Mckee, M. L.; Page, M. Computing reaction pathways on molecular potential energy surfaces. *Reviews in Computational Chemistry, Volume 4* **2007**, 35-65.

23. Jónsson, H.; Mills, G.; Jacobsen, K. W. In *Nudged elastic band method for finding minimum energy paths of transitions;* Classical and quantum dynamics in condensed phase simulations; World Scientific: 1998; pp 385-404.

24. Henkelman, G.; Jónsson, H. A dimer method for finding saddle points on high dimensional potential surfaces using only first derivatives. *J. Chem. Phys.* **1999**, *111*, 7010-7022.

25. Henkelman, G.; Uberuaga, B. P.; Jónsson, H. A climbing image nudged elastic band method for finding saddle points and minimum energy paths. *J. Chem. Phys.* **2000**, *113*, 9901-9904.

26. Karplus, M.; McCammon, J. A. Molecular dynamics simulations of biomolecules. *Nature Structural and Molecular Biology* **2002**, *9*, 646.

27. Schuler, B.; Lipman, E. A.; Eaton, W. A. Probing the free-energy surface for protein folding with single-molecule fluorescence spectroscopy. *Nature* **2002**, *419*, 743.

28. Friedrichs, M. S.; Eastman, P.; Vaidyanathan, V.; Houston, M.; Legrand, S.; Beberg, A. L.; Ensign, D. L.; Bruns, C. M.; Pande, V. S. Accelerating molecular dynamic simulation on graphics processing units. *Journal of Computational Chemistry* **2009**, *30*, 864-872.

29. Cheong, W.; Zhang, L. Molecular dynamics simulation of phase transformations in silicon monocrystals due to nano-indentation. *Nanotechnology* **2000**, *11*, 173.

30. Raty, J.; Gygi, F.; Galli, G. Growth of carbon nanotubes on metal nanoparticles: a microscopic mechanism from ab initio molecular dynamics simulations. *Phys. Rev. Lett.* **2005**, *95*, 096103.

31. Sanchez, A.; Abbet, S.; Heiz, U.; Schneider, W.; Häkkinen, H.; Barnett, R.; Landman, U. When gold is not noble: nanoscale gold catalysts. *The Journal of Physical Chemistry A* **1999**, *103*, 9573-9578.

32. Verlet, L. Computer" experiments" on classical fluids. I. Thermodynamical properties of Lennard-Jones molecules. *Physical Review* **1967**, *159*, 98.

33. Weiner, P. K.; Kollman, P. A. AMBER: Assisted model building with energy refinement. A general program for modeling molecules and their interactions. *Journal of Computational Chemistry* **1981**, *2*, 287-303.

34. van Gunsteren, W. F.; Berendsen, H. J. Computer simulation of molecular dynamics: methodology, applications, and perspectives in chemistry. *Angewandte Chemie International Edition in English* **1990**, *29*, 992-1023.

35. Rappé, A. K.; Casewit, C. J.; Colwell, K.; Goddard Iii, W.; Skiff, W. UFF, a full periodic table force field for molecular mechanics and molecular dynamics simulations. *J. Am. Chem. Soc.* **1992**, *114*, 10024-10035.

36. Clark, M.; Cramer, R. D.; Van Opdenbosch, N. Validation of the general purpose Tripos 5.2 force field. *Journal of Computational Chemistry* **1989**, *10*, 982-1012.

37. Van Duin, A. C.; Dasgupta, S.; Lorant, F.; Goddard, W. A. ReaxFF: a reactive force field for hydrocarbons. *The Journal of Physical Chemistry A* **2001**, *105*, 9396-9409.

38. Van Duin, A. C.; Baas, J. M.; van de Graaf, B. Delft molecular mechanics: a new approach to hydrocarbon force fields. Inclusion of a geometry-dependent charge calculation. *Journal of the Chemical Society, Faraday Transactions* **1994**, *90*, 2881-2895.

39. Han, S. S.; Kang, J. K.; Lee, H. M.; van Duin, A. C.; Goddard, W. A. The theoretical study on interaction of hydrogen with single-walled boron nitride nanotubes. I. The reactive force field $ReaxFF_{HBN}$ development. *J. Chem. Phys.* **2005**, 123, 114703

40. Kresse, G.; Furthmüller, J. Efficiency of ab-initio total energy calculations for metals and semiconductors using a plane-wave basis set. *Computational Materials Science* **1996**, *6*, 15-50.

41. Blöchl, P. E. Projector augmented-wave method. *Physical Review B* **1994**, *50*, 17953.

42. Plimpton, S.; Crozier, P.; Thompson, A. LAMMPS-large-scale atomic/molecular massively parallel simulator. *Sandia National Laboratories* **2007**, *18*, 43-43.

Chapter 3 - hBN Growth from Ni-Cr Flux

Part of Chapter 3 is reproduced with permission from:

Vuong, T.; Cassabois, G.; Valvin, P.; Liu, S.; Edgar, J.; Gil, B. Exciton-phonon interaction in the strong-coupling regime in hexagonal boron nitride. *Physical Review B* **2017**, *95*, 201202.

3.1 Introduction

High-quality hBN crystals can be grown with Ni solvent,[1,2] but, due to its small nitrogen solubility, the growth rates are limited at atmospheric pressure. Kowanda *et al.*[3] claimed that nitrogen solubility in Ni solvent can be enhanced by the addition of Mo. Afterwards, Kubota *et al.*[1] first demonstrated atmospheric hBN crystal growth from a Ni-Mo solvent. According to Kowanda *et al.*[3], the effect of Cr on nitrogen solubility in the Ni flux is much stronger than that of Mo. The Ni-Cr phase diagram has a eutectic point at 1345 °C with 49 wt% Ni and 51 wt% Cr.[4] Consequently, the synthesis of hBN crystals from Ni-Cr solvent was demonstrated at atmospheric pressure by Kubota *et al.*[5] They reported a Raman peak width of 9.0 cm^{-1} at 1367 cm^{-1}, which is much narrower than what is typically reported for hBN produced by chemical vapor deposition, i.e., > 15 cm^{-1}.[6,7] The maximum cathodoluminescence energy of their crystals was 5.77 eV.

The electronic and optical properties in semiconductors are highly dependent on its lattice vibrations, i.e., phonons. The temperature dependence of the excitonic optical response in semiconductors comprises the modification of the bandgap energy and the broadening of the excitonic resonance due to the exciton-phonon collisions.[8-10] Toyozawa[11] pointed out that there are strong and week coupling regimes for the exciton-phonon interactions. For the strong coupling regime, the excitonic emission line has a Gaussian profile and the linewidth increases as the square

root of the temperature ($\sqrt{T}$). In the weak coupling regime, the excitonic emission line has a Lorentzian profile, and the linewidth increases linearly with temperature.

In this chapter, the nitridation procedures of those source materials in hBN growth will be first discussed to understand how chromium increases the nitrogen solubility in nickel solvent. Then the tilting experiment will be described, with its aim of separating large-scale free-standing hBN crystals from the metal flux without using mechanical exfoliation methods. After that, several characterizations performed on hBN crystals will be presented to qualify the crystal quality and properties. The exciton-phonon interaction in hBN will be studied by performing photoluminescence spectroscopy at different temperatures. Lastly, hBN growth from several other metal fluxes will be presented.

3.2 Experimental Methods

The experiments discussed in this chapter were performed using a combination of the horizontal and tilting CM furnaces. The experimental process for hBN crystal growth from Ni-Cr metal flux was described in Chapter 2. Characterization of these samples was performed using optical microscopy, Raman, x-ray photoelectron spectroscopy (XPS), x-ray diffraction (XRD), and photoluminescence spectroscopy (PL).

For the nitridation experiments discussed in this chapter, pure nickel, chromium, boron, and Ni-Cr-B powders were used as the source materials loaded into separate alumina boats. The alloy weight was equal to the total of nickel, chromium, and boron powders in the other boats. An empty boat was used as reference. Before the loading of the source materials, all the alumina boats were heated at 1500 °C under forming gas for ten hours to remove volatile impurities. The five alumina boats were placed into a multiple-zone furnace (Mellen Furnace), to make sure the

temperatures for all the boats were equal. The furnace was evacuated and then filled with N_2 and forming gas (5% hydrogen in balance argon) gas to a constant pressure of 850 Torr. During the reaction process, the N_2 and forming gases continuously flowed through the system at rates of 125 sccm and 25 sccm, respectively. After a dwell time of 4 hours at the reaction temperatures, the system was quickly quenched to room temperature.

3.3 Results and Discussion

3.3.1 Nitridation Analysis

The addition of Cr to Ni significantly improves the hBN crystal quality grown from metal flux method because of a higher nitrogen solubility in Ni-Cr-B alloy than that in Ni-B. In order to investigate the mechanism in detail, we performed a group of nitridation experiments in different temperatures, i.e., 1400 °C, 1450 °C and 1500 °C.

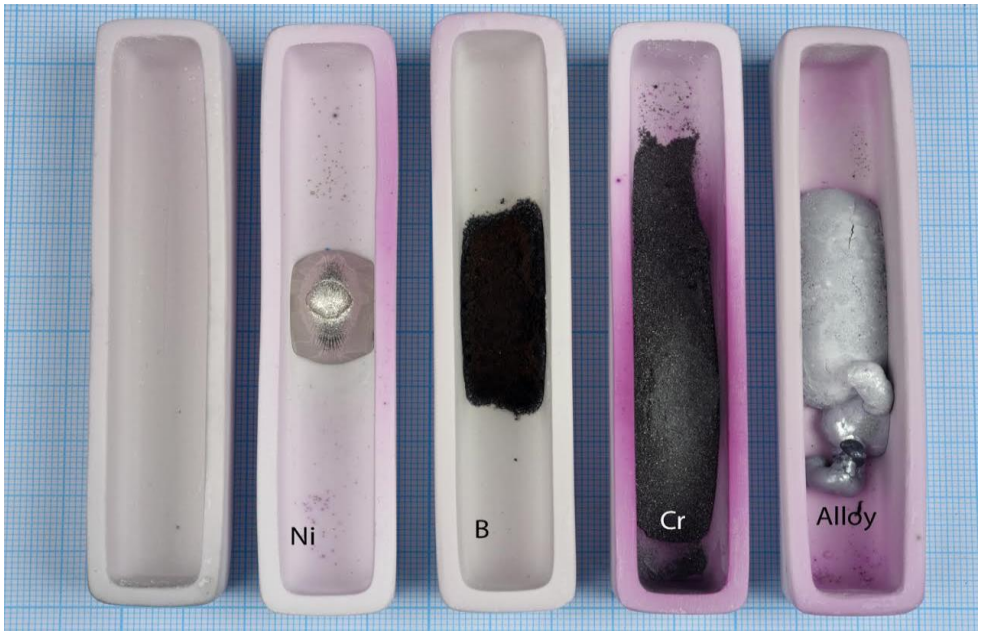

Figure 3.1. Optical photograph of the nitridation products of nickel, chromium, boron and Ni-Cr-B alloy at 1500 °C.

The optical photograph in Figure 3.1 illustrates the nitridation products at 1500 °C. The nickel and alloy powders were melted to ingots at the reaction temperature, while the boron and chromium powders remained in the solid phase as their melting points are higher than 1500 °C. The boats holding chromium and alloy were various shades of pink, much more than the other three. This has been caused by the slight oxidation of chromium during the reaction, where the oxygen may come from the impurities in the nickel and chromium source materials.

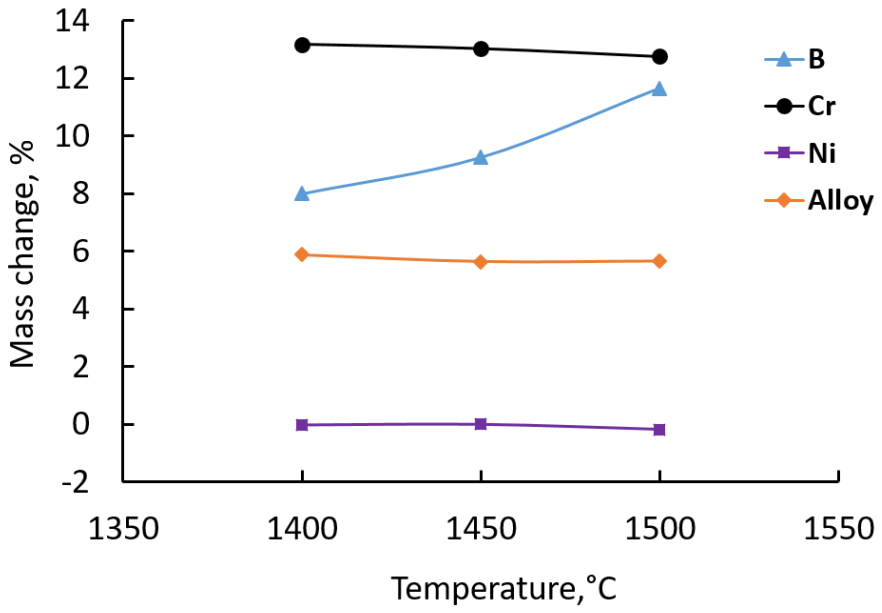

Figure 3.2. Mass change percentages of nickel, chromium, boron and alloy after the nitridation reactions at temperatures of 1400 °C, 1450 °C and 1500 °C.

Figure 3.2 shows the mass change percentages of the source materials after the nitridation reactions at different reaction temperatures. The mass change of nickel was nearly zero at all the three reaction temperatures, which indicates that nickel doesn't react with nitrogen. The boron mass change displayed an uptrend from 8% at 1400 °C to 11.5% at 1500 °C, which means the transformation from boron and nitrogen gas to boron nitride was greater at higher temperature. The mass change percentages for chromium were higher than 12% at all three temperatures, which means that chromium had dissolved the most nitrogen gas. However, its mass change percentage decreased slightly with increasing temperature. To understand this, x-ray diffraction was taken on the chromium samples as described in the next paragraph. The mass change of alloy also experienced a slight decrease with the increasing of reaction temperature, which is mainly caused by the lower chromium mass change at higher temperature.

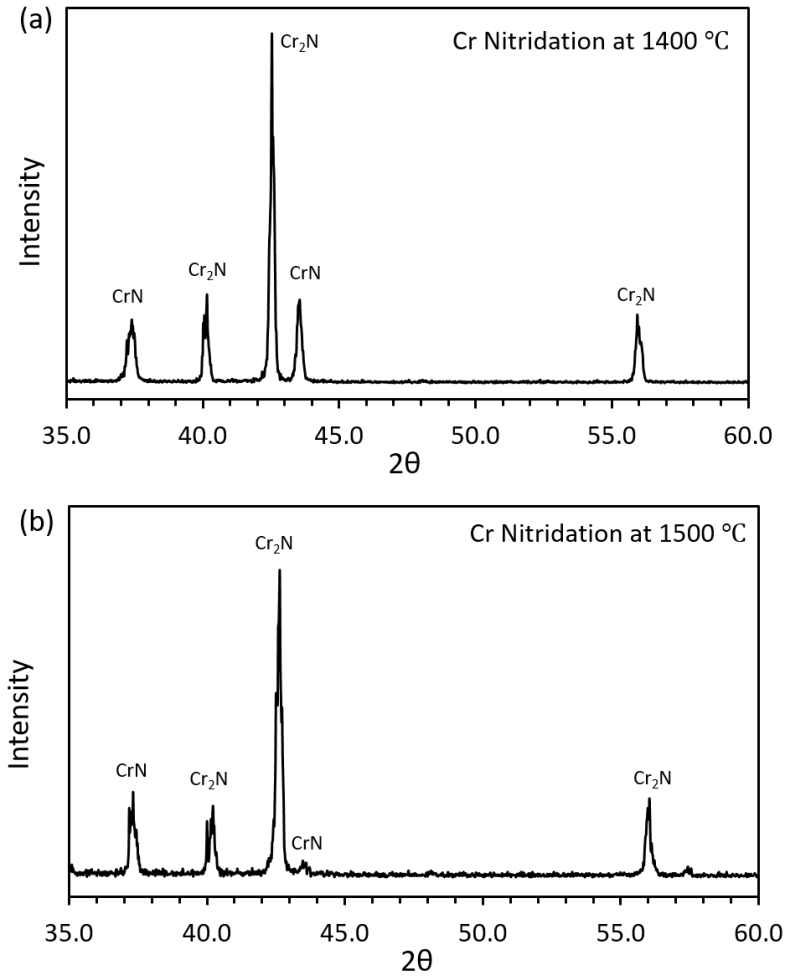

Figure 3.3. XRD spectra from chromium nitridation products at temperatures of (a) 1400 °C and (b) 1500 °C. The characterization peaks of CrN and Cr_2N are labeled.

Two possible Cr-nitrides, i.e., CrN and Cr_2N, can form at temperature higher than 600 °C:[14]

$$Cr_{(s)} + \frac{1}{2}N_2 \rightarrow CrN_{(s)} \tag{13}$$

$$Cr_{(s)} + \frac{1}{4}N_2 \rightarrow \frac{1}{2}Cr_2N_{(s)} \tag{14}$$

we therefore analyzed the chromium nitridation products at 1400 °C and 1500 °C by XRD, scanning from 35° and 60.0°, as shown in Figure 3.3. In the XRD patterns, three Cr_2N peaks were observed at 40.1°, 42.5° and 56.0°, respectively, while two CrN peaks were located at 36.3° and 43.7°. Compared to the 1400 °C spectrum, the CrN peak at 43.7° has a much lower intensity at 1500 °C, while the peak at 36.3° slightly increased, which means the chromium nitridation reaction produces less CrN at 1500 °C than that at 1400 °C. To further confirm this conclusion, we calculated the CrN/ Cr_2N ratio of intensity; it was lower at 1500 °C (0.32) than at 1400 °C (0.38). This suggests that the production of CrN is preferred at lower temperature, but Cr_2N is more favored at higher temperature. The higher Cr_2N production leads to a lower mass change by using the same amount of chromium source, which explained the decrease trend of chromium mass change in Figure 3.2.

3.3.2 hBN Separation at High Temperature

In order to separate large-scale, free-standing hBN from the metal surface, tilting experiments were performed. The experimental details were described in Chapter 2. Figure 3.4a shows the separated Ni-Cr metal and hBN layer, which are located on opposite sides. The metal flux was originally at the right side. As the furnace was tilted, it broke through the precipitated hBN layer, and flowed to the left side. Figure 3.4b shows a free-standing hBN flake obtained from the separate hBN layer with a size of over 4 mm^2. Although the tilting experiment is a promising method to obtain large-scale free-standing hBN crystals, the success rate of the separation was low as it is dependent on many factors, such as the metal mass, the groove shape of the BN boat, hBN

layer thickness formed on the metal surface, and the furnace tilting operation. Future work should include a more detailed investigation of those factors on crystal separation.

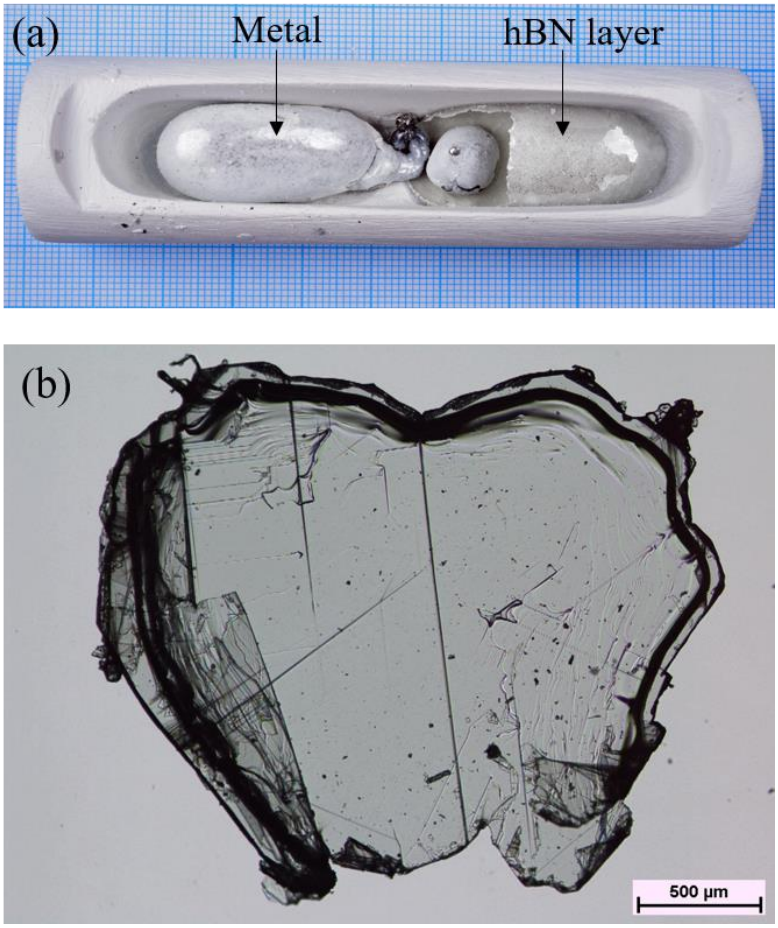

Figure 3.4. Optical micrographs of (a) separated Ni-Cr metal and hBN layer in the BN hot-pressed boat, (b) free-standing hBN flake obtained from the separated hBN layer.

3.3.3 Characterizations

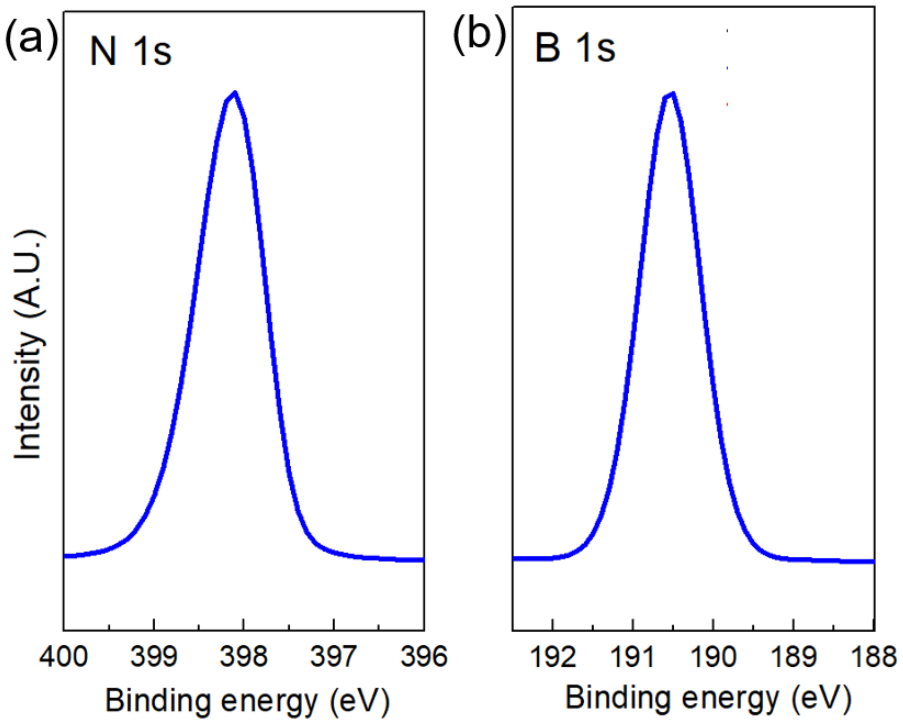

Figure 3.5. XPS spectra of (a) N 1s and (b) B 1s from hBN crystals grown from a Ni-Cr metal flux.

X-ray photoelectron spectroscopy (XPS) was carried out to investigate the chemical bonding in hBN. Figure 3.5 shows the XPS spectra of the N 1s and B 1s peaks from hBN crystals grown from Ni-Cr metal flux. The binding energies for N 1s and B 1s in hBN are 398.1 eV and 190.5 eV, respectively, which are in good agreement with previously reported literature values[15-17]. The B/N ratio from our XPS spectrum was calculated to be 1.19, which is also very close to the values reported before.[18,19]

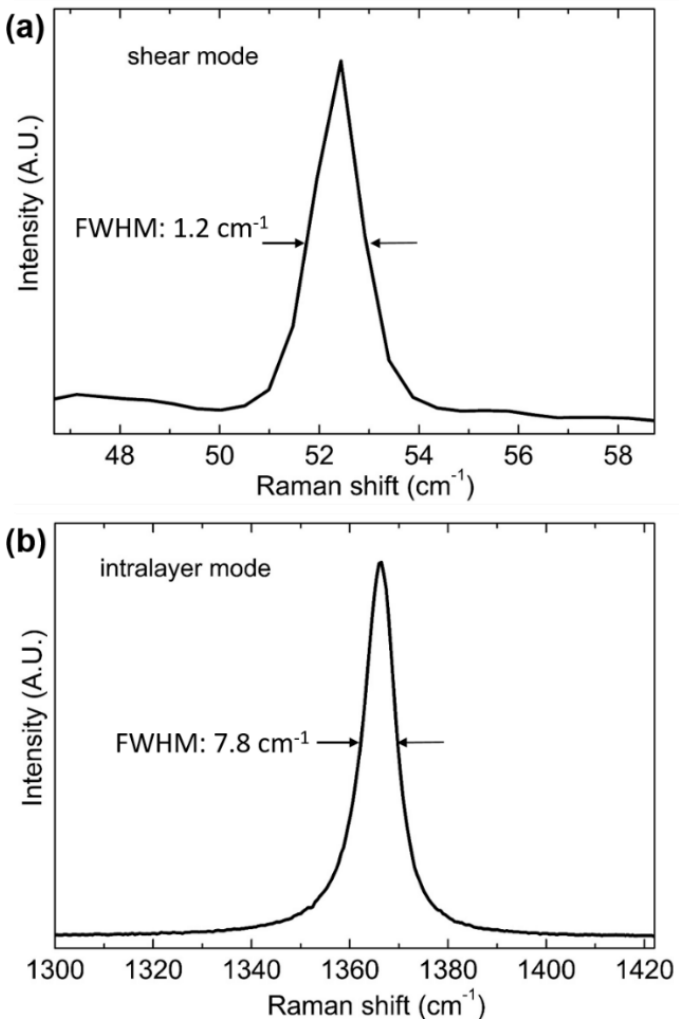

Figure 3.6. Raman spectra of (a) shear mode and (b) intralayer mode from hBN crystals grown from a Ni-Cr metal flux.

Figure 3.6 displays the Raman spectra from the hBN crystals grown with the Ni-Cr flux. The low-frequency spectrum in Figure 3.6a, which is attributed to the rigid shearing oscillation between adjacent layers, shows that the hBN crystals have an intense peak at 52.5 cm^{-1}, which is consistent with previously reported references.[20,21] The full width at half-maximum (FWHM) is 1.2 cm^{-1}, which indicates our hBN crystals are of high quality. The high-frequency spectrum in Figure 3.6b, which corresponds to the intralayer E_{2g} vibrational mode between in-plane boron and

nitrogen, show that hBN crystal grown from Ni-Cr has an intense peak at 1366.1 cm^{-1} with an FWHM of 7.8 cm^{-1}, which is among the smallest values reported in the literature.[22,23]

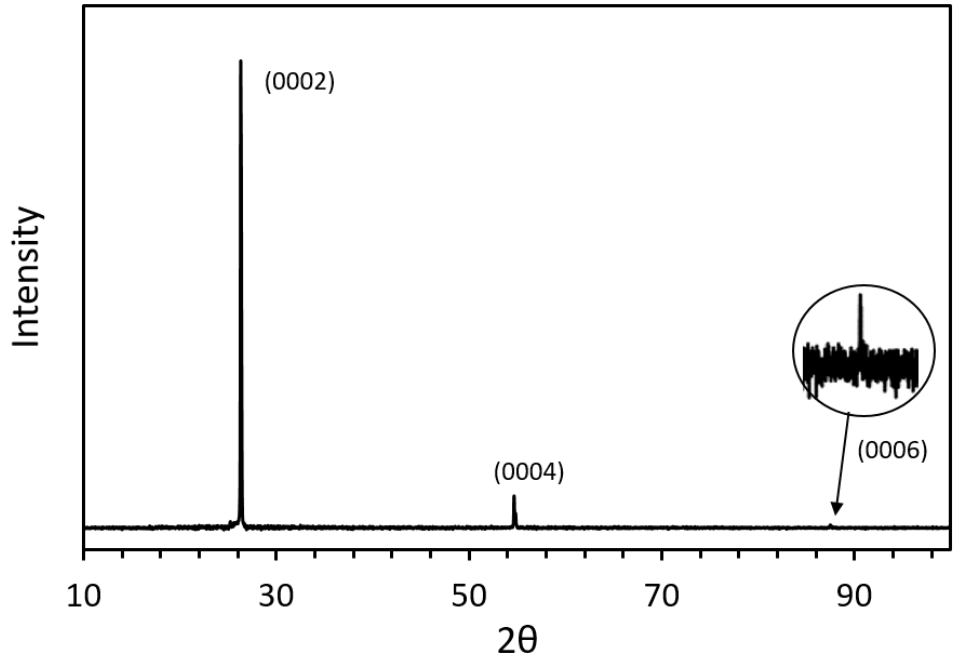

Figure 3.7. XRD spectrum of hBN crystals grown from a Ni-Cr metal flux.

The hBN crystals grown form Ni-Cr metal flux were also characterized by XRD, scanning from 10° and 100.0°, as shown in Figure 3.7. The hBN (0002) peak at around 26.4° can be identified. The estimated interlayer distance according to Bragg's law, as shown in Equation (15), is 0.33 nm, which is consistent with the literature values.[24-27] Additionally, the (0004) and (0006) peaks were observed at 54.7° and 87.5°, respectively. The absence of defect peaks and narrowing hBN peaks showing in the XRD spectrum indicate the hBN crystals grown from Ni-Cr metal flux are well-ordered and of high-quality.

$$\lambda = 2dsin(\theta) \quad (15)$$

where $\lambda = 0.154\ nm$, and $\theta = 26.4°/2 = 13.2°$.

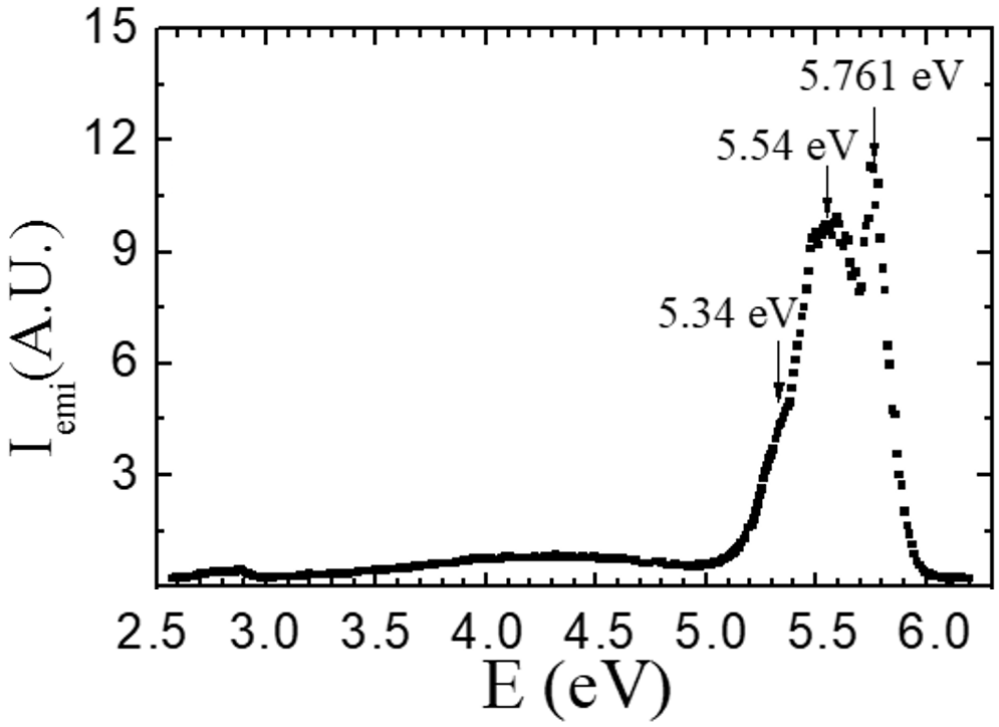

Figure 3.8. Room temperature photoluminescence (PL) spectrum of hBN crystals grown from a Ni-Cr metal flux.

The quality of the hBN crystals was accessed by Photoluminescence (PL) spectroscopy. Figure 3.8 shows the room temperature band-edge PL emission spectra of hBN crystals grown from a Ni-Cr solvent. The intense ultraviolet luminescence peaks were at 5.761 eV and 5.54 eV, which is characteristic of a high-purity, high-quality hBN crystal.[27] The energy bands indicating defects and impurities, located around 4.3 eV and 2.9 eV, were relatively weak in intensity, confirming a low residual impurity concentration in those crystals.

3.3.4 Strong-coupling regime of the Exciton-phonon Interaction in hBN

The PL spectra from hBN over temperatures ranging from 8K to 300K were collected (Figure 3.9). At 8K, the PL spectrum is composed of several emission peaks, reflecting the various paths for recombination assisted by phonon emission in hBN. Specifically, there are four main peaks located at 5.765, 5.79, 5.86, and 5.89 eV corresponding to the recombination assisted by the emission of LO, TO, LA, and TA phonon, respectively. On the low-energy side of X_{LO} and X_{TO} peaks, there are sidebands, which extend over tens of meV and arise from overtones of the interlayer shear modes in hBN.[28] These lattice vibrations are exclusive in layered compound since they correspond to the shear rigid motion between adjacent layers, with a characteristic energy of about 6-7 meV in bulk hBN.[29] The green solid line is a theoretical calculation of the emission lines in the framework of model developed in Ref. [28], which presents a Gaussian profile. The superior fit of the PL pattern by the Gaussian function demonstrates the strong-couple regime of the exciton-phonon interaction in hBN.

The temperature-dependent study of the PL spectrum in hBN is shown in Figure 3.9. With the temperature increase, the phonon replicas broaden, leading first to a reduced visibility of the doublet fine-structure of the LO and TO phonon replicas at 20 K. Above 20 K, the doublets disappeared, indicating that the full width at half maximum (FWHM) of the emission peaks becomes larger than the doublet splitting with an order of 6-7 meV. At 100 K, we noted that the LO and TO phonon replicas, which are separated by roughly 30 meV, are no longer spectrally resolved, and that the merged emission band of those replicas is almost symmetric. From 100 K up to room temperature, the modifications of the PL spectrum are less dramatic. The above phenomenology suggests that the thermally induced broadening is rapidly growing in a first stage,

followed by smoother variations up to room temperature. The nonlinear trend confirms strong-coupling regime of the exciton-phonon interaction in hBN.

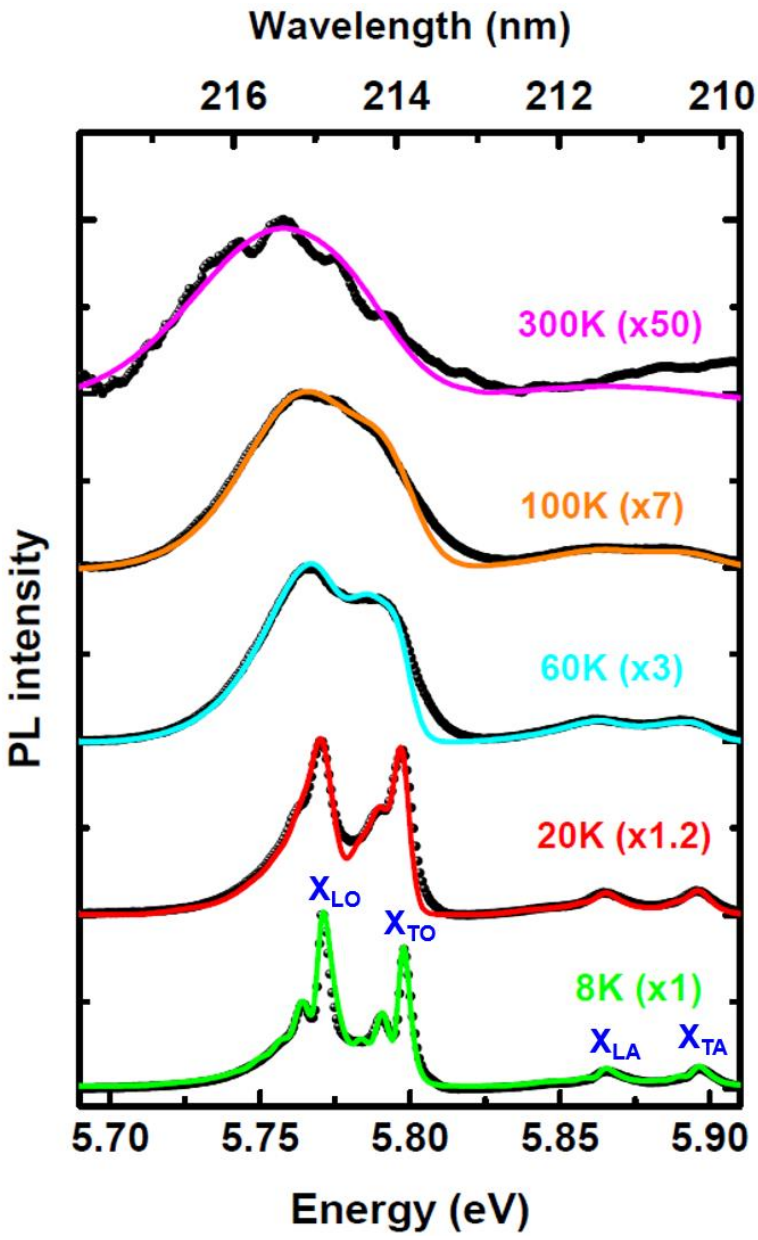

Figure 3.9. PL spectrum in hBN as a function of temperature, from 8 to 300 K: experimental data (symbols); theoretical fit (solid lines). The full width at half maximum (FWHM) Δ is the only varying parameter as a function of temperature.

3.3.5 hBN Growth from Other Metal Fluxes

To investigate the effect of metal fluxes on the hBN crystal quality, various kind of solvents, including Fe, Mg-Ni-Cr, Ti-Ni-Cr and Si-Ni-Cr, were tested under the same experimental conditions. Crystals prepared from a Ni-Cr flux serve as the reference. The optical micrographs of hBN crystals grown from those solvents are shown in Figure 3.10.

Using Fe as a solvent is advantageous, as it has a much lower price compared to Ni (one seventh to one tenth of the price). As shown in Figure 3.10a, crystals prepared with Fe were clear and colorless, but have much smaller sizes than the crystals grown from Ni-Cr metal flux. With the addition of Mg into Ni-Cr flux, the synthesized hBN crystals (Figure 3.10b) became smaller, but still clear and colorless. In order to dope Si into hBN crystals, Ni and Cr mixed with high-purity Si power were used as a solvent. However, a SiN layer covering on the metal surface was formed by the reaction between Si and BN at high temperature, which blocked the hBN crystal precipitation onto the surface, and eventually formed nonuniform crystals with small sizes, as shown in Figure 3.10c. When using Ti-Ni-Cr, TiN crystals (golden color) were formed on the metal surface, as illustrated in Figure 3.10d, which were produced by the reaction of Ti and N_2 at temperatures higher than 1200 °C. In addition, hBN crystals grown from Ti-Ni-Cr were generally smaller than 50 μm.

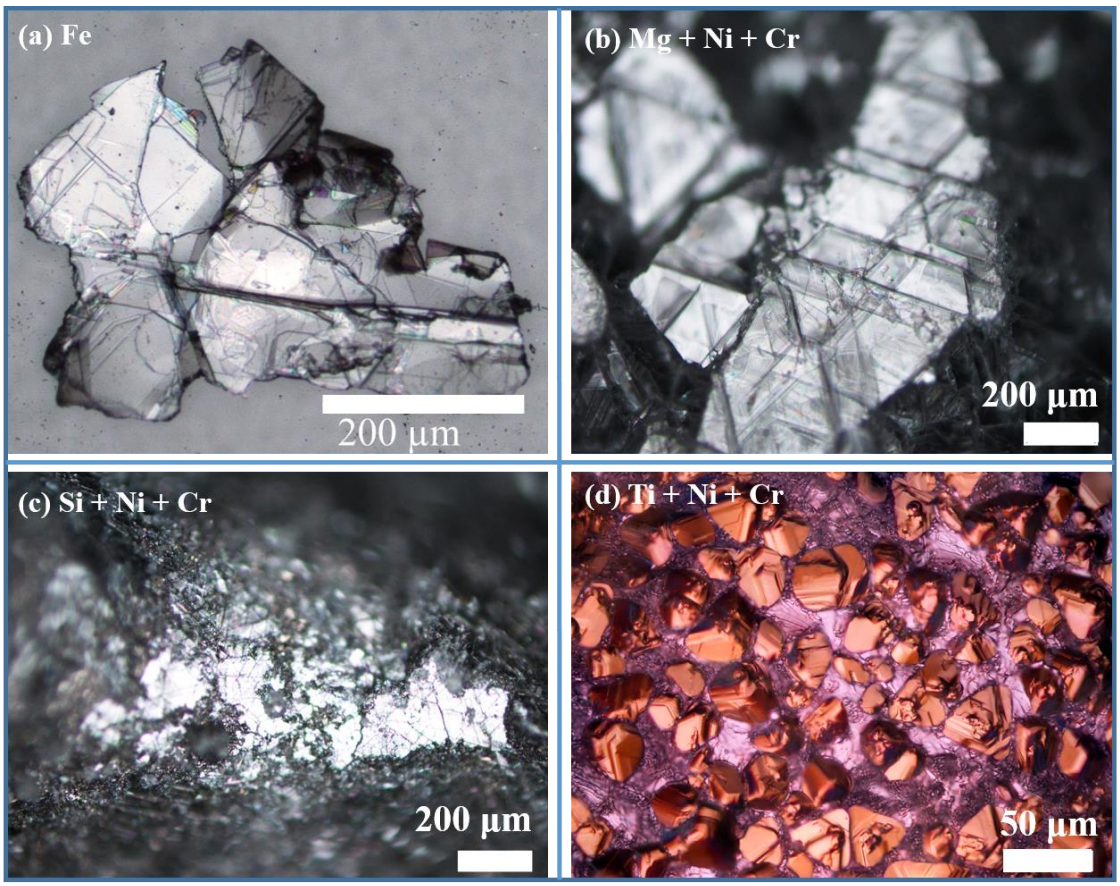

Figure 3.10. Optical micrograph of hBN crystals grown from (a) Fe, (b) Mg-Ni-Cr, (c) Si-Ni-Cr, and (d) Ti-Ni-Cr metal flux.

The hBN crystals grown from the above metal solvents were characterized by photoluminescence (PL) spectroscopy at 10 K. The PL spectra in Figure 3.11 illustrate that the crystals grown from those solvents have remarkably similar patterns except for the Si-doped sample in which the emission peaks had a small left shift compared with others. Moreover, the addition of Si elements disappeared the maximum peak at 5.799 eV, and suppressed the peak intensity at 5.77 eV. This indicates that Si elements have doped into hBN, and slightly changed its band structure. Therefore, further investigation on the electric properties of Si-doped hBN is

needed. The overall results illustrate that the crystals grown from Ni-Cr, Fe, Ti-Ni-Cr and Mg-Ni-Cr metal solvents have similar quality, and Si elements can be doped into hBN.

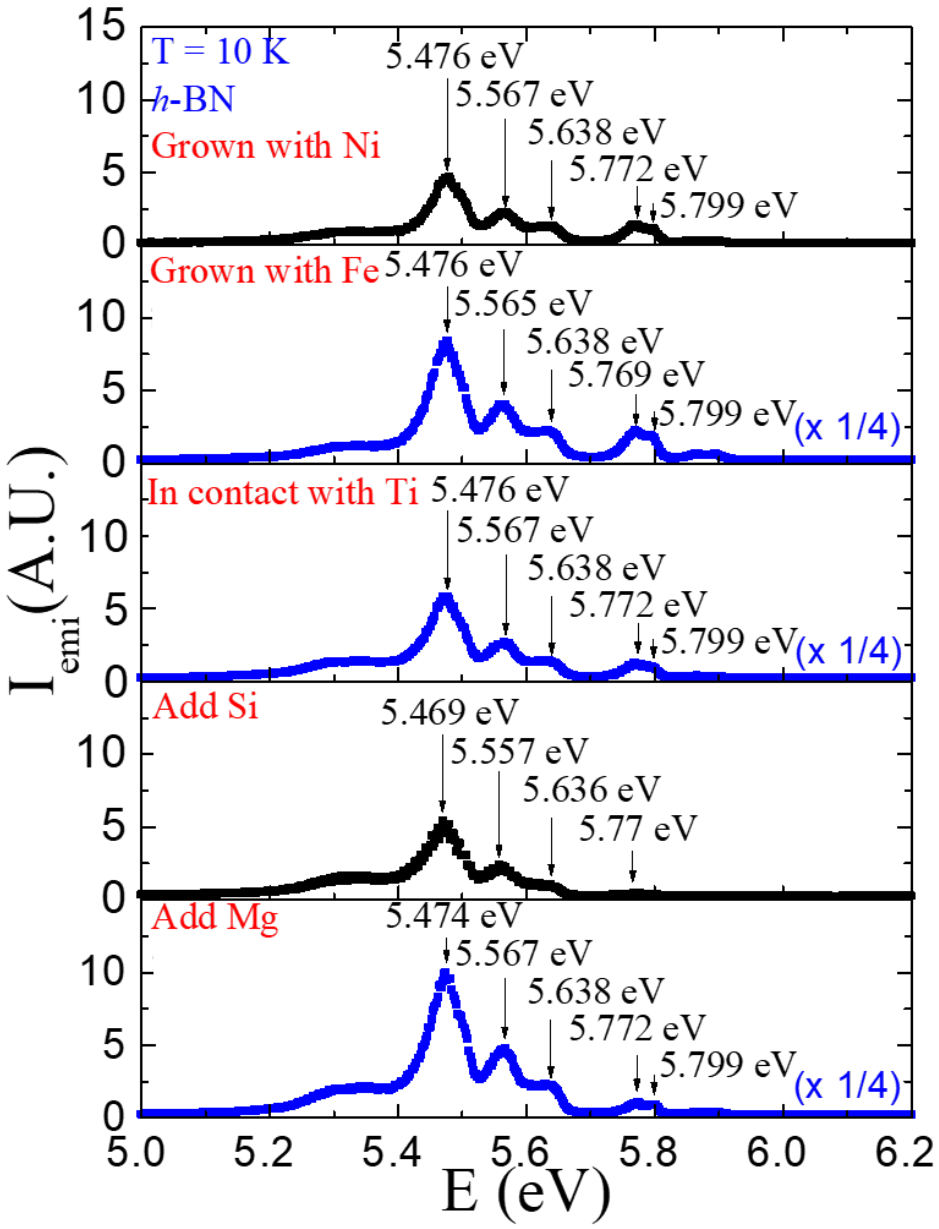

Figure 3.11. PL spectra of hBN crystals grown from Ni-Cr, Fe, Ti-Ni-Cr, Si-Ni-Cr, and Mg-Ni-Cr solvents.

3.4 Conclusions

This study has shown that large-scale, high-quality bulk hBN single crystals can be successfully formed from Ni-Cr solvent at atmospheric pressure. Nickel does not react with nitrogen during the crystal grown, while chromium is preferred to be nitrided to Cr_2N at higher temperature. Large-scale free-standing hBN crystals can be separated at high temperature by using a tiltable furnace at high temperature while the metal flux is still liquid. The XPS spectrum illustrates that the B 1s and N 1s binding energies in our hBN samples are in good agreement with the literature values. The XRD pattern indicates the hBN crystals are well-ordered and high quality. The Raman spectrum of both shear mode and intralayer mode also shows the high-quality of the crystals. The band-edge PL emission spectra imply that the hBN crystals grown from Ni-Cr have a high quality and low defect and impurity density. The temperature dependent PL spectra show that the exciton-phonon interaction in hBN is in the strong-coupling regime. Moreover, the hBN crystals grown from Fe, Ti-Ni-Cr and Mg-Ni-Cr metal solvents have similar quality but smaller sizes compared with the crystals from Ni-Cr, and Si elements can be doped into hBN.

3.5 Acknowledgement

Support from the Materials Engineering and Processing program of the National Science Foundation, award number 1538127, and the II−VI Foundation is greatly appreciated. The Raman measurement at University of North Iowa was supported by the National Science Foundation (NSF CAREER Grant No. DMR-1552482). The photoluminescence work at Texas Tech University was supported by ARO (W911NF-16-1-0268) and monitored by Dr. Michael Gerhold. Thanks to Dr. Siyuan Zhang for her support of the XPS measurements.

References

1. Kubota, Y.; Watanabe, K.; Tsuda, O.; Taniguchi, T. Deep ultraviolet light-emitting hexagonal boron nitride synthesized at atmospheric pressure. *Science* **2007**, *317*, 932-934.
2. Kubota, Y.; Watanabe, K.; Taniguchi, T. Synthesis of cubic and hexagonal boron nitrides by using Ni solvent under high pressure. *Japanese Journal of Applied Physics* **2007**, *46*, 311.
3. Kowanda, C.; Speidel, M. Solubility of nitrogen in liquid nickel and binary Ni–Xi alloys (Xi= Cr, Mo, W, Mn, Fe, Co) under elevated pressure. *Scr. Mater.* **2003**, *48*, 1073-1078.
4. Pan, Y.; Nash, P. Binary alloy phase diagrams, 2nd edn, ed. by TB Massalski. *Metals Park, Ohio, American Society for Metals* **1986**, 2406-2408.
5. Kubota, Y.; Watanabe, K.; Tsuda, O.; Taniguchi, T. Hexagonal Boron Nitride Single Crystal Growth at Atmospheric Pressure Using Ni− Cr Solvent. *Chemistry of Materials* **2008**, *20*, 1661-1663.
6. Ahmed, K.; Dahal, R.; Weltz, A.; Lu, J.; Danon, Y.; Bhat, I. Growth of hexagonal boron nitride on (111) Si for deep UV photonics and thermal neutron detection. *Appl. Phys. Lett.* **2016**, *109*, 113501.
7. Li, X.; Jordan, M. B.; Ayari, T.; Sundaram, S.; El Gmili, Y.; Alam, S.; Alam, M.; Patriarche, G.; Voss, P. L.; Salvestrini, J. P. Flexible metal-semiconductor-metal device prototype on wafer-scale thick boron nitride layers grown by MOVPE. *Scientific Reports* **2017**, *7*, 786.
8. O'Donnell, K.; Chen, X. Temperature dependence of semiconductor band gaps. *Appl. Phys. Lett.* **1991**, *58*, 2924-2926.
9. Wei, S.; Zunger, A. Electronic and structural anomalies in lead chalcogenides. *Physical Review B* **1997**, *55*, 13605.

10. Göbel, A.; Ruf, T.; Cardona, M.; Lin, C.; Wrzesinski, J.; Steube, M.; Reimann, K.; Merle, J.; Joucla, M. Effects of the isotopic composition on the fundamental gap of CuCl. *Physical Review B* **1998**, *57*, 15183.
11. Toyozawa, Y. Theory of line-shapes of the exciton absorption bands. *Progress of Theoretical Physics* **1958**, *20*, 53-81.
12. Basu, A.; Majumdar, J. D.; Chowdhury, S. G.; Ajikumar, P.; Shankar, P.; Tyagi, A.; Raj, B.; Manna, I. Microstructural and texture studies of gas-nitrided Cr-coated low-alloy high-carbon steel. *Surface and Coatings Technology* **2007**, *201*, 6985-6992.
13. Moulder, J. F.; Stickle, W. F.; Sobol, P. E.; Bomben, K. D. Handbook of X-ray Potoelectron Spectroscopy; Chastain, J., Ed.; PerkinElmer Corporation: Waltham, MA, **1992**; pp 254−257.
14. Miyamoto, Y.; Rubio, A.; Cohen, M. L.; Louie, S. G. Chiral tubules of hexagonal BC_2N. *Physical Review B* **1994**, *50*, 4976.
15. Park, K.; Lee, D.; Kim, K.; Moon, D. Observation of a hexagonal BN surface layer on the cubic BN film grown by dual ion beam sputter deposition. *Appl. Phys. Lett.* **1997**, *70*, 315-317.
16. Shi, Y.; Hamsen, C.; Jia, X.; Kim, K. K.; Reina, A.; Hofmann, M.; Hsu, A. L.; Zhang, K.; Li, H.; Juang, Z. Synthesis of few-layer hexagonal boron nitride thin film by chemical vapor deposition. *Nano Letters* **2010**, *10*, 4134-4139.
17. Liu, Z.; Ma, L.; Shi, G.; Zhou, W.; Gong, Y.; Lei, S.; Yang, X.; Zhang, J.; Yu, J.; Hackenberg, K. P. In-plane heterostructures of graphene and hexagonal boron nitride with controlled domain sizes. *Nature Nanotechnology* **2013**, *8*, 119.
18. Kuzuba, T.; Era, K.; Ishii, T.; Sato, T. A low frequency Raman-active vibration of hexagonal boron nitride. *Solid State Commun.* **1978**, *25*, 863-865.

19. Pakdel, A.; Bando, Y.; Golberg, D. Nano boron nitride flatland. *Chem. Soc. Rev.* **2014**, *43*, 934-959.

20. Gorbachev, R. V.; Riaz, I.; Nair, R. R.; Jalil, R.; Britnell, L.; Belle, B. D.; Hill, E. W.; Novoselov, K. S.; Watanabe, K.; Taniguchi, T. Hunting for monolayer boron nitride: optical and Raman signatures. *Small* **2011**, *7*, 465-468.

21. Nemanich, R.; Solin, S.; Martin, R. M. Light scattering study of boron nitride microcrystals. *Physical Review B* **1981**, *23*, 6348.

22. Solozhenko, V.; Will, G.; Elf, F. Isothermal compression of hexagonal graphite-like boron nitride up to 12 GPa. *Solid State Commun.* **1995**, *96*, 1-3.

23. Paszkowicz, W.; Pelka, J.; Knapp, M.; Szyszko, T.; Podsiadlo, S. Lattice parameters and anisotropic thermal expansion of hexagonal boron nitride in the 10–297.5 K temperature range. *Applied Physics A* **2002**, *75*, 431-435.

24. Marini, A.; García-González, P.; Rubio, A. First-principles description of correlation effects in layered materials. *Phys. Rev. Lett.* **2006**, *96*, 136404.

25. Kern, G.; Kresse, G.; Hafner, J. Ab initio calculation of the lattice dynamics and phase diagram of boron nitride. *Physical Review B* **1999**, *59*, 8551.

26. Vuong, T.; Cassabois, G.; Valvin, P.; Jacques, V.; Cuscó, R.; Artús, L.; Gil, B. Overtones of interlayer shear modes in the phonon-assisted emission spectrum of hexagonal boron nitride. *Physical Review B* **2017**, *95*, 045207.

27. Cuscó, R.; Gil, B.; Cassabois, G.; Artús, L. Temperature dependence of Raman-active phonons and anharmonic interactions in layered hexagonal BN. *Physical Review B* **2016**, *94*, 155435.

Chapter 4 - hBN Growth from Fe-Cr Flux

Chapter 4 is reproduced in part with permission from:

Liu, S.; He, R.; Ye, Z.; Du, X.; Lin, J.; Jiang, H.; Liu, B.; Edgar, J. H. Large-Scale Growth of High-Quality Hexagonal Boron Nitride Crystals at Atmospheric Pressure from an Fe–Cr Flux. *Cryst. Growth Des.* **2017**, *17*, 4932-4935.

4.1 Introduction

The best quality hBN single crystals have been precipitated from molten metal solutions. Taniguchi *et al*.[1] and Zhigadlo *et al*.[2] both produced hBN crystals from solutions at high pressures (>30 kbar). However, crystals of similar quality can also be produced at atmospheric pressure. For example, Kubota *et al.*[3] first demonstrated atmospheric hBN crystal growth from a Ni-Mo solvent. They reported a Raman peak width of 9.0 cm^{-1} at 1367 cm^{-1}, which is much narrower than what is typically reported for hBN produced by chemical vapor deposition, i.e., >15 cm^{-1}.[4,5] The maximum cathodoluminescence energy of Kubota *et al*.'s crystals was 5.76 eV.

Near atmospheric growth is advantageous, since the crystal growth apparatus is simpler and thus easier to implement at lower cost. A later study by Kubota *et al*.[6] demonstrated that a 50 wt% mixture of nickel and chromium is an even better solvent for the atmospheric pressure solution growth of hBN single crystals. This alloy succeeds because nickel is a good solvent for boron with a maximum solubility of 18.5 at%,[7] and chromium can dissolve more nitrogen when compared to molybdenum.[8]

We have previously employed the Ni-Cr flux to produce hBN crystals that were (0001) orientated, a couple of millimeters across, and up to 200 microns thick.[9] These crystals had

excellent high energy deep ultraviolet photoluminescence spectra with an S-series excitonic emission at 5.897 eV at low temperature.[10] They were also sufficiently thick (200 microns) to demonstrate interference-less absorption at infrared frequencies.[11]

In the present note, we tested whether an iron-chromium solvent can also produce hBN crystals of comparable quality as the Ni-Cr solvent at atmospheric pressure. Like nickel, liquid iron has high comparable boron solubility, 17 at%.[12] The main advantage of iron is that it is less expensive than nickel, by a factor of 5 to 10.

Prior studies related to steel manufacturing suggest hBN crystal formation from an iron-based alloy should be possible[30,31]. The joint solubility of boron and nitrogen in iron has been the subject of a number of studies. Fountain and Chipman[13] studied these elements in solid iron between 950 °C and 1150 °C to understand their impact on the hardenability of steel. They reported that the presence of boron enhances nitrogen solubility in solid iron, and the solubility of both elements increases with temperature. For iron with and without boron, the solubility of nitrogen in the solid increased with its partial pressure. Morita *et al*[14] examined the impact of boron on the rate constants for nitrogen incorporation into liquid iron between 1873 K and 2023 K. They reported the rate constant for nitrogen decreased with the boron concentration. In contrast, the nitrogen incorporation rate constant increased with the chromium concentration.

In this study, the process of producing hBN crystals from a Fe-Cr flux was developed. The crystal sizes, shapes, and morphologies were determined by optical microscopy. Then the Raman and photoluminescence spectra were taken to assess the quality of the hBN crystals. Comparisons were made of these crystals to previous studies.

4.2 Growth Method

hBN crystals with the natural distribution of isotopes (20% B^{10} and 80% B^{11}) were synthesized by precipitation from solution in a high temperature single-zone tube furnace. A 50 wt% Fe and 50 wt% Cr mixed powder was loaded into a hot-pressed boron nitride crucible, which was both the source for the boron nitride and the container for the solution. The crucible with the source materials was then transferred into the furnace. The reaction tube was evacuated, and then filled with N_2 and forming gas (5% hydrogen in balance argon) to a constant pressure of 850 Torr. In this experiment, the forming gas was used to minimize oxygen and carbon impurities that are recognized as the main contaminants in hBN crystals. During the reaction, the N_2 and forming gases continuously flowed through the system at rates of 125 sccm and 25 sccm, respectively. The liquid solution was formed by heating the furnace up to 1550 °C and holding for a dwell period of 24 hours. The hBN crystals were then precipitated by cooling at a rate of 1 °C /h to 1500 °C. After growth, the system was quickly quenched to room temperature.

4.3 Results and Discussion

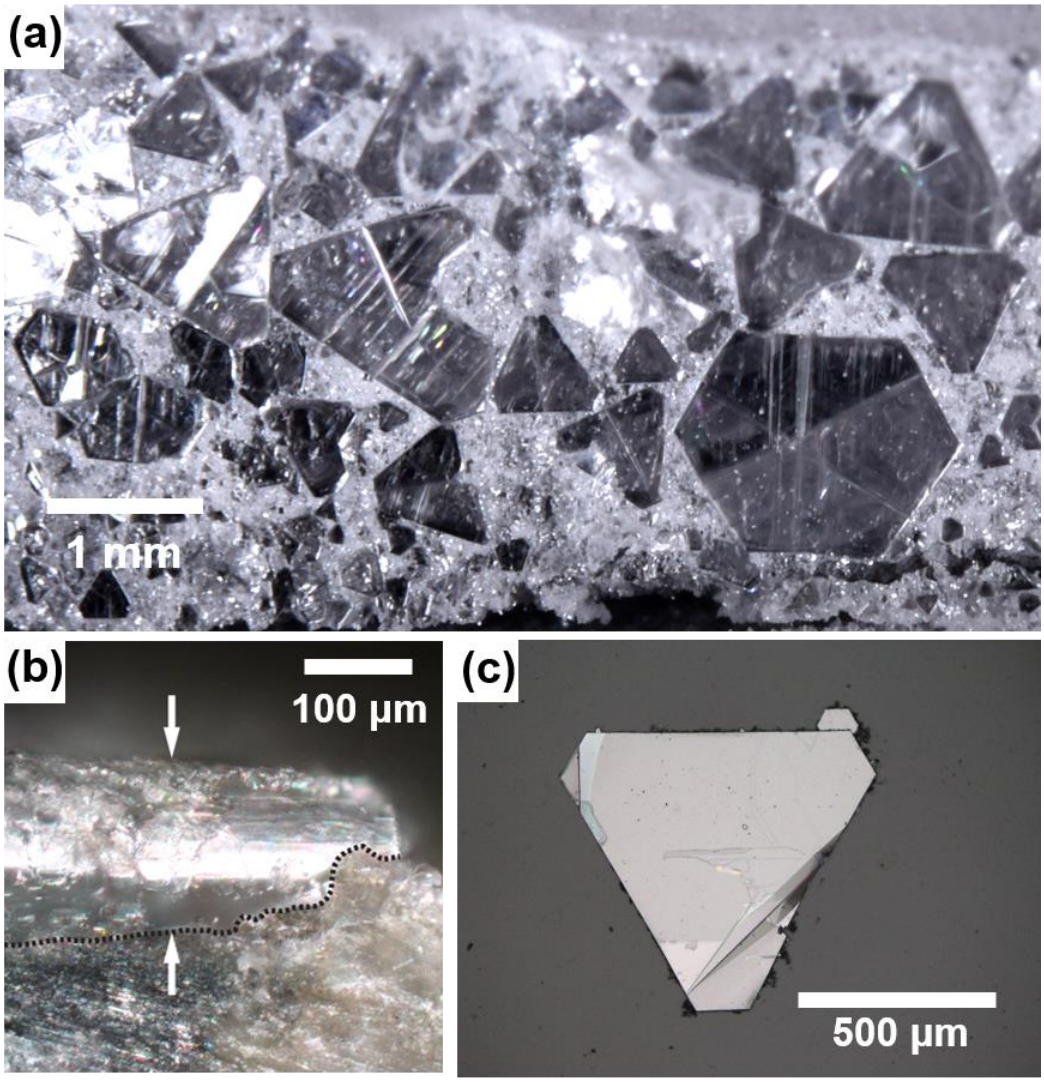

Figure 4.1. Optical micrograph of (a) hBN crystals on Fe-Cr ingot top surface (b) edge-on view of hBN crystal thickness and (c) hBN flake transferred from ingot onto the substrate.

Figure 4.1a is an optical image of hBN crystals on the solidified Fe-Cr solvent, showing that the grown hBN crystals are clear and colorless. There are two main crystal shapes on the metal surface: hexagonal and triangular. The largest domain is more than 2-mm across. The edge-on view of hBN crystal, as shown in Figure 4.1b, illustrates that the crystal thickness is around 200-

μm. Both crystal size and thickness are comparable with our previous prepared hBN crystals from Ni-Cr solvent, in which Ni and Cr also have weight ratio of 1: 1. Figure 4.1c shows an optical micrograph of hBN flake transferred from the metal surface onto a glass substrate, which has a dimension of about 1-mm across.

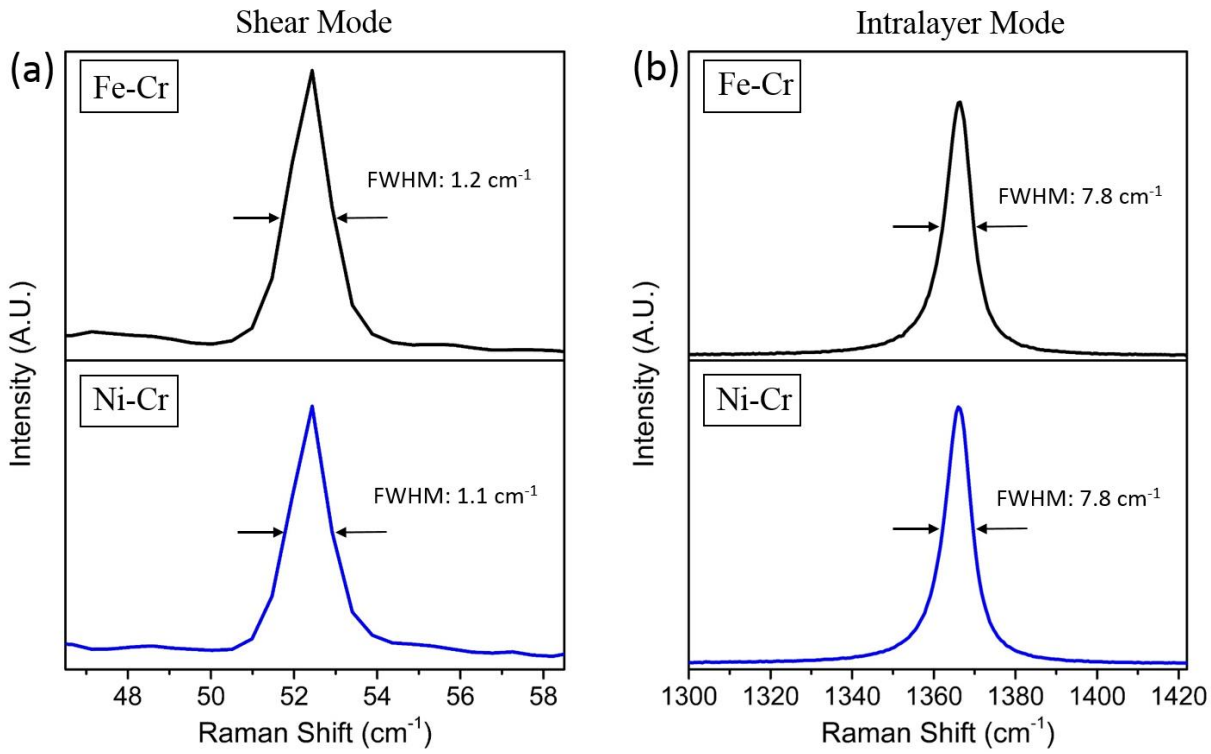

Figure 4.2. Raman spectra of shear mode (a) and intralayer mode (b) from hBN crystals grown with Fe-Cr (top) and Ni-Cr (bottom) flux.

A comparison of the Raman spectrum for the hBN crystals grown with the Fe-Cr (top) and Ni-Cr (bottom) flux is shown in Figure 4.2. The low-frequency spectrum in Figure 4.2a, which is attributed to the rigid shearing oscillation between adjacent layers, shows that hBN crystals from both solvents have an intense peak at the same position 52.5 cm^{-1}, which is consistent with

previously reports.[15,16] The full width at half-maximum (FWHM) values for the two peaks are 1.2 cm^{-1} and 1.1 cm^{-1}, respectively, which indicates our hBN crystals are of high quality. The high-frequency spectra in Figure 4.2b, which corresponds to the intralayer E_{2g} vibrational mode between in-plane boron and nitrogen, show that hBN crystal grown from Fe-Cr has an intense peak at 1366.1 cm^{-1} with an FWHM of 7.8 cm^{-1}, which is among the smallest values reported in the literature.[17,18] This is also comparable to our previously prepared high-quality hBN from Ni-Cr flux, which has a consistent peak position and FWHM value, as shown in Figure 4.2b.

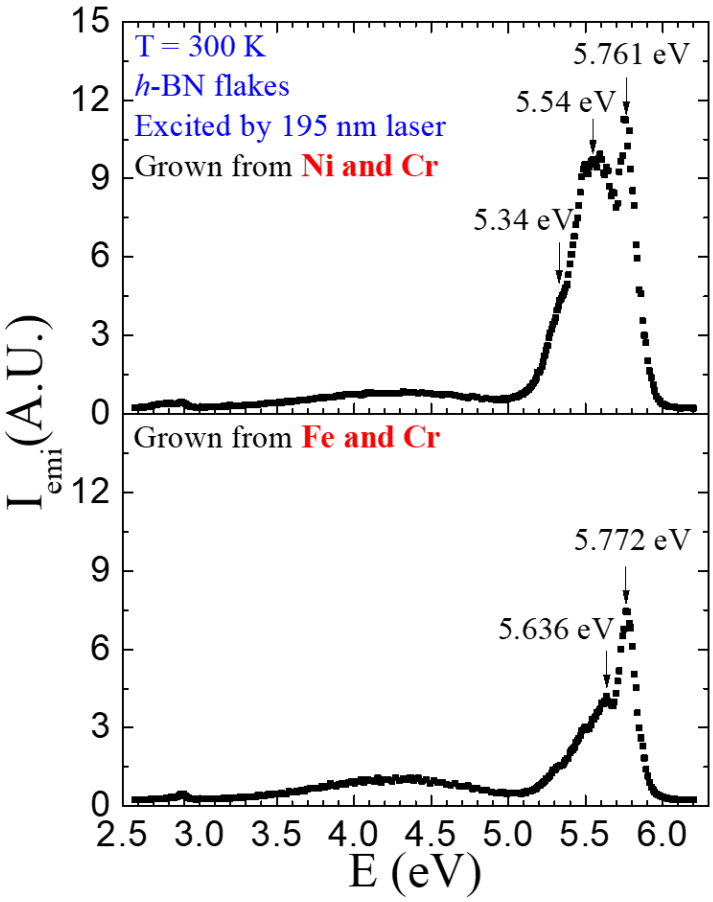

Figure 4.3. Room temperature PL spectrum comparing hBN crystals growth from (*bottom*) Fe-Cr and (*top*) Ni-Cr flux.

Figure 4.3 shows the room temperature band-edge PL emission spectra of hBN crystals grown with Fe-Cr and Ni-Cr solvents. The intense ultraviolet luminescence peaks of the Fe-Cr prepared crystal were at 5.772 eV and 5.636 eV, which is characteristic of a high-purity, high-quality hBN crystal.[10] The slightly higher energy compared to the hBN crystals from Ni-Cr solvent at respective 5.761 eV and 5.54 eV indicates a better crystal quality. Intensity for energy bands responsible for defects and impurities, located around 4.3 eV and 2.9 eV, were relatively weak in intensity, confirming a low residual impurity concentration in those crystals. Further investigations will be conducted to quantify the impurity concentration.

4.4 Conclusion

Large-scale, high-quality bulk hBN single crystals were successfully formed from a new Fe-Cr solvent at atmospheric pressure. The hBN crystals produced this way are clear and colorless, and have a maximum domain size of around 2-mm with a thickness of around 200-μm, which is comparable with the crystals grown from Ni-Cr solvent. The Raman spectrum of both shear mode and intralayer mode shows the high-quality of the crystals. The band-edge PL emission spectra also indicate that the crystals from Fe-Cr have a high quality and low defect and impurity density. Consequently, we have established an alternative growth route for large scale of high quality hBN crystal under atmospheric pressure with much lower cost.

4.5 Acknowledgement

Support from the Materials Engineering and Processing program of the National Science Foundation, award number 1538127, and the II−VI Foundation is greatly appreciated. The Raman measurement at University of North Iowa was supported by the National Science Foundation (NSF

CAREER Grant No. DMR-1552482). The work at Texas Tech University was supported by ARO (W911NF-16-1-0268) and monitored by Dr. Michael Gerhold.

References

1. Taniguchi, T.; Watanabe, K. Synthesis of high-purity boron nitride single crystals under high pressure by using Ba–BN solvent. *J. Cryst. Growth* **2007**, *303*, 525-529.

2. Zhigadlo, N. Crystal growth of hexagonal boron nitride (hBN) from Mg–B–N solvent system under high pressure. *J. Cryst. Growth* **2014**, *402*, 308-311.

3. Kubota, Y.; Watanabe, K.; Tsuda, O.; Taniguchi, T. Deep ultraviolet light-emitting hexagonal boron nitride synthesized at atmospheric pressure. *Science* **2007**, *317*, 932-934.

4. Ahmed, K.; Dahal, R.; Weltz, A.; Lu, J.; Danon, Y.; Bhat, I. Growth of hexagonal boron nitride on (111) Si for deep UV photonics and thermal neutron detection. *Appl. Phys. Lett.* **2016**, *109*, 113501.

5. Li, X.; Jordan, M. B.; Ayari, T.; Sundaram, S.; El Gmili, Y.; Alam, S.; Alam, M.; Patriarche, G.; Voss, P. L.; Salvestrini, J. P. Flexible metal-semiconductor-metal device prototype on wafer-scale thick boron nitride layers grown by MOVPE. *Scientific Reports* **2017**, *7*, 786.

6. Kubota, Y.; Watanabe, K.; Tsuda, O.; Taniguchi, T. Hexagonal Boron Nitride Single Crystal Growth at Atmospheric Pressure Using Ni− Cr Solvent. *Chemistry of Materials* **2008**, *20*, 1661-1663.

7. Portnoi, K.; Romashov, V.; Chubarov, V.; Levinskaya, M. K.; Salibekov, S. Phase diagram of the system nickel-boron. *Powder Metallurgy and Metal Ceramics* **1967**, *6*, 99-103.

8. Kowanda, C.; Speidel, M. Solubility of nitrogen in liquid nickel and binary Ni–Xi alloys (Xi= Cr, Mo, W, Mn, Fe, Co) under elevated pressure. *Scr. Mater.* **2003**, *48*, 1073-1078.

9. Hoffman, T. B.; Clubine, B.; Zhang, Y.; Snow, K.; Edgar, J. H. Optimization of Ni–Cr flux growth for hexagonal boron nitride single crystals. *J. Cryst. Growth* **2014**, *393*, 114-118.

10. Cao, X.; Clubine, B.; Edgar, J.; Lin, J.; Jiang, H. Two-dimensional excitons in three-dimensional hexagonal boron nitride. *Appl. Phys. Lett.* **2013**, *103*, 191106.

11. Baranov, D.; Edgar, J. H.; Hoffman, T.; Bassim, N.; Caldwell, J. D. Perfect interferenceless absorption at infrared frequencies by a van der Waals crystal. *Physical Review B* **2015**, *92*, 201405.

12. Kubaschewski, O. *Iron—Binary phase diagrams;* Springer Science & Business Media: 2013;

13. Fountain, R.; Chipman, J. Solubility and precipitation of boron nitride in iron-boron alloys. *Trans. Met. Soc. AIME* **1962**, *224*.

14. Morita, K.; Hirosumi, T.; Sano, N. Effects of aluminum, silicon, and boron on the dissolution rate of nitrogen into molten iron. *Metallurgical and Materials Transactions B* **2000**, *31*, 899-904.

15. Kuzuba, T.; Era, K.; Ishii, T.; Sato, T. A low frequency Raman-active vibration of hexagonal boron nitride. *Solid State Commun.* **1978**, *25*, 863-865.

16. Pakdel, A.; Bando, Y.; Golberg, D. Nano boron nitride flatland. *Chem. Soc. Rev.* **2014**, *43*, 934-959.

17. Gorbachev, R. V.; Riaz, I.; Nair, R. R.; Jalil, R.; Britnell, L.; Belle, B. D.; Hill, E. W.; Novoselov, K. S.; Watanabe, K.; Taniguchi, T. Hunting for monolayer boron nitride: optical and Raman signatures. *Small* **2011**, *7*, 465-468.

18. Nemanich, R.; Solin, S.; Martin, R. M. Light scattering study of boron nitride microcrystals. *Physical Review B* **1981**, *23*, 6348.

Chapter 5 - Monoisotopic hBN Growth

Part of Chapter 5 is reproduced with permission from:

Vuong, T.; Liu, S.; Van der Lee, A.; Cuscó, R.; Artús, L.; Michel, T.; Valvin, P.; Edgar, J.; Cassabois, G.; Gil, B. Isotope engineering of van der Waals interactions in hexagonal boron nitride. *Nature Materials* **2018**, *17*, 152.

Giles, A. J.; Dai, S.; Vurgaftman, I.; Hoffman, T.; Liu, S.; Lindsay, L.; Ellis, C. T.; Assefa, N.; Chatzakis, I.; Reinecke, T. L. Ultralow-loss polaritons in isotopically pure boron nitride. *Nature Materials* **2018**, *17*, 134.

Li, P.; Dolado, I.; Alfaro-Mozaz, F. J.; Casanova, F.; Hueso, L. E.; Liu, S.; Edgar, J. H.; Nikitin, A. Y.; Vélez, S.; Hillenbrand, R. Infrared hyperbolic metasurface based on nanostructured van der Waals materials. *Science* **2018**, *359*, 892-896.

5.1 Introduction

Hexagonal boron nitride (hBN) is a polar dielectric material that is particularly well suited for nanophotonic components.[1-7] As a two-dimensional van der Waals crystal, hBN exhibits an extremely large crystalline anisotropy. This anisotropy results from the strong, in-plane, covalently bonded boron and nitrogen atoms and weak, out-of-plane, van der Waals bonding. This gives rise to two spectrally distinct bands where phonon polaritons (PhPs) can be supported, designated as the lower (LR, ~760-820 cm^{-1}) and upper (UR, ~1365-1610 cm^{-1}) Reststrahlen bands.[1,6] Further, this strong anisotropy results in a large birefringence, where within the Reststrahlen bands, the

dielectric permittivities along orthogonal crystal axes are not only different, but opposite in sign. Such materials are referred to as hyperbolic.[8] In the case of hBN, the in-plane permittivity is isotropic and is defined with a single value, ε_t, which is negative (positive) in the UR (LR), while the out-of-plane component ε_z is positive (negative). Previous results have shown that the long optic phonon lifetimes enabled quality factors in hBN nanostructures that are well in excess of the best reported values in PP-based systems.[1,7]

The hBN utilized in most of current research has the natural distribution of boron isotopes, which is 19.9 at% ^{10}B and 80.1 at% ^{11}B. It was realized early that isotopically substituted molecules may react at different rates, a phenomenon known as the kinetic isotope effect,[9,10] showing that the electronic properties also depend on isotope composition.[11] The ^{10}B and ^{11}B isotopes are strong and weak thermal neutron absorbers, respectively, hence h^{10}BN has the potential of many applications in nuclear energy industries[12] and cancer treatment by boron neutron capture therapy[13]. The room temperature thermal conductivity in hBN is predicted to increase 40% with isotopically pure materials, as the phonon-isotope scattering in the crystal is much weaker than that in naturally abundant hBN.[14-16] Recently, isotope engineering has appeared as an important resource for preserving the quantum information, or encoding a qubit on a nuclear spin.[17-19] Therefore, it is of interest to investigate the novel properties and applications in monoisotopic hBN.

Although monoisotopic hBN single crystals are advantageous in many applications, its synthesis method, to the best of our knowledge, has not been reported. Our group has previously demonstrated the atmospheric growth of large-scale and high-quality hBN single crystals with natural abundance (h^{Na}BN) from both Ni-Cr and Fe-Cr solvents using a hot-pressed hBN source[20,21]. hBN crystals from both solvents had intense ultraviolet luminescence peaks at 5.77 eV

at room temperature. A narrow Raman peak width of 7.8 cm^{-1} at 1366 cm^{-1}, which is among the smallest values reported in the literature, indicates a great crystallographic orientation in the crystals. However, the isotopically pure hBN cannot be synthesized through same method, as the hot-pressed BN source contains boron with the natural isotope distribution. Alternatively, we used monoisotopic boron sources, i.e., ^{10}B and ^{11}B powders, as the precursor.

Here, we report on the atmospheric growth of large-scale high-quality monoisotopic hBN single crystals from a Ni-Cr flux, isotopically pure boron, and nitrogen. The crystal sizes, shapes and morphologies were determined by optical microscopy. Raman and X-ray photoelectron spectroscopy (XPS) were performed to evaluate the phonon energy and surface composition of the hBN crystals. Photoluminescence (PL) and X-ray diffraction were used to characterize the bandgap energy and electron density distribution in monoisotopic hBN. The phonon lifetime in monoisotopic hBN was determined using scattering-type scanning near-field optical microscopy (s-SNOM), which was systematically compared to the naturally abundant hBN. Further, infrared (IR) hyperbolic metasurfaces were fabricated using these monoisotopic hBN crystals.

5.2 Experimental Methods

The monoisotopic hexagonal boron nitride crystals were grown from high-purity elemental ^{10}B (99.22 at%) and ^{11}B (99.41 at%) powders by using the metal flux method. A Ni-Cr-B powder mixture at respective 48wt%, 48 wt%, and 4 wt% was loaded into an alumina crucible and placed in a single-zone furnace. The furnace was evacuated and then filled with N_2 and H_2 gas to a constant pressure of 850 Torr. During the reaction process, the N_2 and H_2 gases continuously flowed through the system at rates of 125 sccm and 5 sccm, respectively. All the nitrogen in the hBN crystal originated from the flowing N_2 gas. H_2 gas was used to minimizes oxygen and carbon

impurities in the h-BN crystal. After a dwell time of 24 hours at 1550 °C, the hBN crystals were precipitated on the metal surface by cooling at a rate of 0.5 °C /h to 1525 °C, and then the system was quickly quenched to room temperature.

Raman spectra were taken at room temperature using a Horiba Labram HR Raman microscope system. Our spectrometer is equipped with an ultralow frequency filter that allows access to the ultralow frequency down to ~5 cm^{-1}. A linearly polarized 532 nm laser light was used and focused to a spot diameter of ~2 μm by a 50× long-working-distance objective lens. Laser power was kept below 0.8 mW to avoid heating the samples. Instrument resolution was ~0.5 cm^{-1} by using an 1800 groove/mm grating.

XPS Spectra were measured on Kratos Axis $Ultra^{DLD}$ system at a base pressure of 10^{-9} Torr, using monochromatic Al Kα line. Survey XPS scans were run at 160 eV pass energy and high-resolution scans at 20 eV pass energy. XPS spectra was calibrated with the C 1s peak from the sample and set to BE = 284.6 eV. All samples were in electronic equilibrium with the spectrometer via a metallic clip on the sample, and characterized at normal take-off angle. XPS peak fits were done with CasaXPS Software 2.2.8 using mixed Gaussian/Lorentzian distributions to minimize *chi* squared value.

The temperature-dependent PL measurements were performed at temperatures from 10 K to room temperature. We perform two-photon excitation spectroscopy, and the excitation beam is provided by the second harmonic of a Ti:Sa oscillator, tuned at 408 nm in resonance with the sharp peak in the two-photon excitation spectrum. The spot diameter is of the order of 100 μm, with a power of 50 mW. An achromatic optical system couples the emitted signal to our detection system, composed of a f=500 mm Czerny-Turner monochromator, equipped with a 1800 grooves/mm grating blazed at 250 nm, and with a back-illuminated charge-coupled device

(CCD) camera (Andor Newton 920), with a quantum efficiency of 50 % at 210 nm. The integration time is of 15 s. We use a band-pass filter around 200 nm with a low transmission at 400 nm, in front of the spectrometer for complete laser stray light rejection.

XRD were carried out at 125, 175, 225 and 275 K, in general to a resolution of 0.7-0.8 Å, but the data collections at 125K were extended to 0.4 Å resolution. The data quality was better for $h^{11}BN$ than $h^{10}BN$; visually this was clear from the better Bragg spot sizes for $h^{11}BN$ than for $h^{10}BN$. During the handling of the crystals $h^{11}BN$ crystals seemed to be mechanically more robust than $h^{10}BN$ crystals. Molybdenum radiation was used (=0.71073 Å) and the scattered intensity was collected using a CCD Sapphire-3 detector (2048x2048 pixels, 16 pixels/mm).

The s-SNOM measurements were performed by focusing the tunable infrared radiation from a Daylight Solutions MirCAT quantum cascade laser system onto the metallized atomic force microscope (AFM) tip of the NeaSpec s-SNOM instrument. Incident light scatters off of the tip, as well as the edge of the hBN flake, providing the necessary change in momentum to[12,23] launch propagating HPhPs provided the light source is within the Reststrahlen band of the hBN. Due to lack of monochromatic laser sources in the LR, our measurements were limited to the UR. The peak-to-peak distance of the interference fringes observed within the s-SNOM spatial plots is equal to λ_{HPhP} and $\lambda_{HPhP}/2$ for the edge- and tip-launched modes, respectively. Plotted in Fig. 3a-c are the s-SNOM plots collected at 1510, 1480 and 1480 cm^{-1} for the ~120 nm thick ^{10}B enriched, naturally abundant, and ^{11}B enriched flakes, for which $Re(\varepsilon)$ = -6.2, -6.25 and -6.3, respectively. The strong dispersion in this regime requires that we image at (or close to) identical permittivity values, which due to the spectral shift in the optical phonons with changing isotopic mass occur at different frequencies for each of the different samples studied. Furthermore, since the dispersion

of the HPhP modes of hBN is strongly thickness dependent, the s-SNOM results presented were all collected from 118-120 nm thick flakes on a 280-nm thick SiO_2-on-Si substrate.

We fabricated infrared hyperbolic metasurfaces by structuring a grating into the isotopically enriched hBN flakes. To that end, we first performed mechanical exfoliation using blue Nitto tape (Nitto Denko Co., SPV 224P). The flakes attached to the tape were subsequently re-exfoliated onto polydimethylsiloxane stamp and using an optical microscope desired flakes were identified in the stamp. Then they were transferred onto a SiO_2/Si substrate (250 nm oxide layer) using the dry transfer technique. For patterning the grating into the flake, we used a high-resolution electron beam lithography system. High density gratings (gap width about 25 nm, with a periodicity of about 100 nm and for areas of approximately 5 μm x 5 μm) were written onto the hBN flakes using a thin PMMA layer (~50 nm). The PMMA resist was developed in MIBK:IPA 1:3 and the uncovered hBN areas were chemically etched in a RIE OXFORD PLASMALAB 80 PLUS reactive ion etcher in a SF6/Ar 1:1 plasma mixture at 20 sccm flow, 100 mTorr pressure and 100 W power for 20s. The PMMA mask was removed by immersing the sample in acetone overnight, rinsing it in IPA and drying it with a N_2 gun.

5.3 Results and Discussion

As noted in previous studies of hBN crystal growth,[22,23] a mixture of nickel and chromium was used as the solvent because of their high solubility for boron and nitrogen, respectively. In pure hot nitrogen, chromium reacts to form Cr_2N while nickel remains unreacted. The use of pure boron sources makes this process different from the natural hBN crystal growth using a hot-pressed hBN source. Specifically, as the solvent and sources are heated, boron reacts with the nitrogen to form boron nitride and then dissolves into the solvent.

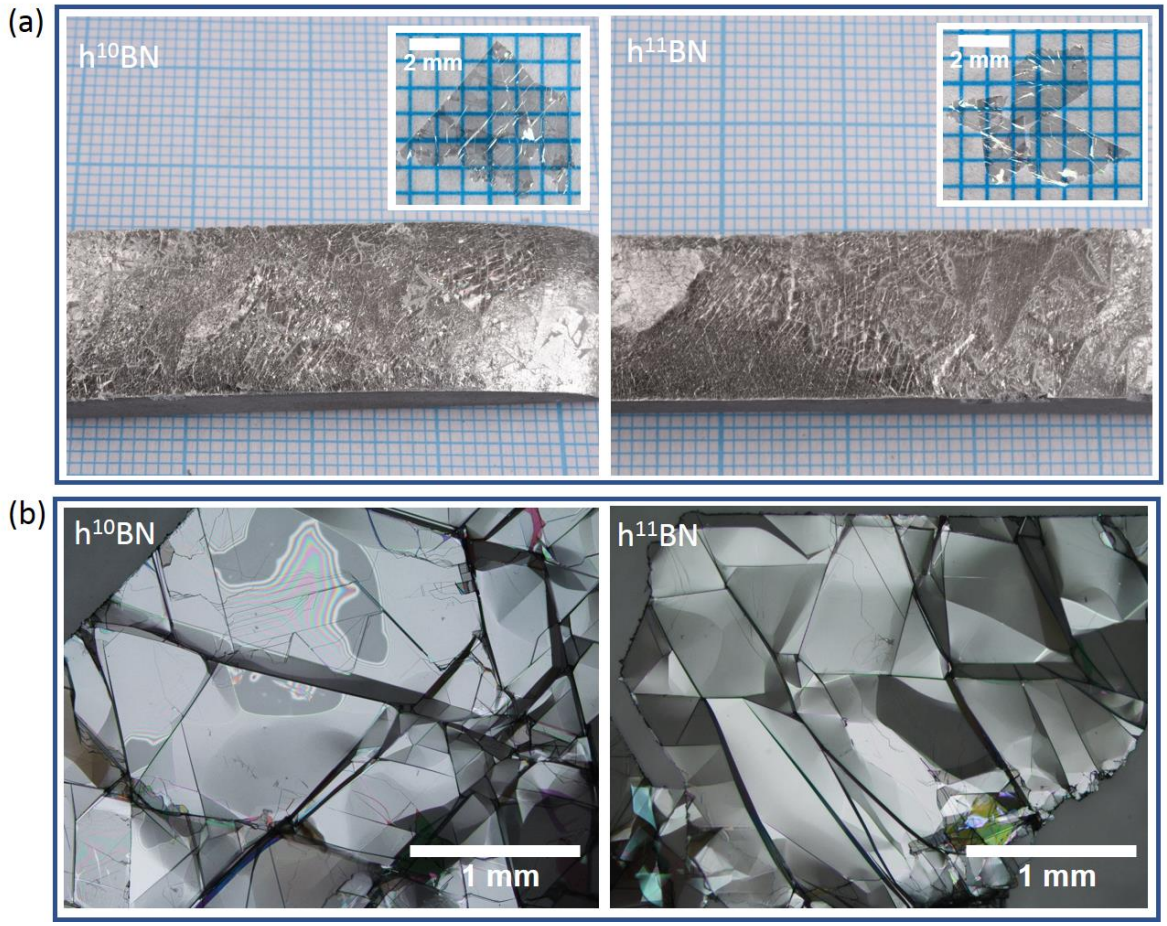

Figure 5.1. (a) Photographs of monoisotopic hBN, i.e., $h^{10}BN$ and $h^{11}BN$, crystals on top of Ni-Cr metal surface. (Inset) The free-standing hBN flakes exfoliated from the metal surfaces. (b) Optical micrographs of free-standing hBN flakes on a glass substrate.

Figure 5.1a illustrates the optical images of monoisotopic hBN, i.e., $h^{10}BN$ and $h^{11}BN$, crystals grown onto the Ni-Cr metal surface, showing that the crystals are clear and colorless. To obtain free-standing hBN crystals, we used thermal release tape to adhere and peel the crystals from the metal surface, and then heated the tape at 150°C for 10 seconds to release the adhesive and transfer the crystals onto a substrate. The inset figures show the free-standing hBN flakes,

around 7-mm across, exfoliated from the metal surface. Figure 5.1b shows the zoom-in optical micrographs of those hBN flakes on a glass substrate. The largest single crystal domain size is about 1-mm across. The size of the monoisotopic hBN crystals we synthesized here is comparable with our previously prepared hBN crystals with natural B abundance ($h^{Na}BN$)[20,21].

5.3.1 Phonon Energy

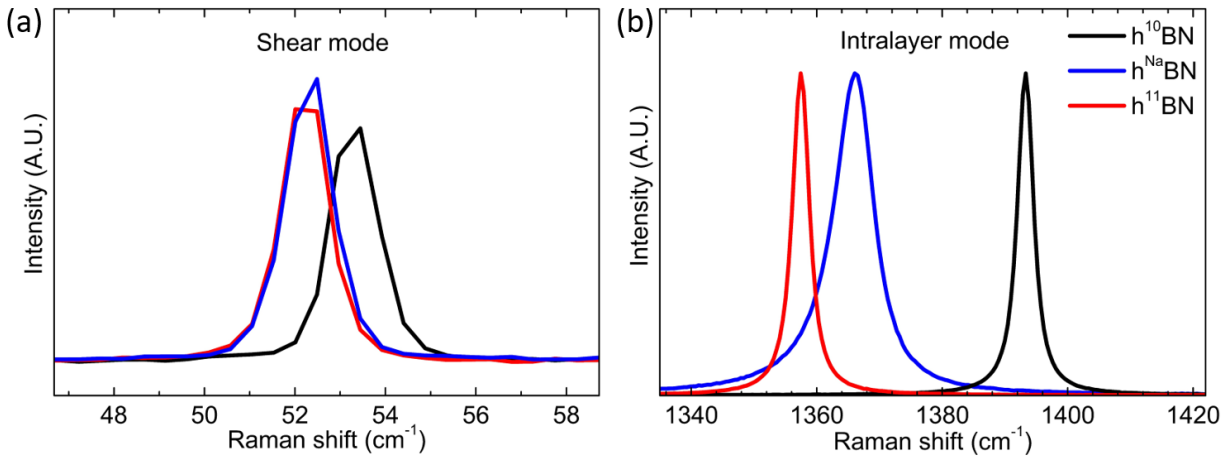

Figure 5.2. Raman spectra of (a) shear mode and (b) intralayer mode from $h^{10}BN$, $h^{11}BN$ and $h^{Na}BN$ crystals grown with Ni-Cr metal flux.

The frequency of lattice vibrations decreases with the atomic mass; this universal behavior is inherited from the frequency ($\sqrt{k/m}$) of the harmonic oscillator. Therefore, when varying the isotope, the frequency of phonons varies, which can be reflected by Raman scattering. Figure 5.2 displays the Raman spectra from $h^{10}BN$, $h^{Na}BN$, and $h^{11}BN$ crystals in both shear and intralayer modes. The low-frequency spectrum in Figure 5.2a, which is attributed to the rigid shearing oscillation between adjacent layers, shows that the peaks in $h^{10}BN$, $h^{Na}BN$, and $h^{11}BN$ are at 53.4

cm^{-1}, 52.5 cm^{-1}, and 52.0 cm^{-1}, respectively. The phonon energy decreases with mass of the boron isotope, which is consistent with our initial prediction. As ^{Na}B includes 80.1% of ^{11}B, the $h^{11}BN$ and $h^{Na}BN$ peaks are close to each other. The full width at half-maximum (FWHM) value for the all three peaks was the same, i.e. 1.3 cm^{-1}.

The high-frequency spectrum in Figure 5.2b, which corresponds to the intralayer E_{2g} vibrational mode between in-plane boron and nitrogen, also shows an intermediate peak value of 1366.1 cm^{-1} for $h^{Na}BN$, in which the peaks for $h^{10}BN$ and $h^{11}BN$ are positioned at 1393.3 cm^{-1} and 1357.4 cm^{-1} respectively. Same as the shear mode, the phonon energy in intralayer mode decreases with mass of the boron isotope. In $h^{10}BN$ and $h^{11}BN$, the FWHM is respective 3.1 cm^{-1} and 3.3 cm^{-1}, which is much narrower than that in $h^{Na}BN$ (7.8 cm^{-1}). The broadening of the Raman line in $h^{Na}BN$ originates from static isotopic mass disorder that breaks the translational invariance and induce elastic scattering of phonons.[24]

The small values of FWHM in both shear and intralayer modes indicate the monoisotopic hBN crystals grown from Ni-Cr metal flux are high-quality. In addition, an estimate of the E_{2g} phonon lifetime can be determined from the Raman linewidth. As we discussed above, the E_{2g} linewidth narrows from 7.8 cm^{-1} in naturally abundant hBN to 3.1 (or 3.3) cm^{-1} in isotopically pure hBN, which demonstrate an approximate three-fold increase in phonon lifetime within the monoisotopic samples.

5.3.2 Binding Energy

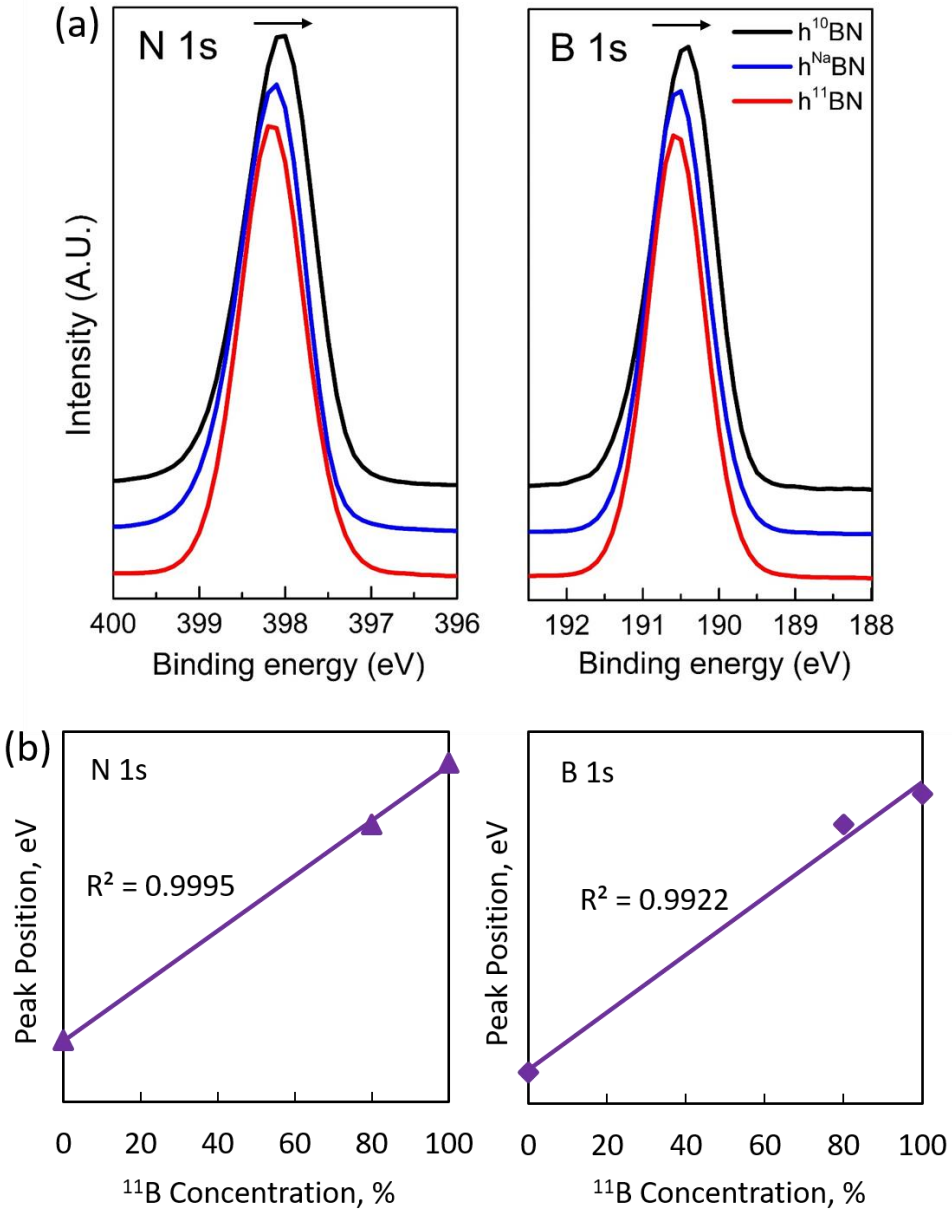

Figure 5.3. X-ray photoelectron spectroscopy (XPS) spectra of (a) N 1s and B 1s from $h^{10}BN$, $h^{11}BN$ and $h^{Na}BN$ crystals grown with Ni-Cr metal flux. (b) N 1s and B 1s peak positions versus ^{11}B concentration in hBN.

As the mass difference of boron isotopes can have an influence on the electron density distribution[25] and chemical kinetics,[26] one could anticipate an isotopic effect on the chemical bonding in hBN. X-ray photoelectron spectroscopy (XPS) was carried out to investigate this effect. Figure 5.3a shows the XPS spectra of respective the N 1s and B 1s peaks from $h^{10}BN$, $h^{11}BN$ and $h^{Na}BN$ crystals. The binding energies for N 1s and B 1s in $h^{Na}BN$ (blue curve) are 398.1 eV and 190.5 eV, respectively, which are in good agreement with previously reported literature values[27-29]. Note that the peak positions for both the N 1s and B 1s in $h^{11}BN$ are slightly higher than that in $h^{10}BN$, and the $h^{Na}BN$ peaks are located between them. Plotting the N 1s and B 1s peak positions versus ^{11}B concentration (Figure 5.3b) shows that both the N 1s and B 1s binding energies linearly increase with the ^{11}B concentration, which suggests that the B-N bond in $h^{11}BN$ is slightly stronger than that in $h^{10}BN$. This trend is similar with a previous study on the carbon doping in MgB_2 that showed the ^{11}B-Mg bond is stronger than the ^{10}B-Mg bond due to the isotope effect, which leads to the smaller amount of C substituting for ^{11}B in the lattice.[30]

5.3.3 Electronic Bandgap

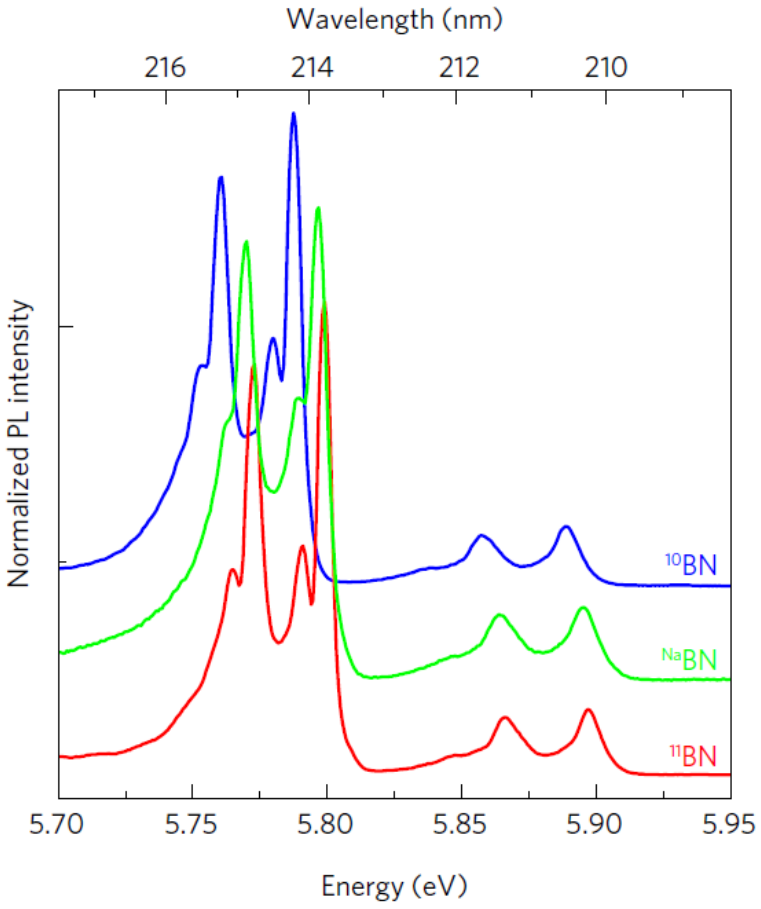

Figure 5.4. Photoluminescence (PL) spectrum for $h^{10}BN$, $h^{11}BN$ and $h^{Na}BN$ crystals at 8 K.

Besides the phonon energy and chemical binding energy, the isotope mass also impacts the electronic properties because of the electron-phonon interaction[24]. This phenomenon was investigated by photoluminescence (PL) spectroscopy. As seen in Figure 5.4, the intrinsic optical response lies in the deep ultraviolet around 6 eV (200 nm), displaying the PL spectra in $h^{10}BN$, $h^{11}BN$ and $h^{Na}BN$ at 8 K. The PL spectrum is globally blue-shifted in $h^{11}BN$ compared to $h^{Na}BN$, while it is red-shifted in $h^{10}BN$, which demonstrate that the isotopic substitution changes the

bandgap energy in hBN. Each of the PL spectrum is composed of four main emission peaks, reflecting the various paths for recombination assisted by phonon emission.[31] The four peaks at around 5.76, 5.79, 5.86 and 5.89 eV correspond to recombination assisted by the emission of different phonons, i.e., LO, TO, LA and TA phonons. As discussed in Chapter 3, the higher the temperature, the fewer the PL peaks in this energy range due to the strong exciton-phonon interaction.

5.3.4 Interlayer Breathing Mode

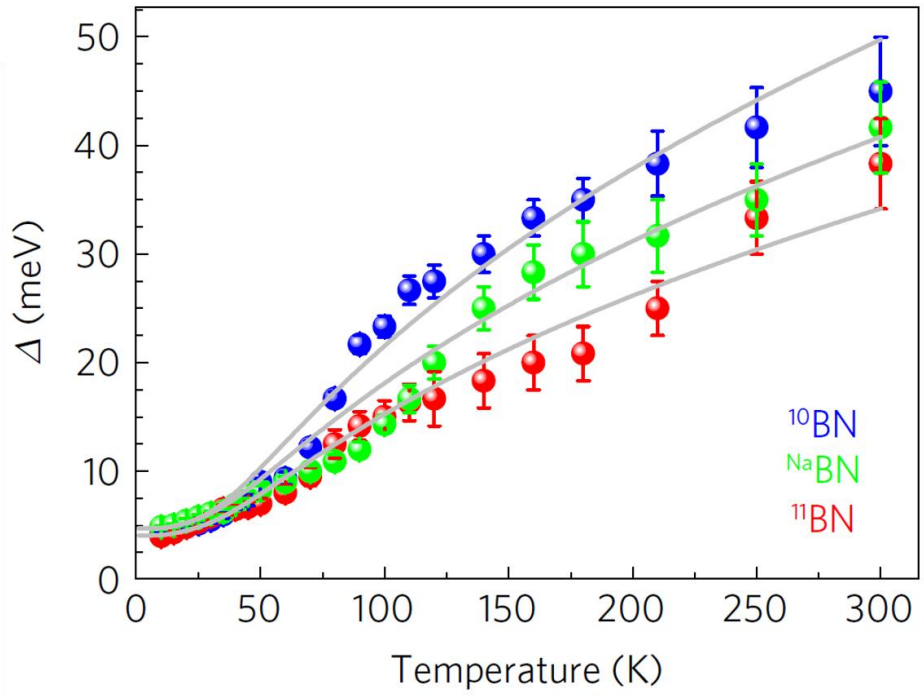

Figure 5.5. Phonon-assisted broadening Δ of the PL spectra in $h^{10}BN$, $h^{11}BN$ and $h^{Na}BN$: experimental data (symbols), fits of the thermally induced broadening (solid lines). Error bars indicate the standard deviations of Δ for least-squares fitting of the emission spectrum.

The phonon with interlayer breathing mode (B_{1g}) corresponds to the anti-phase rigid motion of adjacent layers along the c-axis. The B_{1g} interlayer breathing mode is neither Raman nor infrared active by symmetry, so that the direct investigation of this silent mode is impossible by optical spectroscopy.[32] However, this phonon contributes to the thermally assisted broadening of the emission spectrum in hBN[31], as we demonstrated the exciton-phonon interaction in Chapter 3. At above 60 K, absorption of such phonons is in fact the dominant broadening process so that the study of the temperature-dependent linewidth in PL spectra provides an accurate measurement of the exciton-phonon interaction for this specific type of phonon. Figure 5.5 shows the PL peak linewidth Δ as a function of temperature for $h^{10}BN$, $h^{11}BN$ and $h^{Na}BN$. Like the interlayer shear mode and intralayer mode, there is a striking dependence of the thermal broadening on the isotopic composition, with the highest and lowest phonon-assisted broadening for $h^{11}BN$ and $h^{10}BN$, respectively.

The solid lines from the experimental data in Figure 5.5 are fits of the thermally induced broadening according to Equation (16):

$$\Delta = \sqrt{\Delta_A^2 + \Delta_O^2} \tag{16}$$

where Δ_A and Δ_O are the broadenings due to the low-energy acoustic phonons and the B_{1g} interlayer breathing mode, respectively[31]. Thus, we infer that isotope engineering in hBN impacts the lattice vibrations controlled by the weak van der Waals coupling between adjacent layers.

5.3.5 Electron Density Distribution

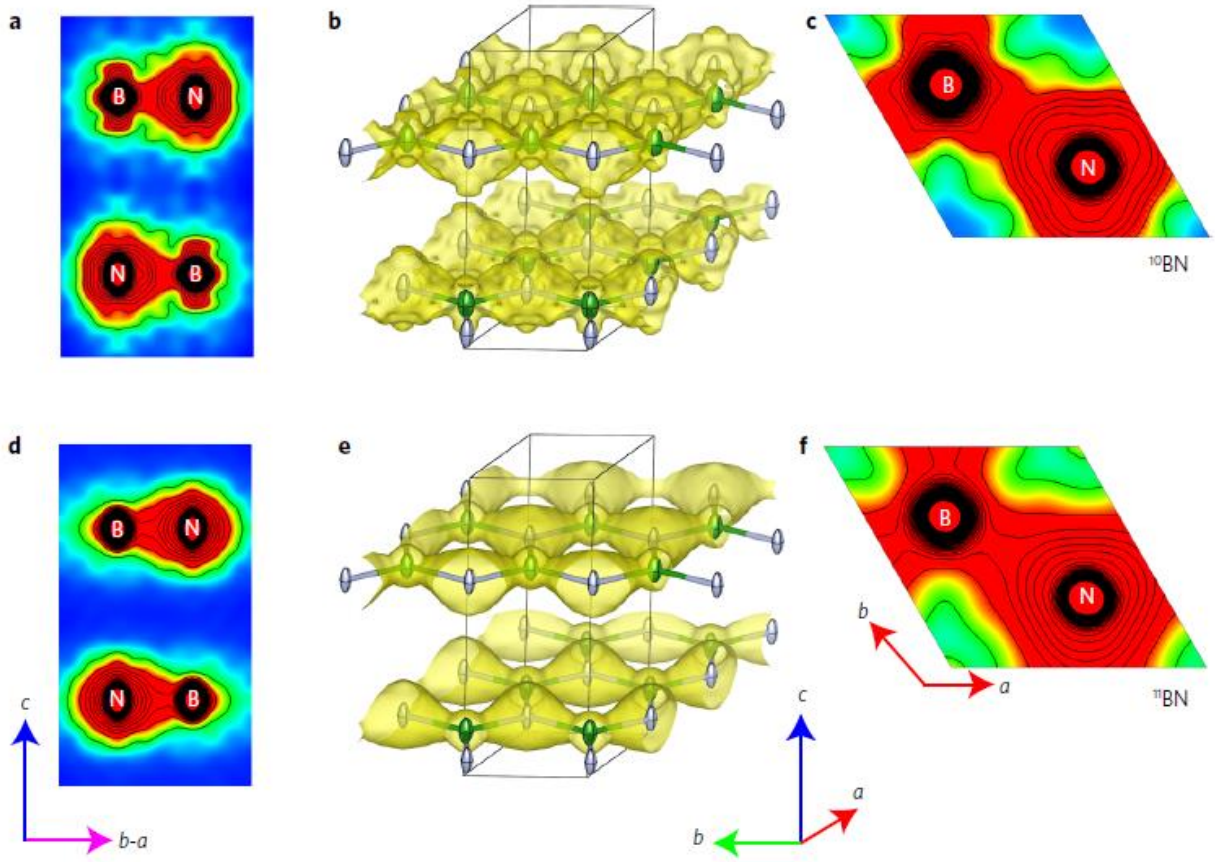

Figure 5.6. Electron density distribution in (a–c) $h^{10}BN$ and (d–f) $h^{11}BN$ using the maximum entropy method against X-ray data collected at 125 K to 0.4 Å resolution. a, d: 2D contour plots in a plane parallel to the *c*-axis. b, e: Side view of 3D contour plots with an iso-contour level at 1 $eÅ^{-3}$. c, f: 2D contour plots in a plane perpendicular to the *c*-axis. The iso-contour levels range from 1 to 30 $eÅ^{-3}$ in steps of 0.5 $eÅ^{-3}$.

The isotope effect on the interlayer electronic distribution was also investigated, which was revealed by x-ray diffraction experiments. Electron density maps were determined using the

maximum energy method (MEM)[33] against XRD data collected at 125 K to 0.4 Å resolution, as shown in Figure 5.6. The 3D iso-surface and 2D contour plots show that the electron density around N protruding towards B, in accordance with the experimental[34] and theoretical[35,36] mapping of electron density in natural hBN. The expanded and gridded maps in Figure 5.7 show that the out-of-plane electron is more spread out (inwards the van der Waals gap) around both nuclei in $h^{10}BN$ than in $h^{11}BN$. This reveals the isotopic modification of the electronic density in-between layers coupled by the van der Waals interaction.

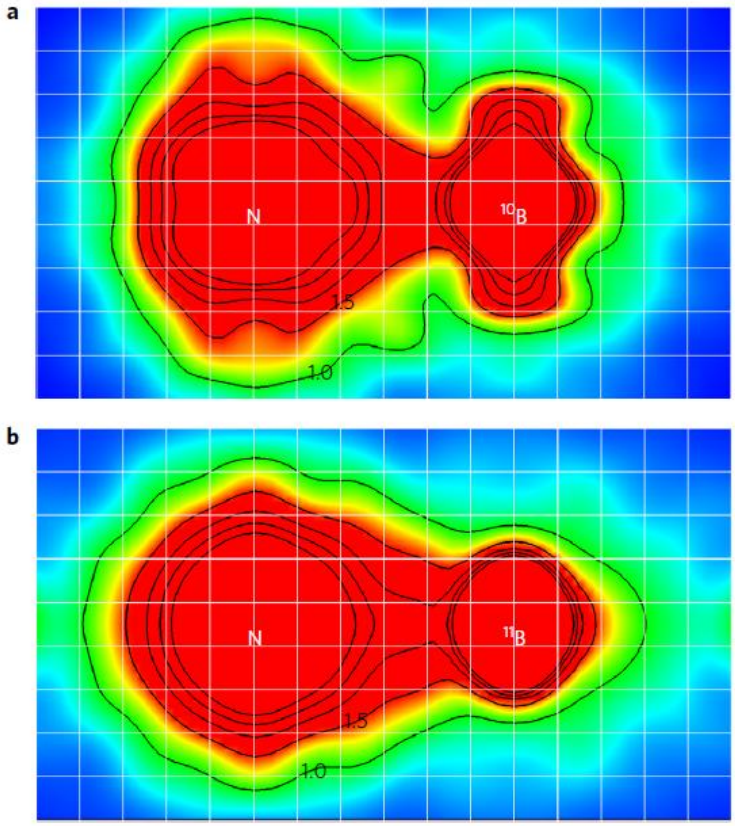

Figure 5.7. Expanded view of Figure 5.6a and d. The orientation is identical, but the vertical section is between z = 0.585 and 0.915 in crystallographic units of the c-lattice parameter (c ~ 6.6 Å). Squares in the white grids have a unit size of 0.242 Å.

5.3.6 Ultralow-loss Polaritons

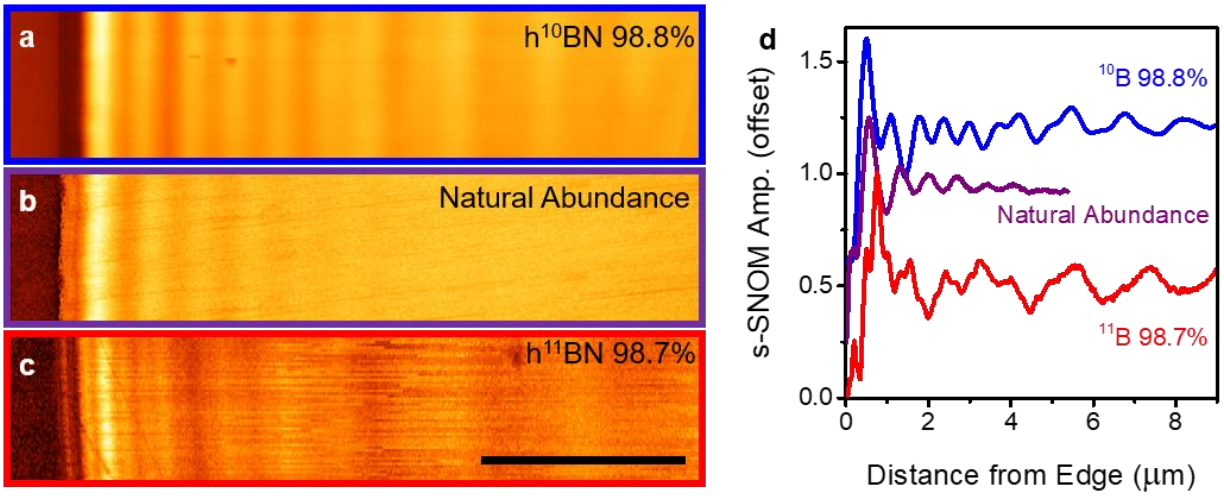

Figure 5.8. Spatial plots of the scattering-type scanning near-field optical microscope (s-SNOM) measurements collected from ~120 nm thick hBN flakes of (a) ^{10}B 98.8%, (b) naturally abundant and (c) ^{11}B 98.7%. The scale bar represents 5 μm. The polaritons were stimulated with a 1510, 1480 and 1480 cm^{-1} incident laser source, respectively, corresponding to Re(e)~-6.25 for each. (d) Linescans extracted from a-c demonstrate the significantly longer propagation lengths in the enriched in comparison to the naturally abundant flake.

As the optical losses of PhPs are intimately tied to the optical phonon scattering rates, an increase in the phonon lifetime within the enriched samples, as discussed above, should also result in significant increases in the propagation lengths of the hyperbolic phonon polaritons (HPhPs) they support. Such increases can be clearly identified in the spatial plots of the PhP propagation within ~120 nm thick flakes of the highest isotopically enriched hBN with respect to the similar thickness naturally abundant material (Figure 5.8a-c). These spatial plots were acquired using s-

SNOM techniques described in methods and elsewhere.[6,37,38] HPhP propagation is visualized in these experiments by the interference between the SNOM-tip-launched, hBN-flake-edge-launched and hBN-flake-edge-reflected HPhPs, resulting in the oscillatory patterns seen in the spatial plots. To accommodate for the spectral shifts in the dielectric functions between each of the hBN materials, the s-SNOM plots presented were collected at frequencies where the magnitude of the real part of the permittivity was approximately the same $[Re(\varepsilon) \sim -6.25]$. From the qualitative comparisons provided in the corresponding line-scans (Figure 5.8d) two clear conclusions can be drawn: (1) a striking increase in the propagation lengths is observed in the highly enriched samples and (2) additional higher-frequency oscillations are clearly present in the interference pattern seen in these enriched samples as well.

5.3.7 Infrared Hyperbolic Metasurface

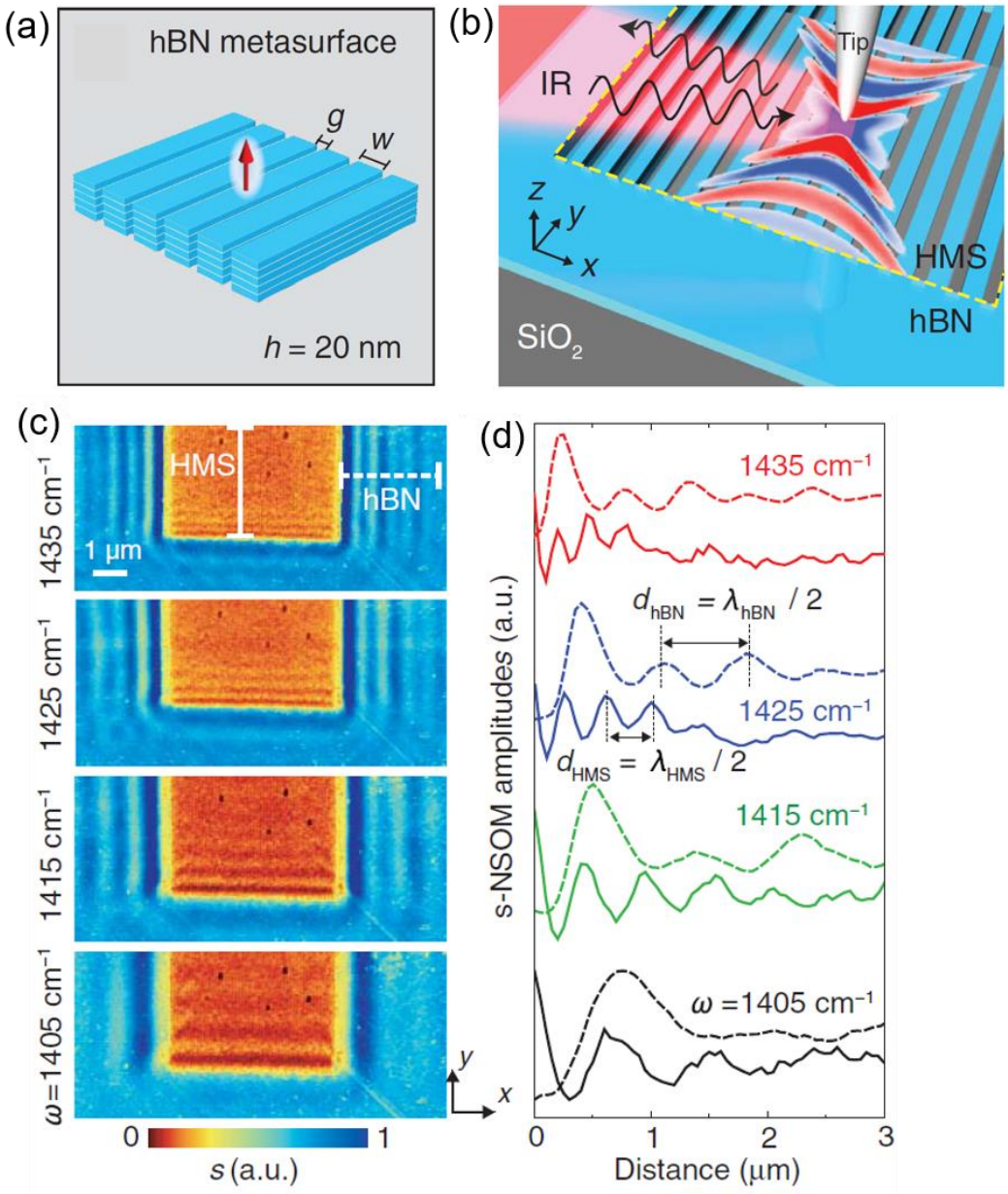

Figure 5.9. (a) Schematic of dipole launching of phonon polaritons on a 20-nm-thick hBN hyperbolic metasurface (ribbon width w=70 nm; gap width g=30 nm). (b) Schematic of the near-field polariton interferometry experiment. (c) Near-field images (amplitude signal s) recorded at four different frequencies. a.u., arbitrary units. (d) s-NSOM amplitude profiles along the solid (vertical) and dashed (horizontal) white lines in (c).

Owing to the layered vdW-crystal structure (resulting in two Restrahlen bands in the mid-infrared spectral range, where in- and out-of-plane permittivities have opposite sign), the h-BN phonon polaritons exhibit an out-of-plane hyperbolic dispersion,[1-3,6] while in-plane propagation is isotropic. However, the polariton propagation changes dramatically when we structure the h-BN. Figure 5.9a shows a h-BN grating consisting of individual stripes (width w = 70 nm) separated by small air gaps (width g = 30nm), yielding the effective in-plane permittivities $\varepsilon_x = \varepsilon_{\text{air}}\varepsilon_{\text{BN}}(w+g)/(\varepsilon_{\text{air}}w+\varepsilon_{\text{BN}}g)$ and $\varepsilon_y = (\varepsilon_{\text{air}}g+\varepsilon_{\text{BN}}w)/(w+g)$, where ε_{air} and ε_{BN} are permittivities of air and h-BN, respectively. Their strong anisotropy can yield polaritons with in-plane hyperbolic dispersion (Figure 5.9b), which subsequently propagate with concave wavefronts.

For an experimental demonstration of our proposed hyperbolic metasurface (HMS), we etched a 5 μm × 5 μm size grating into a 20-nm-thick exfoliated flake of isotopically enriched h-BN (schematics in Figure 5.9c). Figure 5.9c shows the polariton interferometry images of our sample measured at four different frequencies. On both the grating (HMS) and the surrounding (unpatterned) h-BN flake we clearly observe polariton fringes. Importantly, we see fringes only parallel to the horizontal HMS boundary, which could be explained by a close-to-zero reflection at the left and right grating boundaries, or more interestingly, by the absence of polariton propagation in x-direction (horizontal), the latter being consistent with hyperbolic polariton dispersion. The fringe spacing on the grating, d_{MS}, is reduced nearly twofold compared to that of the unpatterned flake, $d_{\text{h-BN}}$ (see line profiles in Figure 5.9d), indicating superior polaritonic field confinement on the grating.

5.4 Conclusions

This study demonstrates that large-scale, high-quality monoisotopic hBN single crystals can be successfully formed from a Ni-Cr metal solvent at atmospheric pressure. The hBN crystals produced this way are clear and colorless, and have a maximum single domain size of around 1-mm, which is comparable to crystals grown with hBN sources with the natural boron abundance. The Raman spectra of both shear mode and intralayer mode demonstrate the high-quality of the crystals. The XPS spectra reveal that the B-N bond in $h^{11}BN$ is stronger than that in $h^{10}BN$. The PL characterization demonstrates that the isotopic substitution changes the electronic bandgap in hBN. The interlayer breathing mode is highly dependent on the thermal broadening on the isotopic composition. The electron density distribution shows that the electron density around N protrudes towards B in both $h^{10}BN$ and $h^{11}BN$, and the out-of-plane electron is more spread out around both nuclei in $h^{10}BN$ than in $h^{11}BN$. Moreover, through the isotopic enrichment of hBN, we have demonstrated that three-fold increases in the phonon lifetimes and phonon-polariton propagation lengths can be achieved over the already low-loss naturally abundant hBN crystals. In addition, the polariton propagation changes dramatically when we fabricate the h-BN to a grating (hyperbolic metasurface), which possesses superior confinement of polaritons.

5.5 Acknowledgement

Support from the Materials Engineering and Processing program of the National Science Foundation, award number CMMI 1538127, and the II−VI Foundation is greatly appreciated.

References

1. Caldwell, J. D.; Kretinin, A. V.; Chen, Y.; Giannini, V.; Fogler, M. M.; Francescato, Y.; Ellis, C. T.; Tischler, J. G.; Woods, C. R.; Giles, A. J. Sub-diffractional volume-confined polaritons in the natural hyperbolic material hexagonal boron nitride. *Nature Communications* **2014**, *5*, 5221.
2. Yoxall, E.; Schnell, M.; Nikitin, A. Y.; Txoperena, O.; Woessner, A.; Lundeberg, M. B.; Casanova, F.; Hueso, L. E.; Koppens, F. H.; Hillenbrand, R. Direct observation of ultraslow hyperbolic polariton propagation with negative phase velocity. *Nature Photonics* **2015**, *9*, 674.
3. Dai, S.; Ma, Q.; Andersen, T.; Mcleod, A.; Fei, Z.; Liu, M.; Wagner, M.; Watanabe, K.; Taniguchi, T.; Thiemens, M. Subdiffractional focusing and guiding of polaritonic rays in a natural hyperbolic material. *Nature Communications* **2015**, *6*, 6963.
4. Li, P.; Lewin, M.; Kretinin, A. V.; Caldwell, J. D.; Novoselov, K. S.; Taniguchi, T.; Watanabe, K.; Gaussmann, F.; Taubner, T. Hyperbolic phonon-polaritons in boron nitride for near-field optical imaging and focusing. *Nature Communications* **2015**, *6*, 7507.
5. Kumar, A.; Low, T.; Fung, K. H.; Avouris, P.; Fang, N. X. Tunable light–matter interaction and the role of hyperbolicity in graphene–hBN system. *Nano Letters* **2015**, *15*, 3172-3180.
6. Dai, S.; Fei, Z.; Ma, Q.; Rodin, A. S.; Wagner, M.; McLeod, A. S.; Liu, M. K.; Gannett, W.; Regan, W.; Watanabe, K.; Taniguchi, T.; Thiemens, M.; Dominguez, G.; Castro Neto, A. H.; Zettl, A.; Keilmann, F.; Jarillo-Herrero, P.; Fogler, M. M.; Basov, D. N. Tunable phonon polaritons in atomically thin van der Waals crystals of boron nitride. *Science* **2014**, *343*, 1125-1129.

7. Giles, A. J.; Dai, S.; Glembocki, O. J.; Kretinin, A. V.; Sun, Z.; Ellis, C. T.; Tischler, J. G.; Taniguchi, T.; Watanabe, K.; Fogler, M. M. Imaging of anomalous internal reflections of hyperbolic phonon-polaritons in hexagonal boron nitride. *Nano letters* **2016**, *16*, 3858-3865.

8. Poddubny, A.; Iorsh, I.; Belov, P.; Kivshar, Y. Hyperbolic metamaterials. *Nature Photonics* **2013**, *7*, 948.

9. Bigeleisen, J.; Mayer, M. G. Calculation of equilibrium constants for isotopic exchange reactions. *J. Chem. Phys.* **1947**, *15*, 261-267.

10. Simmons, E. M.; Hartwig, J. F. On the Interpretation of Deuterium Kinetic Isotope Effects in C-H Bond Functionalizations by Transition-Metal Complexes. *Angewandte Chemie International Edition* **2012**, *51*, 3066-3072.

11. Kohen, A.; Limbach, H. *Isotope effects in chemistry and biology;* CRC Press: 2005.

12. Subramanian, C.; Suri, A.; Murthy, T. Development of Boron-based materials for nuclear applications. *Barc Newsletter* **2010**, *313*, 14.

13. Barth, R. F.; Soloway, A. H.; Fairchild, R. G.; Brugger, R. M. Boron neutron capture therapy for cancer. Realities and prospects. *Cancer* **1992**, *70*, 2995-3007.

14. Chang, C.; Fennimore, A.; Afanasiev, A.; Okawa, D.; Ikuno, T.; Garcia, H.; Li, D.; Majumdar, A.; Zettl, A. Isotope effect on the thermal conductivity of boron nitride nanotubes. *Phys. Rev. Lett.* **2006**, *97*, 085901.

15. Lindsay, L.; Broido, D.; Reinecke, T. Phonon-isotope scattering and thermal conductivity in materials with a large isotope effect: A first-principles study. *Physical Review B* **2013**, *88*, 144306.

16. Cuscó, R.; Artús, L.; Edgar, J. H.; Liu, S.; Cassabois, G.; Gil, B. Isotopic effects on phonon anharmonicity in layered van der Waals crystals: Isotopically pure hexagonal boron nitride. *Physical Review B* **2018**, *97*, 155435.
17. Kane, B. E. A silicon-based nuclear spin quantum computer. *Nature* **1998**, *393*, 133.
18. Balasubramanian, G.; Neumann, P.; Twitchen, D.; Markham, M.; Kolesov, R.; Mizuochi, N.; Isoya, J.; Achard, J.; Beck, J.; Tissler, J. Ultralong spin coherence time in isotopically engineered diamond. *Nature Materials* **2009**, *8*, 383.
19. Itoh, K. M.; Watanabe, H. Isotope engineering of silicon and diamond for quantum computing and sensing applications. *MRS Communications* **2014**, *4*, 143-157.
20. Hoffman, T. B.; Clubine, B.; Zhang, Y.; Snow, K.; Edgar, J. H. Optimization of Ni–Cr flux growth for hexagonal boron nitride single crystals. *J. Cryst. Growth* **2014**, *393*, 114-118.
21. Liu, S.; He, R.; Ye, Z.; Du, X.; Lin, J.; Jiang, H.; Liu, B.; Edgar, J. H. Large-Scale Growth of High-Quality Hexagonal Boron Nitride Crystals at Atmospheric Pressure from an Fe–Cr Flux. *Crystal Growth & Design* **2017**, *17*, 4932-4935.
22. Kubota, Y.; Watanabe, K.; Tsuda, O.; Taniguchi, T. Hexagonal Boron Nitride Single Crystal Growth at Atmospheric Pressure Using Ni− Cr Solvent. *Chemistry of Materials* **2008**, *20*, 1661-1663.
23. Liu, S.; van Duin, A. C.; van Duin, D. M.; Liu, B.; Edgar, J. H. Atomistic Insights into Nucleation and Formation of Hexagonal Boron Nitride on Nickel from First-Principles-Based Reactive Molecular Dynamics Simulations. *ACS Nano* **2017**, *11*, 3585-3596.
24. Cardona, M.; Thewalt, M. Isotope effects on the optical spectra of semiconductors. *Reviews of Modern Physics* **2005**, *77*, 1173.

25. Vuong, T.; Liu, S.; Van der Lee, A.; Cuscó, R.; Artús, L.; Michel, T.; Valvin, P.; Edgar, J.; Cassabois, G.; Gil, B. Isotope engineering of van der Waals interactions in hexagonal boron nitride. *Nature Materials* **2018**, *17*, 152.

26. Chkhartishvili, L. Isotopic effects of boron. *Trends Inorg.Chem* **2009**, *11*, 105-167.

27. Moulder, J. F.; Stickle, W. F.; Sobol, P. E.; Bomben, K. D. Handbook of X-ray Potoelectron Spectroscopy; Chastain, J., Ed.; PerkinElmer Corporation: Waltham, MA, **1992**; pp 254−257.

28. Miyamoto, Y.; Rubio, A.; Cohen, M. L.; Louie, S. G. Chiral tubules of hexagonal BC_2N. *Physical Review B* **1994**, *50*, 4976.

29. Park, K.; Lee, D.; Kim, K.; Moon, D. Observation of a hexagonal BN surface layer on the cubic BN film grown by dual ion beam sputter deposition. *Appl. Phys. Lett.* **1997**, *70*, 315-317.

30. Cheng, F.; Liu, Y.; Ma, Z.; Al Hossain, M. S.; Somer, M. The isotope effect of boron on the carbon doping and critical current density of $Mg^{11}B_2$ superconductors. *Journal of Materials Chemistry C* **2017**, *5*, 663-668.

31. Vuong, T.; Cassabois, G.; Valvin, P.; Liu, S.; Edgar, J.; Gil, B. Exciton-phonon interaction in the strong-coupling regime in hexagonal boron nitride. *Physical Review B* **2017**, *95*, 201202.

32. Serrano, J.; Bosak, A.; Arenal, R.; Krisch, M.; Watanabe, K.; Taniguchi, T.; Kanda, H.; Rubio, A.; Wirtz, L. Vibrational properties of hexagonal boron nitride: inelastic X-ray scattering and ab initio calculations. *Phys. Rev. Lett.* **2007**, *98*, 095503.

33. Smaalen, S. v.; Palatinus, L.; Schneider, M. The maximum-entropy method in superspace. *Acta Crystallographica Section A: Foundations of Crystallography* **2003**, *59*, 459-469.

34. Yamamura, S.; Takata, M.; Sakata, M. Charge density of hexagonal boron nitride using synchrotron radiation powder data by maximum entropy method. *Journal of Physics and Chemistry of Solids* **1997**, *58*, 177-183.

35. Catellani, A.; Posternak, M.; Baldereschi, A.; Freeman, A. Bulk and surface electronic structure of hexagonal boron nitride. *Physical Review B* **1987**, *36*, 6105.

36. Topsakal, M.; Aktürk, E.; Ciraci, S. First-principles study of two-and one-dimensional honeycomb structures of boron nitride. *Physical Review B* **2009**, *79*, 115442.

37. Chen, J.; Badioli, M.; Alonso-González, P.; Thongrattanasiri, S.; Huth, F.; Osmond, J.; Spasenović, M.; Centeno, A.; Pesquera, A.; Godignon, P. Optical nano-imaging of gate-tunable graphene plasmons. *Nature* **2012**, *487*, 77.

38. Fei, Z.; Rodin, A.; Andreev, G.; Bao, W.; McLeod, A.; Wagner, M.; Zhang, L.; Zhao, Z.; Thiemens, M.; Dominguez, G. Gate-tuning of graphene plasmons revealed by infrared nano-imaging. *Nature* **2012**, *487*, 82.

Chapter 6 - Graphite Growth from Fe-Cr

6.1 Introduction

The earliest application of graphite as a refractory material can be traced back to the late 19th century.[1] Since then, graphite has been widely used for batteries, electrical conductors, lubricants, compaction additives and steelmaking.[2-5] These applications usually have low fabrication requirements for graphite's domain size, crystallographic orientation, and defects. However, over the last decade, graphene, which is an individual layer of graphite, has gained huge attention due to its unique properties. A variety of applications have been exploited for graphene, such as electronics, optoelectronics, photonics, catalyst supports and energy storage.[6-10] For these applications, control of the thickness, domain size and defects is essential.

Several graphene preparation methods have been developed since it was successfully exfoliated from graphite in 2004.[11] Among them, chemical vapor deposition (CVD) using catalytic metal substrates produces large-area films but only in limited quantities.[12] Instead, the requirement of large amounts of graphene can be prepared by physical and chemical exfoliation of bulk graphite.[13,14] Moreover, compared to exfoliated graphene, graphene prepared by the CVD method generally has lower electron mobility, higher impurity concentrations, and higher asymmetry between electron and hole conduction.[15-18] Thus, the preparation of high-quality graphite bulk crystal in crucial.

The most common crystal growth technique for single crystal graphite is the metal flux method, in which Fe or Ni has been widely used as a flux.[19-22] However, the crystal size are generally less than 100 μm. Our group has previously demonstrated that the addition of Cr into Ni or Fe metal flux could significantly improve the size and quality of hexagonal boron nitride (hBN)

single crystals.[23,24] As graphite has a similar structure with hBN, we tested whether an Fe-Cr alloy flux can also improve the graphite crystal size and quality.

In this study, the process of producing graphite crystals from a Fe-Cr flux was developed. The crystal sizes, shapes and morphologies were determined by optical microscopy. Then the Raman and X-ray diffraction spectra were taken to assess the quality of the graphite crystals. After that, X-ray photoelectron spectroscopy was utilized to evaluate the chemical bonding in the crystals. Lastly, the topography of the crystal surface and the layer thickness was investigated by atomic force microscopy.

6.2 Experimental Methods

Graphite crystals were synthesized by precipitation from a Fe-Cr solution in a high temperature, single-zone tube furnace. A mixture of 48 wt% Fe, 48 wt% Cr and 4 wt% graphite powders was loaded into an alumina crucible. The crucible with the source materials was then transferred into the furnace. The reaction tube was evacuated, and then filled with N_2 and CO gas to a constant pressure of 850 Torr. In this experiment, the CO gas was used to minimize oxygen impurity that are recognized as the main contaminants in graphite crystals. During the reaction, the N_2 and CO gases continuously flowed through the system at rates of 125 sccm and 25 sccm, respectively. The liquid solution was formed by heating the furnace up to 1550 °C and holding for a dwell period of 24 hours. The graphite crystals were then precipitated by cooling at a rate of 4 °C /h to 1400 °C. Then, the system was quickly quenched to room temperature.

Raman spectra were taken at room temperature using a Renishaw inVoa Raman microscope system. A linearly polarized 532 nm laser light was used. It was focused to a spot

diameter of ~2 μm by a 50× long-working-distance objective lens. Laser power was kept below 0.8 mW. Instrument resolution was ~0.5 cm^{-1} by using the 1800 groove/mm grating.

X-ray photoelectron spectroscopy (XPS) Spectra were measured on Phi VersaProbe II system at a base pressure of 10^{-9} Torr, using monochromatic Al Kα line. Survey XPS scans were run at 160 eV pass energy and high-resolution scans at 20 eV pass energy. All samples were in electronic equilibrium with the spectrometer via a metallic clip on the sample, and characterized at normal take-off angle. XPS peak fits were done with CasaXPS Software 2.2.8 using mixed Gaussian/Lorentzian distributions to minimize *chi* squared value.

X-ray powder diffraction (XRD) was carried out using a Rigaku Miniflex II desktop X-ray diffractometer with monochromatic Cu Kα radiation ($\lambda = 0.154$ nm) with a step size of 0.1° and a scan speed of 2.0° per minute. Values of 2θ were in the range 20–90°. Phases were identified by comparing patterns obtained with a JCPDS database.

The surface topography of the samples was investigated by a Bruker Innova atomic force microscopy (AFM) system. This instrument includes stacked piezo XY and Z scanners with resolution as high as < 0.02 nm and < 0.01 nm, respectively. The 3 primary AFM modes are included in this system, i.e., Contact Mode, Tapping Mode and Non-Contact Mode. A sample size up to 45 mm*45 mm*18 mm can be measurement by this instrument.

6.3 Results and Discussion

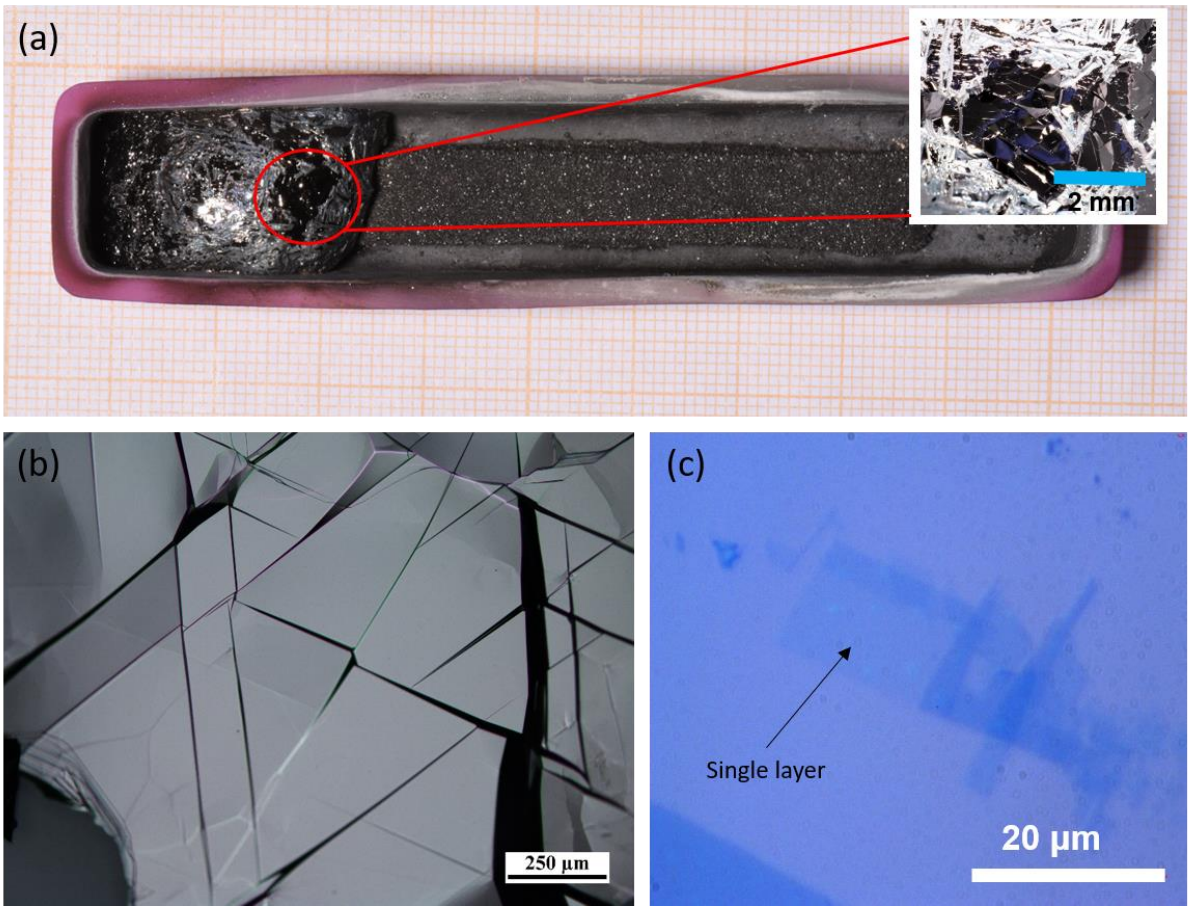

Figure 6.1. (a) Photograph of precipitated graphite crystals on top of Fe-Cr metal surface. The insert figure highlights a graphite domain on the metal surface. (b)-(c) Optical micrographs of free-standing graphite flakes transferred from metal surface and single layer graphene exfoliated on silicon.

Figure 6.1a illustrates the optical image of graphite crystals grown onto the Fe-Cr metal surface, showing that the grown crystals are black and glossy. The insert figure highlights a graphite domain which is on the order of 5-mm across. To obtain free-standing graphite crystals, we used thermal release tape to adhere and peel the crystals from the metal surface. Then we heated

the tape at 150°C for 10 seconds to release the adhesive and transfer the crystals onto a glass substrate (Figure 6.1b). The largest single crystal domain size is about 1-mm across. We also performed mechanical exfoliation of our graphite crystals using Nitto tape to obtain layers of graphite, which were subsequently re-exfoliated until monolayers obtained. Figure 6.1c shows the exfoliated single layer graphene with a size around 20 μm cross.

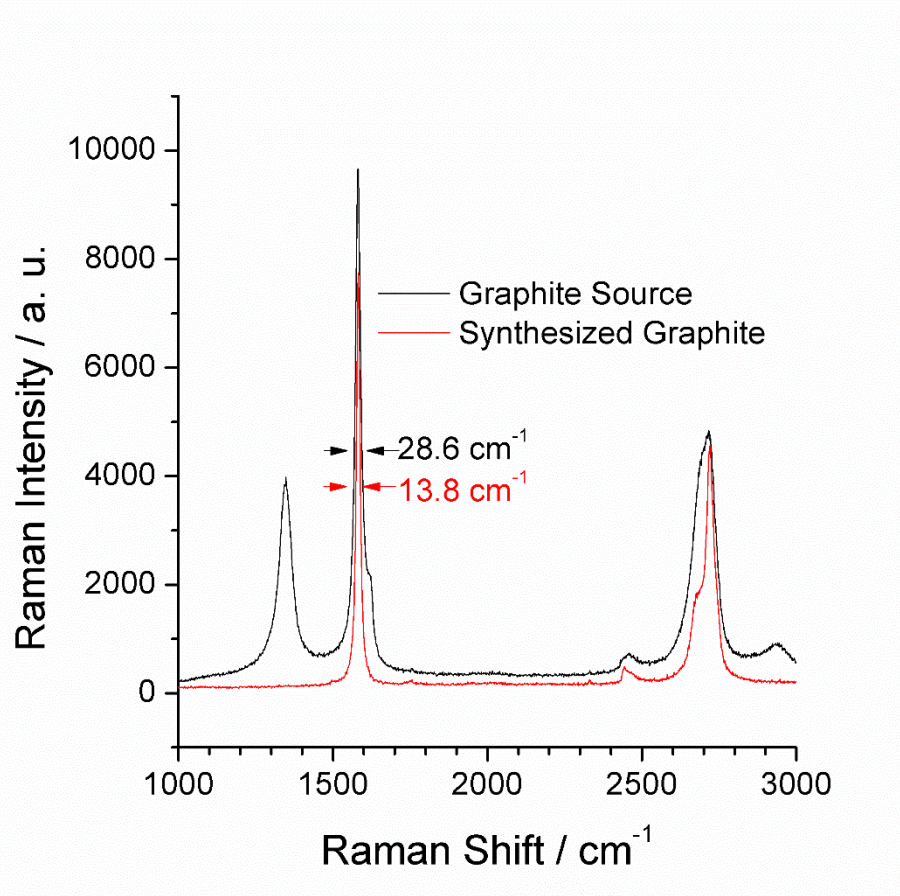

Figure 6.2. Raman spectra of graphite source powder and synthesized graphite crystals from Fe-Cr metal flux.

The most intense features in Raman spectra of graphite are the G peak at ~1580 cm^{-1}, the D peak at ~1350 cm^{-1}, and 2D peak at ~2700 cm^{-1}. The G peak is a doubly degenerate phonon

mode (E_{2g}) at the Brillouin zone center that is Raman active for sp^2 carbon networks.[25] The D peak is due to the breathing modes of rings and requires a defect for its activation.[26] Thus this band cannot be seen in a highly crystalline graphite.[27] The 2D peak is the second order of zone-boundary phonons.[28] Figure 6.2 displays the Raman spectra of graphite source powder and synthesized graphite crystals. The D-peak, which shows an intense peak at 1349 cm^{-1} in the raw graphite source, is not seen in the synthesized graphite crystal, which indicates the absence of defects in our synthesized graphite crystals. The G peak (at 1580 cm^{-1}) of the synthesized crystal has a FWHM of 13.8 cm^{-1}, which is among the smallest values reported by previous literatures,[29-31] and only half of the width of the G peak in the raw graphite powder. This demonstrates the high quality of the graphite crystals. The 2D peak at 2719 cm^{-1} also shows a good agreement with literature values.[26,28] The asymmetry of this peak results from the band splitting into two components, i.e., $2D_1$ and $2D_2$, in bulk graphite.[28]

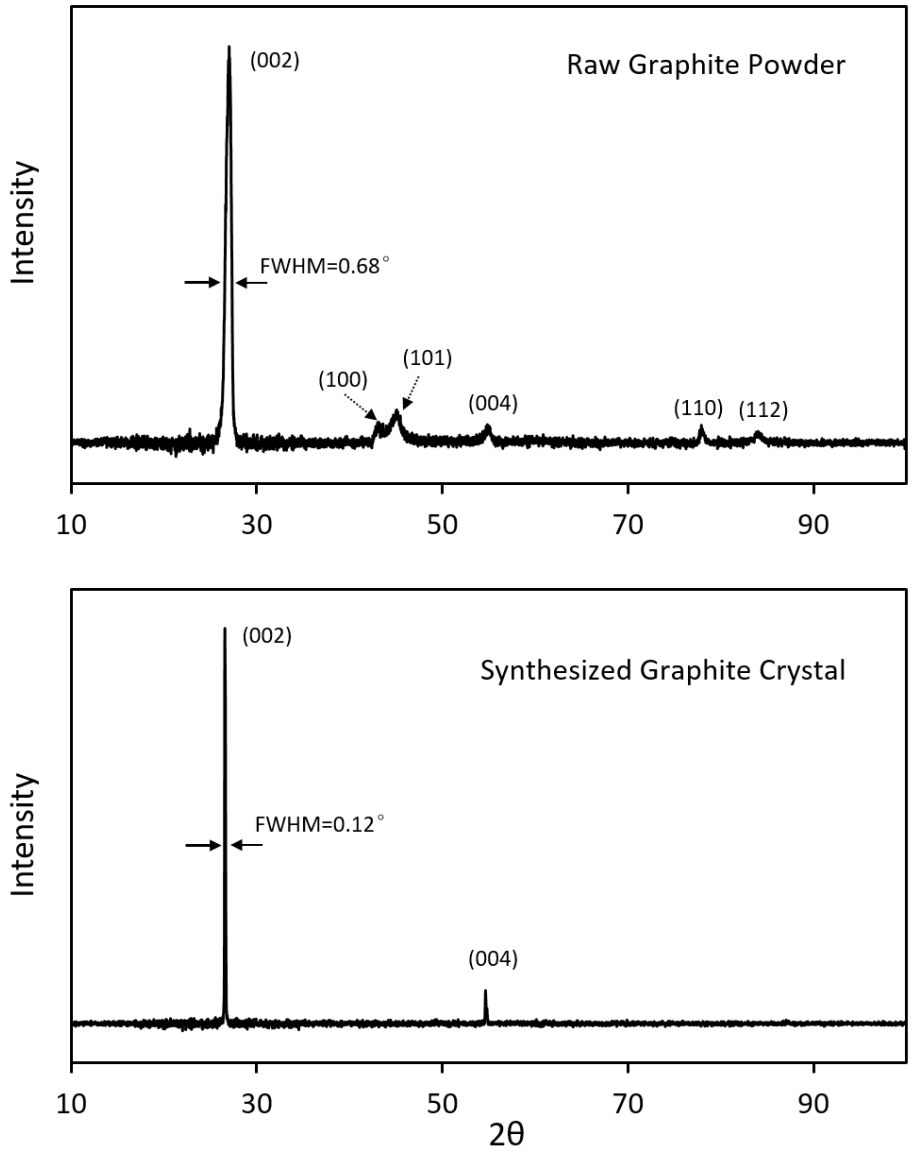

Figure 6.3. X-ray Diffraction (XRD) spectra from the graphite source powder and graphite crystals grown with the Fe-Cr metal flux.

The raw graphite powder and synthesized graphite crystals from Fe-Cr metal flux were characterized by x-ray diffraction (XRD), scanning from 10° and 100.0°, as shown in Figure 6.3. The (002) and (004) peaks, which are the most intense features in the XRD pattern of graphite, were observed at 26.52° and 54.62°. The estimated interlayer distance according to Bragg's law is

0.33 nm, in agreement with the literature values.[32,33] The synthesized graphite crystals were significantly more ordered than their source material, indicated by the narrowing of the (002) peak from 0.68° for the raw graphite powder to 0.12° for the graphite crystal. In addition, the (100), (101), (110) and (112) peaks seen in the source powder were absent in the crystal, confirming that it had a single crystal orientation.

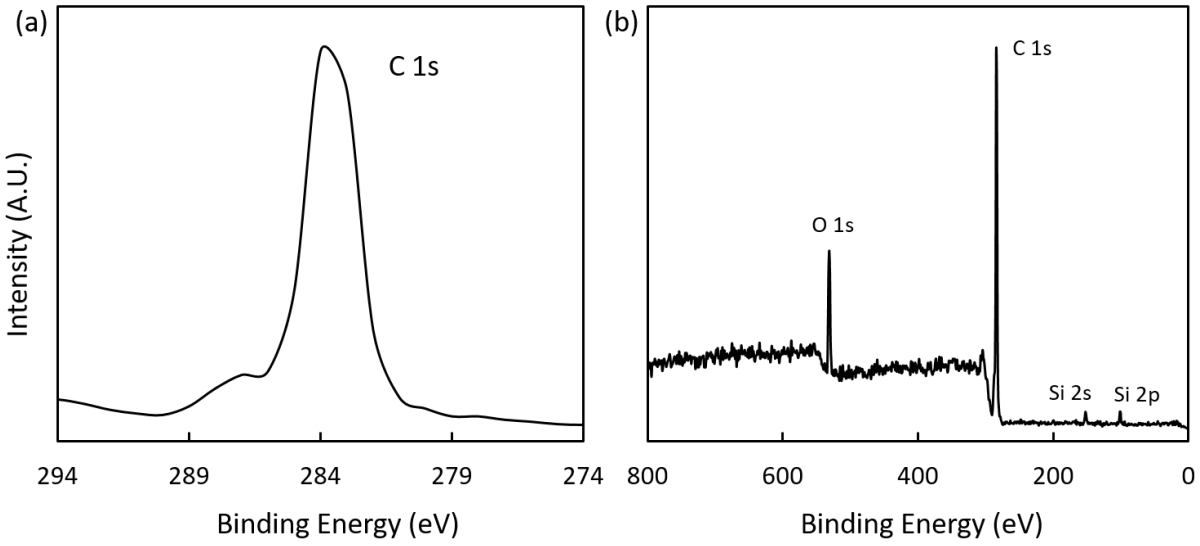

Figure 6.4. X-ray photoelectron spectroscopy (XPS) spectra of (a) C 1s from graphite crystals, and (b) graphite crystals.

X-ray photoelectron spectroscopy (XPS) was applied to characterize the elemental stoichiometry of the synthesized graphite crystals. As shown in Figure 6.4a, the binding energy of C 1s was at 284.8 eV, which indicates hexagonal phase consisting of C-C (sp^2) bonds exists in our graphite crystals.[34] The additional oxygen peak showing in Figure 6.4b could result from the exposure of the sample to air in between the synthesis and XPS measurement. The appearance of small Si 2s and 2p peaks could be attributed to the underlying substrate.

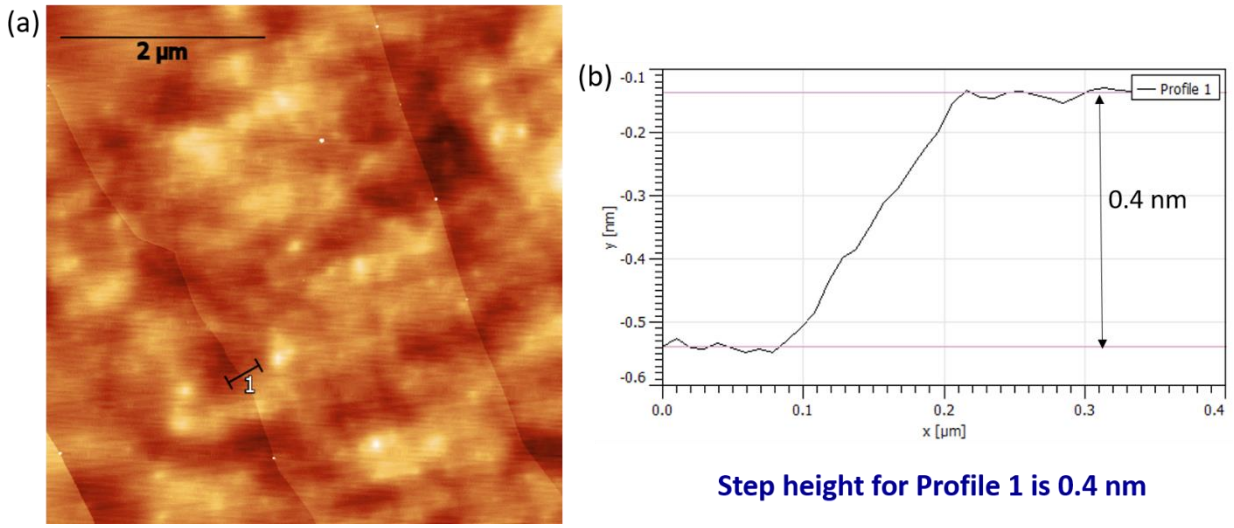

Figure 6.5. (a) Atomic Force Microscopy (AFM) spectrum and (b) associated step profile of the graphite crystal surface.

To structurally characterize the sample, atomic force microscopy (AFM) measurements were performed. As shown in Figure 6.5, the graphite crystal surface was smooth and uniform, and without any obvious defects. The step height (Figure 6.5b) for profile 1 marked in Figure 6.5a is 0.4 nm.

6.4 Conclusions

This study demonstrates that large-scale, high-quality graphite single crystals can be successfully formed from Fe-Cr metal solvent at atmospheric pressure. The graphite crystals produced this way are black and glossy, and have a maximum domain size of around 5-mm. The Raman and XRD spectra demonstrate the high-quality of the synthesized crystals. The XPS

spectrum indicates the hexagonal phase consisting of C-C (sp^2) bonds exists in our graphite crystals. AFM image shows that the graphite crystal surface is smooth, uniform, and defect-free.

6.5 Acknowledgement

Support from the Materials Engineering and Processing program of the National Science Foundation, award number CMMI 1538127, and the II−VI Foundation is greatly appreciated.

References

1. Wissler, M. Graphite and carbon powders for electrochemical applications. *J. Power Sources* **2006**, *156*, 142-150.
2. Lee, W. E.; Moore, R. E. Evolution of in situ refractories in the 20th century. *J Am Ceram Soc* **1998**, *81*, 1385-1410.
3. Sun, B.; Skyllas-Kazacos, M. Modification of graphite electrode materials for vanadium redox flow battery application—I. Thermal treatment. *Electrochim. Acta* **1992**, *37*, 1253-1260.
4. Shaji, S.; Radhakrishnan, V. Analysis of process parameters in surface grinding with graphite as lubricant based on the Taguchi method. *J. Mater. Process. Technol.* **2003**, *141*, 51-59.
5. Orumwense, F.; Okorie, B.; Okeakpu, E.; Obiora, E.; Onyeji, L. Sintered copper–graphite powder compacts forindustrial applications. *Powder Metallurgy* **2001**, *44*, 62-66.
6. Dean, C. R.; Young, A. F.; Meric, I.; Lee, C.; Wang, L.; Sorgenfrei, S.; Watanabe, K.; Taniguchi, T.; Kim, P.; Shepard, K. L. Boron nitride substrates for high-quality graphene electronics. *Nature Nanotechnology* **2010**, *5*, 722.

7. Gu, T.; Petrone, N.; McMillan, J. F.; van der Zande, A.; Yu, M.; Lo, G.; Kwong, D.; Hone, J.; Wong, C. W. Regenerative oscillation and four-wave mixing in graphene optoelectronics. *Nature Photonics* **2012**, *6*, 554.

8. Bonaccorso, F.; Sun, Z.; Hasan, T.; Ferrari, A. Graphene photonics and optoelectronics. *Nature Photonics* **2010**, *4*, 611.

9. Jafri, R. I.; Rajalakshmi, N.; Ramaprabhu, S. Nitrogen doped graphene nanoplatelets as catalyst support for oxygen reduction reaction in proton exchange membrane fuel cell. *Journal of Materials Chemistry* **2010**, *20*, 7114-7117.

10. Yang, X.; Cheng, C.; Wang, Y.; Qiu, L.; Li, D. Liquid-mediated dense integration of graphene materials for compact capacitive energy storage. *Science* **2013**, *341*, 534-537.

11. Novoselov, K. S.; Geim, A. K.; Morozov, S. V.; Jiang, D.; Zhang, Y.; Dubonos, S. V.; Grigorieva, I. V.; Firsov, A. A. Electric field effect in atomically thin carbon films. *Science* **2004**, *306*, 666-669.

12. Cai, M.; Thorpe, D.; Adamson, D. H.; Schniepp, H. C. Methods of graphite exfoliation. *Journal of Materials Chemistry* **2012**, *22*, 24992-25002.

13. Schniepp, H. C.; Li, J.; McAllister, M. J.; Sai, H.; Herrera-Alonso, M.; Adamson, D. H.; Prud'homme, R. K.; Car, R.; Saville, D. A.; Aksay, I. A. Functionalized single graphene sheets derived from splitting graphite oxide. *The Journal of Physical Chemistry B* **2006**, *110*, 8535-8539.

14. Stankovich, S.; Piner, R. D.; Chen, X.; Wu, N.; Nguyen, S. T.; Ruoff, R. S. Stable aqueous dispersions of graphitic nanoplatelets via the reduction of exfoliated graphite oxide in the presence of poly (sodium 4-styrenesulfonate). *Journal of Materials Chemistry* **2006**, *16*, 155-158.

15. Bae, S.; Kim, H.; Lee, Y.; Xu, X.; Park, J.; Zheng, Y.; Balakrishnan, J.; Lei, T.; Kim, H. R.; Song, Y. I. Roll-to-roll production of 30-inch graphene films for transparent electrodes. *Nature Nanotechnology* **2010**, *5*, 574.

16. Huang, P. Y.; Ruiz-Vargas, C. S.; van der Zande, Arend M; Whitney, W. S.; Levendorf, M. P.; Kevek, J. W.; Garg, S.; Alden, J. S.; Hustedt, C. J.; Zhu, Y. Grains and grain boundaries in single-layer graphene atomic patchwork quilts. *Nature* **2011**, *469*, 389.

17. Petrone, N.; Dean, C. R.; Meric, I.; van Der Zande, Arend M; Huang, P. Y.; Wang, L.; Muller, D.; Shepard, K. L.; Hone, J. Chemical vapor deposition-derived graphene with electrical performance of exfoliated graphene. *Nano Letters* **2012**, *12*, 2751-2756.

18. Venugopal, A.; Chan, J.; Li, X.; Magnuson, C. W.; Kirk, W. P.; Colombo, L.; Ruoff, R. S.; Vogel, E. M. Effective mobility of single-layer graphene transistors as a function of channel dimensions. *J. Appl. Phys.* **2011**, *109*, 104511.

19. Massalski, T. B.; Okamoto, H.; Subramanian, P.; Kacprzak, L.; Scott, W. W. *Binary Alloy Phase Diagrams;* American Society for Metals Metals Park, OH: 1986; Vol. 1.

20. Massalski, T.; Subramanian, P.; Okamoto, H.; Kacprzak 2nd, L. Edition. *Binary Alloy Phase Diagrams* **1990**, *2*.

21. Noda, T.; Sumiyoshi, Y.; Ito, N. Growth of single crystals of graphite from a carbon-iron melt. *Carbon* **1968**, *6*, 813-816.

22. Shimada, S.; Watanabe, J.; Kodaira, K.; Matsushita, T. Flux growth and characterization of TiC crystals. *J. Mater. Sci.* **1989**, *24*, 2513-2515.

23. Liu, S.; He, R.; Ye, Z.; Du, X.; Lin, J.; Jiang, H.; Liu, B.; Edgar, J. H. Large-Scale Growth of High-Quality Hexagonal Boron Nitride Crystals at Atmospheric Pressure from an Fe–Cr Flux. *Crystal Growth & Design* **2017**, *17*, 4932-4935.

24. Hoffman, T. B.; Clubine, B.; Zhang, Y.; Snow, K.; Edgar, J. H. Optimization of Ni–Cr flux growth for hexagonal boron nitride single crystals. *J. Cryst. Growth* **2014**, *393*, 114-118.

25. Roy, D.; Chhowalla, M.; Wang, H.; Sano, N.; Alexandrou, I.; Clyne, T.; Amaratunga, G. Characterisation of carbon nano-onions using Raman spectroscopy. *Chemical Physics Letters* **2003**, *373*, 52-56.

26. Mohiuddin, T.; Lombardo, A.; Nair, R.; Bonetti, A.; Savini, G.; Jalil, R.; Bonini, N.; Basko, D.; Galiotis, C.; Marzari, N. Uniaxial strain in graphene by Raman spectroscopy: G peak splitting, Grüneisen parameters, and sample orientation. *Physical Review B* **2009**, *79*, 205433.

27. Ferrari, A. C. Raman spectroscopy of graphene and graphite: disorder, electron–phonon coupling, doping and nonadiabatic effects. *Solid State Commun.* **2007**, *143*, 47-57.

28. Ferrari, A. C.; Meyer, J.; Scardaci, V.; Casiraghi, C.; Lazzeri, M.; Mauri, F.; Piscanec, S.; Jiang, D.; Novoselov, K.; Roth, S. Raman spectrum of graphene and graphene layers. *Phys. Rev. Lett.* **2006**, *97*, 187401.

29. Lazzeri, M.; Piscanec, S.; Mauri, F.; Ferrari, A.; Robertson, J. Phonon linewidths and electron-phonon coupling in graphite and nanotubes. *Physical Review B* **2006**, *73*, 155426.

30. Yang, D.; Velamakanni, A.; Bozoklu, G.; Park, S.; Stoller, M.; Piner, R. D.; Stankovich, S.; Jung, I.; Field, D. A.; Ventrice Jr, C. A. Chemical analysis of graphene oxide films after heat and chemical treatments by X-ray photoelectron and Micro-Raman spectroscopy. *Carbon* **2009**, *47*, 145-152.

31. Rollings, E.; Gweon, G.; Zhou, S.; Mun, B.; McChesney, J.; Hussain, B.; Fedorov, A.; First, P.; De Heer, W.; Lanzara, A. Synthesis and characterization of atomically thin graphite films on a silicon carbide substrate. *Journal of Physics and Chemistry of Solids* **2006**, *67*, 2172-2177.

32. Sun, G.; Li, X.; Qu, Y.; Wang, X.; Yan, H.; Zhang, Y. Preparation and characterization of graphite nanosheets from detonation technique. *Mater Lett* **2008**, *62*, 703-706.

33. Shi, H.; Barker, J.; Saidi, M.; Koksbang, R. Structure and lithium intercalation properties of synthetic and natural graphite. *J. Electrochem. Soc.* **1996**, *143*, 3466-3472.

34. Świątowska, J.; Lair, V.; Pereira-Nabais, C.; Cote, G.; Marcus, P.; Chagnes, A. XPS, XRD and SEM characterization of a thin ceria layer deposited onto graphite electrode for application in lithium-ion batteries. *Appl. Surf. Sci.* **2011**, *257*, 9110-9119.

Chapter 7 - Atomistic Insights of hBN Thin Film Growth

Chapter 7 is reproduced in part with permission from:

Liu, S.; van Duin, A. C.; van Duin, D. M.; Liu, B.; Edgar, J. H. Atomistic Insights into Nucleation and Formation of Hexagonal Boron Nitride on Nickel from First-Principles-Based Reactive Molecular Dynamics Simulations. *ACS Nano* **2017***, 11*, 3585-3596.

7.1 Introduction

Chemical vapor deposition (CVD) is one of the most commonly employed method to grow thin films of 2-D materials, including hBN, on transition metal surfaces, such as Ni,[1-6] Cu,[7-10] Pd,[11] and Pt[12]. However, hBN obtained from CVD often contains high-density grain boundaries and other defects that degrade its properties and limit its applications.[1,6,13] Fundamentally, a detailed mechanistic understanding of the crystal growth facilitated by substrate surface in a CVD environment is critical to improve the synthesis technique for high quality hBN materials. There are still unresolved issues regarding hBN single crystal growth on transition metal substrates: how the termination and shape of hBN islands are governed by the chemical environment; how the defect structures are induced during growth; and how the hBN nucleation and growth are influenced by the crystal facets and electronic character of the substrate.

It is one of the intents of this thesis to develop theoretical modeling methods and tools, centered on density functional theory (DFT), to investigate and understand the growth mechanism of hBN. The initial effort focuses on hBN thin film growth on crystalline metal substrate. Nickel, a common substrate metal, has been chosen as a model.

Computationally, DFT calculations have matured into a powerful tool to accurately

characterize the atomic structures and chemical bonding in relation to hBN synthesis. For instance, Grad *et al.*[14] and Díaz *et al.*[15] used periodic DFT modeling to examine hBN monolayer adsorption on different transition metal substrates. For instance, on Ni(111), the nitrogen species in hBN show preference on the Ni top sites, while B prefers either the fcc or the hcp sites. DFT calculations have also been employed to identify the favorable edge termination and the shape of hBN islands.[16] Furthermore, the decomposition chemistry of hBN precursors (*e.g.*, BH_2NH_2) and the relationship with the compositions of substrates (*e.g.*, Ni, Ni-Cu alloy) have been modeled.[1] Most recently, using first-principles-based analysis, Zhang *et al.*[17] explored the shapes of hBN islands at varying boron chemical potentials on Cu(111) and Ni(111) with detailed growth kinetics of hBN edge structures.

However, the computational cost inherent to the quantum mechanical approach often limits the modeling of materials synthesis on a system scale, and thus rendering explicit DFT calculations inefficient or even unfeasible for understanding the dynamic evolution leading to hBN lattice formation. Hence, it is highly desirable to develop the capability to extend the modeling power of quantum mechanics and to ultimately address the key outstanding issues outlined previously. Reactive molecular dynamics (rMD) simulation, based on classical formulations for chemical bond formation, is an appealing alternative since it can provide dynamic perspectives of crystal growth by simulating large molecular systems at much lower computational costs compared to quantum mechanical calculations. With the combination of periodic DFT calculations and rMD simulations, the efforts to develop a self-consistent modeling utility is presented and demonstrated.

A ReaxFF reactive force field[18] will be developed and adopted for the Ni/B/N system to investigate the growth mechanism of atomically thin hBN on crystalline Ni substrates in this thesis. First, elementary events involved in the hBN growth, such as atomic B and N adsorptions,

diffusions, and B-N bond formation producing B_xN_y (x, y = 1-2) were studied in the periodic DFT setting. The governing reaction energetics and kinetics were obtained on Ni(111) and Ni(211), to account for the chemistries taking place on both terraces and step-edges of the substrates. Parameterization of the ReaxFF for the B–Ni and N–Ni atomic pairs was then carried out. With the simulated hBN growth from elemental B and N deposited onto a single crystal Ni substrate model, the rMD simulation trajectories were then analyzed to derive the elementary growth mechanism at the atomistic level. Finally, key findings obtained from the rMD simulations were validated by additional DFT calculations.

7.2 Computation Methods and Simulation Details

7.2.1 Density Functional Theory (DFT) Calculations

All periodic DFT calculations were performed with spin polarization using the Vienna Ab initio Simulation Package (VASP) program.[19] The pseudopotentials for B, N, and Ni elements were generated from the projector augmented wave (PAW)[20] method with the plane-wave basis set energy cutoff to 400 eV. The generalized gradient approximation (GGA) Perdew−Burke−Ernzerhof (PBE)[21] functional was employed to account for the electron exchange-correlation potential. The Brillouin zone integrations were carried out using a 4 × 4 × 1 Monkhorst-Pack mesh.[22] A Methfessel-Paxton smearing[23] of 0.2 eV was used, with the total energies then extrapolated to 0 K. The geometry optimization stops when all the forces on the system become smaller than 0.02 eV/Å. The bulk Ni lattice constant and magnetic moment from the bulk optimization are 3.52 Å, and 0.62 μ_B/Ni atom, respectively, in good agreement with experimental values of 3.52 Å and 0.61 μ_B.[24]

The Ni surface was modeled by considering the close-packed terrace sites and the stepped sites, where the single crystal Ni(111) and Ni(211) facets were used. The Ni(111) and Ni(211) surfaces were represented by a 4-layer $p(3 \times 3)$ unit cell and a 12-layer Ni(211) slab with $p(1 \times 3)$ unit cell respectively, for periodic DFT calculations. For respective (111) and (211) slabs, the bottom two layers and the bottom six layers were fixed at their optimized bulk lattice values. A 30 Å thick vacuum space was used for both unit cells to avoid interference between periodic images along the perpendicular direction to the surface. The climbing-image Nudged Elastic Band (CI-NEB)[25] and the Dimer[26] calculations were performed in order to identify the minimum energy pathways (MEPs) and the transition state (TS) structures of the elementary nucleation and growth steps. Each transition state was confirmed by the vibrational frequency analysis with a single imaginary frequency.

7.2.2 Reactive Molecular Dynamics (MD) Simulations

The rMD simulations of hBN growth on Ni surface were performed with LAMMPS.[27] A rectangular shaped nickel slab with the close-packed (111) facet was used to represent the Ni substrate, where elemental B and N were deposited initially for hBN nucleation and growth. The Ni slab consists of 5 atomic layers with lateral dimensions of 12 × 12 Ni atoms for a total of 720 Ni atoms. Periodic boundary conditions were imposed on all dimensions. The bottom (5th) layer was fixed so that the Ni atoms remained in their bulk lattice structures during the simulation to represent the interior bulk region, while the top 4 layers were relaxed along the vertical direction to represent the surface and sublayer regions. There is a vacuum of 90 Å above and below the slab.

In the current simulation procedure, an equal number of B and N atoms (200 each), based on the stoichiometric ratio of hBN, were sequentially introduced in pairs from the gas phase with random x, y coordinates above the Ni surface at an interval of 0.25 ps. To minimize premature B–N bond formation, the distance between the initial B and N sources is set to be at least 1.90 Å, which is much larger than the typical BN bond length of 1.44 Å. All the B and N were deposited only on the relaxed side of the slab with controlled initial momenta. The simulations were run at different temperatures, *i.e.*, 900 K, 1100 K, 1300 K and 1500 K, controlled by the Nose Hoover thermostat.[28] Each MD simulation was run for at least 6 ns using a time step of 0.25 fs. The equation of motion was numerically solved using the velocity Verlet integration scheme.[29]

7.3 Results and Discussion

7.3.1 Adsorptions of Building Block Species for hBN Formation on Ni

The adsorptions of elemental B and N occur upon the release from the decomposition of B and N-containing precursors (*e.g.*, diborane and ammonia),[1,5] and thus can be considered as the first step toward hBN lattice formation. In this section, the adsorption geometries and energetics of atomic B and N, and representative hBN building block units were considered using periodic DFT calculations.

The nickel substrates were modeled using the close-packed and stepped (111) and (211) facets respectively to approximate the respective flat terrace and step substrate surfaces.[30,31] The optimized structures of adsorbed B_xN_y species (x = 0 - 2; y = 0 - 2) on their preferred sites on Ni(111) and Ni(211) are illustrated in Figure 7.1(a) and 1(b), respectively. The binding energies (BEs) were calculated according to Equation (17):

$$BE = E_{B_xN_y^*} - E_{Ni} - E_{B_xN_y} \quad (17)$$

where $E_{B_xN_y^*}$, E_{Ni}, and $E_{B_xN_y}$ are the total energies of the adsorbed B_xN_y* species, clean Ni surface, and the total energy of corresponding B_xN_y species in gas phase, respectively. These calculations, corresponding to each preferred adsorption site, are summarized in Table 7.1.

Table 7.1. DFT calculated binding energies of B_xN_y species (x = 0, 1, 2; y = 0, 1, 2) adsorption on Ni (111), Ni (211) surfaces and Ni sublayer.

Species	**Ni(111)**		**Ni(211)**	
	Site	E_{ads}/eV	Site	E_{ads}/eV
N	fcc	-5.29	4-fold	-5.58
B	hcp	-5.84	4-fold	-6.95
N (sublayer)	octahedral	-4.65	octahedral	-4.55
B (sublayer)	octahedral	-6.47	octahedral	-6.48
BN	hcp(B)-fcc(N)	-6.51	4-fold	-7.57
B_2N	hcp(B)-hcp(B)	-6.11	4-fold(B)-4-fold(B)	-7.20
BN_2	fcc(N)-fcc(N)	-7.10	4-fold(N)-4-fold(N)	-7.97
B_2N_2	hcp(B)-fcc(N)	-7.25	4-fold(B)-4-fold(B)-fcc(N)	-7.78

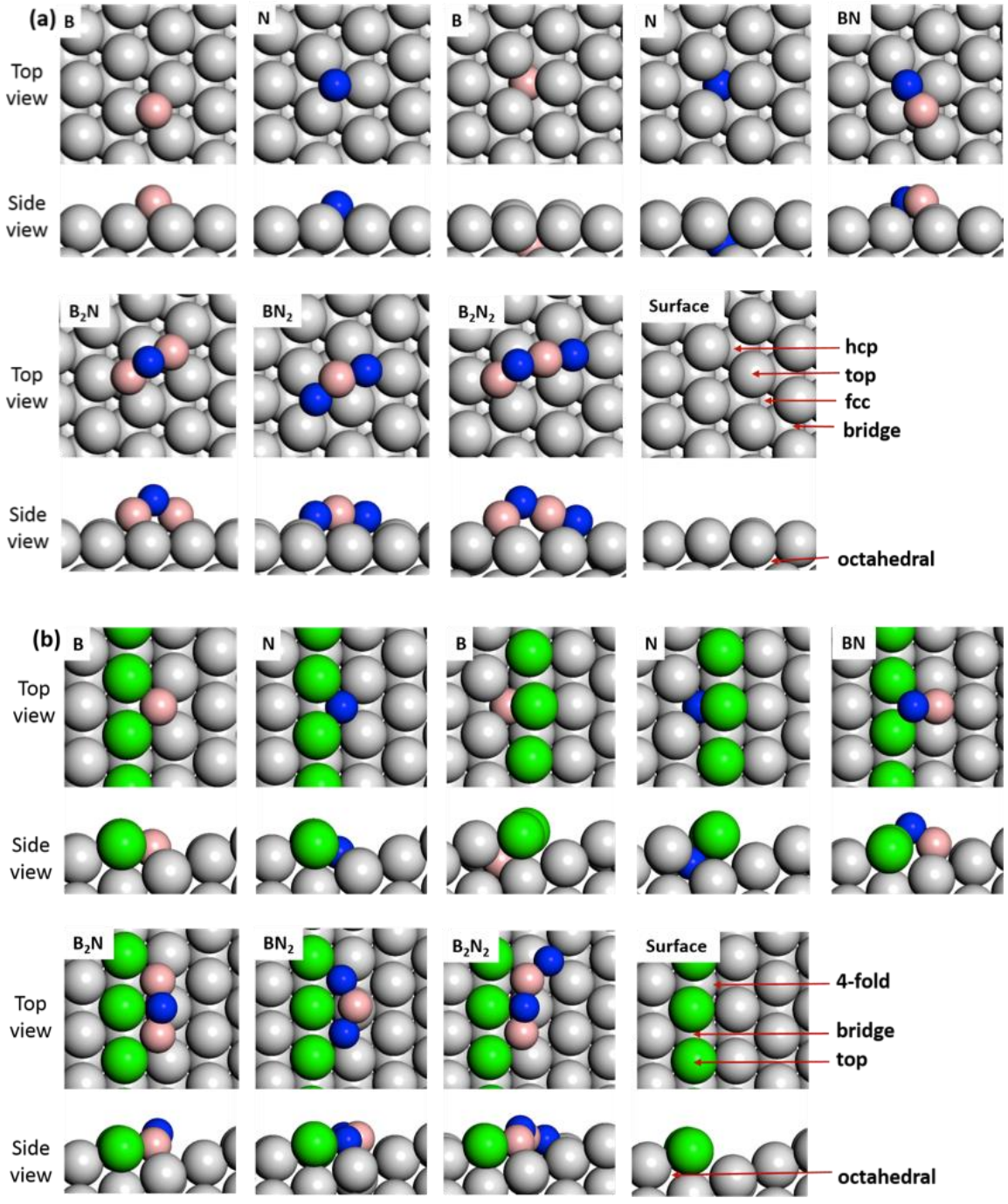

Figure 7.1. Top and side views of optimized B, N, BN, BNB, NBN, B_2N_2 adsorptions on (a) Ni(111); and (b) Ni(211). Adsorption sites are indicated on the respective clean (111) and (211) surface. The N, B, Ni, and edge Ni atoms are represented by the blue, pink, grey, and green spheres, respectively.

On Ni(111), B atoms prefer to bind at the 3-fold hcp site, while N atoms prefer the 3-fold fcc site. In the Ni sublayer, atomic B and N both prefer the octahedral site. However, the sublayer B atom is even more energetically stable, by 0.63 eV, compared to its surface adsorption. On the other hand, the sublayer N is less energetically favorable by 0.64 eV. The predicted atomic adsorption preference is in good agreement with a previous study by Zhang *et al.*[17] The DFT calculated energetics suggest that, thermodynamically, elemental B would prefer the octahedral lattice spacing in the subslayer region.

Among other building block species, the BN dimer prefers to bind on adjacent hcp(B)-fcc(N) dual sites on Ni(111). BNB, NBN and B_2N_2 all bind with the terminal B and/or N species, at their respective preferred 3-fold hcp/fcc sites (Table 7.1). Hence, as the molecular length of B_xN_y grows, the binding sites are separated further apart. As shown in Figure 7.1(a), B_2N and BN_2 bind on the two next nearest 3-fold sites, while B_2N_2 binds on the sites separated by two 3-fold sites. The middle sections of BNB, NBN, B_2N_2 are not in direct contact with the surface, and buckled as illustrates in the Figure 7.1(a) site views.

On Ni(211), the B_xN_y species are generally more strongly bound than on the Ni(111) surface, as shown in Table 7.1, due to the low-coordinated Ni on the Ni(211) step edge. The B and N atoms prefer the 4-fold site near the edge, as shown in Figure 7.1(b). The BN dimer binds on Ni(211) with its N- and B-ends on the bridge sites of the edge and the lower terrace, respectively. The binding energy of BN is 1 eV stronger than that on the terrace. The linear BNB, NBN, and B_2N_2 molecules all prefer to bind parallel to the edge to maximize the interactions with the low-coordinated edge atoms. The terminal B and N atoms bind at the 4-fold sites for B_2N and BN_2, as shown in Figure 7.1(b), respectively. For B_2N_2, the B-end binds at the 4-fold site, while its N-end binds at the 3-fold site of the lower terrace. The binding energies of sublayer B and N species are

comparable to those in the (111) sublayer, showing less influence from the low-coordination sites on the surface.

7.3.2 Surface Diffusions of B and N on Ni

The diffusions of hBN constituent B and N species are also critical to crystal nucleation and growth.[32] Therefore, DFT calculations were performed to investigate different elemental B and N diffusion pathways to reveal their behaviors on surface, in the sublayer, and in the bulk region of Ni substrate. The proposed overall B and N diffusion schemes in this study are presented in Figure 7.2, where the B/N atom is moved as a probe from one 4-fold step edge site (labeled as A) to another 4-fold step edge site (labeled as B) on a model surface terminated with both terrace and step sites. The (211) step edge site was used as the starting and ending points because it is the most stable binding site for both B and N atoms (Table 7.1).

As illustrated in Figure 7.2, the solid yellow path represents the diffusion pathway on the surface, which consists of four elementary diffusion steps: (1) from one 4-fold site to the neighboring 4-fold site, (2) from the 4-fold site to the 3-fold hcp/fcc on the terrace, (3) from the 3-fold site to the neighboring 3-fold fcc/hcp site on the terrace, and (4) from the fcc/hcp site to the step 4-fold site. With a similar notation, the green dashed path represents B/N diffusion into the substrate sublayer. It consists of three steps: (5) from the 3-fold site to the octahedral site in the sublayer, (6) from one octahedral site to the next octahedral site in the sublayer, and (7) from the octahedral site in the sublayer emerging to the 4-fold step edge site. The bulk diffusion pathway is represented by red dashed path, consisting of two steps: (8) from the octahedral site in the sublayer to the octahedral site in the bulk, and (9) from one bulk octahedral site to the next octahedral site in the bulk.

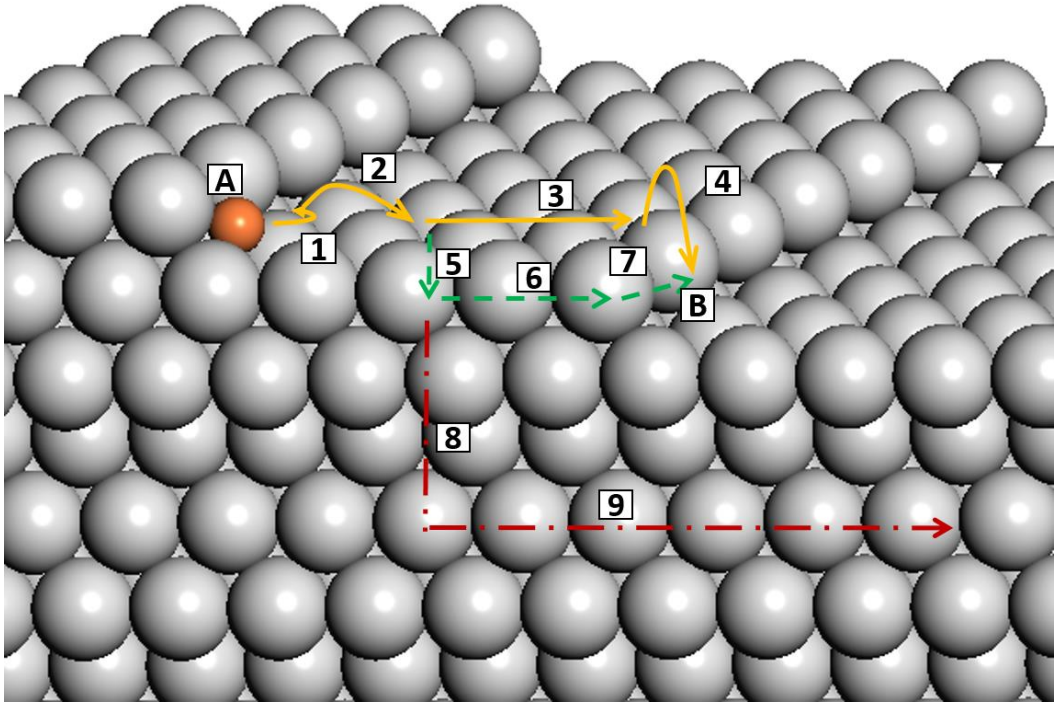

Figure 7.2. A schematic illustration of atomic B and N diffusion pathways on surface, in the sublayer, and in the bulk region of a model Ni surface consisting of terrace and step sites. The solid yellow path, steps (1) – (4), represents for surface diffusions. The dashed green path, steps (5) – (7), represents the sublayer diffusion. The dashed red path, steps (8) – (9), represents the bulk diffusion. The grey spheres represent the Ni atoms. The orange sphere represents the diffusing atom.

The potential energy surfaces (PES) describing the atomic B and N diffusion energetics and kinetics are established in Figure 7.3(a) and (b), respectively, using the DFT-calculated energy barriers of the elementary steps (1-9) listed in Table 7.2**.** The overall energy barrier for B surface diffusion, referenced to the state at location A, occurring at step (4), is 1.99 eV. In comparison, the overall energy barrier of sublayer diffusion is 2.18 eV, occurring at the diffusion into sublayer,

i.e., step (5), is only 0.19 eV higher than the surface diffusion pathway and exergonic. Therefore, the sublayer diffusion pathway should be competitive to atomic B surface diffusion, and may be able to assist B migration. B diffusion in the bulk has the highest overall energy barrier of 2.42 eV (step (9)), and is the least competitive diffusion pathway.

The overall energy barrier for N diffusion on the surface is 1.38 eV, occurring at step (1), while the energy barriers for subsequent steps are rather modest. However, the overall barriers for sublayer and bulk diffusion pathways are 2.20 eV and 3.33 eV, corresponding to steps (5) and (9), respectively. Therefore, unlike B diffusion, the surface diffusion pathway is clearly much more competitive.

Table 7.2. DFT calculated energy barriers of atomic B and N diffusion corresponding to the elementary steps labeled in **Figure 7.2**.

Diffusion Step	N	B
	E_a[§]/eV	E_a[§]/eV
Step 1 (step edge → step edge)	1.38	1.03
Step 2 (step edge → terrace)	0.56	1.05
Step 3 (terrace → terrace)	0.56	0.22
Step 4 (terrace edge → step edge)	0.44	0.94
Step 5 (terrace → subsurface)	1.42	1.13
Step 6 (subsurface →subsurface)	1.00	0.34
Step 7 (subsurface →step edge)	0.18	0.36
Step 8 (subsurface → bulk)	1.76	1.74
Step 9 (bulk → bulk)	1.76	1.74

[§]Energy barriers (E_a) were calculated according to $E_a = E_{TS} - E_{IS}$, where the E_{TS} and E_{IS} represent the total energies of the transition state and the initial state, respectively.

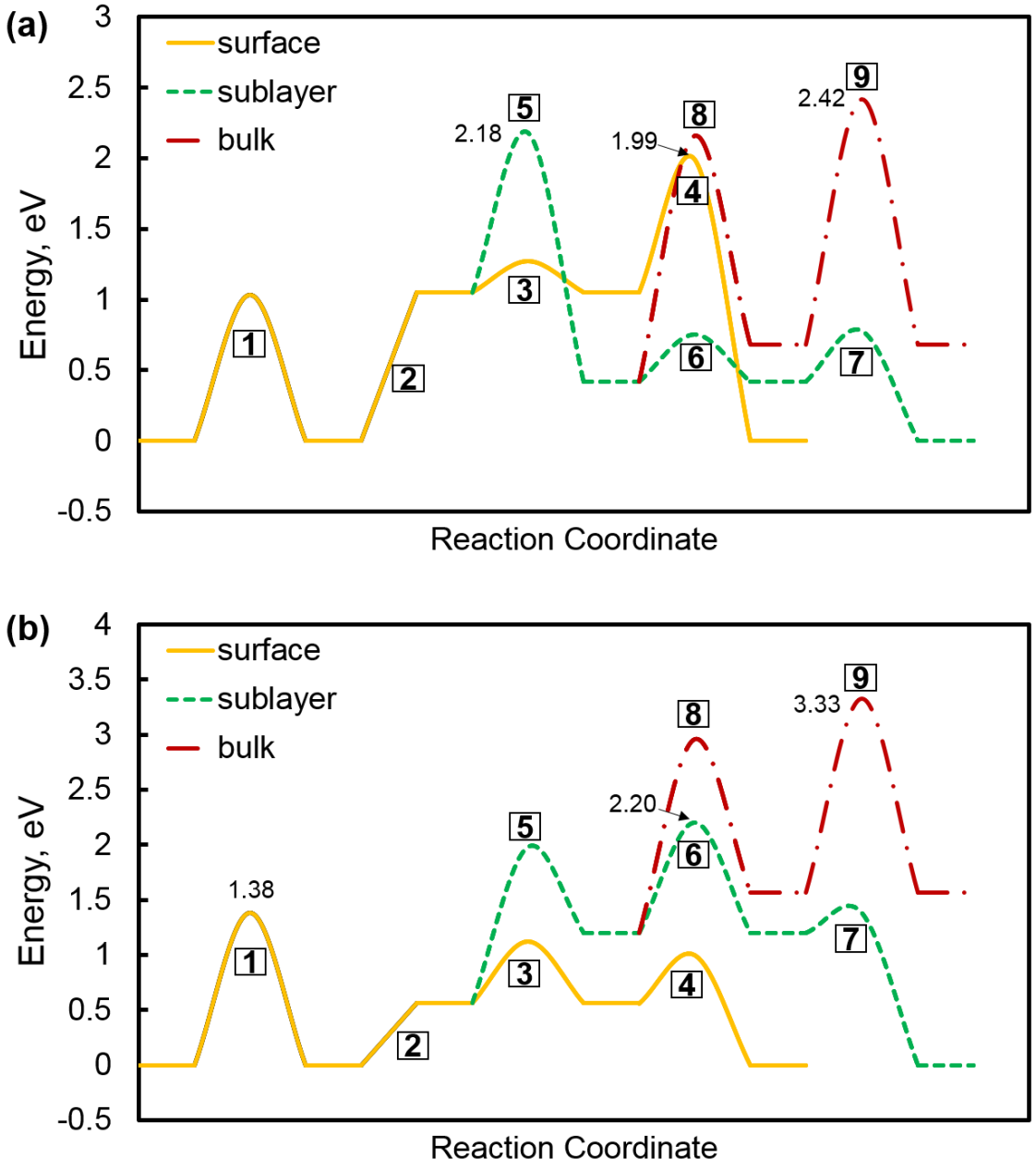

Figure 7.3. PES depicting the (a) B diffusion, and (b) N diffusion pathways illustrated in Figure 7.2. The overall diffusion energy barrier, relative to the zero potential energy reference, for each path is labeled numerically.

7.3.3 Force Field Development

ReaxFF for B–N pair interactions have been developed and applied to modeling BH_3-NH_3 decomposition, and single-walled BN nanotubes formation by Han, Weismiller, van Duin, and coworkers.[33-35] Furthermore, the ReaxFF force field for single crystal phase nickel also exists.[36-38] This work focuses on the establishment of the N–Ni, B–Ni pair potentials that will extend the capability of simulating the elementary chemical events in relation to the hBN growth process on a Ni substrate.

Periodic DFT calculations, based on Ni(111) surface, were converted into a ReaxFF training set, consisting of the adsorption structures of the B_xN_y building block species, binding energies, reaction energies of the above basic building block formations, atomic B/N diffusion barriers, and B–N bond formation energy barriers. The force field parameters were then optimized to reproduce the DFT data. The full ReaxFF training set and force field parameters are provided in Appendix A.

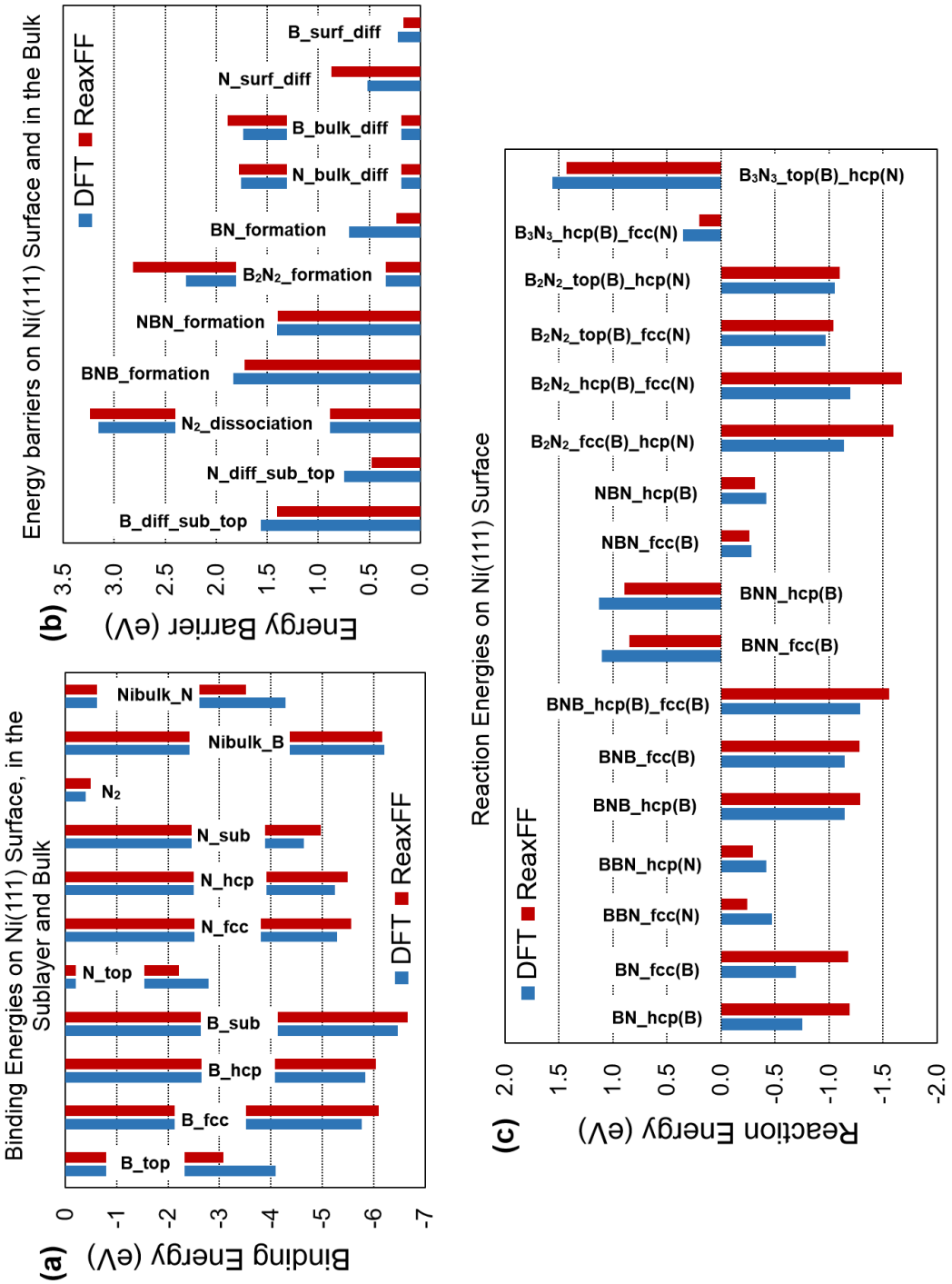

Figure 7.4. Comparisons between DFT (blue) and ReaxFF (red) for: (a) binding energies of atomic B and N adsorptions; (b) energy barriers of B/N diffusions and B–N bond formations; and (c) reaction energies.

In Figure 7.4(a), the binding energies of B_xN_y (x, y = 0, 1, 2, 3) on Ni(111), in the sublayer and bulk obtained from DFT calculations and ReaxFF predictions are shown. The training puts particular emphasis on the data located at the global energy minima, such as B at the sublayer octahedral site (B_sub), and N at the fcc site (N_fcc) on Ni(111). In Figure 7.4(b), the DFT-calculated elementary step energy barriers, describing diffusion and bond formation on Ni(111) surface and in Ni bulk for building block species are considered. The reaction energies correspond to the formation of building block species ($\Delta E_{B_xN_y}$), are computed using Equation (18),

$$\Delta E_{B_xN_y} = E_{B_xN_y^*} + E_* - E_A - E_B \quad (18)$$

where E_A and E_B refer to the total energies of reactants A and B at their most stable configurations on Ni(111), respectively. In this training, the reaction energetics of the hBN growth elementary steps was considered as well, as shown in Figure 7.4(c).

7.3.4 hBN Nucleation and Growth on Ni(111) Surface.

Figure 7.5 shows the evolution of the hBN growth process on a Ni(111) surface from the ReaxFF based rMD simulation performed at 1300 K, which is comparable to experimental CVD conditions, under which high quality hBN crystal formation has been reported.[39-41]

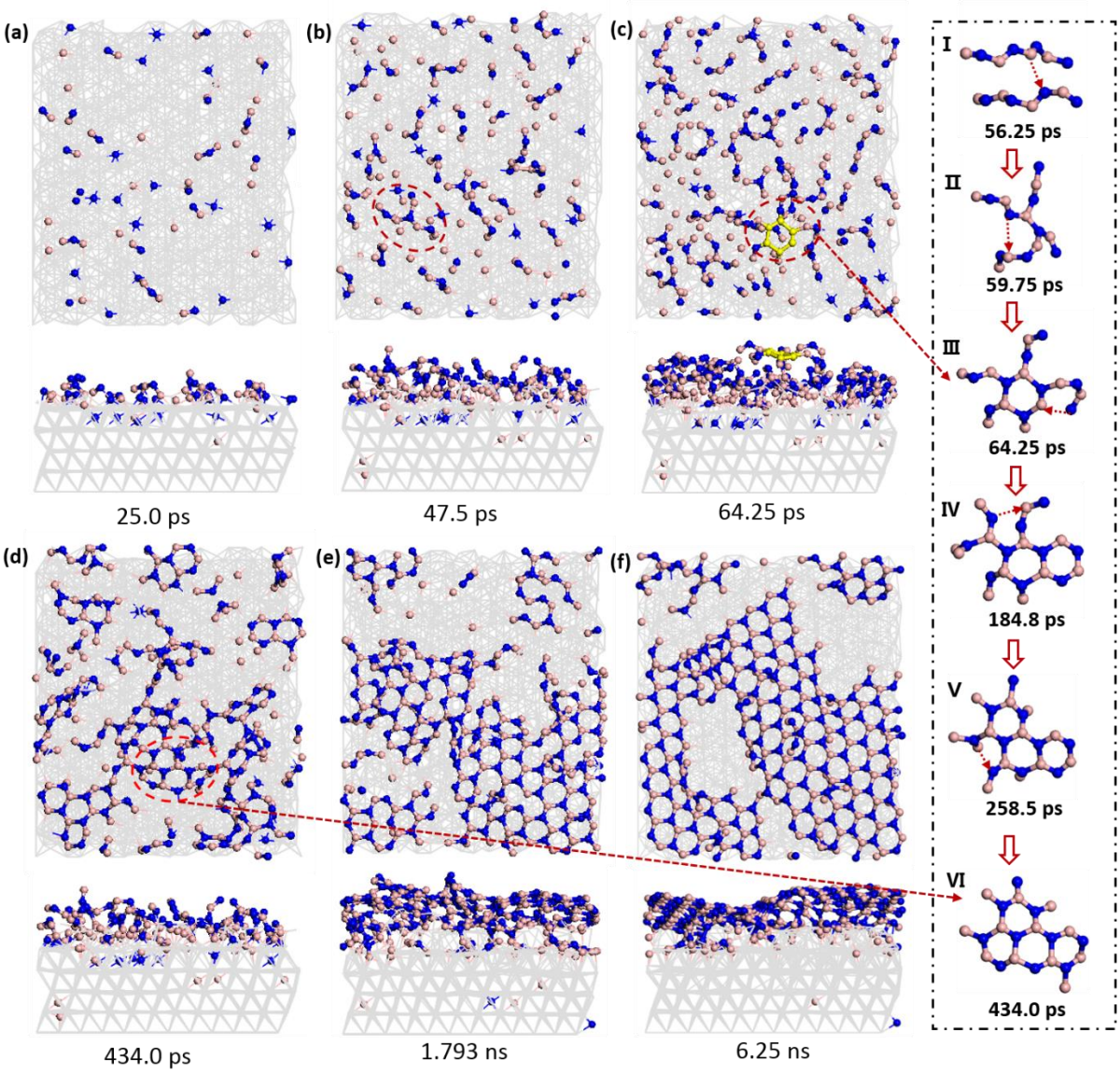

Figure 7.5. Snapshot images (both top and side views) taken from the trajectories of rMD simulations at 1300 K at various timeframes: (a) t=25.0 ps, (b) 47.5 ps, (c) 64.25 ps, (d) 434.0 ps, (e) 1.793 ns, and (f) 6.25 ns. The blue and pink spheres represent N, B atoms, respectively. The atoms in the Ni substrate are represented in grey for clarity. The yellow spheres in (c) illustrate the first hexagonal ring formed in this particular MD run. Both the top and side views are shown, and the B and N atoms in the interior of the Ni substrate can also be seen. The inset figures (I - VI) highlight the process of the first hexagon formation and subsequent hBN nucleation.

Initially, the randomly deposited B and N atoms on the nickel substrate started to form BN dimers, trimers (*e.g.*, BNB, NBN), and short chains (*e.g.*, BNBN), which are illustrated in Figure 7.5(a), at the timeframe of 25 ps. With the increase of the deposited B and N atoms, long linear and branched BN chains up to 10 atoms (highlighted in the red dash circle in Figure 7.5(b)) have formed, and the central atoms (B or N) of each 'Y'-shaped junction resemble an sp^2–type hybridization. In this simulation, the first hexagon ring appears at 64.25 ps (highlighted in yellow in the red dashed circle in Figure 7.5(c)), which serves as the initial nucleus, and then grows into a larger hBN island consisting of four connecting hexagons at 434.1 ps (highlighted in red dashed circle in Figure 7.5(d)).

A closer examination of the structural evolution in relation to initial hBN nucleation is shown by the isolated structures I – VI in the Figure 7.5 inset: a ramose 'X-type' BN species in II is first formed through the coalescence of two linear BN chains formed and illustrated in I. Following structure II, a hexagon is formed (III), as a result of the folding of the two branches. This hBN hexagon, with alternating B and N atoms, has multiple dangling branches, which indeed facilitate the formation of the next hexagon by simply bending the longer branch. Subsequently, the third and fourth hexagons coalesce through a similar process, *i.e.* folding of two branches, as illustrated in IV and V. Hence, multiple fused hexagons clusters, consisting of 2-4 rings, are formed and observed in Figure 7.5(d).

Simulations performed up to 1.793 ns, as depicted in Figure 7.5(e), showed that a continuous, atomically thin hBN network is established on the Ni surface. At 6.25 ns, the surface is covered by a continuous hBN sheet, dominated with BN hexagons (see Figure 7.5(f)).

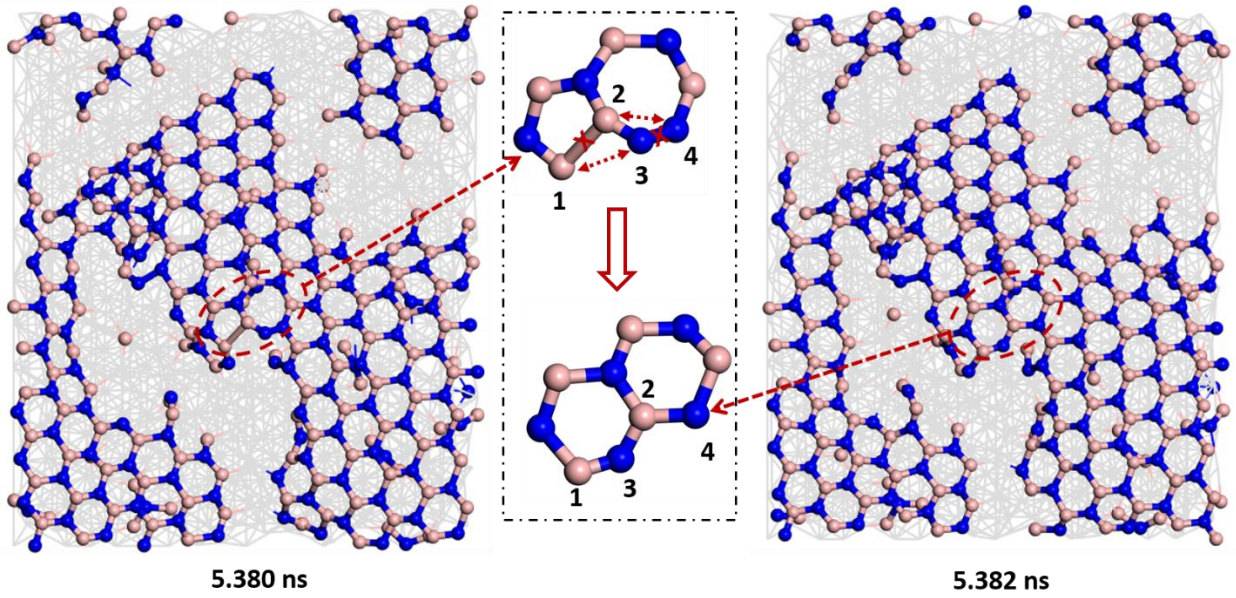

Figure 7.6. The transformation of pentagon-heptagon (5|7) dislocation structure into joint hexagons at the respective 5.38 ns and the 5.382 ns timeframes during the rMD simulation at 1300 K. The local atoms involved are further highlighted with dashed circles, and the participating atoms in the rearrangements of the structures are labeled in the inset dashed box in the middle, where the B–B, and the N–N bond (in the 1-2 and 3-4 atom pairs) that are broken are marked with red crosses, and the B–N bonds (between the 1-3, and 2-4 atom pairs) formed are indicated with dashed double-headed arrows. The B and N atoms are represented by pink and blue spheres, while atoms in the Ni substrates are in grey.

The pentagon-heptagon (5|7) dislocation structure, consisting of adjacent 5-membered and 7-memebered rings, as shown in Figure 7.6, have also been noticed in the simulation, in this case at 5.38 ns at 1300K. This (5|7) dislocation, containing homoelemental B–B or N-N bonds, has been predicated theoretically as a main type of grain boundary in hBN crystals,[35,42] and also experimentally observed by Gibb et. al,[25] and Wang et. al.[13,43] As displayed in the dashed box with the participating atoms numerically labeled, this (5|7) structure, consisting of a homoelemental B-

B bond (between the 1-2 atom pair) and an N-N bond (between the 3-4 atom pair), is located at the edge of a larger hBN fragment, highlighted by the dashed circles in Figure 7.6. It is possible that this (5|7) dislocation occurs at the hBN growth frontier. The analysis of the rMD trajectory revealed that the (5|7) dislocation structure is able to evolve into two joint hexagons after 2 ps. In the illustrated snapshot, a close examination of the transformation showed that the B–B bond distance is 2.208 Å, elongated from the typical B –B bond length of 1.924 Å.[44] At 5.382 ns, atom 3 moves closer to atom 1 forming the energetically more favorable heteroelemental B–N bond, while also breaking the N-N bond (3-4 atom pair and 1-2 atom pair). At this time, another B–N bond is formed between atoms 2 and 4, resulting in two adjacent hexagonal geometries with alternating B-N bonds.

7.3.5 Diffusion and Distribution of Sublayer B and N Atoms

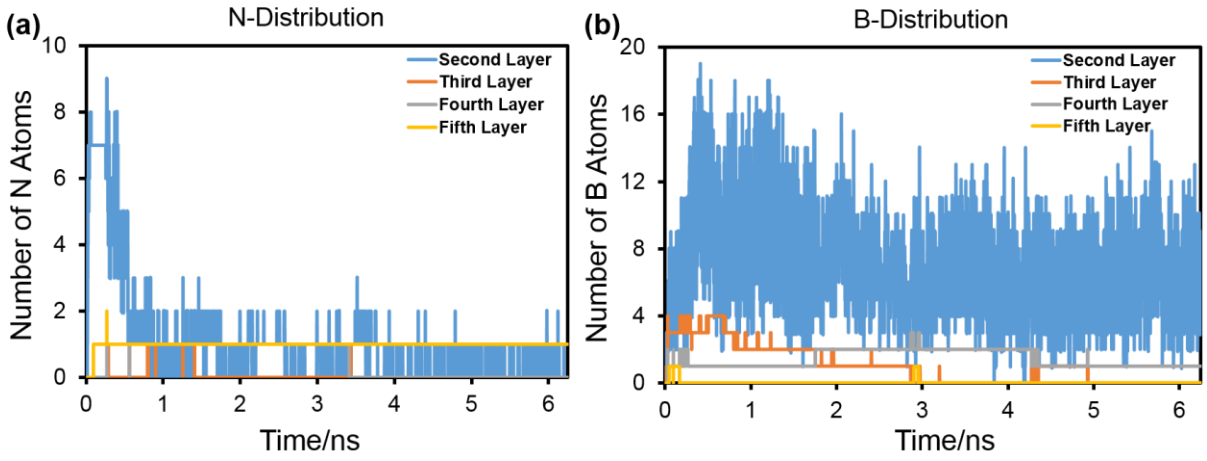

Figure 7.7. The distributions of (a) N and (b) B atoms in Ni sublayers as the function of the simulation time (in ns) at 1300K. The blue, orange, grey, and yellow colors represent the 2nd, 3rd, 4th, and 5th substrate layer, respectively.

The analyses of the atomic B and N distributions in the sublayers (2nd – 5th layers) of the Ni substrate have been performed and the elemental distributions, as a function of simulation time (in ns), are shown in Figure 7.7(a-b), respectively. At the beginning of the simulation (*i.e.*, within the first 50 ps), equal numbers of B and N atoms are deposited, and the second layer B and N atoms experience a sharp increase (shown in blue in Figure 7.7(a-b)), as a result of the momenta of impinging atoms. After the deposition, the second layer N atoms quickly diffuse onto the surface. The number of second layer N fluctuates around one in the entire sub-surface after 1 ns, and remains so for the rest the simulation (Figure 7.7(a)). This is supported by our DFT calculations that show atomic N at the sublayer octahedral site is metastable by 0.64 eV, and would rather the 3-fold fcc site on the Ni(111) surface. In contrast, the total number of B atoms in the second layer continues to rise even after the deposition until 0.5 ns (Figure 7.7(b)), further

contributed by B diffusion from surface to the sublayer. Then, the number of B atoms fluctuates and stabilizes at around 8 for the rest of the simulation. The behavior of sublayer B species can also be explained by the DFT calculations, where the B atom prefers the sublayer octahedral site, and is 0.63 eV more stable than the surface hcp site. The B and N atoms in the third-to-fifth layers are much more scarce, reflecting less penetration during the deposition and also the much higher energy barriers of bulk diffusion. The number of N atoms in these sublayers remains almost unchanged, while the number of B atoms slightly decreases throughout the course of the simulation at 1300K. The higher B concentration in the substrate sublayer region obtained from rMD can also be supported by a number of experimental measurements performed by Kowanda and Kubota *et al*., which have shown that B has a much higher solubility in Ni than N.[45,46]

7.3.6 hBN Growth at Different Temperatures

Simulations were also performed at 900 K, 1100 K, and 1500 K while the number of deposited B and N, and other simulation setup remained the same. The snapshot images, taken from the final timeframe of each simulation (*i.e.* 6.25 ns) as shown in Figure 7.8, illustrate the variations of the growth states at different temperatures. At 900 K (Figure 7.8(a)), most B and N species exist in small hBN islands consisting of fused hexagons, along with a number of pentagons, heptagons, and octagons. In addition, open structures with branches are also abundant. At 1100 K, hBN domains with larger size, such as the upper right corner of Figure 7.8(b), have formed. At 1300K and 1500 K (Figure 7.8(c-d)), structures with continuous hBN lattice, throughout the substrate surfaces, are well established.

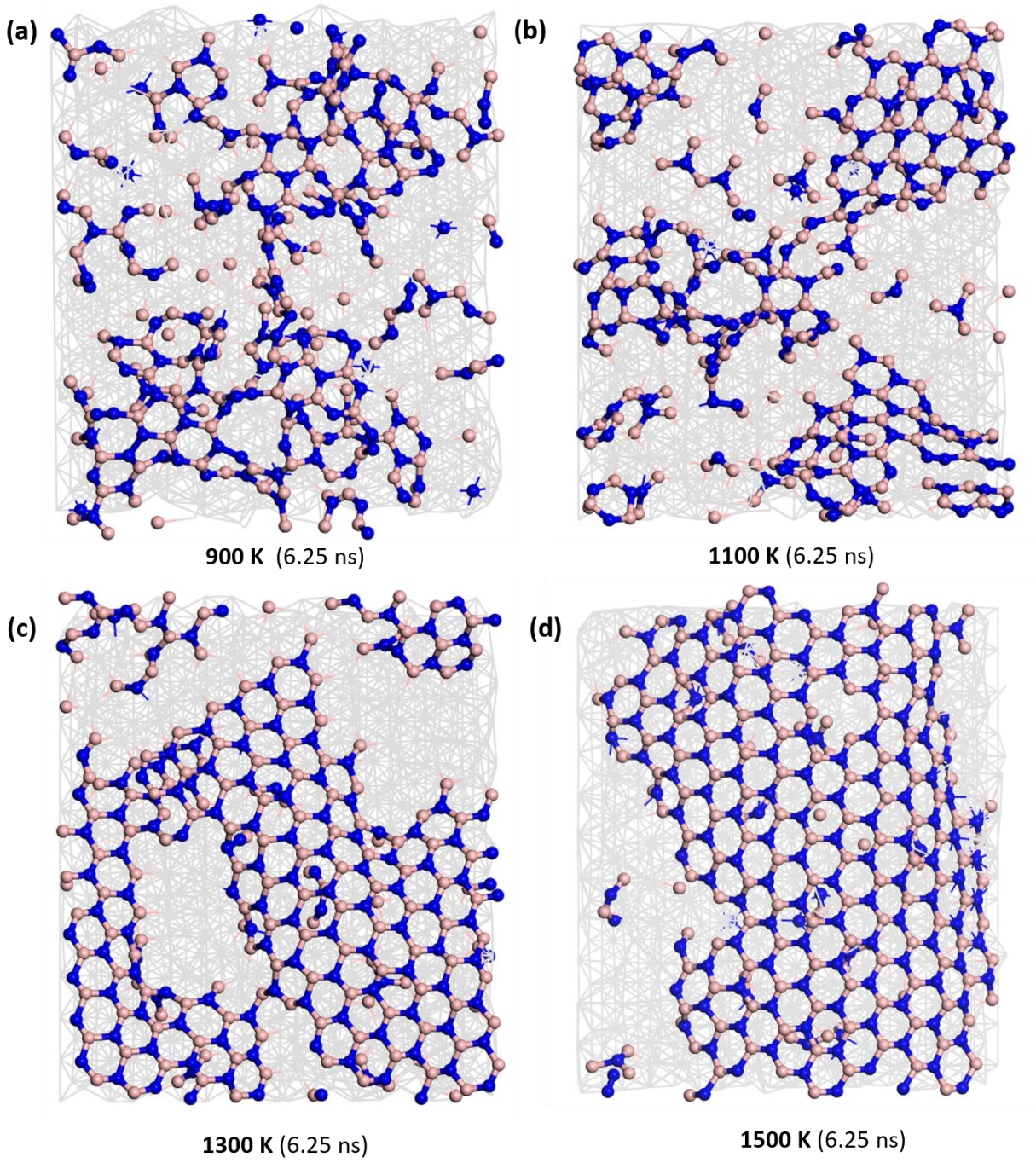

Figure 7.8. Snapshots taken from the trajectories of the rMD simulations at 6.25 ns depicting hBN formations (200 boron and 200 nitrogen) on Ni substrates at temperatures of (a) 900 K, (b) 1100 K, (c) 1300 K, and (d) 1500 K, respectively. The B and N atoms are represented by pink and blue spheres, while atoms in the Ni substrates are in grey.

Furthermore, the numbers of hexagons throughout the simulation (up to 6.25 ns) were collected for each temperature and compared in Figure 7.9. As expected, the numbers in each case increase monotonically with both the simulation temperature and time. At 900 K, the number of hexagons reached 20 at 2 ns (*i.e.*, 10 hexagons/ns based on a simple linear approximation), and then nearly plateaued. At 1100 K, the number of hexagons continues to increase up to 40 (grey) and stabilizes at approximately 3 ns (*i.e.*, 13.3 hexagons/ns). Overall, the number of hexagons has nearly doubled compared to that at 900K within the same timeframe. At 1300 K and 1500 K, there are approximately 100 (Figure 7.9, orange) and 110 (Figure 7.9, purple) hexagons, where the theoretical maximum based on the stoichiometric B and N deposited in the simulation (200 each) is 200. In addition, the two distinct growth regimes, *i.e.*, (1) a rapid initial growth before respective 1.8 ns (*i.e.*, 41 hexagons/ns) and 1.5 ns (*i.e.*, 53 hexagons/ns); and (2) slow growth afterwards, at an approximate rate of 5.8 hexagons/ns and 6.3 hexagons/ns, become more distinct compared to the profiles obtained at 900K and 1100K.

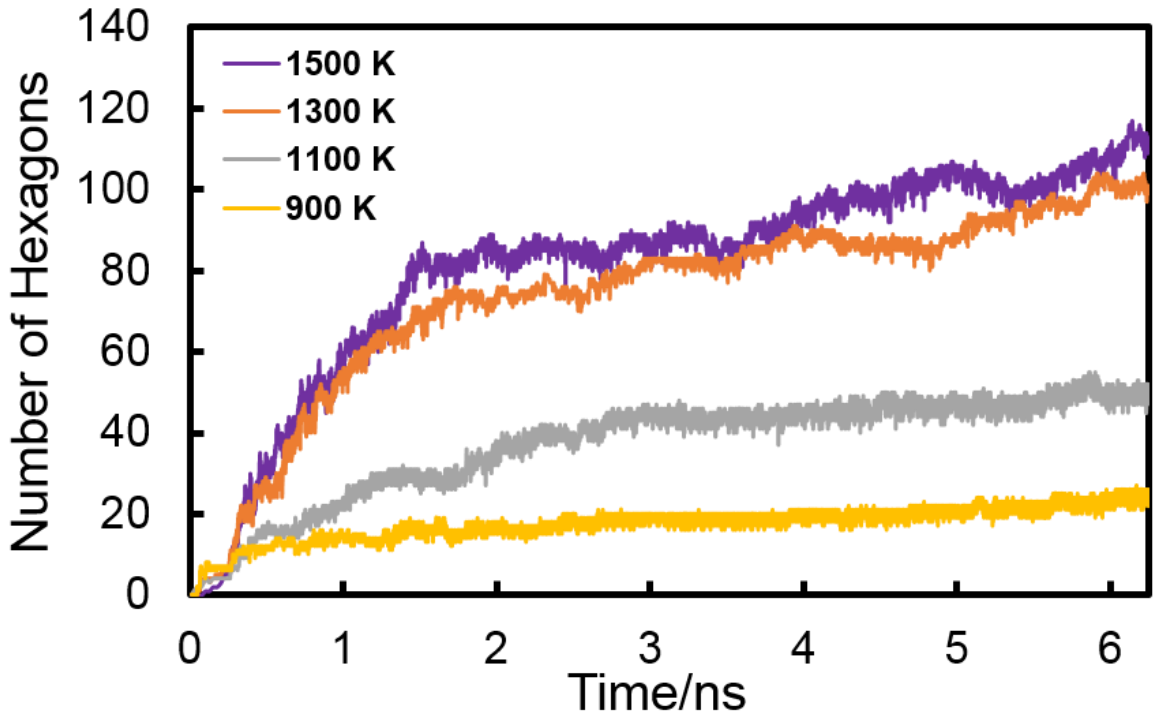

Figure 7.9. Number of hexagons as function of the simulation time (in ns) for temperatures of 900 K (yellow), 1100 K (grey), 1300 K (orange), and 1500 K (purple), respectively

7.3.7 Confirmation of Nucleation and Growth Mechanism with DFT

To further validate the simulated nucleation and formation of hexagonal BN structure on Ni substrate, periodic DFT calculations are performed to confirm the linear-branch-ring mode from the reaction energetic perspective. These molecular models constructed for the DFT calculations are inspired by the motifs from previous rMD simulations, and will prove to be an effective strategy to obtain insights by integrating with first-principles calculations in future studies.

For quantitative analysis, a stoichiometric B-N pair was used to represent the growth unit (*i.e.*, with an increment of BN per step). The adsorption energies (AE) are calculated according to Equation (19):

$$AE = (E_{B_xN_y^*} + E_{Ni} - x * E_{BN})/x \quad (19)$$

where $E_{B_xN_y^*}$ and E_{Ni} are the respective total energies of the adsorbed $(BN)_x$ species and the clean Ni surface. E_{BN} is the total energy of the BN dimer in gas phase, and x denotes the stoichiometry.

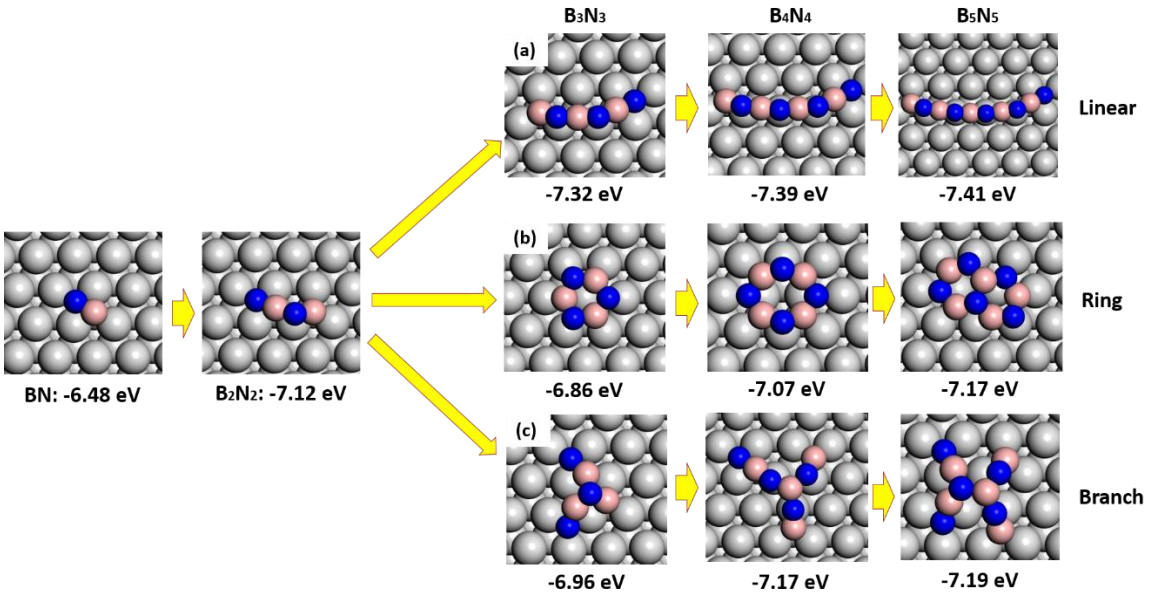

Figure 7.10. Optimized geometries and corresponding adsorption energies (AEs, shown underneath each configuration), (a) linear, (b) ring, and (c) branched configurations from BN to B_5N_5, on Ni(111). The B, N, and Ni atoms are represented in pink, blue, and grey sphere, respectively.

The nucleation process of hBN is considered to start from the most stable BN dimer on the Ni(111) surface, as shown on the leftmost side of Figure 7.10. A B_2N_2 molecular chain is formed with the addition of a second B-N pair. In the following steps, three types of geometries – linear, ring, and branched configurations (Figure 7.10 (a-c)) – were considered; only the structures with

the lowest AE in each type are shown in the figure. The linear $(BN)_x$ (x = 3-5) structures bind with their terminal B and N ends, with the atoms in the middle section buckled and detached from the substrate. The B and N terminals prefer the hcp and fcc sites, respectively, consistent with the trend noted from DFT calculations performed on the building block species. Meanwhile, the corresponding AEs become more energetically favorable as the chain length grows.

For the smallest isolated ring, $(BN)_3$, the constituent N and B atoms bind close to the bridge sites. As the size and number of rings grow, N atom binds at either bridge or the near-top site, and some B atoms bind at the 3-fold site, as illustrated in $(BN)_4$ and $(BN)_5$ in Figure 7.10(b). Also, the structure becomes more energetically stable as the ring grows. For $(BN)_5$, the joint hexagonal structure is energetically favored than the single ten-membered ring, and is approximately 0.3 eV more stable than $(BN)_3$ per B-N pair. Nevertheless, the calculated AEs suggest that the overall ring configurations are approximately 0.3 - 0.5 eV metastable than their linear counterparts.

For the branched structures, the additional B-N pairs were added to the middle B_2N_2 or $(BN)_3$. As shown in Figure 7.10(c), the branched configurations also tend to bind with their terminal B and N atom species at their preferred 3-fold sites. Like the linear structure, there is no direct contact between the atoms in the middle section of the structure with the Ni substrate. The AE also decreases as $(BN)_x$ grows. For x = 3 - 5, the branched configurations are not as energetically favorable as the linear configurations with the same number of BN unit, but slightly more favorable than the ring configurations.

The above analysis indicates that, for BN unit numbers, the linear structures dominate the initial nucleation stage of hBN growth, consistent with the structures observed from the rMD simulations. Similarly, such behavior has been predicted for early-stage graphene formation from

its elemental constituent carbon species by Li *et al*,[47] who claim that the branches formed from the linear carbon chains.

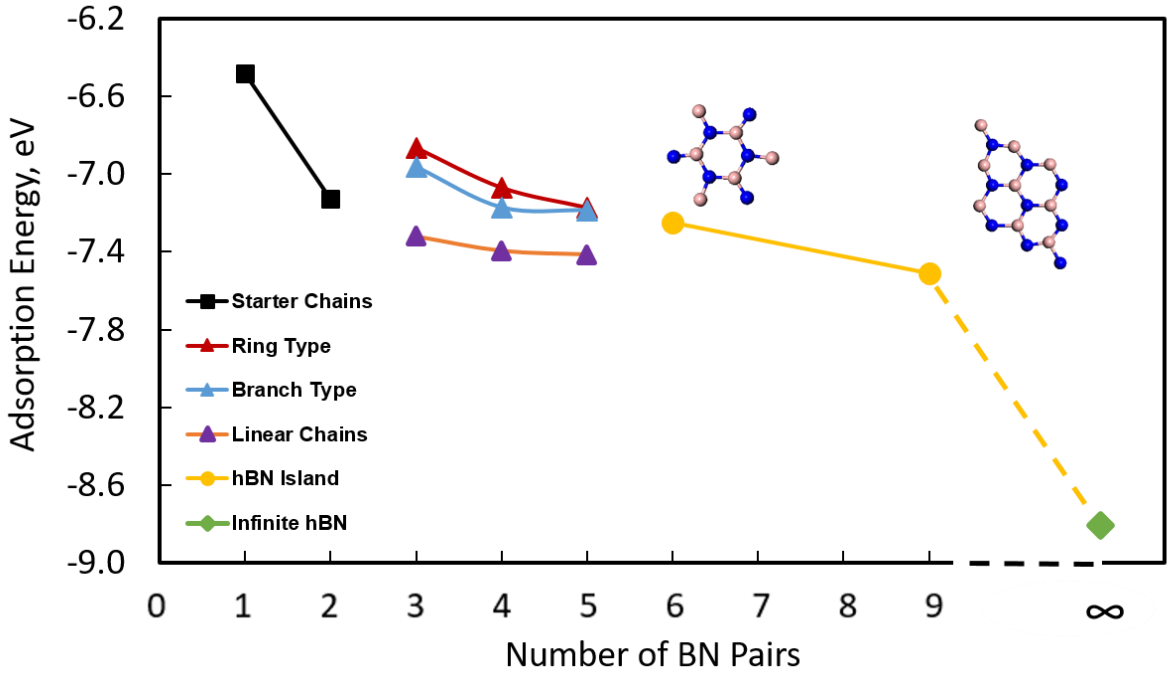

Figure 7.11. The energy profile showing the variations of adsorption energies (AEs) as a function of the number of BN pairs in the BN units considered. The B and N atoms are in pink and blue, respectively.

Given the energetic preference to linear BN chains at the initial nucleation stage, two possible ways are proposed to form hexagonal rings: (1) the formation of a branch type structure through the combination of linear chains, which then folds; and (2) the bending of a single linear chain. As shown in Figure 7.11, the AEs of branch type BN species (x = 3 - 5) are closer to the linear chains comparing with the ring type, thus it is likely that the next step following the formation of linear chians is to form branched structures. This is consistent with the observed hBN

nucleation process noted in rMD simulations. Once the branched BN speices are formed, the formation of the first hexagon (x= 6) becomes energetically favored. As x becomes sufficiently large, *i.e.*, x = 9, the AE of the structure with joint hexagonal rings is becoming more and more favorable. The lower AE limit (*i.e.*, -8.81 eV/ B-N pair), in Figure 7.11, corresponds to the periodic hBN on Ni(111) surface, and reveals that the overall energetics will eventually drive the process to form the hBN monolayer. Compared to graphene growth, the heteratomic structure of hBN has definitely introduced additional chemical complexity in the nucleation and growth mechanism. In this study, the trend predicted by deterministic rMD simulations has shown rather satisfactory agreement with detailed DFT analysis, and provided clear evidence that the linear-branch-ring pathway can indeed be used to describe hBN formation from elemental B and N.

7.4 Conclusions

In order to elucidate the mechanism of hBN growth on Ni, DFT calculations were first performed to obtain the energetics and kinetics of BN species on Ni(111) and Ni(211) surfaces. We showed that B atoms prefer the sublayer octahedral site, while N atoms prefer the 3-fold fcc surface sites. In addition, the adsorbed B_xN_y (x = 0 - 2; y = 0 - 2) species bind more strongly to the low-coordinated Ni in the Ni(211) step edge. DFT calculations have also indicated that surface diffusions are still kinetically favored for both B and N atoms. However, sublayer diffusion can also be competitive for B atoms.

These DFT calculations data were subsequently used to construct a quantum mechanical training set for Ni-B and Ni-N pair potentials. Furthermore, rMD simulations of B/ N deposition on Ni(111) were performed at temperatures ranging from 900 K to 1500 K. Detailed examination of rMD trajectories showed that linear and branched BN species are formed first on the Ni surface.

Subsequently, the first BN hexagon is formed as the branches fold, acting as the nucleus for further hBN growth. The restructuring of (5|7) dislocation can take place at 1300K through N-N and B-B bond breaking, accompanied by B-N bond formations. The atomic B and N distribution analysis is consistent with DFT calculations, indicating that B is more abundant in the interior of Ni substrate than N. By comparing the number of hexagons at different temperatures, our simulations have demonstrated the formation of continuous, atomically thin hBN on Ni substrate can be favored higher temperature (*e.g.*, 1300K, and 1500K) within the simulation timeframe considered in this study. Additional DFT calculations have been performed to validate the nucleation process observed during the rMD simulation, with outcome supporting the mechanism derived from the newly developed ReaxFF potential.

7.5 Acknowledgements

Supports from the Materials Engineering and Processing program of the National Science Foundation, Award number 1538127, and the II-VI Foundation are greatly appreciated. DFT and rMD calculations were carried out thanks to the supercomputing resources and services from the Center for Nanoscale Materials (CNM) supported by the Office of Science of the US Department of Energy under the contract No. DE-AC02-06CH11357; the Beocat Research Cluster at Kansas State University, which is funded in part by NSF grants CNS-1006860; and the National Energy Research Scientific Computing Center (NERSC) under the contract No. DE-AC0205CH11231.

References

1. Lu, G.; Wu, T.; Yuan, Q.; Wang, H.; Wang, H.; Ding, F.; Xie, X.; Jiang, M. Synthesis of large single-crystal hexagonal boron nitride grains on Cu–Ni alloy. *Nature Communications* **2015**, *6*.

2. Kobayashi, Y.; Nakamura, T.; Akasaka, T.; Makimoto, T.; Matsumoto, N. Hexagonal boron nitride on Ni (111) substrate grown by flow-rate modulation epitaxy. *J. Cryst. Growth* **2007**, *298*, 325-327.

3. Chatterjee, S.; Luo, Z.; Acerce, M.; Yates, D. M.; Johnson, A. C.; Sneddon, L. G. Chemical vapor deposition of boron nitride nanosheets on metallic substrates via decaborane/ammonia reactions. *Chemistry of Materials* **2011**, *23*, 4414-4416.

4. Auwärter, W.; Suter, H. U.; Sachdev, H.; Greber, T. Synthesis of one monolayer of hexagonal boron nitride on Ni (111) from B-Trichloroborazine $(ClBNH)_3$. *Chemistry of Materials* **2004**, *16*, 343-345.

5. Ismach, A.; Chou, H.; Ferrer, D. A.; Wu, Y.; McDonnell, S.; Floresca, H. C.; Covacevich, A.; Pope, C.; Piner, R.; Kim, M. J. Toward the controlled synthesis of hexagonal boron nitride films. *ACS Nano* **2012**, *6*, 6378-6385.

6. Lee, Y.; Liu, K.; Lu, A.; Wu, C.; Lin, C.; Zhang, W.; Su, C.; Hsu, C.; Lin, T.; Wei, K. Growth selectivity of hexagonal-boron nitride layers on Ni with various crystal orientations. *RSC Advances* **2011**, *2*, 111-115.

7. Kim, K. K.; Hsu, A.; Jia, X.; Kim, S. M.; Shi, Y.; Hofmann, M.; Nezich, D.; Rodriguez-Nieva, J. F.; Dresselhaus, M.; Palacios, T. Synthesis of monolayer hexagonal boron nitride on Cu foil using chemical vapor deposition. *Nano Letters* **2011**, *12*, 161-166.

8. Song, L.; Ci, L.; Lu, H.; Sorokin, P. B.; Jin, C.; Ni, J.; Kvashnin, A. G.; Kvashnin, D. G.; Lou, J.; Yakobson, B. I. Large scale growth and characterization of atomic hexagonal boron nitride layers. *Nano Letters* **2010**, *10*, 3209-3215.

9. Gibb, A.; Alem, N.; Zettl, A. Low pressure chemical vapor deposition synthesis of hexagonal boron nitride on polycrystalline metal foils. *Phys. Status Solidi B* **2013**, *250*, 2727-2731.

10. Guo, N.; Wei, J.; Fan, L.; Jia, Y.; Liang, D.; Zhu, H.; Wang, K.; Wu, D. Controllable growth of triangular hexagonal boron nitride domains on copper foils by an improved low-pressure chemical vapor deposition method. *Nanotechnology* **2012**, *23*, 415605.

11. Nagashima, A.; Tejima, N.; Gamou, Y.; Kawai, T.; Oshima, C. Electronic structure of monolayer hexagonal boron nitride physisorbed on metal surfaces. *Phys. Rev. Lett.* **1995**, *75*, 3918.

12. Kim, G.; Jang, A.; Jeong, H. Y.; Lee, Z.; Kang, D. J.; Shin, H. S. Growth of high-crystalline, single-layer hexagonal boron nitride on recyclable platinum foil. *Nano Letters* **2013**, *13*, 1834-1839.

13. Gibb, A. L.; Alem, N.; Chen, J.; Erickson, K. J.; Ciston, J.; Gautam, A.; Linck, M.; Zettl, A. Atomic resolution imaging of grain boundary defects in monolayer chemical vapor deposition-grown hexagonal boron nitride. *J. Am. Chem. Soc.* **2013**, *135*, 6758-6761.

14. Grad, G.; Blaha, P.; Schwarz, K.; Auwärter, W.; Greber, T. Density functional theory investigation of the geometric and spintronic structure of h-BN/Ni (111) in view of photoemission and STM experiments. *Physical Review B* **2003**, *68*, 085404.

15. Díaz, J. G.; Ding, Y.; Koitz, R.; Seitsonen, A. P.; Iannuzzi, M.; Hutter, J. Hexagonal boron nitride on transition metal surfaces. *Theoretical Chemistry Accounts* **2013**, *132*, 1-17.

16. Liu, Y.; Bhowmick, S.; Yakobson, B. I. BN white graphene with “colorful” edges: The energies and morphology. *Nano Letters* **2011**, *11*, 3113-3116.
17. Zhang, Z.; Liu, Y.; Yang, Y.; Yakobson, B. I. Growth Mechanism and Morphology of Hexagonal Boron Nitride. *Nano Letters* **2016**.
18. Van Duin, A. C.; Dasgupta, S.; Lorant, F.; Goddard, W. A. ReaxFF: a reactive force field for hydrocarbons. *The Journal of Physical Chemistry A* **2001**, *105*, 9396-9409.
19. Kresse, G.; Furthmüller, J. Software VASP, vienna (1999). *Phys.Rev.B* **1996**, *54*, 169.
20. Blöchl, P. E. Projector augmented-wave method. *Physical Review B* **1994**, *50*, 17953.
21. Ernzerhof, M.; Scuseria, G. E. Assessment of the Perdew–Burke–Ernzerhof exchange-correlation functional. *J. Chem. Phys.* **1999**, *110*, 5029-5036.
22. Monkhorst, H. J.; Pack, J. D. Special points for Brillouin-zone integrations. *Physical Review B* **1976**, *13*, 5188.
23. Methfessel, M.; Paxton, A. High-precision sampling for Brillouin-zone integration in metals. *Physical Review B* **1989**, *40*, 3616.
24. Bhatia, B.; Sholl, D. S. Chemisorption and diffusion of hydrogen on surface and subsurface sites of flat and stepped nickel surfaces. *J. Chem. Phys.* **2005**, *122*, 204707.
25. Henkelman, G.; Uberuaga, B. P.; Jónsson, H. A climbing image nudged elastic band method for finding saddle points and minimum energy paths. *J. Chem. Phys.* **2000**, *113*, 9901-9904.
26. Henkelman, G.; Jónsson, H. A dimer method for finding saddle points on high dimensional potential surfaces using only first derivatives. *J. Chem. Phys.* **1999**, *111*, 7010-7022.
27. Plimpton, S.; Crozier, P.; Thompson, A. LAMMPS-large-scale atomic/molecular massively parallel simulator. *Sandia National Laboratories* **2007**, *18*.
28. Evans, D. J.; Holian, B. L. The nose–hoover thermostat. *J. Chem. Phys.* **1985**, *83*, 4069-4074.

29. Swope, W. C.; Andersen, H. C.; Berens, P. H.; Wilson, K. R. A computer simulation method for the calculation of equilibrium constants for the formation of physical clusters of molecules: Application to small water clusters. *J. Chem. Phys.* **1982**, *76*, 637-649.

30. Auwärter, W.; Kreutz, T.; Greber, T.; Osterwalder, J. XPD and STM investigation of hexagonal boron nitride on Ni (111). *Surf. Sci.* **1999**, *429*, 229-236.

31. Auwärter, W.; Muntwiler, M.; Osterwalder, J.; Greber, T. Defect lines and two-domain structure of hexagonal boron nitride films on Ni (111). *Surf. Sci.* **2003**, *545*, L735-L740.

32. Venables, J.; Spiller, G.; Hanbucken, M. Nucleation and growth of thin films. *Reports on Progress in Physics* **1984**, *47*, 399.

33. Weismiller, M. R.; Duin, A. C. v.; Lee, J.; Yetter, R. A. ReaxFF reactive force field development and applications for molecular dynamics simulations of ammonia borane dehydrogenation and combustion. *The Journal of Physical Chemistry A* **2010**, *114*, 5485-5492.

34. Han, S. S.; Kang, J. K.; Lee, H. M.; van Duin, A. C.; Goddard, W. A. The theoretical study on interaction of hydrogen with single-walled boron nitride nanotubes. I. The reactive force field $ReaxFF_{HBN}$ development. *J. Chem. Phys.* **2005**, 123, 114703

35. Han, S. S.; Kang, J. K.; Lee, H. M.; van Duin, A. C.; Goddard III, W. A. Theoretical study on interaction of hydrogen with single-walled boron nitride nanotubes. II. Collision, storage, and adsorption. *J. Chem. Phys.* **2005**, *123*, 114704.

36. Mueller, J. E.; van Duin, A. C.; Goddard III, W. A. Development and validation of ReaxFF reactive force field for hydrocarbon chemistry catalyzed by nickel. *The Journal of Physical Chemistry C* **2010**, *114*, 4939-4949.

37. Liu, B.; Lusk, M. T.; Ely, J. F. Reactive molecular dynamic simulations of hydrocarbon dissociations on Ni (111) surfaces. *Surf. Sci.* **2012**, *606*, 615-623.

38. Liu, B.; Lusk, M.; Ely, J. Hydrogen dissociations on small nickel clusters. *Molecular Simulation* **2009**, *35*, 928-935.

39. Shi, Y.; Hamsen, C.; Jia, X.; Kim, K. K.; Reina, A.; Hofmann, M.; Hsu, A. L.; Zhang, K.; Li, H.; Juang, Z. Synthesis of few-layer hexagonal boron nitride thin film by chemical vapor deposition. *Nano Letters* **2010**, *10*, 4134-4139.

40. Tsuda, O.; Watanabe, K.; Taniguchi, T. Band-edge luminescence at room temperature of boron nitride synthesized by thermal chemical vapor phase deposition. *Japanese journal of applied physics* **2007**, *46*, L287.

41. Huang, J.; Pan, C.; Lii, D. Investigation of the BN films prepared by low pressure chemical vapor deposition. *Surface and Coatings Technology* **1999**, *122*, 166-175.

42. Liu, Y.; Zou, X.; Yakobson, B. I. Dislocations and grain boundaries in two-dimensional boron nitride. *ACS Nano* **2012**, *6*, 7053-7058.

43. Wang, J.; Li, S.; Liu, J. Migrations of Pentagon–Heptagon Defects in Hexagonal Boron Nitride Monolayer: The First-Principles Study. *The Journal of Physical Chemistry A* **2015**, *119*, 3621-3627.

44. Shoji, Y.; Matsuo, T.; Hashizume, D.; Gutmann, M. J.; Fueno, H.; Tanaka, K.; Tamao, K. Boron–Boron σ-Bond Formation by Two-Electron Reduction of a H-Bridged Dimer of Monoborane. *J. Am. Chem. Soc.* **2011**, *133*, 11058-11061.

45. Kowanda, C.; Speidel, M. Solubility of nitrogen in liquid nickel and binary Ni–X i alloys (X i= Cr, Mo, W, Mn, Fe, Co) under elevated pressure. *Scr. Mater.* **2003**, *48*, 1073-1078.

46. Kubota, Y.; Watanabe, K.; Tsuda, O.; Taniguchi, T. Deep ultraviolet light-emitting hexagonal boron nitride synthesized at atmospheric pressure. *Science* **2007**, *317*, 932-934.

47. Li, Y.; Li, M.; Wang, T.; Bai, F.; Yu, Y. DFT study on the atomic-scale nucleation path of graphene growth on the Cu (111) surface. *Physical Chemistry Chemical Physics* **2014**, *16*, 5213-5220.

Chapter 8 - Theory and Prediction of Preferred Shapes and Edges of hBN on Metal Substrates

8.1 Introduction

Hexagonal boron nitride (hBN) exhibits many exceptional physical, optical, electrical, thermal, and chemical properties fit for unique applications. Two-dimensional hBN structurally resembles graphene: its properties are often compared with graphene as well. Both hBN and graphene have strong covalent sp^2 bonding and high elastic moduli, 0.33 TPa and 1TPa, for monolayer hBN and graphene respectively.[1] With increasing thickness, the strength of few-layer hBN rises above that of graphene thanks to stronger hBN interlayer forces.[1] The thermal conductivity of hBN monolayers ranges from 360 to 2000 W/mK,[2] which is comparable to that of graphene (2500 –5000 W/mK).[3] Moreover, hBN has higher thermal stability; it is stable in air up to 1000 °C while graphene is etched at 600 °C.[4,5]

With its wide energy band gap (6.5 eV) and an exciton binding energy of 149 meV,[6] hBN is a good candidate for optical devices operating in the ultraviolet spectral region,[7,8] and for exciton-based quantum information processing.[9] In addition, the photoluminescence intensity of hBN is 100 times higher than AlN.[10] hBN is an excellent electrical insulator and is thus used as a gate dielectric in electronic devices.[7] The boron-10 isotope has an exceptionally large thermal neutron capture cross-section (3840 b) (at a neutron energy of 0.025 eV),[11] suggesting that hBN is suitable for solid-state neutron detectors. While the hBN basal-plane is chemical inert, edges and defective sites are catalytically active for selective hydrocarbon oxidative dehydrogenation and CO oxidation reactions,[12,13] with extremely promising potential for other catalytic applications. Many, if not all, hBN applications require specific layer thickness,[14-16] surface areas,[16-19] structural

integrity,[10,15,20] edge orientation,[21] quality, and purity.[8] In fact, controlling the shape and edge properties is important for many monolayer 2D materials such as MoS_2,[22] GaSe,[23] and others. Achieving these specifications requires the ability to effectively tailor synthesis and preparation conditions governed by underlying materials chemistry, particularly, the thermodynamics of constituent species (B, N) and the formation of hexagonal lattice structures consisting of alternating B–N bonds.

Experimental studies on hBN have been extensively reported.[19,24-28] Atomically thin hBN materials are most commonly prepared using chemical vapor deposition (CVD) on transition metals substrates, such as Ni,[9,29-33] Cu,[34-36] Pd,[37] Pt,[38] and their alloys.[39] They report that before hBN thin films completely coalesce, there are domains of various shapes, most commonly triangles or hexagons.[27,40-42] Stehle *et al*.[40] reported that the dominant shape of hBN synthesized on copper (triangular or hexagonal) depended on the B: N ratio. Tay *et al*.[24] showed that hBN morphologies are sensitive to both surface structures and the substrate oxygen concentration. Thus, a detailed understanding of the crystal growth mechanism, especially the factors governing the hBN morphology, is critical to improve the synthesis technique for high quality hBN.

The thermodynamic and kinetic stabilities of hBN domain edges play critical roles in determining the quality of the synthesized crystals.[43] Thus, pertinent aspects have been investigated at the molecular level with first-principles methods. Liu *et al*.[44] and Zhao *et al*.[43,45] calculated hBN edge energies with DFT, then established a linear relation to describe the continuous shape transition from triangle to hexagon, and then back to triangle.

Aided with the ReaxFF reactive force field developed for the Ni/B/N system,[46] the nucleation and growth of hBN on Ni(111), from elemental B and N species via sequential B–N bond formation mediated by metal substrates, are simulated with molecular dynamics (MD)

calculations. The hBN domain's size, shape, edge terminations, and structural defects are predicted as functions of the constituent B: N ratios. Moreover, molecular trajectories are analyzed to derive the growth mechanism. The simulation describes molecular details of the hBN growth materials chemistry as well as roles of substrate and gas phase atmosphere that elude both quantum mechanical modeling and *in situ* characterizations.

8.2 Computational Methods and Simulation Details

8.2.1 Density Functional Theory (DFT) Calculations

Periodic, spin-polarized DFT calculations were employed based on the projector-augmented wave (PAW) method[47,48] and the generalized gradient approximation of Perdew-Burke-Ernzerhof (GGA-PBE) exchange-correlation functional[49] implemented in the Vienna Ab initio Simulation Package (VASP).[50] The Kohn-Sham valence states are expanded in a plane-wave basis set up to 350 eV. The self-consistent iterations were converged with a criterion of 1×10^{-6} eV, and the ionic steps are converged to 0.02 eV/Å.

The nickel substrate for DFT calculations was represented by a 3-layer $p(7 \times 7)$ (111) slab. The large lateral dimensions were employed to sufficiently accommodate hBN domain sizes considered, yet mitigate the lateral interactions among periodic images. The bottom two layers were fixed at the optimized bulk lattice value (3.52 Å). A vacuum of 30 Å (along the perpendicular direction) was used to separate the top slab layer from the bottom of its own periodic image. Considering the large unit cell, only a single gamma point was used to sample the reciprocal Brillouin zone. The Methfessel-Paxton smearing of 0.2 eV was used,[51] with the total energies then extrapolated to 0 K.

8.2.2 Edge Energies of hBN Domains on Ni(111)

The edge energies of supported 2-D hBN can be considered to gain insights into the domain's relative stability on a substrate.[30,52-54] DFT calculations pointed out that van der Waals forces play a significant role among the interactions between continuous hBN monolayers and their supporting metal substrates.[55] However, for finite hBN structures, chemical bonding at the domain edges coupled with charge transfer,[13] will also contribute to the hBN/substrate interactions.

Structures of triangular and hexagonal BN domains, which are two most common shapes from hBN synthesis, with varying edge lengths (L = 1–5) supported on Ni(111), were optimized using the method described above, as shown in Figure 8.1 (in both top and side views). Both the triangular and hexagonal geometries are equilateral (i.e., equal edge length). Hence, L = 3 denotes that there are 3 B–N units in each edge. As shown in Figure 8.1(a) and (b), B- and N- terminated zigzag edges mean that the outermost atoms along the edge are B and N, respectively. The hexagonal geometries in Figure 8.1(c) have interchanged B/N edges. The optimized monolayer hBN domains (both triangular and hexagonal in Figure 8.1) consistently have N binding on the top site and B binds on the 3-fold (either hcp or fcc) site of Ni(111). Furthermore, from the side views inn Figure 8.1, we can see that the middle sections of the hBN domains are all protuberant, while the edge atoms are tightly contact with the surface, which indicate a strong binding between the edge atoms and the metal surface.

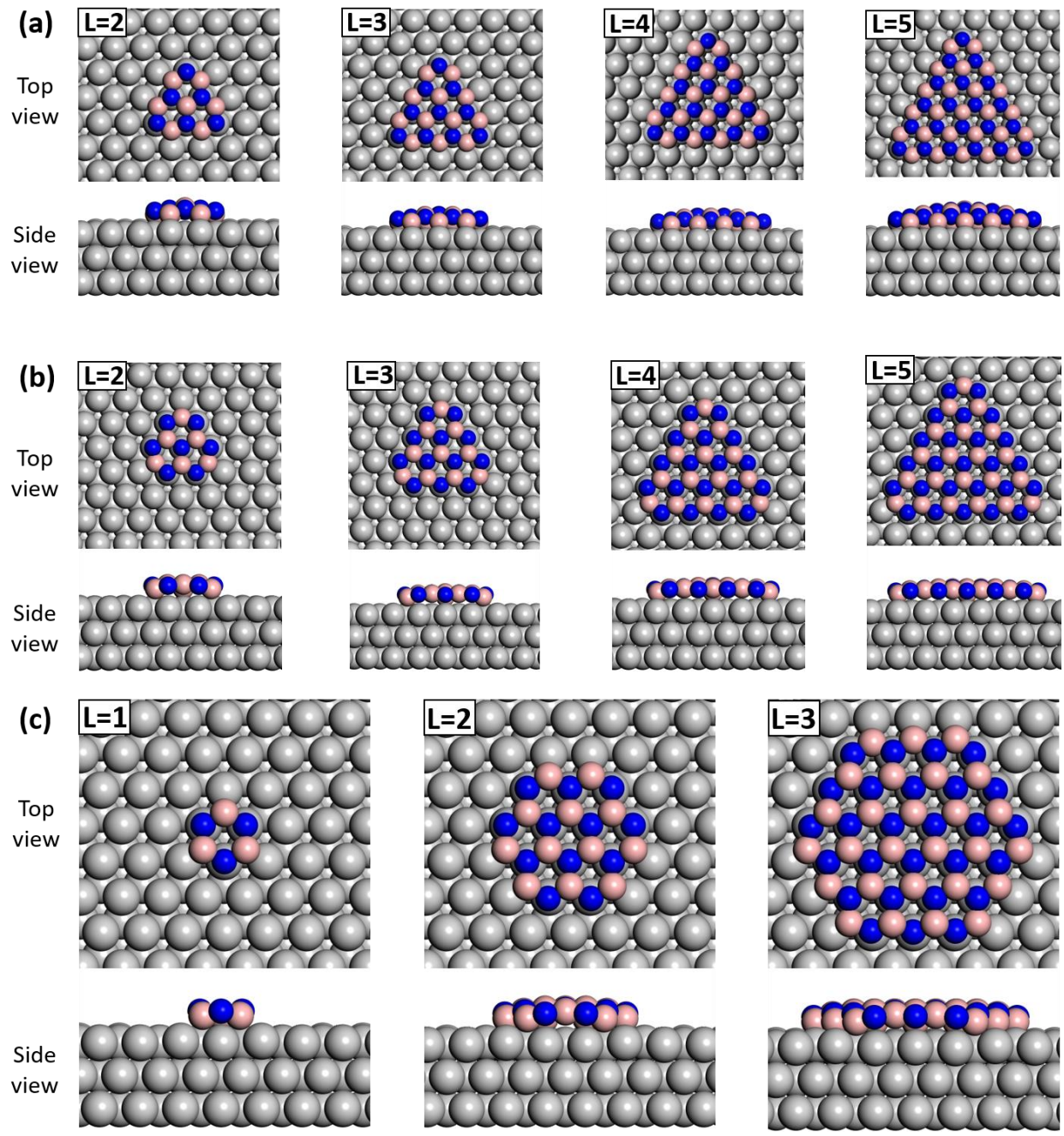

Figure 8.1. Optimized hBN domains with (a) B- and (b) N- terminated edges in triangular geometries at lengths L = 2–5, and (c) interchanged B/N edges in hexagonal geometries at lengths L = 1–3 on Ni(111) surface. N, B, and Ni are shown in blue, pink, and gray, respectively.

The edge energies (γ_{ZB} and γ_{ZN}) of triangular hBN on Ni(111) can be described by Equations (20) and (21),

$$\gamma_{ZB} = \frac{E_T - E_{Ni} - M_{BN}\mu_{BN} - \mu_B - L\mu_B}{3L} = \gamma_{ZB}^* - \frac{\mu}{3} \quad (20)$$

$$\gamma_{ZN} = \frac{E_T - E_{Ni} - M_{BN}\mu_{BN} - \mu_N - L\mu_N}{3L} = \gamma_{ZN}^* + \frac{\mu}{3} \quad (21)$$

where E_T and E_{Ni} are the total energies of adsorbed hBN and clean Ni(111), as first discussed by Yakobson and coworkers.[44] M_{BN} is the number of BN pairs in each hBN domain. μ_{BN}, μ_B, and μ_N represent the chemical potentials of a BN pair, and elemental B and N species in an infinite, flat hBN monolayer, respectively. Moreover, they obey the relationships, as in Equations (22) and (23),

$$\mu_{BN} = \mu_B + \mu_N \quad (22)$$

$$\mu_{B/N} = \frac{1}{2}\mu_{BN} \pm \mu \quad (23)$$

where μ in Equation (23) is an arbitrary parameter, which can be used to tune the chemical potentials of B and N species.

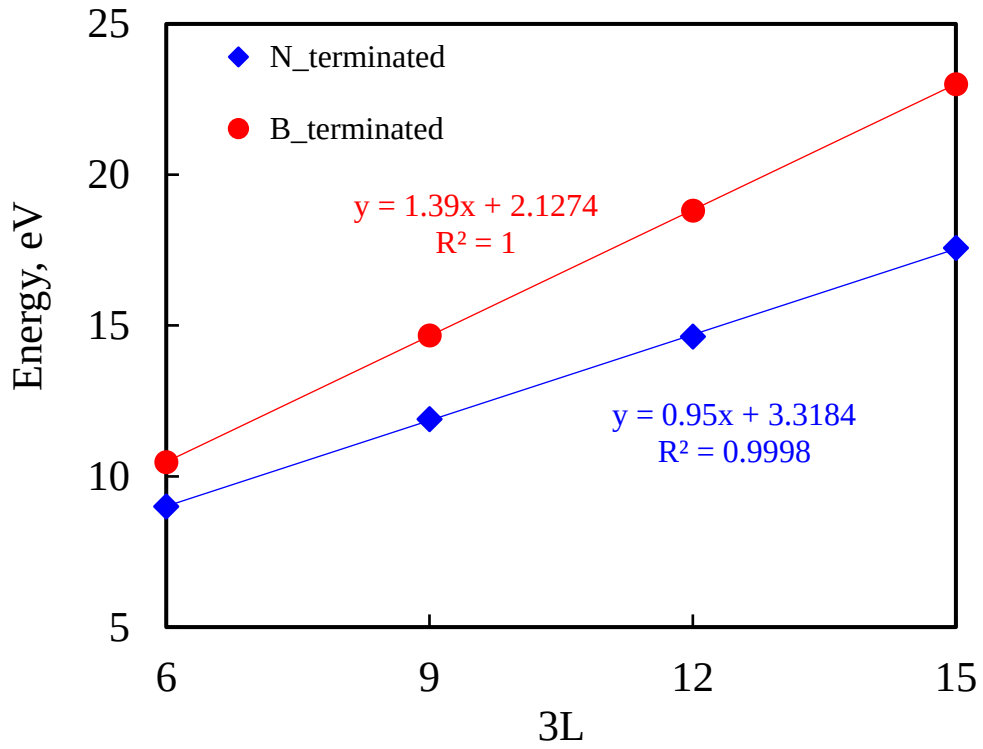

Figure 8.2. Energies of triangular-shaped hBN on Ni(111) as a function of their size L.

The energy calculations for the B/N-terminated triangular domains illustrated in Figure 8.1(a-b) exhibit a linear relationship with the edge length L, as in Figure 8.2. The edge energies can be then determined by their slopes based on Equations (20) and (21). By letting μ = 0, we obtain$\gamma_{ZB}^{*} = 1.39\ eV$ and $\gamma_{ZN}^{*} = 0.95\ eV$. Thus, the edge energies of B- and N- terminated hBN with zigzag configurations can be represented by Equations (24) and (25), respectively.

$$\gamma_{ZB} = 1.39 - \frac{\mu}{3} \tag{24}$$

$$\gamma_{ZN} = 0.95 + \frac{\mu}{3} \tag{25}$$

For hexagonal BN domains on Ni(111), the edge energy (γ_Z) can be defined by Equation (26), which is independent of μ. The energy calculations for hexagonal hBN geometries in Figure 8.1(c) also show a strict linear relationship with the edge length L, as shown in Figure 8.3. The edge energy can be then determined by the slope, and expressed as Equation (27).

$$\gamma_Z = \frac{E_T - E_{Ni} - M_{BN}\mu_{BN}}{6L} \tag{26}$$

$$\gamma_Z = 1.12 \tag{27}$$

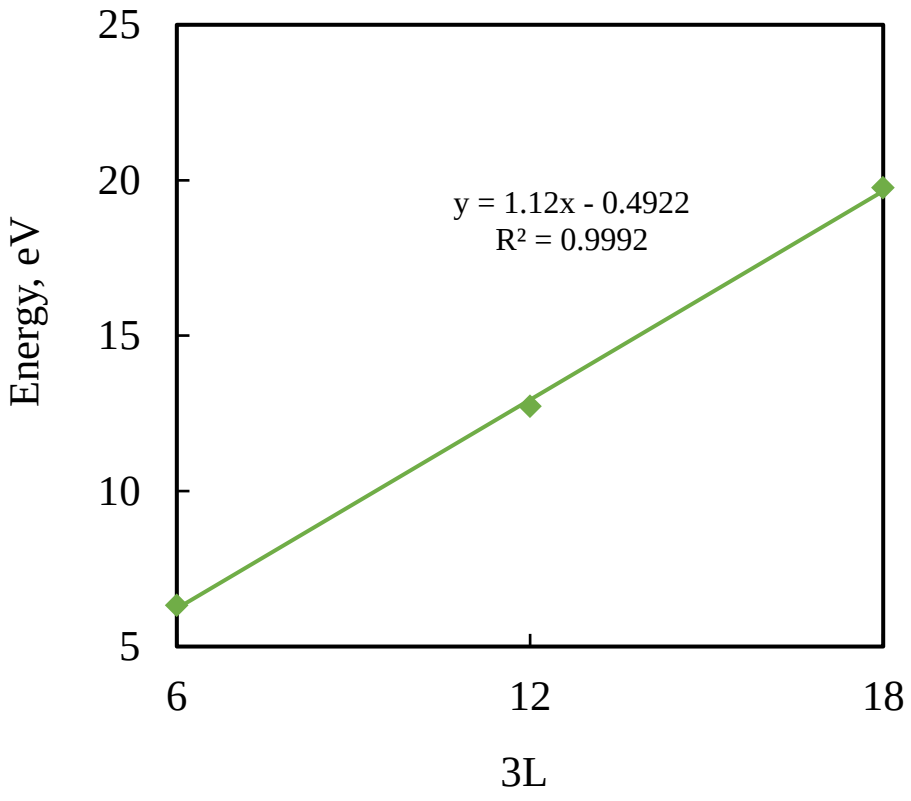

Figure 8.3. Energies of hexagonal-shaped hBN on Ni(111) as a function of their size 3L.

Using Equations of (24), (25), and (27), the preferred shape and edge termination of Ni(111)-supported hBN monolayer are summarized in Figure 8.4. The N-terminated triangular hBN is preferred in the lower range of μ (more negative). As μ increases, hexagonal hBN and then B-terminated triangular hBN, in turn, become more energetically favored. Thus, the equilibrium morphologies of hBN depend on μ, which can then be connected to the specific conditions of the system.

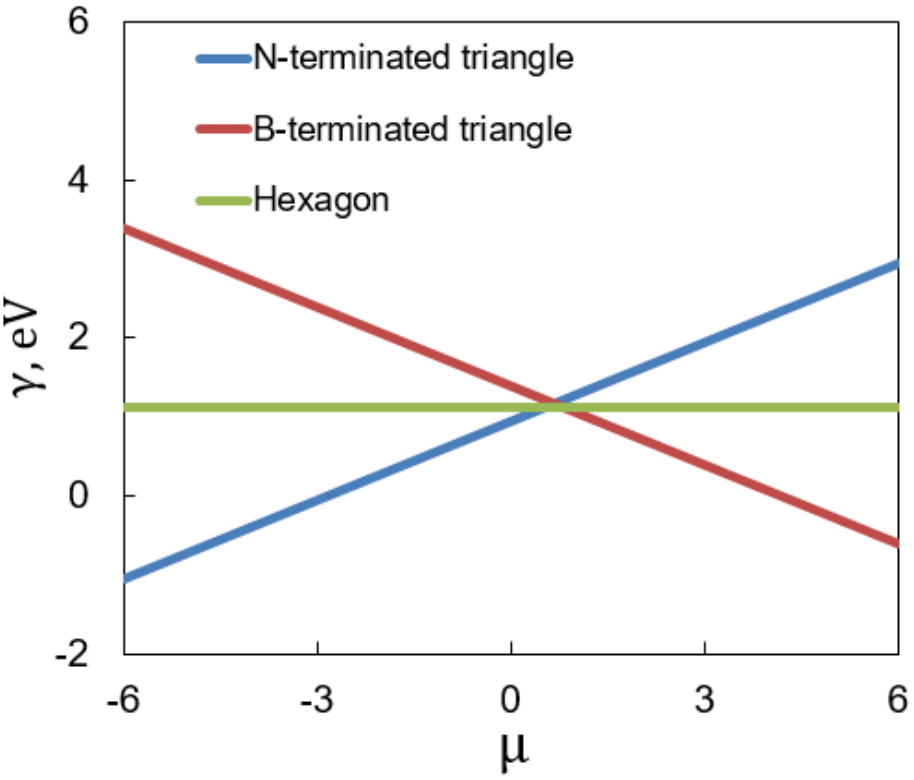

Figure 8.4. Edge energies of B- and N- terminated triangular and hexagonal hBN domains with zigzag edge configurations.

8.2.3 Molecular Dynamics (MD) Simulations

All MD simulations were performed with LAMMPS. The nickel substrate is modeled using the same 5-layer rectangular slab with the (111) facet for elemental B and N deposition and subsequent hBN nucleation and growth. The lateral dimensions of the periodically bounded Ni slab were 12 × 12 repetition, with a total of 720 Ni atoms. The bottom (5^{th}) layer was fixed to the bulk lattice value to represent the interior bulk region, while the top four layers were relaxed. There is a vacuum of 90 Å separating successive images along the vertical direction. Initially, the Ni slab is clean, and free from elemental B and N species.

At the beginning of the simulation, B and N were assigned with random x, y coordinates in the gas phase above Ni(111), and were sequentially deposited onto the substrate at an interval of 0.25 ps. To prevent premature B–N bond formation, the minimal distance between the initial B and N sources was set to be 1.90 Å, larger than the B–N bond length of 1.44 Å in the hBN lattice. All B and N were deposited on one (relaxed) side of the slab with controlled initial momenta. The simulations were run with B: N ratios, but the other simulation procedures remain the same. All simulations were performed at 1300K, controlled by the Nosé-Hoover thermostat. The equation of motion was numerically solved using the velocity Verlet integration scheme. Each MD run was run for 10 ns with a time step of 0.25 fs.

The ReaxFF force field was employed so that phenomena involving B–N, B–B, N–N pairs and interactions between constituent elements (i.e., B and N) with Ni substrate can be properly described. The total potential energy in ReaxFF is formulated as a functional of bond-orders of interacting atomic pairs.[56] The ReaxFF force field used was developed for Ni/B/N systems as reported in Ref. [46].

8.2.4 MD simulations of hBN Growth at Different B: N Ratios on Ni(111)

According to first-principles calculations, the morphology of hBN is controlled by μ. With molecular simulations, μ can be varied by changing the elemental B and N source supplied to the system. In our previous work,[46] B: N ratio was fixed at B: N = 1:1. Here, the B: N ratio was varied from 3:1 and 2:1 (boron rich), to 1:1 (stoichiometric), and then to 1:2, 1:3, and 1:4 (nitrogen rich). The stoichiometry of "1" in each ratio was set to be 100 atoms. For example, there are 300 boron atoms and 100 nitrogen atoms for B: N = 3:1.

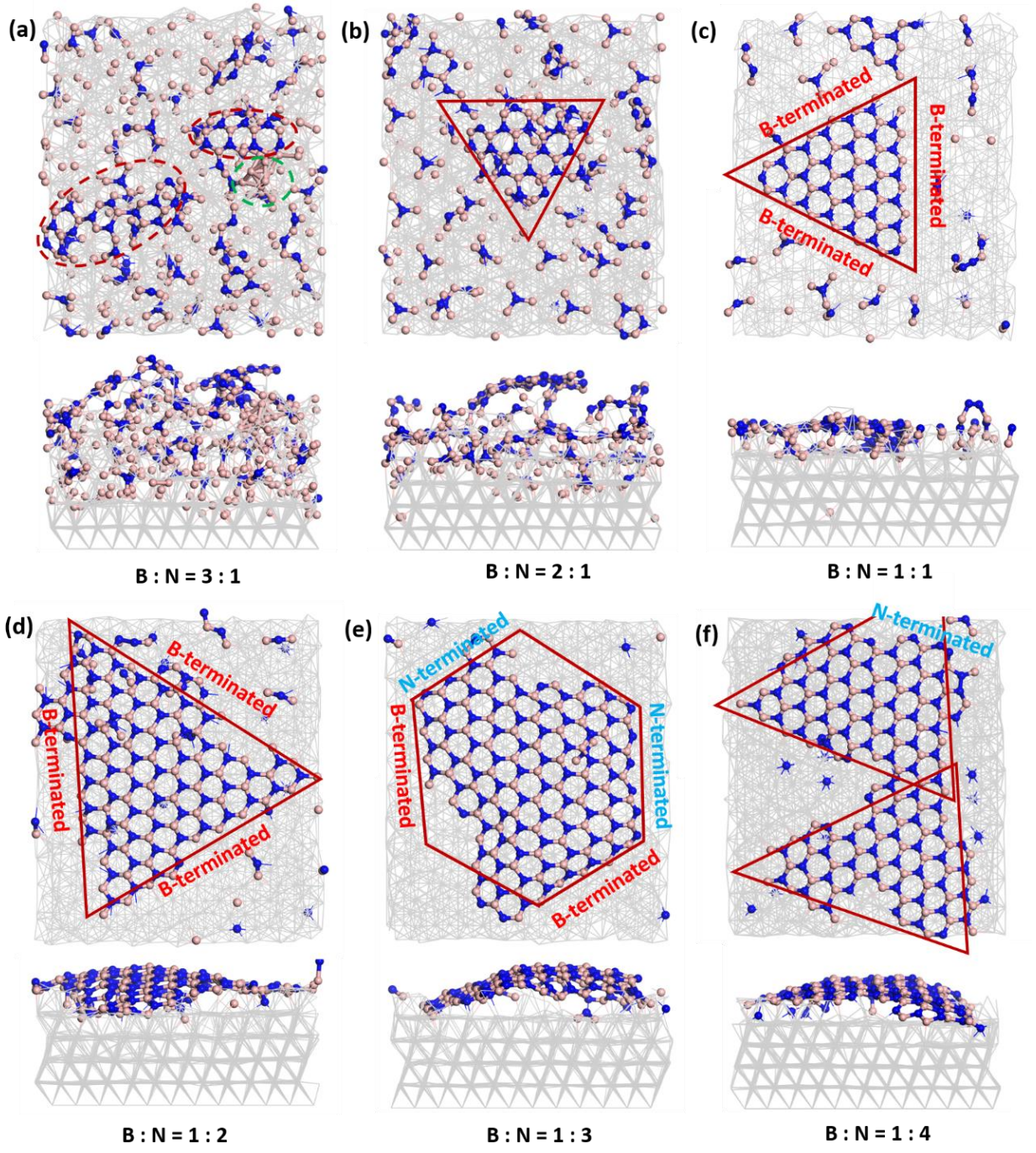

Figure 8.5. Snapshot images (top and side views) of hBN growth (at 1300K) obtained from MD simulations at 10 ns at B: N ratio of: (a) 3:1, (b) 2:1, (c) 1:1, (d) 1:2, (e) 1:3, and (f) 1:4, respectively. N and B atoms are in blue and pink. The Ni(111) substrate is depicted in gray. The boundaries of hBN domains and edge terminations are highlighted and labeled.

The monolayer hBN domains formed under different B: N ratios, obtained after 10 ns of simulations at 1300K on Ni(111), are illustrated in Figure 8.5. Under the B-rich condition (300 boron atoms versus 100 nitrogen atoms at B: N = 3:1), as depicted in Figure 8.5(a), small hBN pieces consisting of 1–4 isolated or joint hexagonal lattice formed, as highlighted by red dashed circles. These structures resemble nucleation centers, with dangling arms attached. The hBN sizes are relatively small as further growth is hindered. This is because the growth centers are terminated mainly by B atoms, which would require additional to sustain the growth. Nevertheless, the remaining un-utilized N species are also bonded, by the excess boron atoms. The side view reveals that excess B atoms are present throughout the sublayers of the substrate. As boron atoms energetically prefer the sublayer of Ni(111), they remain in the sublayers after 10 ns of simulation. Due to the high dose of boron deposited, the strong B–Ni bonds severely distort the Ni crystal lattice. Also from the side view, the hBN domains seem to be detached from the highly distorted substrate surface. Moreover, multi-atom boron-only clusters have been formed, as highlighted by the green dashed circle.

When 100 nitrogen atoms and 200 boron atoms are deposited, B: N ratio of 2:1, small hBN islands (approximately four BN lateral unit length) with triangular geometry form, as shown in Figure 8.5(b). In comparison to Figure 8.5(a), the un-utilized nitrogen on Ni still exist in isolated hexagonal BN units, but are mainly bounded by boron atoms. The remaining excess boron remain on the substrate top layer, as well as in the sublayer. Nevertheless, sublayer boron species are mainly limited in the top two layers (see Figure 8.5(b) side view).

At the stoichiometric B: N ratio (100 nitrogen and 100 boron atoms), the most significant structure on the substrate is the triangular shaped hBN domain with B-terminated edges on all sides (Figure 8.5(c)). This triangular domain is nearly equilateral, with L = 6. As shown in our

previous work,[46] where a stoichiometry ratio was used with identical simulation procedure, a much larger – almost continuous – hBN sheet forms when larger amount of boron and nitrogen (200 atoms each) are supplied. Regardless, at this B: N ratio, nearly all deposited boron and nitrogen participate in forming hBN lattices, which is almost parallel to the substrate. From the top view of Figure 8.5(c), unincorporated boron and nitrogen formed a second, but much smaller hBN lattice (near the top of the substrate boundary above the main domain). The remaining elemental species exist mainly on the top layer, as B-N-B, and B-N-B-N. The lattice of Ni substrate is relatively intact. This run suggests that, by controlling the amounts of constituent deposited, the morphologies of hBN can be manipulated correspondingly.

Under nitrogen-rich conditions, where 100 boron and 200 nitrogen atoms were introduced at B: N=1:2, an even larger hBN domain in triangular shape with B-terminated edges was obtained, as shown in Figure 8.5(d). There are only few isolated BN dimers and trimers remaining on the surface, and most of B atoms have been utilized for the triangular hBN formation.

At B: N = 1:3, a hexagonal hBN geometry appears. As shown in Figure 8.5(e), this structure possesses both N- and B- terminated edges. At an even higher N excess (i.e., B: N = 1:4), the simulated structure returns, once again, back to a triangular geometry as shown in Figure 8.5(f). At the stoichiometric and nitrogen-rich ratios, the number of boron deposited remains constant at 100, thus, it can be deduced that sufficient amounts of nitrogen can be critical in achieving larger hBN domain sizes.

From the structure and morphology evolution exhibited in Figure 8.5, both the sizes and geometries of grown hBN responded to the B: N stoichiometry used in the simulation. At higher B: N ratios (i.e., B-rich), hBN prefers triangular geometries, terminated by boron species. As the B: N ratio shifts toward N-rich conditions, the size of grown hBN increases. Even more interesting,

the shape evolves into multifaceted triangular pattern. Concomitantly, the edge orientations exhibit a higher level of variety. For instance, N-terminated edges and armchair-type edges appeared in the grown domains. With excessive elemental N species, triangular shape is preferred again. Thus, the evolutionary path shows a surprisingly high level of resemblance to first-principles predictions.

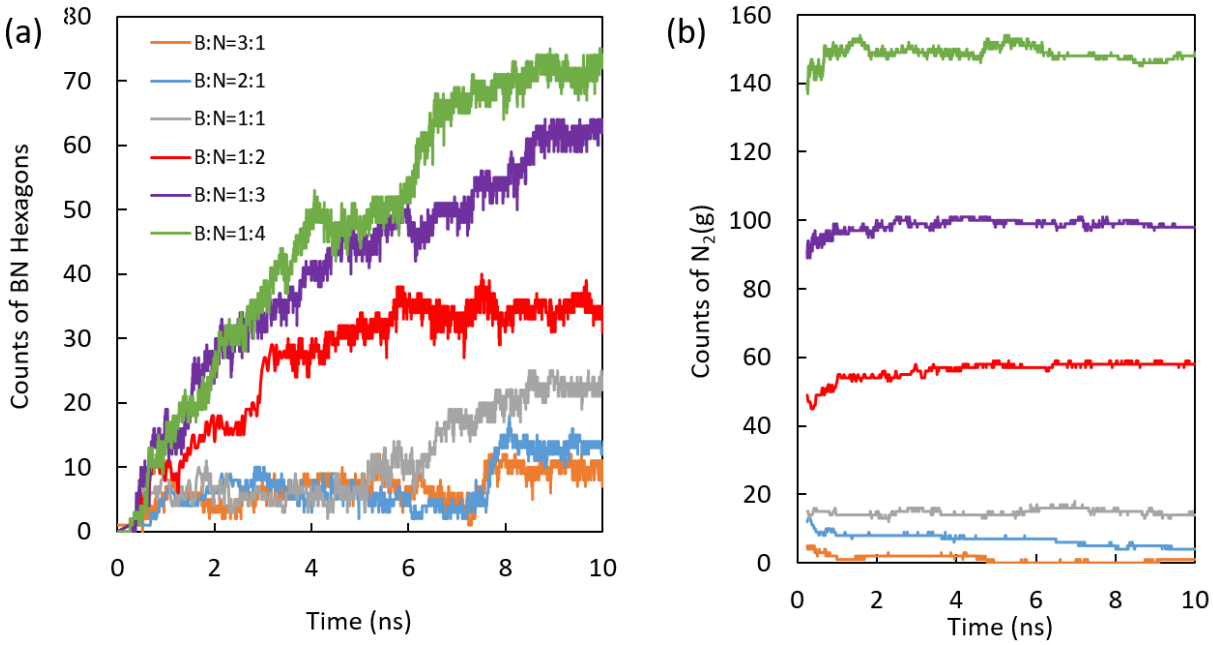

Figure 8.6. Counts of (a) BN hexagons, and (b) gas phase N_2 over a period of 10 ns at B: N ratios: 3:1 (orange), 2:1(blue), 1:1(grey), 1:2(red), 1:3(purple), and 1:4(green).

To further quantify the growth of hBN on Ni(111), the number of BN hexagons and gas phase N_2 were counted to monitor the species during 10 ns of MD simulations, as shown in Figure 8.6(a) and (b). At B: N = 3: 1 (orange) and 2: 1 (blue), in Figure 8.6(a), the number of BN hexagons grew slowly; up to 5 formed in the first 7 ns, most of which were formed in the initial period (within the 1st ns). The numbers of BN hexagons finally reached approximately 10 counts in both

cases at around 8 ns. At the stoichiometric B: N ratio (grey), the initial grow is at a similar pace (in the first 6 ns) to those at boron-rich conditions. However, the number of BN hexagons nearly doubled and reached a count of 22 in the next 4 ns. The slow growth at the initial stage suggests that growth is limited by the arrival of sufficient nitrogen, which is the limiting species. Under nitrogen-lean and stoichiometric conditions, an induction period is required before the growth occurs. At B: N = 1: 2 (yellow), the growth rate in BN hexagon counts grew at much faster rates, with more than 15 counted after 2 ns of MD run. At 3 ns, the number of BN hexagon increased significantly, reaching 27. During the remaining 7 ns, the number of BN hexagon grows at a slower pace and eventually reached approximately 30. The slower growth after 3 ns can be attributed to the depletion of nitrogen and boron sources. As shown in Figure 8.6(a) (in purple and green), 64 and 75 hexagons formed by 10 ns, respectively. At the early stage (in the first 2 ns), the number of BN hexagons grew at a pace of 15 hexagons/ns. The main difference between simulations performed at nitrogen excess conditions is that at, B: N = 1:4, the domain growth outpaces that at B: N = 1:3 after 6 ns.

$$2N^{*} \leftrightarrow N_{2(g)} \qquad (28)$$

N_2 molecules formed in the vacuum space during simulations at all B: N ratios, as shown in Figure 8.6(b). These molecular species apparently originate from the recombination of deposited elemental N, according to Equation (28). DFT calculations strongly suggest that, unlike boron, which energetically prefers the sublayer of Ni,[46] elemental N prefers the top layer of Ni(111). Hence, sublayer N reemerges via sublayer diffusion onto the Ni top layer. By monitoring throughout the simulation as noted in Figure 8.6(b), the stabilized counts of N_2 molecules are

proportional to the B: N ratio – higher N_2 counts corresponding to lower B: N ratios. At B: N = 3:1 and 2:1, gas phase N_2 counts reach maximum values at respective 5 and 15 within the initial 0.25 ns, and then slowly decay during the remaining simulations. At the highest B: N ratio, nearly all the N_2 are completely consumed eventually. Thus, in the presence of excessive B, N_2 will dissociate and participate in hBN growth. At B: N =1:1, the number of N_2 remains stable throughout the simulation at approximately 15. Below the B: N stoichiometric ratio (i.e. B: N =1:2, 1:3, and 1:4), the gas phase N_2 counts gradually increases until it reached an equilibrium at around 6 ns, suggesting that the excess N species will recombine and desorbed from the substrate. Under these simulation conditions, the fluctuating number of N_2 reflects a dynamic process between surface adsorbed N and gas phase N_2.

8.2.5 Growth Mechanisms of Triangular and Hexagonal hBN Domains.

Molecular trajectories obtained from the MD simulation run at the stoichiometric ratio (Figure 8.7) illustrate how triangular-shaped hBN domains form. As indicated in Figure 8.6, with lower B and N loading (100 atoms for each species), the growth rate in terms of BN hexagon count is reduced. The first BN hexagon, essentially the initial nucleation site, did not appear until 5.15 ns, in comparison to the simulation (200 atoms for each species reported in Ref. [46]), where the first hexagon appears at 64.25 ps.

In Figure 8.7(a), the first nucleus centers, a hexagonal BN ring with two linear branches on the opposite ends, appears at 5.16 ns. Then, at 5.86 ns, the same structure evolves into a nucleus consisting of three joint BN hexagons (Figure 8.7(b)). This center can further grow multiple *dangling arms*. In Figure 8.7(c), the size of the center nearly doubled as a second structure consisting of multiple BN hexagons is attached to the right side based on the image captured at

5.93 ns. Within the next 0.5 ns, numerous re-arrangements occur, and consequently, a 10-hexagon membered domain is formed at 6.45 ns (Figure 8.7(d)). The edges of this domain are still rather energetic. For instance, as highlighted (by the red dashed circle in Figure 8.7(e)), the B–N bond on the upper left side is cleaved at 6.66 ns, creating a $–NB_2$ dangling arm attached to the main center stacked by 1-2-4-2 BN hexagons. For the next 0.9 ns, this hBN center grows mainly on the upper and lower sides, which act as the growth frontiers as illustrated by Figure 8.7(f-h). At 8.16 ns, Figure 8.7(i), the right side of the domain is mainly bounded by the B-terminated zigzag edge, while the remaining sides (upper, left, and bottom) are bounded by –BNB and –NB groups, which will prompt additional growth. As anticipated, in the next 1.2 ns as illustrated by Figure 8.7(j-l), the hBN domain evolves by forming B-terminated zigzag edges on both left and bottom sides. The BN hexagons in Figure 8.7(l) are stacked in a pyramidal geometry as 2-3-4-5-6, with a few dangling –B and –NB bonds attached on the upper and left edges.

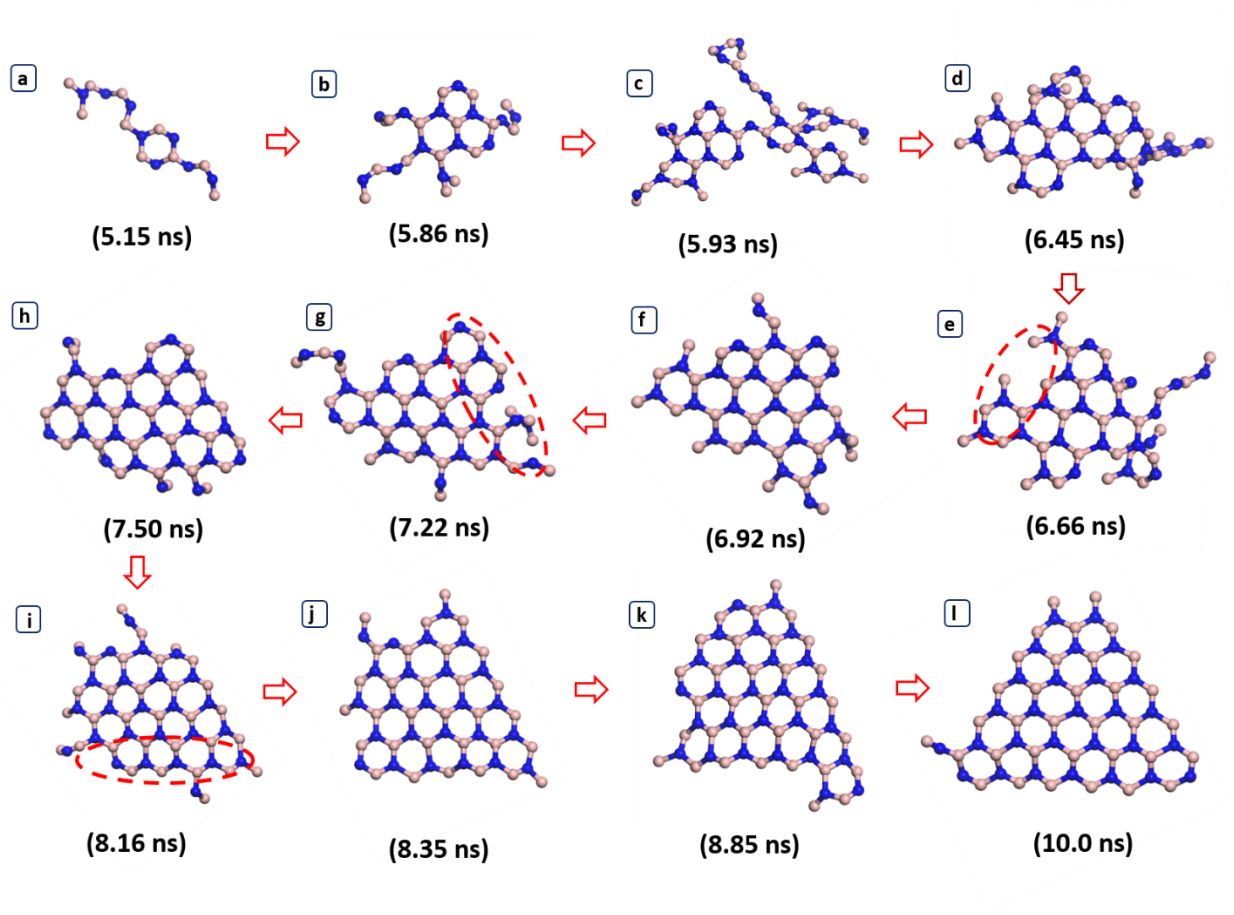

Figure 8.7. Growth of a triangular BN domain on Ni(111) at 1300 K and 1:1 B: N ratio. N and B are in blue and pink, respectively. The red dashed circles indicate the actively growing area in the structure. The Ni substrate is omitted for clarity. The timeframes corresponding to each captured image is shown in the parentheses.

Similarly, the formation of a hexagonal-shaped hBN domain at the B: N = 1:3 ratio is illustrated in Figure 8.8. The growth center is established when the first BN hexagon forms as illustrated in Figure 8.8(a) at 0.44 ns, and then monitored throughout the growth process. Several branches, including $–BN_2$, –NB, and –B, are attached. Then a four-membered growth center develops at 0.46 ns (Figure 8.8(b)). Note that this structure contains one heptagon (at the lower left side) with a homoelemental N–N bond. This is possible when excess nitrogen species are

deposited (B: N = 1:3). At 1.48 ns (Figure 8.8(d)), a second hBN island is added to the nucleus via the linkage of a B–N bond. This behavior also occurred at a 1:1 B: N ratio (Figure 8.7(c)), thus suggesting multiple hBN domains can possibly grow in separate domains. In subsequent steps, these two structures integrate, but a vacancy, at the center of the hBN domain (highlighted by the red dash circle) was formed at 2.31 ns (Figure 8.8(e)). Within the same domain, this vacancy remained in the structure for over 5 ns. During this time (Figure 8.8(e-j)), the size of the vacancy shrank as isolated B and N atoms from the Ni surface are incorporated to fill this gap. Within the last 2 ns (Figure 8.8(i-j)), the vacancy mainly exists as a B-point defect. Meanwhile, the outer region of this hBN domain continues to grow and re-arrange. According to Figure 8.6(a), the number of BN hexagons has increased by 20 (red). The additional BN hexagons are mainly added to the left and right sides of the existing domain as show in Figure 8.8(g-l). At 8.19 ns (Figure 8.8(k)), the B-point defect has been *repaired*, and the entire domain structure became defect-free. This mechanism is similar to the triangle hBN growth demonstrated in last part. It is postulated that B species in the Ni sublayer may play a role by diffusing onto the top layer and access the defect location. The hexagonal-shaped hBN geometry is facilitated by the ability of the domain to grow in multiple directions. In this case, the growth is slowed down due to the depletion of B species (even though N mainly exist as N_2(g)). As shown by Figure 8.8(l), hBN is bounded by B- and N-terminated zigzag edges at the bottom and lower-right sides. The remaining sides, which are bounded by high edge energy termination and even dangling bonds, will prompt further growth given additional elemental sources are supplied.

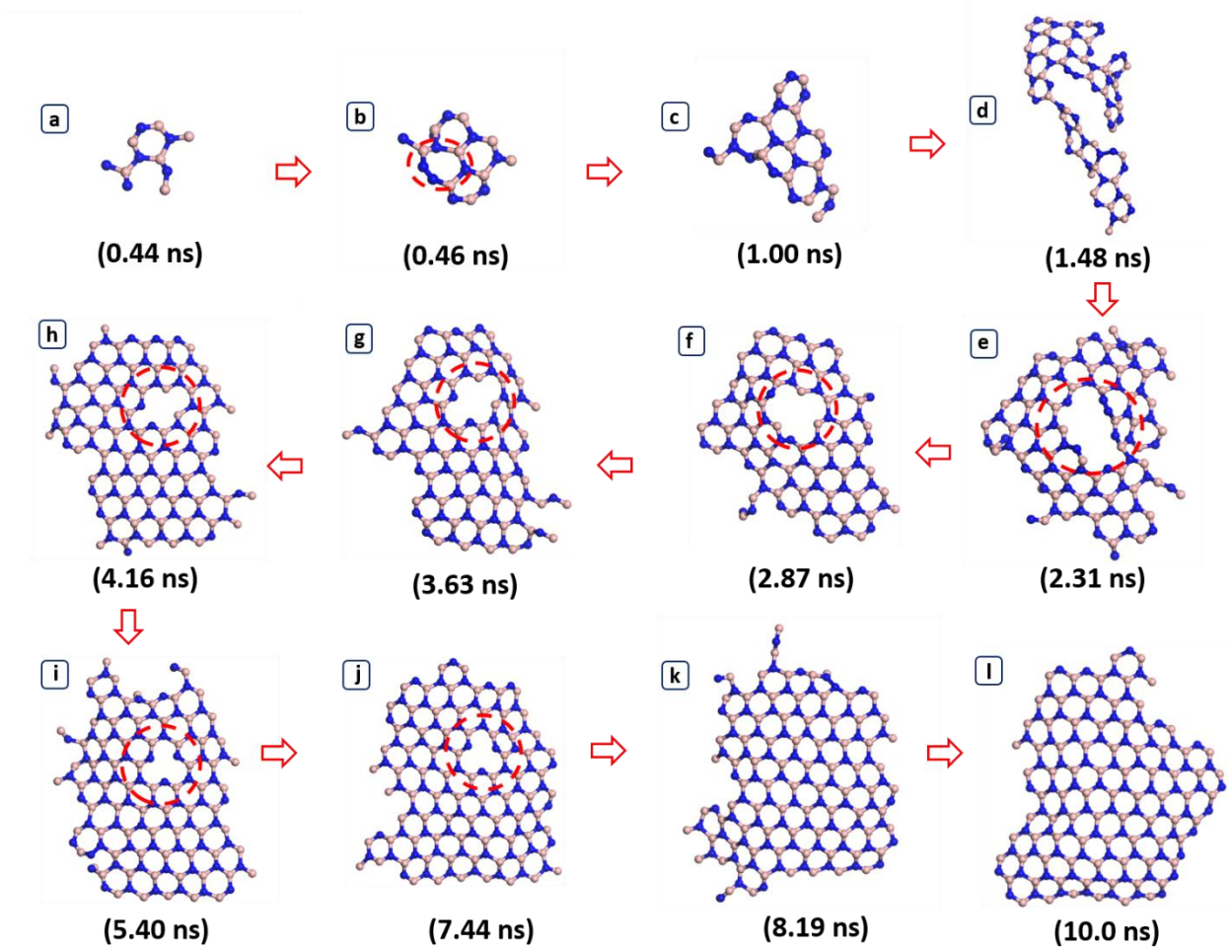

Figure 8.8. Growth of hexagonal BN domain on Ni(111) at 1300 K and B: N =1:3 ratio. N and B are shown in blue and pink, respectively. Defective vacancies are highlighted by red dash circles. The Ni substrate is omitted for clarity. The timeframes corresponding to each captured image is shown in the parentheses.

8.3 Conclusions

By combining first-principles calculations and MD simulations using ReaxFF, the growth chemistry of monolayer hBN on Ni(111) was understood. As demonstrated in this paper, the most

significant insights gained through reactive molecular dynamics simulations can be summarized as follows:

- hBN growth and morphologies are indeed sensitive to the B: N ratio supplied to the system.
- Nitrogen plays a critical role in sustaining the growth of hBN. Larger hBN domain sizes are obtained when nitrogen is supplied in excess to the system.
- Surplus boron will remain on the substrate, and can enter the sublayer of the Ni substrate. On the other hand, surplus nitrogen remains either on the substrate top layer, or recombine, by forming N_2, in the gas phase.
- The ReaxFF force field, developed from first-principles calculations, show the capability to faithfully describe the behaviors of constituent B and N species on Ni substrate and B–N bond formation. Hence, it can be regarded as a useful tool to explore and gain insights into the chemistries of the hexagonal BN phase.
- Lastly, the hBN growth rate, particularly the rate of nucleus formation, depends on the amount of constituent elemental sources. However, subsequent growth mechanisms are similar, regardless of the shape and size of hBN domains obtained.

8.4 Acknowledgements

Supports from the Materials Engineering and Processing program of the National Science Foundation, Award number 1538127, and the II-VI Foundation are greatly appreciated. DFT and rMD calculations were carried out thanks to the supercomputing resources and services from the Beocat Research Cluster at Kansas State University, which is funded in part by NSF grants CNS-1006860; and the National Energy Research Scientific Computing Center (NERSC) under the contract No. DE-AC0205CH11231.

References

1. Falin, A.; Cai, Q.; Santos, E. J.; Scullion, D.; Qian, D.; Zhang, R.; Yang, Z.; Huang, S.; Watanabe, K.; Taniguchi, T. Mechanical properties of atomically thin boron nitride and the role of interlayer interactions. *Nature Communications* **2017**, *8*, 15815.
2. Ouyang, T.; Chen, Y.; Xie, Y.; Yang, K.; Bao, Z.; Zhong, J. Thermal transport in hexagonal boron nitride nanoribbons. *Nanotechnology* **2010**, *21*, 245701.
3. Balandin, A. A. Thermal properties of graphene and nanostructured carbon materials. *Nature Materials* **2011**, *10*, 569.
4. Kho, J.; Moon, K.; Kim, J.; Kim, D. Properties of Boron Nitride (B_xN_y) Films Produced by the Spin-Coating Process of Polyborazine. *J. Am. Ceram. Soc.* **2000**, *83*, 2681-2683.
5. Chen, Y.; Zou, J.; Campbell, S. J.; Le Caer, G. Boron nitride nanotubes: pronounced resistance to oxidation. *Appl. Phys. Lett.* **2004**, *84*, 2430-2432.
6. Watanabe, K.; Taniguchi, T.; Kanda, H. Direct-bandgap properties and evidence for ultraviolet lasing of hexagonal boron nitride single crystal. *Nature Materials* **2004**, *3*, 404.
7. Dahal, R.; Li, J.; Majety, S.; Pantha, B.; Cao, X.; Lin, J.; Jiang, H. Epitaxially grown semiconducting hexagonal boron nitride as a deep ultraviolet photonic material. *Appl. Phys. Lett.* **2011**, *98*, 211110.
8. Kubota, Y.; Watanabe, K.; Tsuda, O.; Taniguchi, T. Deep ultraviolet light-emitting hexagonal boron nitride synthesized at atmospheric pressure. *Science* **2007**, *317*, 932-934.
9. Kobayashi, Y.; Nakamura, T.; Akasaka, T.; Makimoto, T.; Matsumoto, N. Hexagonal boron nitride on Ni (1 1 1) substrate grown by flow-rate modulation epitaxy. *J. Cryst. Growth* **2007**, *298*, 325-327.

10. Hoffman, T. B.; Clubine, B.; Zhang, Y.; Snow, K.; Edgar, J. H. Optimization of Ni–Cr flux growth for hexagonal boron nitride single crystals. *J. Cryst. Growth* **2014**, *393*, 114-118.
11. Li, J.; Dahal, R.; Majety, S.; Lin, J.; Jiang, H. Hexagonal boron nitride epitaxial layers as neutron detector materials. *Nuclear Instruments and Methods in Physics Research Section A: Accelerators, Spectrometers, Detectors and Associated Equipment* **2011**, *654*, 417-420.
12. Grant, J. T.; Carrero, C. A.; Goeltl, F.; Venegas, J.; Mueller, P.; Burt, S. P.; Specht, S. E.; McDermott, W. P.; Chieregato, A.; Hermans, I. Selective oxidative dehydrogenation of propane to propene using boron nitride catalysts. *Science* **2016**, *354*, 1570-1573.
13. Zhu, W.; Wu, Z.; Foo, G. S.; Gao, X.; Zhou, M.; Liu, B.; Veith, G. M.; Wu, P.; Browning, K. L.; Lee, H. N. Taming interfacial electronic properties of platinum nanoparticles on vacancy-abundant boron nitride nanosheets for enhanced catalysis. *Nature Communications* **2017**, *8*, 15291.
14. Zhi, C.; Bando, Y.; Tang, C.; Kuwahara, H.; Golberg, D. Large-scale fabrication of boron nitride nanosheets and their utilization in polymeric composites with improved thermal and mechanical properties. *Adv. Mater.* **2009**, *21*, 2889-2893.
15. Edgar, J.; Liu, S.; Hoffman, T.; Zhang, Y.; Twigg, M.; Bassim, N. D.; Liang, S.; Khan, N. Defect sensitive etching of hexagonal boron nitride single crystals. *J. Appl. Phys.* **2017**, *122*, 225110.
16. Liu, S.; He, R.; Ye, Z.; Du, X.; Lin, J.; Jiang, H.; Liu, B.; Edgar, J. H. Large-Scale Growth of High-Quality Hexagonal Boron Nitride Crystals at Atmospheric Pressure from an Fe–Cr Flux. *Crystal Growth & Design* **2017**, *17*, 4932-4935.

17. Dean, C. R.; Young, A. F.; Meric, I.; Lee, C.; Wang, L.; Sorgenfrei, S.; Watanabe, K.; Taniguchi, T.; Kim, P.; Shepard, K. L. Boron nitride substrates for high-quality graphene electronics. *Nature Nanotechnology* **2010**, *5*, 722.

18. Meng, J.; Zhang, X.; Wang, Y.; Yin, Z.; Liu, H.; Xia, J.; Wang, H.; You, J.; Jin, P.; Wang, D. Aligned Growth of Millimeter-Size Hexagonal Boron Nitride Single-Crystal Domains on Epitaxial Nickel Thin Film. *Small* **2017**, *13*, 1604179.

19. Tay, R. Y.; Wang, X.; Tsang, S. H.; Loh, G. C.; Singh, R. S.; Li, H.; Mallick, G.; Teo, E. H. T. A systematic study of the atmospheric pressure growth of large-area hexagonal crystalline boron nitride film. *Journal of Materials Chemistry C* **2014**, *2*, 1650-1657.

20. Edgar, J. H.; Hoffman, T. B.; Clubine, B.; Currie, M.; Du, X.; Lin, J.; Jiang, H. Characterization of bulk hexagonal boron nitride single crystals grown by the metal flux technique. *J. Cryst. Growth* **2014**, *403*, 110-113.

21. Mohsin, A.; Cross, N. G.; Liu, L.; Liu, P.; Duscher, G.; Gu, G. Experimentally determined edge orientation of triangular crystals of hexagonal boron nitride. *Phys. Status Solidi B* **2017**, *254*, 1700069.

22. Cao, D.; Shen, T.; Liang, P.; Chen, X.; Shu, H. Role of chemical potential in flake shape and edge properties of monolayer MoS2. *The Journal of Physical Chemistry C* **2015**, *119*, 4294-4301.

23. Li, X.; Dong, J.; Idrobo, J. C.; Puretzky, A. A.; Rouleau, C. M.; Geohegan, D. B.; Ding, F.; Xiao, K. Edge-controlled growth and etching of two-dimensional GaSe monolayers. *J. Am. Chem. Soc.* **2016**, *139*, 482-491.

24. Tay, R. Y.; Griep, M. H.; Mallick, G.; Tsang, S. H.; Singh, R. S.; Tumlin, T.; Teo, E. H. T.; Karna, S. P. Growth of large single-crystalline two-dimensional boron nitride hexagons on electropolished copper. *Nano Letters* **2014**, *14*, 839-846.

25. Tay, R. Y.; Tsang, S. H.; Loeblein, M.; Chow, W. L.; Loh, G. C.; Toh, J. W.; Ang, S. L.; Teo, E. H. T. Direct growth of nanocrystalline hexagonal boron nitride films on dielectric substrates. *Appl. Phys. Lett.* **2015**, *106*, 101901.

26. Ji, Y.; Calderon, B.; Han, Y.; Cueva, P.; Jungwirth, N. R.; Alsalman, H. A.; Hwang, J.; Fuchs, G. D.; Muller, D. A.; Spencer, M. G. Chemical Vapor Deposition Growth of Large Single-Crystal Mono-, Bi-, Tri-Layer Hexagonal Boron Nitride and Their Interlayer Stacking. *ACS Nano* **2017**, *11*, 12057-12066.

27. Kim, K. K.; Hsu, A.; Jia, X.; Kim, S. M.; Shi, Y.; Hofmann, M.; Nezich, D.; Rodriguez-Nieva, J. F.; Dresselhaus, M.; Palacios, T. Synthesis of monolayer hexagonal boron nitride on Cu foil using chemical vapor deposition. *Nano Letters* **2011**, *12*, 161-166.

28. Song, L.; Ci, L.; Lu, H.; Sorokin, P. B.; Jin, C.; Ni, J.; Kvashnin, A. G.; Kvashnin, D. G.; Lou, J.; Yakobson, B. I. Large scale growth and characterization of atomic hexagonal boron nitride layers. *Nano Letters* **2010**, *10*, 3209-3215.

29. Chatterjee, S.; Luo, Z.; Acerce, M.; Yates, D. M.; Johnson, A. C.; Sneddon, L. G. Chemical vapor deposition of boron nitride nanosheets on metallic substrates via decaborane/ammonia reactions. *Chemistry of Materials* **2011**, *23*, 4414-4416.

30. Auwärter, W.; Suter, H. U.; Sachdev, H.; Greber, T. Synthesis of one monolayer of hexagonal boron nitride on Ni (111) from B-Trichloroborazine $(ClBNH)_3$. *Chemistry of Materials* **2004**, *16*, 343-345.

31. Ismach, A.; Chou, H.; Ferrer, D. A.; Wu, Y.; McDonnell, S.; Floresca, H. C.; Covacevich, A.; Pope, C.; Piner, R.; Kim, M. J. Toward the controlled synthesis of hexagonal boron nitride films. *ACS Nano* **2012**, *6*, 6378-6385.

32. Lee, Y.; Liu, K.; Lu, A.; Wu, C.; Lin, C.; Zhang, W.; Su, C.; Hsu, C.; Lin, T.; Wei, K. Growth selectivity of hexagonal-boron nitride layers on Ni with various crystal orientations. *RSC Advances* **2011**, *2*, 111-115.

33. Gibb, A. L.; Alem, N.; Chen, J.; Erickson, K. J.; Ciston, J.; Gautam, A.; Linck, M.; Zettl, A. Atomic resolution imaging of grain boundary defects in monolayer chemical vapor deposition-grown hexagonal boron nitride. *J. Am. Chem. Soc.* **2013**, *135*, 6758-6761.

34. Gibb, A.; Alem, N.; Zettl, A. Low pressure chemical vapor deposition synthesis of hexagonal boron nitride on polycrystalline metal foils. *Phys. Status Solidi B* **2013**, *250*, 2727-2731.

35. Guo, N.; Wei, J.; Fan, L.; Jia, Y.; Liang, D.; Zhu, H.; Wang, K.; Wu, D. Controllable growth of triangular hexagonal boron nitride domains on copper foils by an improved low-pressure chemical vapor deposition method. *Nanotechnology* **2012**, *23*, 415605.

36. Li, Q.; Zou, X.; Liu, M.; Sun, J.; Gao, Y.; Qi, Y.; Zhou, X.; Yakobson, B. I.; Zhang, Y.; Liu, Z. Grain boundary structures and electronic properties of hexagonal boron nitride on Cu (111). *Nano Letters* **2015**, *15*, 5804-5810.

37. Nagashima, A.; Tejima, N.; Gamou, Y.; Kawai, T.; Oshima, C. Electronic structure of monolayer hexagonal boron nitride physisorbed on metal surfaces. *Phys. Rev. Lett.* **1995**, *75*, 3918.

38. Kim, G.; Jang, A.; Jeong, H. Y.; Lee, Z.; Kang, D. J.; Shin, H. S. Growth of high-crystalline, single-layer hexagonal boron nitride on recyclable platinum foil. *Nano Letters* **2013**, *13*, 1834-1839.

39. Lu, G.; Wu, T.; Yuan, Q.; Wang, H.; Wang, H.; Ding, F.; Xie, X.; Jiang, M. Synthesis of large single-crystal hexagonal boron nitride grains on Cu–Ni alloy. *Nature Communications* **2015**, *6*, 6160.

40. Stehle, Y.; Meyer III, H. M.; Unocic, R. R.; Kidder, M.; Polizos, G.; Datskos, P. G.; Jackson, R.; Smirnov, S. N.; Vlassiouk, I. V. Synthesis of hexagonal boron nitride monolayer: control of nucleation and crystal morphology. *Chemistry of Materials* **2015**, *27*, 8041-8047.

41. Wu, T.; Zhang, X.; Yuan, Q.; Xue, J.; Lu, G.; Liu, Z.; Wang, H.; Wang, H.; Ding, F.; Yu, Q. Fast growth of inch-sized single-crystalline graphene from a controlled single nucleus on Cu–Ni alloys. *Nature Materials* **2016**, *15*, 43.

42. Yin, J.; Yu, J.; Li, X.; Li, J.; Zhou, J.; Zhang, Z.; Guo, W. Large single-crystal hexagonal boron nitride monolayer domains with controlled morphology and straight merging boundaries. *Small* **2015**, *11*, 4497-4502.

43. Zhang, Z.; Liu, Y.; Yang, Y.; Yakobson, B. I. Growth mechanism and morphology of hexagonal boron nitride. *Nano Letters* **2016**, *16*, 1398-1403.

44. Liu, Y.; Bhowmick, S.; Yakobson, B. I. BN white graphene with “colorful” edges: The energies and morphology. *Nano Letters* **2011**, *11*, 3113-3116.

45. Zhao, R.; Li, F.; Liu, Z.; Liu, Z.; Ding, F. The transition metal surface passivated edges of hexagonal boron nitride (h-BN) and the mechanism of h-BN's chemical vapor deposition (CVD) growth. *Physical Chemistry Chemical Physics* **2015**, *17*, 29327-29334.

46. Liu, S.; Van Duin, A. C.; Van Duin, D. M.; Liu, B.; Edgar, J. H. Atomistic insights into nucleation and formation of hexagonal boron nitride on nickel from first-principles-based reactive molecular dynamics simulations. *ACS Nano* **2017**, *11*, 3585-3596.

47. Blöchl, P. E. Projector augmented-wave method. *Physical Review B* **1994**, *50*, 17953.

48. Kresse, G.; Hafner, J. Ab initio molecular dynamics for liquid metals. *Physical Review B* **1993**, *47*, 558.

49. Perdew, J. P.; Burke, K.; Ernzerhof, M. Generalized gradient approximation made simple. *Phys. Rev. Lett.* **1996**, *77*, 3865.

50. Kresse, G.; Furthmüller, J. Efficient iterative schemes for ab initio total-energy calculations using a plane-wave basis set. *Physical Review B* **1996**, *54*, 11169.

51. Methfessel, M.; Paxton, A. High-precision sampling for Brillouin-zone integration in metals. *Physical Review B* **1989**, *40*, 3616.

52. Auwärter, W.; Muntwiler, M.; Osterwalder, J.; Greber, T. Defect lines and two-domain structure of hexagonal boron nitride films on Ni (1 1 1). *Surf. Sci.* **2003**, *545*, L735-L740.

53. Grad, G.; Blaha, P.; Schwarz, K.; Auwärter, W.; Greber, T. Density functional theory investigation of the geometric and spintronic structure of h-BN/Ni (111) in view of photoemission and STM experiments. *Physical Review B* **2003**, *68*, 085404.

54. Huda, M.; Kleinman, L. h-BN monolayer adsorption on the Ni (111) surface: A density functional study. *Physical Review B* **2006**, *74*, 075418.

55. Diaz, J. G.; Ding, Y.; Koitz, R.; Seitsonen, A. P.; Iannuzzi, M.; Hutter, J. Hexagonal boron nitride on transition metal surfaces. *Theoretical Chemistry Accounts* **2013**, *132*, 1350.

56. Van Duin, A. C.; Dasgupta, S.; Lorant, F.; Goddard, W. A. ReaxFF: a reactive force field for hydrocarbons. *The Journal of Physical Chemistry A* **2001**, *105*, 9396-9409.

Chapter 9 - Conclusions

In this dissertation, large-scale, high-quality bulk hBN single crystals were successfully formed from Ni-Cr and Fe-Cr solvents at atmospheric pressure. The use of Fe-Cr mixture provides a lower cost alternative to the more common Ni-Cr solvent for growing comparable crystals. A tiltable furnace was used to separate free-standing hBN from metal flux while it is still liquid. The clear and colorless crystals have a maximum domain size of around 2 mm and a thickness of around 200 μm. The XRD, Raman and PL spectra indicate the hBN crystals have a high quality and low defect and impurity density.

A new growth method for monoisotopic hBN single crystals, i.e. $h^{10}BN$ and $h^{11}BN$, was developed, by which hBN single crystals were grown using a Ni-Cr solvent and pure boron and nitrogen sources at atmospheric pressure. The quality of the monoisotopic hBN crystals produced this way is comparable to the crystals grown from BN sources with the natural boron abundance. Several characterizations demonstrate that the inherent physical and chemical properties of hBN can be tuned by the isotopic substitutions, which opens the door to isotopically engineering the performance of hBN devices.

In order to investigate the mechanism of hBN growth, multiscale modeling combining density functional theory (DFT) and reactive molecular dynamics (rMD) was performed. The DFT calculations were performed to describe the adsorption and reaction energetics of the hBN building-block species on Ni surface. Those quantum mechanical data were then used to generate a classical description of the Ni−B and Ni−N pair interactions within the formulation of the reactive force field, ReaxFF. Detailed examination of rMD trajectories showed that the nucleation initiates from the growth of linear BN chains, which evolve into branched and then hexagonal lattices. Moreover, molecular dynamics simulations demonstrated that the

thermodynamics preference of hBN geometries varying from triangle to hexagonal can be tuned by B to N molar ratios, and gas phase N_2 partial pressure, which is also supported by quantum mechanics calculations.

Appendix A – ReaxFF Force Field for Ni/B/N System

```
39      ! Number of general parameters
  50.0000    !Overcoordination parameter
   9.5469    !Overcoordination parameter
  26.5405    !Valency angle conjugation parameter
   1.7224     !Triple bond stabilisation parameter
   6.8702     !Triple bond stabilisation parameter
  60.4850     !C2-correction
   1.0588     !Undercoordination parameter
   4.6000     !Triple bond stabilisation parameter
  12.1176    !Undercoordination parameter
  13.3056    !Undercoordination parameter
 -70.5044    !Triple bond stabilization energy
   0.0000     !Lower Taper-radius
  10.0000     !Upper Taper-radius
   2.8793     !Not used
  33.8667     !Valency undercoordination
   6.0891     !Valency angle/lone pair parameter
   1.0563     !Valency angle
   2.0384    !Valency angle parameter
   6.1431    !Not used
   6.9290    !Double bond/angle parameter
   0.3989    !Double bond/angle parameter: overcoord
```

```
 3.9954      !Double bond/angle parameter: overcoord
-2.4837      !Not used
 5.7796      !Torsion/BO parameter
10.0000      !Torsion overcoordination
 1.9487      !Torsion overcoordination
-1.2327      !Conjugation 0 (not used)
 2.1645      !Conjugation
 1.5591      !vdWaals shielding
 0.1000      !Cutoff for bond order (*100)
 2.1365      !Valency angle conjugation parameter
 0.6991      !Overcoordination parameter
50.0000      !Overcoordination parameter
 1.8512      !Valency/lone pair parameter
 0.5000      !Not used
20.0000      !Not used
 5.0000      !Molecular energy (not used)
 0.0000      !Molecular energy (not used)
 2.6962      !Valency angle conjugation parameter

3    ! Nr of atoms; cov.r; valency; a.m; Rvdw; Evdw; gammaEEM; cov.r2;#
       alfa; gammavdW; valency; Eunder; Eover; chiEEM; etaEEM; n.u.
       cov r3; Elp; Heat inc.; n.u.; n.u.; n.u.; n.u.
       ov/un; val1; n.u.; val3, vval4
```

B 1.5446 3.0000 10.8110 1.6500 0.1008 0.9925 1.0000 3.0000

10.0681 2.3647 3.0000 0.7036 80.0000 5.4904 7.3367 0.0000

-1.3000 0.0000 151.3700 9.0516 2.7272 1.0943 0.0000 0.0000

-2.5000 4.0000 1.0564 3.0000 2.8413 0.0000 0.0000 0.0000

N 1.6157 3.0000 14.0000 1.9376 0.1203 1.0000 1.2558 5.0000

9.4267 26.8500 4.0000 8.6294 100.0000 7.6099 7.7500 2.0000

1.0439 0.1000 119.9837 1.7640 2.7409 2.3814 0.9745 0.0000

-6.5798 4.4843 1.0183 4.0000 2.8793 0.0000 0.0000 0.0000

Ni 1.8201 2.0000 58.6900 1.9449 0.1880 0.8218 0.1000 2.0000

12.1594 3.8387 2.0000 0.0000 0.0000 4.8038 7.3852 0.0000

-1.0000 0.0000 95.6300 50.6786 0.6762 0.0981 0.8563 0.0000

-3.7733 3.6035 1.0338 8.0000 2.5791 0.0000 0.0000 0.0000

6 ! Nr of bonds; Edis1; LPpen; n.u.; pbe1; pbo5; 13corr; pbo6;

pbe2; pbo3; pbo4; n.u.; pbo1; pbo2; ovcorr

1 1 83.1999 0.0000 0.0000 1.0000 -0.2500 1.0000 25.0000 0.4184

0.7965 -0.2000 25.0000 1.0000 -0.0830 8.6364 1.0000 0.0000

1 2 100.5825 112.2528 0.0000 0.9000 -0.2500 1.0000 25.0000 1.0000

1.0000 -0.2292 10.2908 1.0000 -0.1853 6.4451 1.0000 0.0000

2 2 134.6492 66.2329 149.2707 -0.7228 -0.1000 1.0000 19.0850 1.0000

0.6060 -0.2050 9.7308 1.0000 -0.1791 5.8008 1.0000 0.0000

3 3 91.2220 0.0000 0.0000 -0.2538 -0.2000 0.0000 16.0000 0.2688

1.4651 -0.2000 15.0000 1.0000 -0.1435 4.3908 0.0000 0.0000

1 3 101.7227 0.0000 0.0000 0.3316 -0.2000 1.0000 16.0000 0.2419

0.9875 -0.2500 15.0000 1.0000 -0.1091 5.2794 1.0000 0.0000

2 3 104.1708 0.0000 0.0000 0.2256 -0.2000 1.0000 16.0000 0.0100

0.8772 -0.2500 15.0000 1.0000 -0.2048 5.1541 1.0000 0.0000

3 ! Nr of off-diagonal terms; Ediss; Ro; gamma; rsigma; rpi; rpi2

1 2 0.0400 1.7000 9.8622 1.4375 1.2210 -1.0000

1 3 0.0800 1.7000 10.2506 1.6205 -1.0000 -1.0000

2 3 0.0800 1.8549 9.9357 1.5291 -1.0000 -1.0000

36 ! Nr of angles; at1; at2; at3; Thetao,o; ka; kb; pv1; pv2

1 1 1 66.8940 9.9560 6.1576 0.0000 3.8304 0.0000 2.1366

1 1 2 50.0000 38.5418 2.9811 0.0000 2.9774 0.0000 2.2185

2 1 2 70.3653 30.1549 3.2434 0.0000 3.0000 0.0000 1.0400

1 2 1 58.3386 21.2632 2.2766 0.0000 3.0000 0.0000 1.1171

1 2 2 82.3402 29.9227 0.1000 0.0000 3.0000 0.0000 2.7918

2 2 2 90.0000 44.3028 1.6659 0.0000 0.7529 0.0000 1.2398

1 1 3 80.5510 10.4981 3.5765 0.0000 0.7750 0.0000 2.0511

1 3 1 60.5604 38.8732 6.1178 0.0000 0.1285 0.0000 1.8574

3 1 3 87.2205 22.6638 3.4715 0.0000 0.1000 0.0000 1.0958

1 3 3 90.0000 16.3568 1.6982 0.0000 1.9165 0.0000 3.6108

2 2 3 11.1039 7.6592 2.8015 0.0000 3.9452 0.0000 1.6594

2 3 2 14.9604 26.4618 7.9541 0.0000 0.2723 0.0000 1.0000

3 2 3 90.0000 17.9145 8.0000 0.0000 3.0994 0.0000 3.3531

2 3 3 66.7138 4.8484 3.0630 0.0000 1.4068 0.0000 1.0377

1 2 3 87.3151 9.0813 7.9702 0.0000 0.1000 0.0000 1.9026

1 3 2 67.3916 11.1627 4.7300 0.0000 0.1736 0.0000 1.0000

2 1 3 60.9246 25.7099 6.8799 0.0000 4.0000 0.0000 2.6922

9 ! Nr of torsions; at1; at2; at3; at4;;V1;V2;V3;V2(BO);vconj;n.u;n

0 1 1 0 0.0000 50.0000 -0.0244 -4.4230 0.0000 0.0000 0.0000

0 1 2 0 0.0000 19.1277 0.2335 -5.4108 0.0000 0.0000 0.0000

0 2 2 0 2.0000 90.0000 -0.7837 -9.0000 -2.0000 0.0000 0.0000

3 1 1 3 0.0000 50.0000 0.0100 -4.4230 0.0000 0.0000 0.0000

3 1 2 3 0.0000 15.8805 0.5176 -4.4637 0.0000 0.0000 0.0000

3 2 2 3 0.0000 88.8295 0.0100 -8.0000 -2.0000 0.0000 0.0000

0 ! Nr of hydrogen bonds;at1;at2;at3;Rhb;Dehb;vhb1